

CHARACTERISATION OF THE CELLULAR AND TRANSCRIPTOMIC PROFILE OF NEUROVASCULAR CELLS IN THE APOE^{-/-} MOUSE MODEL OF ATHEROSCLEROSIS

By

Monica Alejandra Rebollar Guagnelli

(BSc, MSc)

Submitted for the degree of Doctor of Philosophy (PhD)

*Sheffield Institute for Translational Neuroscience
University of Sheffield*

September 2021



ACKNOWLEDGEMENTS

I wish to show my gratitude to my supervisor, Prof. Steve Wharton, for his guidance and support throughout my PhD. Thank you for your support and for trusting me to take this project forward.

I will be forever thankful to Dr. Julie Simpson for her continuous help and encouragement throughout my postgraduate studies. Thank you for sharing your knowledge and telling me to always make lots of lists. You helped me to feel calm and confident even when the whole world was struggling to keep optimistic.

I would like to thank my secondary supervisor Dr. Sheila Francis for sharing her valuable knowledge and advice. I would also like to thank Dr. Irina Vazques and Dr. Rachel Waller for their help in the lab, their advice and patience. Thank you to Dr. Paul Heath, Catherine Gelsthorpe, Lynne Baxter and Daniel Fillingham and to all members of the Neuropathology group for your assistance during my PhD.

To my friends in England, that are now my family away from home. Thank you for making me laugh and being there for me. Thanks to Lily and Em for your understanding and for teaching me how to have fun outside the lab. To Matt and Tobi, for the endless conversations over multiple cups of coffee. To Jess, Anushka, Charlotte, Mirinda, Meltem, this journey would not have been the same without you.

I would not have gotten through writing my thesis without Alex, you have been there for me at my lowest and still managed to make me laugh. Your positive and contagious attitude towards life encouraged me more than you will ever know.

Finally to my family, I would not be here without you. You always made me believe I was capable and never let me give up. Thank you to parents for their encouragement and for providing me with every opportunity in life, even if it meant leaving them behind.

This achievement would not have been possible without my best friend and partner in crime, Ruy, thank you understanding me, speak my language and remind me to drink water.

ABSTRACT

Systemic atherosclerosis (ATH) is a chronic disease affecting major blood vessels, including cerebral blood supply. Cerebral microvascular dysfunction is implicated in the pathogenesis of dementia, but how systemic vascular disease affects the microvasculature within the central nervous system (CNS) is currently unknown. Evidence of neuroinflammatory changes in the ATH Apolipoprotein E knockout (*ApoE*^{-/-}) mouse model suggests impairment of the neurovascular unit (NVU). The hypothesis is that ATH is associated with changes in the brain microvasculature, including glial responses that could lead to dysfunction of the NVU and contribute to neurodegeneration.

Detailed immunohistological assessment of astrocytes (GFAP), microglia (IBA-1) and endothelial cells (ICAM-1) was performed on two cohorts of *ApoE*^{-/-} mice fed on a high-fat diet (Atherosclerotic n = 6) and a normal low-fat diet (Control = 6). Iba-1⁺ microglia were a prominent feature of all brain regions from atherosclerotic mice with significantly higher levels of % area of immunoreactivity detected in the hippocampus, corpus callosum (CC), and cerebral cortex (COR). ICAM1⁺ microglia have also detected an increase in atherosclerotic mice in all brain areas investigated. GFAP⁺ astrocytes and ICAM1⁺ endothelial cells were significantly higher in the CC. Gene expression profiling was performed on the hippocampus of *ApoE*^{-/-} mice cohort 2 using laser capture microdissection and microarray analysis. Although cohort 2 did not replicate cohort 1 cellular characterisation findings, significant down-regulation of key proteins involved in the calcium signalling pathway and up-regulated of metabolic and immune-response pathways were found. Validation using qRT-PCR showed no significant difference in the immune-related pathways and contradictory results of metabolic pathways.

The current study demonstrates the presence of neuroinflammation in the absence of cerebral occlusion, suggesting the mechanisms associated with systemic atherosclerosis also affect the CNS. Furthermore, this research is the first to characterise IBA-1, GFAP and ICAM-1 in the whole hippocampus, COR and CC in atherosclerotic mice. The research presented in this thesis suggests that changes driving systemic atherosclerosis have an effect on neuroinflammation potentially leading to metabolic and BBB changes followed by neurodegeneration and cognitive impairment.

TABLE OF CONTENTS

- Acknowledgements – ii •
- Abstract – iv •
- Table of contents – vi •
- List of figures – xii •
- List of tables – xx •
- Abbreviations – xxiii •

CHAPTER I

INTRODUCTION TO ATHEROSCLEROSIS AND VASCULAR DEMENTIA	1
1.1 Systemic atherosclerosis	2
1.2 Systemic atherosclerosis and cerebrovascular disease.....	5
1.2.1 Cerebral small vessel disease	7
1.2.2 Neurovascular dementia	7
1.2.3 Mixed dementia	8
1.3 Proposed mechanisms underlying the pathology in vascular dementia.....	9
1.3.1 Genetical influences on vascular dementia	9
1.4 Proposed pathophysiology of atherosclerosis in the central nervous system – inflammation unrelated to occlusion.....	10
1.4.1 The neurovascular unit	10
1.4.2 Neurovascular unit dysfunction.....	25
1.5 Cholesterol in the brain and peripheral circulation: animal models to study atherosclerosis and the brain	27
1.5.1 Brain cholesterol homeostasis.....	27
1.5.2 Apolipoprotein E knockout (<i>ApoE^{-/-}</i>) to study atherosclerosis.....	28
1.5.3 Proprotein convertase subtilisin/ kexin type 9 overexpressing adeno-associated virus (PCSK9 -AAV8)	30

1.6	Neuroinflammation in association with atherosclerosis and a high-fat diet..	30
1.7	Hypothesis of this study.....	31
1.8	Aims and objectives of this research.....	31

CHAPTER II

Materials and methods.....	33
2.1 ApoE^{-/-} mouse cohort.....	34
2.2 Pcsk9 induced mouse cohort.....	34
2.3 Environment and diet.....	35
2.4 Brain dissection and tissue processing.....	37
2.5 Histological characterisation	Error! Bookmark not defined.
2.5.1 Haematoxylin & Eosin (H&E) stain	Error! Bookmark not defined.
2.5.2 Luxol Fast Blue	40
2.5.3 Identification of the neuroanatomical regions of interest	40
2.5.4 Immunohistochemistry (IHC)	40
2.5.5 Immunofluorescence	46
2.5.6 Semi-quantitative analysis	48
2.5.7 Quantitative image analysis.....	48
2.5.8 Statistical analysis	52
2.6 Transcriptomics.....	53
2.6.1 Tissue source	53
2.6.2 LCM sample preparation - Toluidine Blue	53
2.6.3 Laser capture microdissection	55
2.6.4 Pre-LCM RNA integrity analysis	55
2.6.5 RNA extraction.....	57
2.6.6 RNA extraction quality control	59
2.6.7 Microarray analysis.....	59
2.6.8 Two round linear RNA amplification	60

2.6.9	Microarray data analysis and quality control.....	62
2.7	Validation RT-PCR and qRT-PCR.....	64
2.7.1	cDNA synthesis for RT-PCR.....	64
2.7.2	Agarose gel electrophoresis of PCR products.....	65
2.7.3	Quantitative real-time Polymerase Chain Reaction (qRT-PCR).....	66
2.7.4	qRT-PCR Data Analysis.....	67
2.7.5	Statistical analysis of qRT-PCR data.....	70

CHAPTER III

	NEUROPATHOLOGICAL CHARACTERIZATION OF THE APOLIPOPROTEIN E KNOCKOUT MOUSE: A MODEL OF SYSTEMIC ATHEROSCLEROSIS	71
3.1	Introduction.....	72
3.2	Aims and objectives.....	74
3.3	Results.....	75
3.3.1	Histological assessment of the <i>ApoE^{-/-}</i> mouse brain after normal or high-fat diet feeding 75	
3.3.2	Assessment of Cells of the NVU.....	78
3.3.3	Increased ionized calcium-binding adaptor molecule 1 (IBA-1) immunoreactive microglia in atherosclerotic <i>ApoE^{-/-}</i> cohort 1 mice.....	78
3.3.4	The immunoreactive profile of IBA-1 is not consistent across <i>ApoE^{-/-}</i> mouse cohorts..	83
3.3.5	Regional variation and glial fibrillary acidic protein expression in astrocytes	96
3.3.6	Glial fibrillary acidic protein is increased in astrocytes in the corpus callosum of atherosclerotic <i>ApoE^{-/-}</i> mice.....	96
3.3.7	Intracellular adhesion molecule -1 (ICAM-1) immunoreactivity expression in both <i>ApoE^{-/-}</i> mice cohorts.	108
3.3.8	Inconsistent PDGFR- β staining on FFPE mouse tissue.	118
3.3.9	Summary of <i>ApoE^{-/-}</i> control and atherosclerotic mice characterisation	121
3.4	Discussion	122
3.4.1	Regional variation in cell activation across atherosclerotic and control mice	122

3.4.2	Increased expression of IBA-1 and ICAM-1 by microglia is a feature of murine atherosclerosis (cohort 1).	125
3.4.3	Increased endothelial cell activation and astrogliosis in the corpus callosum of murine atherosclerosis (cohort 1).	129
3.4.4	Limitations and future immunohistochemical studies	136
3.4.5	Conclusion	141

CHAPTER IV

NEUROINFLAMMATION IN PROPROTEIN CONVERTASE SUBTILISIN/KEXIN

TYPE 9 OVER EXPRESSING ADENO-ASSOCIATED VIRUS MOUSE MODEL.. 142

4.1	Introduction.....	143
4.2	Aims and objectives.....	145
4.3	Results.....	146
4.3.1	Astrocytic expression of glial fibrillary acidic protein in the proprotein convertase subtilisin/kexin type 9 (PCSK9) induced mouse model	146
4.3.2	Expression of ICAM-1 in blood vessels and microglia on PCSK9 induced mouse model of atherosclerosis.....	150
4.3.3	Ionized calcium-binding adaptor molecule 1 (IBA-1) immunoreactivity in the PCSK9 induced atherosclerotic mouse model	157
4.3.4	Neuroinflammatory response to atherosclerosis in PCSK9 induced mice compared to <i>ApoE^{-/-}</i> mice.....	161
4.3.5	Summary of PCSK9 induced control and atherosclerotic mice characterisation.....	187
4.4	Discussion	188
4.4.1	Comparison of neuroinflammation in the PCSK9 induced and <i>ApoE^{-/-}</i> mouse models of atherosclerosis.....	189
4.4.2	Endothelial cell activation in the cerebral cortex of PCSK9 induced mice is higher than in <i>ApoE^{-/-}</i> mice cohort 2	190
4.4.3	The effect of atherosclerosis on PCSK9 induced mouse brain.	191
4.4.4	Possible link between atherosclerotic PCSK9 induced mice and neuroinflammation ..	192

4.4.5	Limitations.....	193
4.4.6	Conclusion	194

CHAPTER V

MICROARRAY ANALYSIS OF THE HIPPOCAMPUS TRANSCRIPTOME IN APOLIPOPROTEIN E KNOCKOUT MOUSE MODEL OF ATHEROSCLEROSIS 195

5.1	Introduction.....	196
5.2	Aims and objectives.....	198
5.3	Results.....	199
5.3.1	Characterisation and isolation of the <i>ApoE^{-/-}</i> mouse hippocampus for gene expression analysis.....	199
5.3.2	Microarray quality control measures	202
5.3.3	Microarray analysis	209
5.3.4	Functional Enrichment Analysis using DAVID bioinformatics tool	214
5.3.5	Pathway enrichment analysis using IMPaLA	215
5.3.6	Pathways of interest	222
5.3.7	Validation of microarray candidate gene expression by qRT-PCR.....	225
5.3.8	Summary of transcriptomic analysis of control and atherosclerotic <i>ApoE^{-/-}</i> cohort 2 hippocampus	Error! Bookmark not defined.
5.4	Discussion	230
5.4.1	Atherosclerotic <i>ApoE^{-/-}</i> mouse cohort 2 presented changes in metabolic, lipid and myelin related transcripts Atherosclerosis induced by a high-fat diet induces changes in the transcriptome of.....	231
5.4.2	Differentially expressed genes associated with mitochondrial metabolic pathways	233
5.4.3	Down-regulation of calcium transport and cAMP pathways	236
5.4.4	Increased immune response	239
5.4.5	Limitations.....	241
5.4.6	Conclusion	244

Chapter VII

GENERAL DISCUSSION	246
6.1 Histological characterisation of control and atherosclerotic mouse model	248
6.2 Different atherosclerotic mice models display similar patterns of inflammation.....	249
6.3 Transcriptomic profiling of ApoE ^{-/-} mice identify dysregulation of calcium signalling.	249
6.4 Potential drivers of the observed changes.....	250
6.5 Future studies and limitations	251
6.6 Conclusion.....	254
References	256
Appendices	I
Appendix I: Mouse cohorts information	I
Appendix II: Laboratory Solutions.....	IV
Appendix III: Antibody optimisation.....	7
Appendix IV: Characterisation of the thalamus and striatum of ApoE ^{-/-} cohort 1 mice	12
Appendix VI: qRT-PCR of the cerebral cortex of ApoE ^{-/-} cohort 2 mice.....	19
Appendix VI: List of differentially expressed transcripts in the hippocampus of control and atherosclerotic ApoE ^{-/-} mouse cohort 2.....	20

LIST OF FIGURES

Chapter I

Figure 1.1 Schematic of systemic atherosclerosis	4
Figure 1.2 Representation of the neurovascular unit.....	12

Chapter II

Figure 2.1 Summary of <i>ApoE</i> ^{-/-} and PCSK9 induced mice and the dissected tissue	39
Figure 2.2 Luxol fast blue staining of control and atherosclerotic <i>ApoE</i> ^{-/-} mouse brains to identify key regions of interest	42
Figure 2.3 Schematic of the immunohistochemistry ABC-HRP process	47
Figure 2.4 Semi-quantitative analysis of GFAP immunostaining.....	50
Figure 2.5. Representative image of the percentage (%) area of immunoreactivity quantification	51
Figure 2.6 Guide images used to obtained the hippocampus and cerebral cortex from frozen mouse brain sections and representative image of toluidine blue <i>ApoE</i> ^{-/-} control cohort 2 mice for LCM	54
Figure 2.7 LCM of the hippocampus of an <i>ApoE</i> ^{-/-} cohort 2 mice under the microscope	56
Figure 2.8 PicoPure RNA extraction process from tissue isolated using LCM.....	58
Figure 2.9. Process of two round linear amplification and labelling of RNA obtain from LCM of <i>ApoE</i> ^{-/-} mouse hippocampus	63

Chapter III

Figure 3.1 Histological comparison of the hippocampus and corpus callosum between control and atherosclerotic <i>ApoE</i> ^{-/-} mouse model.	77
Figure 3.2 Representation of negative controls.	79

Figure 3.3 Representative images of the corpus callosum showing increased IBA-1 microglia immunoreactivity in <i>ApoE</i> ^{-/-} cohort 1 atherosclerotic mice.	80
Figure 3.4 Representative images of the cerebral cortex showing increased IBA-1 microglia immunoreactivity in <i>ApoE</i> ^{-/-} cohort 1 atherosclerotic mice	81
Figure 3.5 Representative images of the hippocampus showing increased IBA-1 microglia immunoreactivity in <i>ApoE</i> ^{-/-} cohort 1 atherosclerotic mice	82
Figure 3.6 Increased percentage (%) area of microglia IBA-1 immunoreactivity the corpus callosum, cerebral cortex and hippocampus of atherosclerotic cohort 1 <i>ApoE</i> ^{-/-} mice compared to controls.	84
Figure 3.7 Inter-run control of IBA-1 staining comparing <i>ApoE</i> ^{-/-} cohort one hippocampus of atherosclerotic and control mice	85
Figure 3.8 Representative images of the corpus callosum showing IBA-1 microglia immunoreactivity in control and atherosclerotic <i>ApoE</i> ^{-/-} cohort 2 mice	86
Figure 3.9 Representative images of the cerebral cortex showing IBA-1 microglia immunoreactivity in control and atherosclerotic <i>ApoE</i> ^{-/-} cohort 2 mice	87
Figure 3.10 Representative images of the hippocampus showing IBA-1 microglia immunoreactivity in control and atherosclerotic <i>ApoE</i> ^{-/-} cohort 2 mice	88
Figure 3.11 Representative images comparing microglial IBA-1 immunoreactivity on the hippocampus of both <i>ApoE</i> ^{-/-} mouse cohorts stained at different time points.	89
Figure 3.12 IBA-1 immunoreactivity differs between <i>ApoE</i> ^{-/-} cohorts.....	91
Figure 3.13 Analysis of the percentage (%) area of microglia IBA-1 immunoreactivity the corpus callosum, cerebral cortex and hippocampus of control and atherosclerotic cohort 2 <i>ApoE</i> ^{-/-} mice	92

Figure 3.14. Representative image showing IBA-1 microglia immunoreactivity in the hippocampus of cohort 1 <i>ApoE</i> ^{-/-} mice controls and atherosclerotic mice during simultaneous cohort staining.	93
Figure 3.15 Representative image showing IBA-1 microglia immunoreactivity in the hippocampus of cohort 1 <i>ApoE</i> ^{-/-} mice controls and atherosclerotic mice during simultaneous cohort staining.	94
Figure 3.16 Comparison analysis of the percentage (%) area of microglia IBA-1 immunoreactivity the corpus callosum, cerebral cortex and hippocampus of control and atherosclerotic <i>ApoE</i> ^{-/-} mice cohort 1 and 2 (simultaneous staining).....	95
Figure 3.17 Analysis of GFAP ⁺ astrocytes histological characterisation of cohort 1 <i>ApoE</i> ^{-/-} mice	98
Figure 3.18 Representative image showing astrocyte expression of GFAP immunoreactivity in the corpus callosum of <i>ApoE</i> ^{-/-} cohort 1 mice	101
Figure 3.19 Representative image showing astrocyte expression of GFAP immunoreactivity in the cerebral cortex of <i>ApoE</i> ^{-/-} cohort 1 mice	102
Figure 3.20 Representative image showing astrocyte expression of GFAP immunoreactivity in the corpus callosum of <i>ApoE</i> ^{-/-} cohort 1 mice	103
Figure 3.21 Representative image comparing astrocyte GFAP immunoreactivity on the hippocampus of both <i>ApoE</i> ^{-/-} mouse cohorts stained at different time points.	104
Figure 3.22 GFAP immunoreactivity differs between <i>ApoE</i> ^{-/-} cohorts.	105
Figure 3.23 Increased percentage (%) area of astrocytes GFAP immunoreactivity in the corpus callosum of atherosclerotic cohort 1 <i>ApoE</i> ^{-/-} mice compared to controls.	107
Figure 3.24. Representative image showing co-localisation of ICAM-1 with IBA1 ⁺ microglial cells	109

Figure 3.25. Representative image showing endothelial cell and microglia expression of ICAM-1 immunoreactivity in the corpus callosum of <i>ApoE</i> ^{-/-} cohort 1 mice	110
Figure 3.26 Representative image showing endothelial cell and microglia expression of ICAM-1 immunoreactivity in the cerebral cortex of <i>ApoE</i> ^{-/-} cohort 1 mice	111
Figure 3.27. Representative image showing endothelial cell and microglia expression of ICAM-1 immunoreactivity in the hippocampus of <i>ApoE</i> ^{-/-} cohort 1 mice.....	112
Figure 3.28 Representative image showing endothelial cell and microglia expression of ICAM-1 immunoreactivity in the corpus callosum of <i>ApoE</i> ^{-/-} cohort 2 mice	114
Figure 3.29 Representative image showing endothelial cell and microglia expression of ICAM-1 immunoreactivity in the cerebral cortex of <i>ApoE</i> ^{-/-} cohort 2 mice	115
Figure 3.30 Representative image showing endothelial cell and microglia expression of ICAM-1 immunoreactivity in the hippocampus of <i>ApoE</i> ^{-/-} cohort 2 mice.....	116
Figure 3.31. Comparison analysis of the percentage (%) area of endothelial cells ICAM-1 immunoreactivity the corpus callosum, cerebral cortex and hippocampus of control and atherosclerotic <i>ApoE</i> ^{-/-} mice cohort 1 and 2.....	117
Figure 3.32. Increased percentage (%) area of microglia ICAM-1 immunoreactivity the corpus callosum, cerebral cortex and hippocampus of atherosclerotic cohort 1 <i>ApoE</i> ^{-/-} mice compared to controls.	119
Figure 3.33. Representative image showing pericyte pattern of staining using PDGFR-β revealed different patterns of immunoreactivity between experiments.....	120

Chapter IV

Figure 4.1 Representative image showing astrocyte expression of GFAP immunoreactivity in the corpus callosum of PCSK9 induced mice	147
Figure 4.2 Representative image showing astrocyte expression of GFAP immunoreactivity in the cerebral cortex of PCSK9 induced mice	148

Figure 4.3 Representative image showing astrocyte expression of GFAP immunoreactivity in the hippocampus of PCSK9 induced mice	149
Figure 4.4 Analysis of the percentage (%) (%) area of astrocytes GFAP immunoreactivity the corpus callosum, cerebral cortex and hippocampus of control and atherosclerotic PCSK9 induced mice	151
Figure 4.5 Representative image showing endothelial cells and microglia expression of ICAM-1 immunoreactivity in the corpus callosum of PCSK9 induced mice.....	152
Figure 4.6 Representative image showing endothelial cells and microglia expression of ICAM-1 immunoreactivity in the cerebral cortex of PCSK9 induced transduced mice	153
Figure 4.7 Representative image showing endothelial cells and microglia expression of ICAM-1 immunoreactivity in the hippocampus of PCSK9 induced mice	154
Figure 4.8 Analysis of the percentage (%) area of endothelial cells and microglia ICAM-1 immunoreactivity the corpus callosum, cerebral cortex and hippocampus of control and atherosclerotic PCSK9 induced mice	156
Figure 4.10 Representative image showing microglia expression of IBA-1 immunoreactivity in the corpus callosum of PCSK9 induced mice.....	158
Figure 4.11 Representative image showing microglia expression of IBA-1 immunoreactivity in the cerebral cortex of PCSK9 induced mice	159
Figure 4.12 Representative image showing microglia expression of IBA-1 immunoreactivity in the cerebral cortex of PCSK9 induced mice	160
Figure 4.13 Analysis of the percentage (%) area of microglia IBA-1 immunoreactivity the corpus callosum, cerebral cortex and hippocampus of control and atherosclerotic PCSK9 induced mice.....	162

Figure 4.14 Representative image comparing ICAM-1 immunoreactive blood vessels on the hippocampus of controls and atherosclerotic PCSK9 induced mice and <i>ApoE</i> ^{-/-} cohort 1 and 2.....	164
Figure 4.15 Representative image comparing ICAM-1 immunoreactive blood vessels on the cerebral cortex of controls and atherosclerotic PCSK9 induced mice and <i>ApoE</i> ^{-/-} cohort 1 and 2	165
Figure 4.16 Representative image comparing ICAM-1 immunoreactive blood vessels on the hippocampus of controls and atherosclerotic PCSK9 induced mice and <i>ApoE</i> ^{-/-} cohort 1 and 2.....	166
Figure 4.17 Analysis of the fold change between controls and atherosclerotic PCSK9 induced mice express higher change of ICAM-1 immunoreactive endothelial cells than <i>ApoE</i> ^{-/-} cohort 1 in the cerebral cortex.....	167
Figure 4.18 Representative image comparing ICAM-1 immunoreactive microglia on the hippocampus of controls and atherosclerotic PCSK9 induced mice and <i>ApoE</i> ^{-/-} cohort 1 and 2.....	170
Figure 4.19 Representative image comparing ICAM-1 immunoreactive microglia on the corpus callosum of controls and atherosclerotic PCSK9 induced mice and <i>ApoE</i> ^{-/-} cohort 1 and 2.....	171
Figure 4.20 Representative image comparing ICAM-1 immunoreactive microglia on the cerebral cortex of controls and atherosclerotic PCSK9 induced mice and <i>ApoE</i> ^{-/-} cohort 1 and 2.....	172
Figure 4.21 Analysis of the fold change between controls and atherosclerotic of PCSK9 induced, <i>ApoE</i> ^{-/-} cohort 1 and cohort 2 in the cerebral cortex, corpus callosum and hippocampus.	173

Figure 4.22 Representative image comparing IBA-1 immunoreactive microglia on the cerebral cortex of controls and atherosclerotic PCSK9 induced mice and <i>ApoE</i> ^{-/-} cohort 1 and 2.....	176
Figure 4.23 Representative image comparing IBA-1 immunoreactive microglia on the corpus callosum of controls and atherosclerotic PCSK9 induced mice and <i>ApoE</i> ^{-/-} cohort 1 and 2.....	177
Figure 4.24 Representative image comparing IBA-1 immunoreactive microglia on the hippocampus of controls and atherosclerotic PCSK9 induced mice and <i>ApoE</i> ^{-/-} cohort 1 and 2.....	178
Figure 4.25 Analysis of the fold change between controls and atherosclerotic of PCSK9 induced, <i>ApoE</i> ^{-/-} cohort 1 and cohort 2 in the cerebral cortex, corpus callosum and hippocampus.	179
Figure 4.26 Representative image comparing GFAP immunoreactive astrocytes on the hippocampus of controls and atherosclerotic PCSK9 induced mice and <i>ApoE</i> ^{-/-} cohort 1 and 2.....	182
Figure 4.27 Representative image comparing GFAP immunoreactive astrocytes on the corpus callosum of controls and atherosclerotic PCSK9 induced mice and <i>ApoE</i> ^{-/-} cohort 1 and 2.....	183
Figure 4.28 Representative image comparing GFAP immunoreactive astrocytes on the cerebral cortex of controls and atherosclerotic PCSK9 induced mice and <i>ApoE</i> ^{-/-} cohort 1 and 2.....	184
Figure 4.29 Comparison between GFAP fold change of control mice to atherosclerosis in PCSK9 induced and <i>ApoE</i> ^{-/-} mice.....	185

Chapter V

Figure 5.1 RNA integrity of pre- and post- LCM RNA profile	200
Figure 5.2 Poly-A RNA spike-in controls	204
Figure 5.3 Hybridisation control assessment s for the hippocampus of controls and atherosclerotic mice.....	206
Figure 5.4 Overall signal intensities histogram for the periventricular microarrays .	207
Figure 5.5 Relative log expression (RLE) box plots for the hippocampus arrays....	208
Figure 5.6 Volcano plot of differential gene expression of control and atherosclerotic <i>ApoE^{-/-}</i> cohort 2 mice hippocampus.....	210
Figure 5.7 PCA Plot.....	211
Figure 5.8 Validation of neuroinflammatory and oxidative phosphorylation up-regulated genes in the hippocampus by qRT-PCR.	227

LIST OF TABLES

Chapter I

Table 1.1 Description of diverse microglia morphology.....	21
Table 1.2 Detailed microglial markers	22

Chapter II

Table 2.1 Mouse diet constituents.....	36
Table 2.2. Antibodies used in the IHC study and their optimal conditions.....	43
Table 2.3 Antibodies tried but not satisfactorily optimised.....	44
Table 2.4 PrimeTime ® standard qPCR assays used for validation of the candidate gene expression changes in control and atherosclerotic ApoE ^{-/-} mice from the microarray analysis.....	69

Chapter III

Table 3.1. Percentage (%) of agreement of GFAP scores assigned based on the astrocytic pattern of staining between two independent observers	97
--	----

Chapter IV

Table 4.1 Descriptive statistics of ICAM-1 immunoreactive endothelial cells preliminary comparison between PCSK9 induced and ApoE ^{-/-} mouse models (cohort1 and cohort 2).	168
Table 4.2 Descriptive statistics of ICAM-1 immunoreactive microglia preliminary comparison between PCSK9 induced and ApoE ^{-/-} mouse models (cohort1 and cohort 2).	174
Table 4.3 Descriptive statistics of IBA-1 immunoreactive microglia preliminary comparison between PCSK9 induced and ApoE ^{-/-} mouse models (cohort1 and cohort 2).	180

Table 4.4 Descriptive statistics of GFAP immunoreactive astrocytes preliminary comparison between PCSK9 induced and <i>ApoE</i> ^{-/-} mouse models (cohort1 and cohort 2).	186
---	-----

Chapter V

Table 5.1 <i>ApoE</i> ^{-/-} and Control hippocampal RNA quality and quantity	201
Table 5.2 Concentrations of cRNA after ss-cDNA synthesis and of ss-cDNA obtained after the second amplification cycle	203
Table 5.3 Analysis of candidate genes related to inflammation and lipid metabolism	212
Table 5.4 DAVID analysis of atherosclerotic hippocampus transcriptomic datasets.	216
Table 5.5 DAVID functional and pathway enrichment analysis of UP-REGULATED genes	217
Table 5.6 DAVID functional and pathway enrichment analysis of DOWN-REGULATED genes	218
Table 5.7 IMPaLA Pathway Analysis of the total number of differentially expressed transcripts in atherosclerotic <i>ApoE</i> ^{-/-} mouse hippocampus	219
Table 5.8 IMPaLA Pathway Analysis of the UP-REGULATED transcripts in atherosclerotic <i>ApoE</i> ^{-/-} mouse hippocampus	220
Table 5.9 IMPaLA Pathway Analysis of the DOWN-REGULATED transcripts in atherosclerotic <i>ApoE</i> ^{-/-} mouse hippocampus	221
Table 5.11 Genes involved in electron transport chain in control and atherosclerotic <i>ApoE</i> ^{-/-} mice hippocampus	223
Table 5.12 Genes involved in calcium and cell signalling in control and atherosclerotic <i>ApoE</i> ^{-/-} mice hippocampus	224

Table 5.10 Genes involved in immune and inflammatory response in atherosclerotic ApoE ^{-/-} mice hippocampus	226
Table 5.14 Summary of pathways of pathogenic interest in the hippocampus of ApoE ^{-/-} cohort 2 mice.....	228
Table 5.15 Candidate genes selected for qRT-PCR validation	228
Table 5.16 Housekeeping gene selection for qRT-PCR analysis.....	228

ABBREVIATIONS

%	Percentage
ABC-HRP	Horseradish Peroxidase-Conjugated Advin-Biotin Complex
ACTB	Actin- β
AD	Alzheimer's Disease
APE1	Apurinic/Apyrimidinic Endonuclease1
APOE	Apolipoprotein E
APOE-/-	Apolipoprotein E Knockout
APOER2	APOE Receptor 2
APP	Amyloid Precursor Protein
AQ4	Aquaporin-4
ATP	Adenosine Triphosphate
AVV	Adeno-Associated Virus Vector
Aβ	Amyloid- β
BBB	Blood Brain Barrier
Ca²⁺	Calcium
CAA	Cerebral Amyloid Angiopathy
CBF	Cerebral Blood Flow
cDNA	Complementary DNA
CFV	Cresyl Fast Violet
CNS	Central Nervous System
Col-IV	Collagen -IV
CSF	Cerebro Spinal Fluid
cSVD	Cerebral Small Vessel Disease

Ct	Cycle Threshold
CVD	Cerebrovascular Disease
DAB	3, 3'-Diaminobenzidine
	Database For Annotation, Visualization And Integrated
DAVID	Discovery
DEPC	Diethylpyrocarbonate
dH₂O	Deionised Water
dNTP	Deoxyribonucleotide Triphosphates
Oligo (dT)	Oligonucleotide
EDTA	Ethylenediaminetetraacetic Acid
ER	Endoplasmic Reticulum
ERAD	Endoplasmic Reticulum Associated Protein Degradation
ETC	Electron Transport Chain
FC	Fold Change
FFPE	Formalin Fixed Paraffin Embedded
GAPDH	Glyceraldehyde 3-Phosphate Dehydrogenase
GLT-1	Glutamate Transporter-1
GRAP	Glial Fibrillary Acidic Protein
H&E	Haematoxylin And Eosin
HDL	High-Density Lipoprotein
HK	Housekeeping Gene
ICAM-1	Intracellular Adhesion Molecule
IFN	Interferon
IGF-1	Insulin-Like Growth Factor-1
IHC	Immunohistochemistry

IL	Interleukin
IMPALA	Integrated Molecular Pathway Level Analysis
IVT	<i>In Vitro</i> Transcription
KEGG	Kyoto Encyclopedia Of Genes And Genomes
LCM	Laser Capture Microdissection
LDL	Low-Density Lipoprotein
LDLR	Low-Density Lipoprotein Receptor
LFB	Luxol Fast Blue
LrP1	Low-Density Lipoprotein Receptor-Related Protein
MHC	Major Histocompatibility Complex
Na	Sodium
NAD⁺	Oxidized Nicotinamide Adenine Dinucleotide
NADH	Reduced Nicotinamide Adenine Dinucleotide
ng	Nanogram
NLRP3	NLR Family Pyrin Domain Containing 3
nNOS	Neuronal Nitric Oxide Synthase
NO	Nitric Oxide
NTC	No Template Control
NVU	Neurovascular Unit
ox-LDL	Oxidised Low-Density Lipoprotein
PCA	Principal Component Analysis
PCR	Polymerase Chain Reaction
PCSK9	Proprotein Convertase Subtilisin/Kexin Type 9
PD	Parkinson's Disease
qRT-PCR	Quantitative Real-Time Polymerase Chain Reaction

RIN	RNA-Integrity Number
ROS	Reactive Oxygen Species
RT	Room Temperature
RT-PCR	Real Time Polymerase Chain Reaction
SD	Standard Deviation
SEM	Standard Error Of The Mean
TBS	Tris-buffered saline
TdT	Terminal Deoxynucleotidyl Transferase
TGFβ	Transforming Growth Factor β
TLR	Toll-Like Receptors
TNFα	Tumour Necrosis Growth Factor α
TSC	Tri-Sodium Citrate
UDG	Uracil-DNA Glycosylase
VaD	Vascular Dementia
VCAM	Vascular Cell Adhesion Molecule
VCI	Vascular Cognitive Impairment
VGCC	Voltage-Gated Calcium Channels
VLDLR	Very Low-Density Lipoprotein Receptor
VSMC	Vascular Smooth Muscle Cells
WM	White Matter
WMH	White Matter Hyperintensities
ZO-1	Zonula Occludens 1
κ	Kappa
μl	Microliter
μm	Micrometre

***CHAPTER I: INTRODUCTION TO ATHEROSCLEROSIS
AND VASCULAR DEMENTIA***

1.1 Systemic atherosclerosis

Myocardial infarction and stroke are the leading causes of death in the world with the major underlying cause being atherosclerotic vascular disease (Lusis, 2000; WHO, 2020). They are also the second and third causes of disability-adjusted life years which measures the years of life lost due to premature mortality and the years lived with the disability. In the United Kingdom approximately 6 million people are affected by cardiovascular diseases that cause myocardial infarction, stroke and are associated with several dementias (Kearney, 2019). The incidence of these diseases will likely continue to rise because of the increased prevalence of risk factors such as; high blood pressure and cholesterol, obesity and type 2 diabetes, which are also risk factors for atherosclerosis (WHO, 2020). Cardiovascular disease is a term for conditions affecting blood vessels and the heart, and atherosclerosis is the most common underlying pathology of cardiovascular disease, commonly affecting people over 65.

The atherosclerotic process develops over many years and results in narrowing of the arteries due to plaques protruding into the lumen, restricting blood flow and endothelial dysfunction with a tendency to thrombosis at the plaques. These lesions are most commonly observed at arterial regions with chaotic changes in blood flow pressure and velocity, as it occurs at bends or branching points, such as the carotid artery bifurcation, a major vessel supplying the brain (Williams and Tabas, 1995).

Atherosclerotic plaques begin by 'damage' to endothelial cells, through smoking, viruses, hypertension or excess low-density lipoprotein (LDL) cholesterol. The endothelial lining of the vessel protects blood vessels and prevents clotting; therefore, damage to endothelial cells by these initiators leads to an increase in arterial wall permeability allowing LDL cholesterol to enter and accumulate in the tunica intima where it undergoes oxidation by reactive oxygen species (ROS), mimics pathogen-

associated molecular patterns, and triggers an inflammatory response (Tabas et al., 2015). Oxidised phospholipids bind to Toll-like receptors (TLR) and trigger the inflammatory response leading to endothelial expression of adhesion molecules, including vascular cell adhesion molecule (VCAM) type-1, and various chemokines, such as, monocyte chemoattractant protein-1 which attract nearby monocytes (Gargiulo et al., 2016; Libby, 2021; Moore and Tabas, 2011) (Figure 1.1 A). Monocytes transmigrate out of the bloodstream into the blood vessel wall by diapedesis. Inside the tunica intima monocytes differentiate into pro-atherogenic macrophages, which produce free radicals and engulf oxidised LDL (ox-LDL). While modified lipids continue to accumulate in the tunica intima, this may lead to the formation of intracellular cholesterol microcrystals that activate the inflammasome, a molecular machinery comprising molecules of the cytosolic nucleotide binding domain and NLR Family Pyrin Domain Containing 3 (NLRP3) that cleaves pro- interleukin (IL)-1 β into its biologically active form (Figure 1.1 B).

Furthermore, vascular smooth muscle cells (VSMC) in the media are activated and enhance the expression of many proinflammatory cytokines and growth factors (e.g. IL-1 β , tumour necrosis growth factor α (TNF α), Transforming growth factor β 1 (TGF- β 1)) which recruit more leukocytes (Gargiulo et al., 2016; Libby, 2021). The macrophages continue to engulf LDL leading cholesterol-laden macrophages with a foamy appearance under the microscope (Tabas et al., 2015; Wolf and Ley, 2019). These 'foam cells' eventually undergo apoptosis and release cell debris and lipids, at this stage the atherosclerotic lesion becomes visible in tissue and is called a fatty streak (Crowther, 2005) (Figure 1.1C).

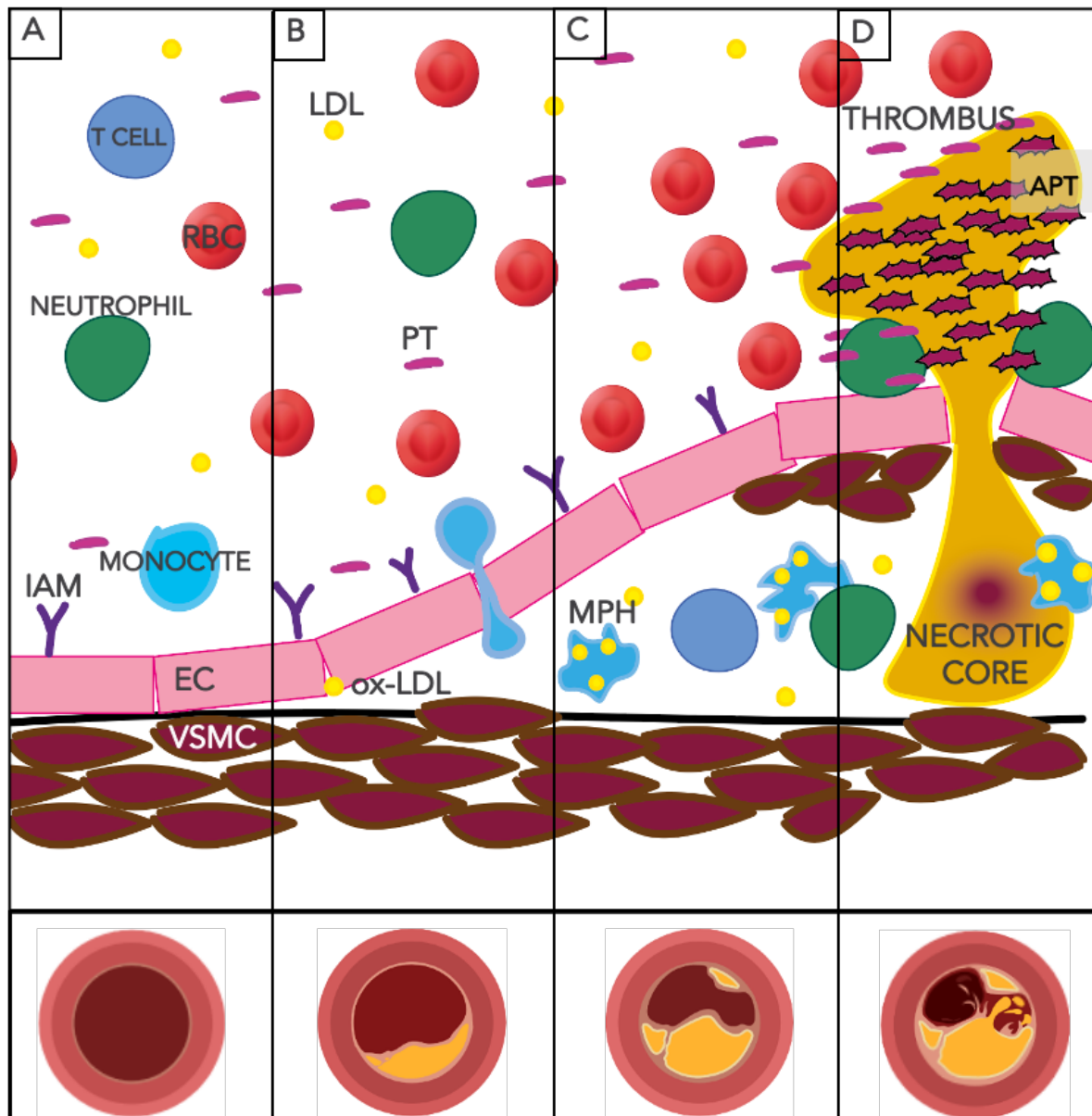


Figure 1.1 Schematic of systemic atherosclerosis

This schematic representation of a longitudinal section showing the development of atherosclerotic plaque with the representation of an arterial vertical section at the bottom. A) Endothelial cell activation occurs due to inflammatory triggers such as smoking or hypertension which leads to the expression of intercellular adhesion molecules (IAM) The activation of IAM leads to the recruitment of monocytes and other immune cells. B) Immune cells that infiltrate the intima layer of the artery where interact with other immune cells such as neutrophils and T-cells and monocytes differentiate into macrophages (MPH). The efflux of cholesterol trapped between the arterial layers is decreased and it oxidises (ox-LDL) which leads to the acceleration of intracellular free cholesterol and promotes the formation of foam cells. C) The foam cells eventually perish and disintegrate, resulting on a necrotic core with cellular debris. D) As atherosclerotic plaques develop, the vulnerable plaques can rupture and lead to an arterial thrombus which can lead to ischaemia. EC, endothelial cell; VSMC, vascular smooth muscle cell; LDL, low density lipoprotein; ox-LDL, oxidised low-density lipoprotein; PT, platelet; APT, activated platelet.

In an attempt to heal and resolve plaque formation, arteries form a fibrous cap that separates the platelets in the blood stream from the pro-thrombotic material (Falk et al., 2013; Libby, 2008). The overlying scar provides a relatively protective barrier, nonetheless, some atherosclerotic lesions are at higher risk of rupturing, leading to acute formation of a clot, known as a thrombosis. This can lead to the occlusion of the vessel and result in organ damage. In these 'unstable' plaques there is a large necrotic area of the intima containing lipids and cell debris, which occurs due to cellular necrosis and the defective removal of apoptotic cells (Moore and Tabas, 2011) (Figure 1.1 D).

The VSMC in the intima produce less or defective collagen which results in a thinner fibrous cap which can be easily broken down and is referred to as a thin-capped fibroatheroma (Hansson and Hermansson, 2011). Finally, the activation of innate immune pathways is accompanied by the infiltration of adaptive immune system B and T cells. The content of lymphocytes and myeloid cells in the atherosclerotic plaques leads to a high degree of inflammation, which is further increased by production of damage –associated molecular pattern molecules expressed by necrotic cells (Hansson and Hermansson, 2011; Libby, 2008). However, most atherosclerotic lesions do not result in critical vascular disease leading to myocardial infarction (VIRMANI et al., 2002) .

1.2 Systemic atherosclerosis and cerebrovascular disease

Cerebrovascular diseases (CVD) include any condition which has an effect on the cerebral circulation or the blood vessels on the central nervous system (CNS) and can lead to a cerebrovascular event (stroke). Vascular pathology in CVD is intrinsically varied; it is common in elderly individuals, and includes, large, lacunar and micro-infarcts; white matter hyperintensities (WMH) due to ischemia and myelin loss;

atherosclerosis is presents on large and small vessels, leptomeningeal cerebral amyloid angiopathy (CAA), and usually predicts cognitive impairment (Grinberg and Heinsen, 2010; Leijenaar et al., 2017).

Intercranial atherosclerosis is the leading cause of ischaemic stroke and a risk factor for recurrent stroke while carotid atherosclerosis is an extracranial factor that is an important source of thromboemboli. Atherosclerosis is the main cause of microinfarct through cardioembolic disease and small vessel disease (Grinberg and Heinsen, 2010), furthermore, there is an association between cognitive decline and carotid atherosclerosis (Dolan et al., 2010; Silvestrini et al., 2011). Systemic atherosclerosis markers, such as narrowing of the carotid artery and calcium present on the wall of the coronary artery, are associated with a decline in cognitive performance, higher risk of vascular cognitive impairment and vascular associated dementia (VaD) (Chen et al., 2017; Yue et al., 2016). Current studies have not determined whether the association between increased level of atherosclerosis through measuring of the carotid intima media thickness and decreased cognitive function is due to vascular risk factors having a parallel impact on cerebral and peripheral circulation or systemic atherosclerosis having an impact on cognitive decline. Potential mechanisms in which atherosclerotic pathology affects cognition, other than through occlusion of large blood vessels through thrombotic events, include hypoperfusion, poor cerebral autoregulation and dysfunction of the blood-brain barrier (BBB). Cerebral small vessels protect and provide nutrients to the brain parenchyma due to the unique characteristic of the BBB therefore CVD is often considered a risk factor involved in the initiation of a number of disorders of the CNS, such as, cerebral small vessel disease (cSVD), stroke, and Alzheimer's disease.

1.2.1 Cerebral small vessel disease

Cerebral small vessel diseases are another leading cause of age-related stroke and dementia. As its name describes cSVDs are a range of diseases that involve a number of diseases that disrupt the brain's small arteries, arterioles, venules and capillaries and entails several pathological processes. cSVD pathologies include arteriolosclerosis, inflammatory and immunologically-mediated small vessel disease, venous collagenosis, and some pathologies are associated with CVD sporadic and hereditary CAA. The pathological changes may result in neuronal apoptosis and demyelination and loss of oligodendrocytes (Li et al., 2018). T1-weighted brain magnetic resonance images of cSVD present WMH, macrohemorrhages, dilated perivascular spaces, microbleeds and brain atrophy (Liu et al., 2019).

Arteriosclerosis is different to large vessel atherosclerosis, it is caused by reduced blood flow to the brain, which commonly occurs due to alterations of small arterioles of the subcortical white matter (WM) and the striatum resulting in a varied degree of ischemic and WM lesions (Pantoni, 2010). cSVD shares some risk factors with atherosclerosis, such as impaired cerebral autoregulation and its association with dementia, but the molecular mechanisms underlying these changes are not completely understood.

1.2.2 Neurovascular dementia

One of the major health challenges of the 21st century is dementia, which progressively and irreversibly impairs cognition (WHO, 2020). VaD, dementia caused solely by vascular pathology, has been considered the second most common type of dementia, after Alzheimer's disease (AD). VaD patients present more severe vascular cognitive impairment (VCI), including memory and executive function problems that are

detrimental to everyday life and are largely attributable to cerebrovascular pathology (Van Der Flier et al., 2018). Large vessel infarcts can be associated with VaD and small vessel disease have also been linked to cognitive impairment and dementia.

Currently, there is no generally accepted criteria to define the neuropathological threshold of CVD due to its variability such as different clinical phenotypes and common comorbidities with other pathologies (Gold et al., 2007). Arvanitakis et al., (2017) screening study demonstrated the prediction of cognitive impairment by large infarcts, microinfarcts, arteriolosclerosis, myelin loss, and perivascular space dilation. Arteriolosclerosis, atherosclerosis and other diseases associated with vessel wall modifications have been suggested to be of crucial importance in VaD and all these disorders should be included on the neuropathological evaluation of dementia.

Other pathophysiological processes are likely to have roles in VaD which include interactive mechanisms with AD and other neuropathological processes, including microglial reactions, amyloid- β ($A\beta$) clearance and local tissue injury or dysfunction, including innate immune processes and disruption of the neurovascular unit (NVU), and BBB dysfunction.

1.2.3 Mixed dementia

VaD is relatively rare in elderly individuals despite the commonality of vascular pathology amongst them. A large number of patients diagnosed VaD consistently present with other pathologies, the most common of which is accumulation of neurofibrillary tangles and $A\beta$ plaques from AD (Van Der Flier et al., 2018). Initially AD and VaD were thought to be two separate disorders with different neuropathologies; however, evidence has demonstrated that they share risk factors, such as age, hypertension and diabetes as risk factors (Iadecola, 2010). Furthermore, patients with

AD-type dementia show a lower cerebral blood flow (CBF) and reactivity to vasoactive stimulation which could indicate cerebrovascular damage associated with the neurovascular unit, leading to the idea that AD and VaD have shared pathogenic mechanisms.

1.3 Proposed mechanisms underlying the pathology in vascular dementia

As previously mentioned, there is no consensus about the criteria to classify VCI and the neuropathological components of VaD are difficult to describe due to the lack of uniformity of samples and neuropathological examination (Arvanitakis et al., 2017; Kalaria, 2016). Haemorrhages, microbleeds, lacunar infarcts and microinfarcts are identified through brain imaging and WM Hare used to identify the most common pathology associated with cSVD and VaD (Grinberg and Thal, 2010). The pathological effects of cSVD are commonly identified through imaging techniques and are commonly found in WM. In histology, small cerebral vessels show signs of inflammation, presenting macrophages and lymphocytes, activated microglia, and astrocytic gliosis – reactive change of astrocytes to stress – and decreased myelin in the perivascular WM (Deramecourt et al., 2012). Also, patients with progressive cognitive deterioration with WM lesions in the periventricular WM and deep subcortical regions show evidence of BBB leakage (Simpson et al., 2010; Wharton et al., 2015).

1.3.1 Genetic influences on vascular dementia

Identification of mutations in a single gene which can lead to the development of VaD have contributed to the understanding of the pathogenesis of the disease (Manso-Calderón, 2019). A hereditary form of VaD was observed in CAA cases, a disorder in which amyloid proteins deposits in the wall of the vessels leading to inflammation and

microbleeds. The mutations were all associated with amyloid proteins including A β precursor protein (APP) (Revesz et al., 2009). Most forms of VaD are sporadic and may be a result of a combination of small effect genetic variants and genetically determined vascular risk factors.

Genetic research in VaD has focused mainly on association studies with candidate genes involved in stroke and AD and/or in pathophysiological mechanisms critical to VaD (Ikram et al., 2017). The genes involved in lipid metabolism, especially the apolipoprotein E (*ApoE*) gene, have been the main focus of research. A recent meta-analysis of 44 studies corroborated a significant association between ϵ 4 allele carriers of APOE and higher risk of VaD (Ikram et al., 2017). On the other hand, angiotensin convertase enzyme (*Ace*) gene which is believed to be increased in atherosclerosis by stimulation of macrophages through ox-LDL in vascular reactivity was not associated with VaD based on the results of two meta-analysis. The same meta-analysis related inflammatory genes with VaD, including *IL-1 α* , *IL-1 β* , *IL-6*, *TNF- α* , *TGF- β 1* (Ikram et al., 2017; Manso-Calderón, 2019).

1.4 Proposed pathophysiology of atherosclerosis in the central nervous system – inflammation unrelated to occlusion

1.4.1 The neurovascular unit

The brain constitutes ~2% of the body weight, nonetheless, it receives 15% of the cardiac output and consumes 25% and 20% of the body's glucose and oxygen respectively (Brown and Ransom, 2015). It has a high demand but limited storage of energy, which requires effective glucose and oxygen transport from the blood into neurons. Also, neurons need to be surrounded by a specific ion concentration in order to elicit an action potential. This environment is provided by the NVU (Zlokovic, 2008),

which is essential for maintaining proper function of neurons and synapses through the rapid and effective delivery of nutrients and preventing the entry of potential neurotoxic substances into the CNS.

The NVU consists of endothelial cells, pericytes, astrocytes, and neurons (Figure 1.2). This complex and functional multicellular unit regulates the activities of the CNS and has an important role on health and disease. The term BBB is used to describe a functional feature of the NVU to strictly control the exchange of molecules, cells and essential nutrients between the brain parenchyma and the blood stream, breakdown of this barrier disrupts the delicate balance of the CNS leading to neuronal damage. The BBB lies at the level of the brain endothelium due to the presence of tight junctions and restricted pinocytosis. Furthermore, the NVU facilitates neurovascular coupling, the mechanism that links neuronal activity and cerebral blood flow (CBF). The following section will discuss the elements and potential cellular markers of the NVU, in detail.

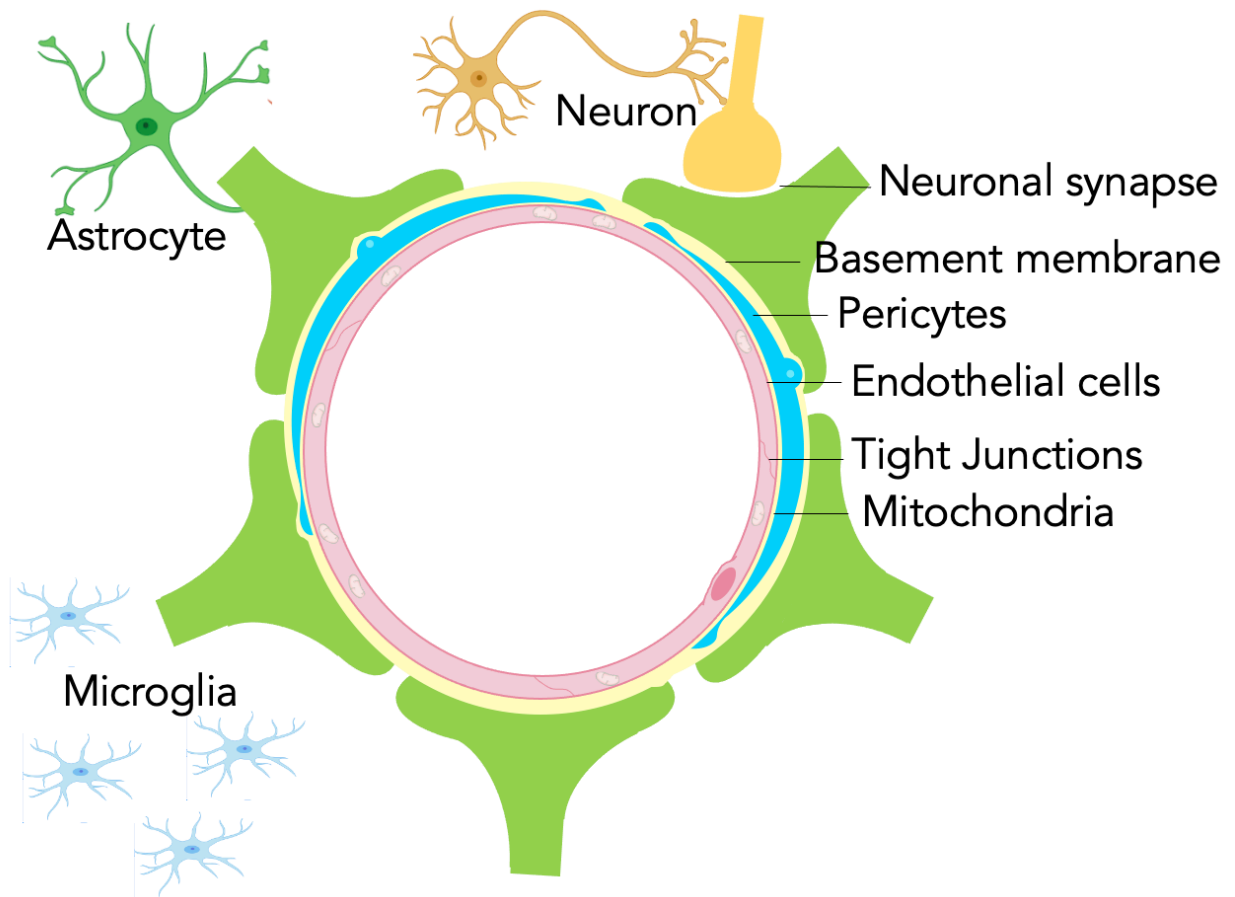


Figure 1.2 Representation of the neurovascular unit

The endothelial cell (pink), contains several mitochondria and forms the capillary wall. The endothelium is partially covered by pericytes (blue) which extend their long cellular processes to cover several endothelial cells. Pericytes are embedded in the basement membrane (yellow), which is made of collagen, laminins and other glycoproteins. Astrocytic end-feet (green) and some neuronal synapses (dark yellow) surround the blood vessel.

Endothelial Cells

Capillary walls are made of a single endothelial cell folded around to form the capillary lumen (Aird, 2007). However, compared to other endothelial cells on the periphery, endothelial cells in the CNS are partially impermeable, highly polarized, lack fenestrations and are held together by tight junction proteins (Castro Dias et al., 2021; Erdo et al., 2017; Fan et al., 2015). Only small lipophilic molecules, oxygen and carbon dioxide can freely diffuse across the BBB, therefore, bigger lipophilic molecules and nutrients require ATP-dependent transporters which require energy. All these components form the barrier (Daneman and Prat, 2015), restrict the transport of nutrients, energy metabolites and other molecules into the CNS. Tight junction proteins such as claudin V, Zonula occludens 1 (ZO-1) and occludin have a crucial role in this process as they block the diffusion of proteins and macromolecules and control paracellular pathways (Luissint et al., 2012; Yang et al., 2019) .

Endothelial cells are also involved in the neuroinflammatory process through the expression of very low levels of leukocyte adhesion molecules such as VCAM type-2 and Intracellular adhesion molecule-1 (ICAM-1) (Aird, 2007). CAM-1 is a common transmembrane glycoprotein present on endothelial cells, and also leukocytes. In the CNS, low levels of ICAM-1 have been shown to be present in capillaries under normal conditions; however, they are up-regulated in the presence of proinflammatory cytokines such as IL-1 β or TNF- α (Meagher et al., 1994; Wang et al., 1995). Endothelial cells also express platelet endothelial cell adhesion molecules (CD31) which functions largely as an immune-inhibitory receptor.

Mural cells

Mural cells refer to VSMCs and pericytes as they are present in arterioles, arteries and veins and are essential for endothelial cell structure and vascular contraction. Pericytes partially cover the abluminal surface of the endothelial cells of capillaries and are surrounded by basement membrane. Both types of cells have contractile proteins which allow them to regulate the diameter of the vascular lumen and consequently blood flow (Peppiatt et al., 2006). Pericytes are not in direct contact with the capillary endothelium as they are embedded within the basement membrane, instead, they form different types of adhesions at specific locations (Courtoy and Boyles, 1983; Gerhardt et al., 2000).

These junctions are crucial for BBB permeability. Pericytes prevent neurotoxic molecules entering the brain and remove these toxins in the improbable case they cross into the BBB (Bell et al., 2010; Winkler et al., 2014). As arterioles turn into capillaries in the parenchyma, cerebral vessels no longer have a coverage of VSMCs and are covered by pericytes. The role of pericytes in the CNS and NVU is still being investigated. Some evidence suggests that astrocytes might regulate vascular tone through regulation of the pericyte tone (Argaw et al., 2012). The changes in CBF are controlled by pial and intracerebral arteries, therefore successful neurovascular coupling requires intact pial circulation and a normal response to vasoactive stimulation from VSMCs and pericytes. Loss of pericytes in AD mouse models leads to extracellular aggregation of A β 40 and A β 42, preceding the development of tau pathology and eventual cognitive decline (Sagare et al., 2013). Furthermore, loss of pericytes in an age-dependent manner in pericyte-deficient mice leads to compromised tight junction integrity, leakage of circulating macromolecules into the brain

parenchyma, associated with neurodegeneration and cognitive decline (Armulik et al., 2011; Bell et al., 2010).

The most currently used and recognised pericyte marker is β -type platelet-derived growth factor receptor (PDGFR- β). Although its expression is low under normal conditions, PDGFR- β expression is significantly increased in pericytes following brain injury such as stroke (Arimura et al., 2012).

Basement membrane

The basement membrane surrounding the abluminal surface of the vessels is a protein network primarily composed of laminin, collagen IV (Col-IV) and heparin sulphate proteoglycans which provides structural support and binds together all the elements of the NVU. This membrane is secreted by the endothelial cells, pericytes and astrocytic end-feet close to the capillaries. In addition to maintaining the structural integrity of the NVU, the basement membrane adds an extra layer of protection to the BBB (Daneman, 2012). The basement membrane is primarily composed of laminin and collagen IV (Col-IV) with Col-IV being the most abundant component (Poschl et al., 2004). Col-IV provides structural support and binds together all the elements of the NVU (Duncombe et al., 2017; Frías-Anaya et al., 2021).

Astrocytes

Astroglia or astrocytes were named after their stellate shape under the microscope (Miller, 2018). Initially the role of astrocytes was thought to only be related to functions nervous system viability and a homeostatic environment for neurons, including buffering excess potassium and neurotransmitters, providing nutrients and structural support around synapses, and contributing to the integrity of the BBB. Over the years it has been shown that astrocytes release molecules that act as modulators of synaptic

activity (gliotransmission) and are important for neuronal survival (Wang and Bordey, 2008). Approximately 60% of excitatory synapses in the CA1 region of the rat hippocampus have astrocyte end-feet next to the presynaptic bouton and the postsynaptic dendritic spine (Ventura and Harris, 1999). This is reflected by the distribution of astrocytes in the cortex and hippocampus showing low overlap between their fine processes (Bushong et al., 2002). Astrocytes can also modulate plasticity by the re-uptake of glutamate from the synaptic cleft through their membrane glutamate transporters (GLT)-1 and ATP.

Furthermore, the end-feet with high levels of aquaporin-4 (AQ4) water channel proteins promote perivascular clearance of toxic solutes by the newly characterized “glymphatic system” (CNS waste clearance system) (Hubbard et al., 2015). AQ4 is also a highly used marker in the investigation of BBB leakage and its expression is significantly reduced in astrocytic end-feet of aged mice (Duncombe et al., 2017).

Astrocytes restrict the entry of peripheral immune cells into the CNS through the BBB under physiological condition. However astrocytes can be active participants in neuroinflammation by contributing to the adaptive immune responses under pathological conditions. However, compared to microglia, astrocytes dominate more quantitatively and might only amplify neuroinflammation as microglia are activated and require ‘reinforcements’, this is facilitated by the astrocytes structure and strategic location to aid the mobilisation of peripheral immune cells.

After brain injury, such as stroke, astrocytes ‘react’ by undergoing a significant morphological and genetic transformation. The two types of reactive astrocytes initially described are: A1 pro-inflammatory and A2 anti-inflammatory. Although it is now known a wide range of morphologies and gene expression can occur simultaneously in the mammalian brain, the simplification of astrocytes based on their different

polarizations are marked by different biochemical and functional characteristics. A1 reactive astrocytes are associated with elevated levels of *C1r*, and *C4* and other genes associated with the classic complement system of the immune system, which are damaging for the NVU. Reactive astrocytes classified as A2 present an upregulation of beneficial inflammatory factors, such as *CLCF1* (cardiotropic-like cytokine factor 1), *HIF* (hypoxia induce factor), *IL-6*, *IL-10*, and thrombospondins, to promote the NVU remodelling (Miller, 2018). The morphological changes include increase size of their cytoskeleton (hypertrophic), processes are extended and there is an increase expression and immunoreactivity of their intermediate filament protein: glial fibrillary acidic protein (GFAP), a hallmark of astrocytes (Sofroniew, 2014; Pekny and Hol, 2015).

Astrocytes were initially classified as A1 and A2 based on their gene expression during neuroinflammation, however this simple dichotomy of astrocytic phenotypes it is not represent the vast variety of astrocyte morphology and gene expression (Liddelow et al., 2017). The simplified classification of these cells facilitates the investigation of astrocytes amongst a range of CNS disorders.

The astrocytic end feet are an integral structural part of the NVU and, by extension, the BBB. Their location between neurons and endothelial cells places them in a strategic position that allows them to modulate CBF to adapt to the dynamic changes of neuronal metabolism and synaptic activity.

Neurovascular coupling

Together with pericytes, astrocytes are thought to help coordinate blood flow with neuronal activity, a concept known as neurovascular coupling (Hall et al., 2014). Astrocytes communicate with blood vessels and the neuronal network in order to regulate the BBB and CBF in response to neuronal activity (Gordon et al., 2011).

Neurovascular coupling involves controlling the contraction and dilation of VSMCs surrounding arterioles and pericytes surrounding capillaries, which dynamically affect CBF. The importance of astrocytes lies in their ability to control contractility of intracerebral arteries and secrete factors that modulate and maintain the BBB once it is formed (Daneman and Prat, 2015; Kuchibhotla et al., 2009). The changes in CBF are controlled by pial and intracerebral arteries, therefore successful neurovascular coupling requires intact pial circulation and a normal response to vasoactive stimulation from VSMCs and pericytes.

Microglia

In 1919 when microglial cells were discovered and their distribution and morphological phenotype were identified, the recognition of ramified cells transformed into rod or amoeboid microglia in different pathologies led to microglia being recognised as the resident macrophages (of myeloid origin) in the CNS (Fernández-Arjona et al., 2017; Rio-Hortega, 1919). Microglia are the primary immune cell and therefore, an important partner of the NVU. During homeostasis 'resting microglia' are sensitive to the parenchyma environment, constantly surveying the brain and acquire 'activated' status if dysfunctions or lesions are detected (Boche et al., 2013; Nimmerjahn et al., 2005). The changes to microglia include morphological and genetic changes, with active microglia displaying inflammatory and phagocytic features and having a key role in the coordination of inflammatory response.

Microglia appear evenly distributed throughout the CNS, but this varies according to the need for microglia across the brain parenchyma. The shape of microglia also changes according to the CNS needs, they have been categorized into broadly four distinct subtypes: compact, longitudinally branched, radially branched, amoeboid (Lawson et al., 1990). These morphologies are closely related to their functional state:

resting, active, 'rod' microglia and reactive respectively (Streit and Kreutzberg, 1988).

Table 1.1 contains a detailed description of microglia morphologies and function.

As with astrocytes, microglia can be classified into pro-inflammatory (M1) and anti-inflammatory (M2) depending on the proteins and genes that they display. M1 cells produce pro-inflammatory cytokines such as TNF- α and IL-1 β upon brain injury while M2 microglia express IL-10 and TGF- β and are prone to remove cellular debris and promote tissue repair. Both of these changes may arise as a consequence of damage induced by inflammation (Fernández-Arjona et al., 2017; Jurga et al., 2020). Chronic hypoperfusion such as stroke causes cerebral endothelial cell dysfunction, leading to the entry of fibrinogen and inflammatory cells into the brain tissue via the disrupted BBB that sustains the M1 type of microglia activation. Activation of M1 type microglia can strongly impact BBB integrity as activated microglia are the main source of ROS in the brain (Crowe et al., 2016).

The initial definition of M1 and M2 microglia was derived from an *in vitro* experiment which were tested in isolation, which does not necessarily reflect the environment of the CNS and microglial behaviour. Furthermore, evidence from various *in vivo* studies demonstrates, that unlike *in vitro* studies, microglial morphology is dependant of their activation state but also their localisation making their phenotype highly variable (Böttcher et al., 2019). The classification of microglia as M1 and M2 appears to oversimplified the wide range of variation amongst these cells.

Different markers have been used throughout the literature in order to identify the morphology of microglia and determine their different function and expression. Microglia present ionized calcium-binding adapter molecule 1 (IBA-1), involved in membrane ruffling of microglia which is essential for the morphological changes from dormant ramified microglia to activated and amoeboid microglia (Lawson et al., 1990;

Sasaki et al., 2001). IBA-1 has been shown to be co-expressed with M1 and M2 polarisation markers and is considered microglia pan-marker (Hendrickx et al., 2017; Sasaki et al., 2001; Waller et al., 2019). A number of commonly used microglial markers and their pattern of expression are listed on Table 1.2

Table 1.1 Description of diverse microglia morphology

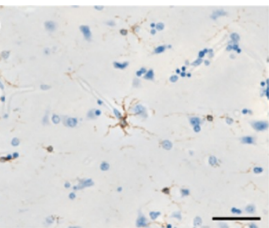
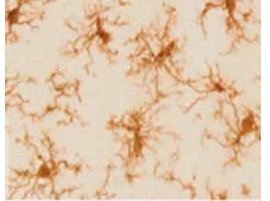
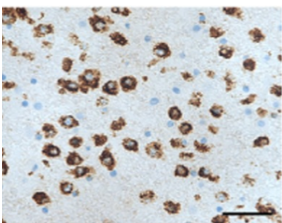
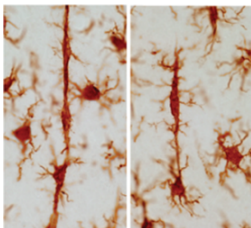
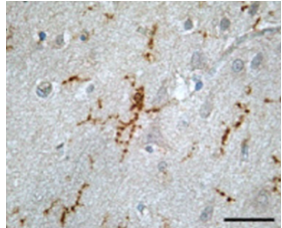
	Resting	Active	Amoeboid.	Rod microglia	Dystrophic
Morphological description	Ramified, with many short fine processes that extend towards other microglia.	Retraction and thickening of processes sometimes with extended tails processes in opposite directions	Spherical shape with few/no processes, containing phagocytic vacuoles (visibly indistinguishable from macrophages)	Elongated nucleolus and cell bodies with a reduced number of processes projecting from the upper and basal ends.	Microglial processes are non-continuous.
Function	Actively senses the brain environment.	Migrate to source and phagocytose debris	Capable of motility and surveillance but non-migratory	Suggested to have a supportive role to damaged neurons and to be involved in the resolution of inflammation	Associated with microdysfunction
Expression	Normal adult CNS	Associated with neuroprotection	- During CNS development - Acute destruction of the CNS (trauma, infection, ageing)	- Chronic, long-lasting disorders - Aging - Injury	Aging
	 <p>(Boche et al., 2013)</p>	 <p>(Fernández-Arjona et al., 2017)</p>	 <p>(Boche et al., 2013)</p>	 <p>(Ziebell et al., 2012)</p>	 <p>(Boche et al., 2013)</p>

Table 1.2 Detailed microglial markers

Marker	Function	Expression	Microglia expression	References
Ionized calcium-binding adapter molecule 1 (IBA1)	Present in monocytic cell lines. Adapter molecule that mediates calcium signals in the monocytic lineage.	<ul style="list-style-type: none"> - Microglia specific - Present on resting and activated microglia - it is up-regulated in activated microglia - Increased during inflammation - randomly present on larger more 'reactive' microglia. 	resting and activated microglia	(Boche et al., 2013; Gehrmann and Kreutzberg, 1991; Hendrickx et al., 2017; Ito et al., 1998)
Cluster of differentiation 68 (CD68)	Glycoprotein expressed on cells of monocytic lineage which binds to tissue-specific lectins (carbohydrate-binding proteins that bind specific sugar groups on cell membranes) or selectins (CAM) allowing macrophages and cells expressing CD68 to home on a particular target.	<ul style="list-style-type: none"> - Expressed on monocyte lineage cells - Present on all activated amoeboid microglia - Associated with phagocytic activity 	activated microglia	(Waller et al., 2019)
Major histocompatibility factor II (MHCII)	MHC-II conjugates with antigens present on activated dendritic cells when they travel to local lymph nodes. They stimulate an adaptive immune response. However, microglia do not have this ability. MHC-II is present on microglia	<ul style="list-style-type: none"> - Present on ramified immune cells - It has been suggested as a marker for M1 (classical activation) of microglia 	resting and activated microglia	(Imamura et al., 2003)
Intracellular adhesion molecule (ICAM-1)	Cell surface glycoprotein necessary for antigen presentation.	Present on endothelial cells and immune cells	ICAM-1 is not a common microglia marker but an endothelial cell activation marker.	(Lee and Benveniste, 1999)

OX-42 (CD11b)	Antibody design to target CD11b which mediates inflammation through regulation of leukocyte adhesion and migration	Several leukocytes including neutrophils and monocytes. Increased expression is associated with brain injury.	Resting and active microglia	(Zhou et al., 2017)
CD 163 (ED2)	Scavenger receptor for the haemoglobin-haptoglobin complex	Present on macrophages and macrophage-like microglia present on the perivascular	Reacts with perivascular microglia but not with ramified microglia	(Jeong et al., 2013)
Receptor for advanced glycation end-product (RAGE)	Multiligand receptor that propagates cellular dysfunction in several inflammatory disorders (tumours and diabetes). It has a role in the inflammatory response.	Present on normal tissue but upregulates on the presence of its ligands which results from pro-inflammatory gene activation	Increased on the presence of an inflammatory stimulus (eg. A β)	(Chavakis et al., 2004)
Human Leukocyte Antigen – DR isotype (HLA-DR)	MHC-II cell surface receptor and constitutes a ligand for the T-cell receptor	-Commonly used to identify leukocytes -Does not overlap with the expression of IBA-1	Ramified/ameboid microglia	(Hendrickx et al., 2017)
Mannose Receptor (CD226)	Phagocytosis and endocytosis of endogenous and exogenous proteins	Present on the surface of macrophages, immature dendritic cells and liver endothelial cells. -Also expressed on astrocytes - Associated with an anti-inflammatory phenotype	Expression of this receptor increases in the presence of certain cytokines.	(Jurga et al., 2020; Zimmer et al., 2003)
Triggering Receptor Expressed on Myeloid cells (TREM2)	Involve in the balance between phagocytic and pro-inflammatory microglial activity.	- myeloid cells -High levels: promotes alternative activation (M2) and phagocytosis -Low levels: promotes M1, pro-inflammatory state		(Mazaheri et al., 2017)
Leucocyte common antigen (CD45)	Signalling molecule with an essential role regulating T- and B-cell antigen receptor signalling	Leukocytes - Monocytes have a higher expression of CD45 than microglia, which makes dual labelling a viable option to distinguish between them.	Detects active microglia however it also detects lymphocytes	(Boche et al., 2013)

P2Y12	Chemoreceptor for adenosine diphosphate. In the CNS it has been exclusively on microglia.	Microglia only -Downregulation is associated with microglia disruption	Ramified microglia. Indicating a rapid response during perturbations of CNS	(Haynes et al., 2006)
TMEM119	Cell-surface protein that is not expressed by macrophages or other immune or neural cell types	Microglia only	Ramified, hypertrophic, and dystrophic morphologies	(Zrzavy et al., 2018)

1.4.2 Neurovascular unit dysfunction

Common neurodegenerative disorders including AD and Parkinson's disease (PD) have shown to present a range of neurovascular dysfunctions involved in the initiation or contribution of the pathogenesis of neurological conditions or is caused as a consequence. The neurovascular dysfunction seen in such disorders can be directly attributed to cardiovascular deficits or a functional breakdown of the neurovascular unit and signalling pathways (Garwood et al., 2017). A consequence of such disruption, CBF is disturbed and leakage of neurotoxins and serum proteins into the CNS can occur, which may activate resident glial cells and impact on neuronal function.

Blood brain barrier damage

Physical breakdown of the BBB frequently occurs due to enzymatic degradation of the capillary basement membrane, an increase in bulk-flow fluid and/or transcytosis. As previously mentioned, tight adherens junctions are essential to maintain the integrity of the BBB. Several studies report a downregulation of tight junction proteins present on the blood vessels leading to BBB leakage in a range of neurodegenerative diseases, included dementia (Bell et al., 2010; Henkel et al., 2009; Zlokovic, 2008). Following ischaemic injury to the CNS the activity of vascular associated matrix metalloproteinases increases (Cheng et al., 2006; Zlokovic, 2011), which may directly degrade tight junction proteins and the basement membrane thereby affecting BBB integrity (Rosenberg, 2009; Zlokovic, 2011).

Dysfunction of the BBB results in leakage of circulating macromolecules having a major impact in the neuroinflammatory response. Plasma proteins such as fibrinogen, thrombin and plasmin promote neuroinflammation and accelerate neurovascular damage and directly impact neuronal function (Chen and Strickland, 1997; Chen et

al., 2010; Mhatre et al., 2004; Paul et al., 2007). The accumulation of albumin and immunoglobulins suppresses blood flow resulting in oedema, and the movement of red blood cells into the cerebral parenchyma leads to the release of iron from haemoglobin which may lead to oxidative stress (Bell et al., 2010; Winkler et al., 2014; Zhong et al., 2008). Atherosclerosis and BBB breakdown have common risk factors, such as high circulatory LDL cholesterol and systemic hypertension. A murine model for hypertension showed that long-term high blood pressure may contribute to the decrease of tight junctions of the BBB and cause WM lesions (Fan et al., 2015)

Neurovascular coupling

Neurovascular coupling is thought to be governed by direct neural and endothelial interactions, and complex neurogliovascular signalling pathways. During neuronal activation the release of nitric oxide (NO) by neurons causes rapid vasodilation in the endothelium through stimulation of VSMC. This process is temporary but ensures that changes in the CBF match the metabolic expenditure demands (Perez-Nievas and Serrano-Pozo, 2018). Further evidence suggest that astrocytes can influence arteriolar tone as a result of their basal Ca^{2+} concentration independently of neuronal activity, therefore astrocyte dysfunction is key to the breakdown of BBB and neurovascular coupling affecting many neurological conditions (Rosenecker et al., 2015; Shabir et al., 2020a). It is evident that regulation of CBF is a complex interplay between various cell types and signalling pathways with many gaps still remaining in our understanding of the exact mechanisms behind neurovascular coupling and the NVU in health and disease.

1.5 *Cholesterol in the brain and peripheral circulation: animal models to study atherosclerosis and the brain*

1.5.1 Brain cholesterol homeostasis

The brain houses an estimated 25 % of the body's total cholesterol. Cholesterol is a principal component of myelin, a fatty sheath that serves an essential role in cellular signalling and blood–brain barrier integrity (Björkhem et al., 2004).

The BBB does not allow the cholesterol to cross over to the CNS therefore the brain relies on *in situ* local cholesterol synthesis (Björkhem et al., 2004). Neurons and other glial cells are able to synthesize cholesterol but over time adult neurons become dependent on astrocyte produced cholesterol (Mino et al., 2017). The transport of astrocyte produced cholesterol to neurons requires coordinated cooperation of multiple cholesterol transporters, including APOE which has been extensively researched in relation to AD. Apolipoprotein E-containing particles transport cholesterol produce in astrocytes through ATP binding cassette transporters A1, G1 and G4 (ABCA1, ABCG1, ABCG4) (Löscher and Potschka, 2005). The particles transporting cholesterol, resemble plasma high-density lipoprotein (HDL) in composition and are incorporated into neurons through APOE binding receptors LDL receptor (LDLR), LDL receptor-related protein 1(LrP1), very low-LDL receptor (VLDLR) and ApoE receptor 2 (APOER2). The intake of cholesterol can be regulated through major regulators of cholesterol homeostasis such as proprotein convertase subtilisin/kexin type 9 (PCSK9). Recent reports have implied the involvement of PCSK9 in cerebral homeostasis due to its increase leading to the degradation of APOER2, LDLr and VLDL (Canuel et al., 2013; Poirier et al., 2008). Disruption of any of the cholesterol intake receptors could lead to a decrease in neuronal cholesterol. A consequence of

depletion of neuronal cholesterol include neural oxidative stress reactions resulting in neurodegeneration. The effect has been demonstrated in the hippocampus of AD rat models (Koudinov and Koudinova, 2005).

The most common animal model to study atherosclerosis is mice, particularly C57Bl/6 strain. Although C57Bl/6 strain contains much lower HDL levels, it becomes obese, diabetic and susceptible to lesion development when fed with an atherogenic diet (Schreyer et al., 1998) However, due to the difference in cholesterol metabolism between mice and humans atherosclerosis-prone genetic mouse models were generated by triggering different genes to increase the contents of LDL and VLDL cholesterol. The models commonly used mouse models of deletion of APOE (*ApoE^{-/-}*) and ectopic introduction of mutant *PCSK9* gene will be discussed in the following section.

1.5.2 Apolipoprotein E knockout (*ApoE^{-/-}*) to study atherosclerosis

Apolipoprotein E in the periphery, as in the CNS, is part of the structure of VLDL and HDL and helps transport cholesterol and triglycerides in to the cells and it is necessary for the uptake of lipoproteins through the LDLR (Martins et al., 2006). Therefore the deletion of *ApoE* in mice results in a significant increase in plasma cholesterol of 400 – 600 mg/dl compared to wild-type mice fed with a normal/chow diet (75-110mg/dl) and humans with normal (200mg/dl) and elevated (240mg/dl) cholesterol (Nakashima et al., 1994). The plasma cholesterol levels could rise higher than <1000 mg/dl when fed with a high cholesterol diet (Kapourchali et al., 2014). The *ApoE^{-/-}* mouse is widely regarded a useful model for experimental atherosclerosis as it allows studying the development and prevention of atherosclerosis as it develops different stages of the disease including spontaneous lesions that progress into fibrous plaques, at an

accelerated pace. Nevertheless this model has not presented any evidence of plaque rupture occurring (Jawien, 2012).

Of note, the biggest risk factor for AD, besides advanced age, is an allelic variant of the APOE gene which is linked to altered lipoprotein profiles and increased cardiovascular mortality (Mahley, 2016). More than 15 genome-wide association studies have implicated APOE ϵ 4 in AD, making it by far the most consistent genetic risk factor (Bertram et al, 2010; Lambert et al, 2013). APOE is also involved in clearance of A β but the three human variants of the gene: *APOE* ϵ 2, *APOE* ϵ 3, and *APOE* ϵ 4 are not expressed in mice (Duong et al., 2021; Tsuang et al., 2013). The *APOE* ϵ 4 isoform increases oxidative stress and inflammation and may also be a risk factor for other dementias, and associated with cognitive decline in dementia with Lewy bodies and PD. However to date there is no research demonstrating cognitive decline on these mice (Bras et al., 2014; Tsuang et al., 2013)

Apolipoprotein E has anti-inflammatory properties in atherosclerosis as it has been shown to inhibit lipoproteins and VSMC proliferation and migration, it is also involved in the phagocytic clearance of cellular debris and apoptotic cells by promoting ingestion by macrophages which is an important step during inflammation (Grainger et al., 2004; Hayek et al., 1994; Hui and Basford, 2005). The anti-atherogenic functions of *ApoE* might contribute to the stronger development of atherosclerosis in *ApoE*^{-/-} mice compared to other models and has been crucial to investigate the inflammatory background of atherosclerosis. Therefore, other mouse models have been developed to study the effect of APOE on atherosclerosis.

1.5.3 Proprotein convertase subtilisin/ kexin type 9 overexpressing adeno-associated virus (PCSK9 -AAV8)

PCSK9 was first identified in the brain with potential involvement in CNS development and apoptosis (Adorni et al., 2019). PCSK9 is manipulated in a new model of atherosclerosis, where an adenovirus constitutively expressing murine PCSK9 (PCSK9-Ad) injected into wild-type mice leads to PCSK9 overexpression and increase in plasma total cholesterol due to increase LDL-cholesterol (Maxwell and Breslow, 2004). As PCSK9 targets LDLR to be degraded by lysosomes to control cholesterol homeostasis, the upregulation of PCSK9 disrupts the natural recycling of LDL and leads to increase plasma LDL cholesterol. These mice have no genetic modifications and express APOE and LDL at normal levels but present increased total plasma cholesterol (VLDL and LDL cholesterol) above 1000mg/dl when fed with a Western diet (high-fat content diet). This allows investigation of lipoprotein metabolism and inflammatory processes of atherosclerosis without the strong impact of LDLR and APOE.

1.6 *Neuroinflammation in association with atherosclerosis and a high-fat diet.*

A strong correlation between inflammation, neuronal stress and consumption of saturated fatty acids in the murine hypothalamus has been found (London et al., 2017). Suggesting microglia could potentially detect changes on the levels of saturated fatty acids which may initiate an inflammatory cascade (Valdearcos et al., 2014). More recently, in the high-fat diet hippocampus of mice, neuroinflammation was evidenced by Iba1+ reactivity and increased expression of TNF α and IL1 β which may impact dendritic spine connectivity (Vinuesa et al., 2019). Other studies have shown that lipid-

laden microglia trigger oxidative stress and release proinflammatory proteins which are also associated with dementia (i.e., *ApoE*, *Abca7*, *Clu*, *Plcy2*, *Trem2*) but are critical to lipid homeostasis (Marschallinger et al., 2020).

A study in *ApoE*^{-/-} mice fed a high fat diet, has linked neuroinflammation to atherosclerosis, it reported increased microglia activation, leukocyte recruitment and vascular inflammation through upregulation of VCAM-1 in the CNS. Both the plaque size and the neuroinflammation were reduced following deletion of interleukin-1 (IL-1), suggesting that this proinflammatory cytokine plays a major role in mediating the neuroinflammatory response (Denes et al., 2012; Drake et al., 2011). There is a limited number of studies investigating the effect of atherosclerosis on the BBB or the NVU, which focus mostly on the inflammation present on endothelial cells.

1.7 Hypothesis of this study

There is extensive evidence in the literature that atherosclerosis impacts the neurovascular supply through ischemic stroke and vascular occlusion. Previous studies found the presence of neuroinflammation in systemic atherosclerosis models without the presence of plaque rupture or cerebrovascular events (Denes et al., 2012). To date there are limited studies that have directly examined the effects of systemic atherosclerosis in the brain and more specifically on the neurovascular unit. We **hypothesise** that systemic atherosclerosis leads to dysfunction of NVU, glial activation and contributes to neurodegeneration.

1.8 Aims and objectives of this research

In order to investigate the impact of systemic atherosclerosis in the CNS, this project **aims** to use the *ApoE*^{-/-} and PCSK9 induced mouse model of systemic atherosclerosis to determine changes in the cellular expression and morphology through

characterisation of key components of the NVU and determine whether specific genes are expressed in atherosclerotic mice by

1. Performing a detailed characterisation of the components of the NVU (astrocytes, microglia, endothelial cells, basement membrane, pericytes and tight junction proteins) in different brain regions of the atherogenic ApoE^{-/-} mouse model and compare it to controls.
2. Performing a detailed characterisation of the components of the NVU (astrocytes, microglia, endothelial cells) in selected brain regions of the atherogenic PCSK9 induced mouse model and compare it to PCSK9 induced controls and ApoE^{-/-} mouse model.
3. Isolating brain regions using laser capture microdissection (LCM) to examine the transcriptomic differences between atherosclerotic mice and controls through the use of microarray technology
4. Validating the results from the microarray analysis through quantitative real-time polymerase chain reaction (qRT-PCR)

CHAPTER II: Materials and methods

All chemicals were purchased from **Sigma-Aldrich** (Poole, Dorset, United Kingdom) unless otherwise stated. Analytical grade solvents and pipette tips were purchased from **Thermo Fisher Scientific** (Hampton, New Hampshire, United States). **Vector Laboratories UK** (Orton Southgate, Peterborough, UK), **Abcam** (Cambridge, UK). All solutions were prepared as recipes specified in Appendix II.

2.1 ApoE^{-/-} mouse cohort

All ApoE^{-/-} mice used in this study were male, from a C57BL/6J background and homozygous for the ApoE targeted mutation 1, University of North Carolina mutation (ApoE^{-/-}). They were obtained from JAX labs (JAX2052, Jackson Laboratories, Bar Harbour, Maine, USA) which uses the ApoE^{-/-} mutant strain originally developed from the 129P2/OlaHsd- derived E14Tg2a embryonic stem cell line (Plump et al., 1992). Of the original purchased mice, 6 were fed with high-fat diet (section 2.3) and used for this project, the rest of the mice used were from a breeding colony maintained at the University of Sheffield biological service unit.

2.2 Pcsk9 induced mouse cohort

Male mice with C57BL/6J background received a single tail vein injection of genome of recombinant adeno-associated virus vector (AAV) encoding mutant mPCSK9 (rAAV8/D377Y- mPCSK9) at 8 weeks of age. The rAAV8/D377Y- mPCSK9 virus concentration was 6.1×10^{12} virus molecules per ml and was dialysed with 350 mM NaCl and 5% D-Sorbitol in phosphate buffer saline, it was produced using the PCSK9 gain-of-function plasmid, and prepared by the Gene Therapy Centre Vector Core at The University of North Carolina (Chapel Hill, NC, USA) (Bjørklund et al., 2014).

2.3 Environment and diet

All mice were housed with littermates, allowed free access to food and water, and maintained under a controlled temperature of 23 °C and a 12 hour light/dark cycle. All the mice were kindly provided by Prof. Sheila Francis, sacrificed, and perfused with the help of Dr Shabir (Section 2.4.). Animal procedures were approved by the University of Sheffield Project Review Committee and adhered to the UK Animals (Scientific Procedures) Act (1986) under project license 70/7992.

Control mice were fed with a normal chow diet while atherogenic mice were fed with a Western diet which consisted of 21% fat, 0.2% cholesterol (0.15% added, 0.03% from cholate), 35% sucrose (#829100, Special Diet Services, Witham, UK) (Table 2.1). Due to the high-fat content this diet is also known as a high-fat diet. Based on previous studies, the total plasma cholesterol of *ApoE*^{-/-} mice fed with a high-fat diet is significantly increased compared to *ApoE*^{-/-} mice fed normal chow diet: <1000 mg/dL and 400 - 600 mg/dL, respectively, leading to the accelerated development of atherosclerotic lesions within 6 weeks and plaques within 15 weeks (Oppi et al., 2019). The total plasma cholesterol of PCSK9 induced mice is ~700 mg/mL with a normal chow diet and <1000 mg/dL when fed with a Western diet (Kumar et al., 2017). Both models were started on the diet at 10 weeks of age and kept on it for 12 weeks. The western diet pellets were replaced twice a week to prevent them from drying out. The overall well-being of the mice was monitored weekly, and their weight measured before being euthanised.

Table 2.1 Mouse diet constituents

	Chow diet (Control)	Western diet (Atherosclerotic)
Fat	4.30%	21%
Protein	15%	17.30%
Sucrose	7%	35%
Cholesterol	0.02%	0.15% (.03% cholate)
Kcal/g	3.5	4.5

2.4 Brain dissection and tissue processing

At 22 weeks of age all mice were euthanized with an overdose of pentobarbital (100 mg/kg, Euthatal, Merial Animal Health Ltd) and transcardially perfused with 0.9% warm saline by Dr Shabir. This project used two *ApoE*^{-/-} mice cohorts for repeatability and to freeze one brain hemisphere from the second cohort (cohort 2) for the transcriptomic research as the whole brains from mice in the first cohort (cohort 1) were placed in formalin and embedded in paraffin wax. The cohorts were obtained a year apart as they became available. All mouse brains were left in formalin for two weeks for reproducibility as cohort 1 was harvested prior to the start of this research.

Cohort 1 of *ApoE*^{-/-} mice (normal diet n=7, western diet = 8, Appendix I) were perfused with saline, the whole brain removed, placed in 10 % formalin, and embedded in paraffin wax two weeks later. The embedding process consists of removing the tissue from the formalin and placing it in increasing concentrations of alcohol (70%, 80%, 95%) for 45 minutes followed by three changes of 100% alcohol of 1 hour each. The tissue is cleaned in two changes of xylene and immerse in three changes of paraffin for 1 hour each. Finally, the tissue is embedded in a paraffin block which can be stored at room temperature (RT) ready to be cut. The processing of the tissue was done with the help of Lynne Baxter.

The same protocol was followed for PCSK9 induced mice fed with a western diet (n = 6). Cohort 2 (normal diet n=6, western diet = 6, Appendix II) and the PCSK9 induced mice fed with a normal diet (later than the PCSK9 mice fed with a western diet as they became available, n=3). They were perfused with 0.9% warm saline before dissecting the brain and placing the right hemisphere in 10% (v/v) buffered paraformaldehyde to be processed to paraffin. The left hemisphere was snap-frozen in -20 °C isopentane and stored at -80°C until required (Figure 2.1).

The formalin fixed cerebrum was cut into three coronal slices to allow the visualisation of different brain areas on the same block. Once the formalin fixed tissue was cut it was immersed in increasing concentrations of alcohol to gently dehydrate it and minimize damage, before being immersed in xylene and finally embedded in paraffin. Formalin fixed paraffin embedded (FFPE) 5 µm sections were prepared using a microtome and collected at RT onto charged slides (StarFrost, Knittel Glass,) dried at 37°C overnight, and stored at RT until needed.

2.5 Histological characterisation

Tissue sections were stained with haematoxylin and eosin (H&E), and with luxol fast blue / cresyl fast violet (LFB/CFV) to assess the structure of the tissue and identify the regions of interest in each section.

2.5.1 Haematoxylin & Eosin (H&E) stain

FFPE sections (5 µm) were dewaxed in xylene (Fisher Scientific, UK), and rehydrated in a graded series of ethanol from 100%, 100%, 95%, to 70% (Fisher Scientific, UK) for 5 minutes in each and submerged in water. The sections were immediately immersed for 2 minutes in Harris haematoxylin (Leica, UK). The reaction was quenched by rinsing all sections with tap water. All sections were submerged in acid/alcohol for approximately 30 seconds to be differentiated and later placed into Scott's tap water and rinse with tap water. Finally the sections were placed in eosin (Leica, UK) for 5 minutes and washed in tap water following by dehydration through a graded series of alcohol [70%, 95%, 100%, 100%] for 30-60 seconds in each. Sections were cleared in xylene for 5 minutes, before being mounted using DPX mounting media (Leica, UK) and glass cover slips (Fisher Scientific, UK).

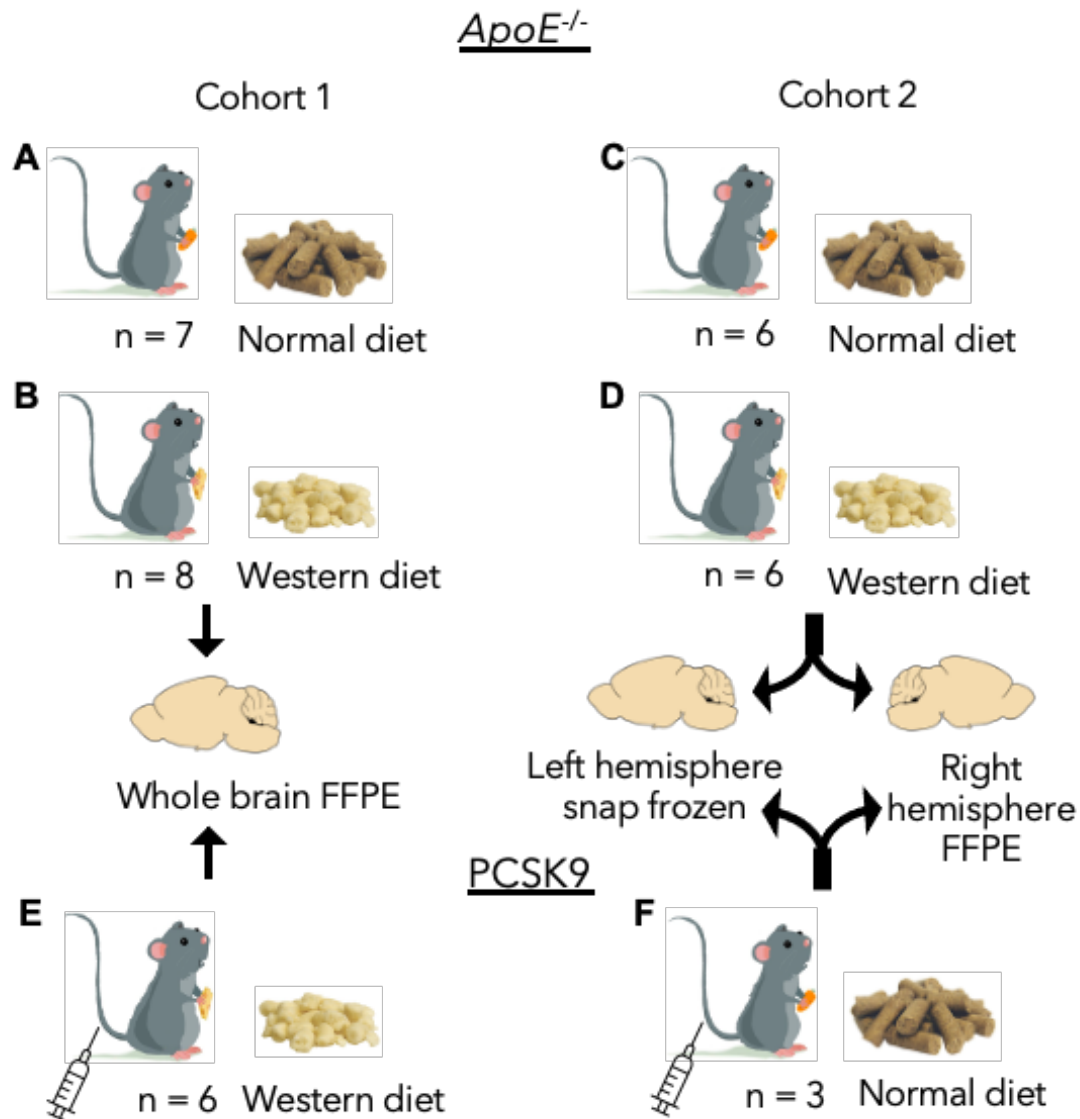


Figure 2.1 Summary of *ApoE^{-/-}* and PCSK9 induced mice and the dissected tissue

Cohort 1 of *ApoE^{-/-}* mice (A and B) were euthanised a year prior to cohort 2 (C and D). All conditions were kept the same. Cohort 1(A) of *ApoE^{-/-}* mice fed with the western diet were purchased directly from JAX laboratories while the other mice (B-D) were obtained from the strain bred at the University of Sheffield. The whole brain of cohort 1 mice was fixed in formalin and embedded in paraffin. For cohort 2, obtained a year later, the right hemisphere was fixed in formalin and embedded in paraffin and the left hemisphere was snap frozen to use for transcriptomic analysis. For the PCSK9 induced mouse model, mice received a tail vein injection of vector genome copies of recombinant adeno-associated virus vector encoding mutant mPCSK9 (E and D). The PCSK9 induced mice fed with a normal diet (F) were obtained at the same time as cohort 2 of *ApoE^{-/-}* mice and underwent the same protocol. All western diet was changed at 10 weeks and all mice were euthanised at 22 weeks of age.

2.5.2 Luxol Fast Blue

FFPE sections (5 µm) were dewaxed in xylene and rehydrated to water through a graded series of ethanol (100%, 100%, 95%, 70%) for 5 minutes in each. All sections were immersed in LFB solution for 2 hours at 60°C. Any excess stain was removed with 95% ethanol and the sections rinsed in distilled water (d.H₂O). Sections were differentiated in lithium carbonate for 30 seconds. The sections were counterstained with CFV for 2 minutes, differentiated in 0.5% acetic acid in alcohol for 30 seconds, and rinsed in water. The sections were dehydrated through a series of graded alcohols and cleared in xylene for 5 minutes before being mounted using DPX mounting media and glass coverslips.

2.5.3 Identification of the neuroanatomical regions of interest

The mouse neuroanatomy visible in a single section was observed using H&E and LFB/CFV. In *ApoE*^{-/-} cohort 1, the brain areas selected for investigation were: the cerebral cortex, corpus callosum, hippocampus, thalamus, and striatum (Figure 2.2). The cases with incomplete or not easily identifiable areas of interest were eliminated from further analysis (from *ApoE*^{-/-} cohort 1 control mice n = 1, atherosclerotic mice n = 2) (Figure 2.2. A). In the *ApoE*^{-/-} cohort 2 and PCSK9 induced cohort, only the cerebral cortex, corpus callosum and hippocampus were analysed, as these areas displayed the greatest variation in the staining of selected markers in *ApoE*^{-/-} cohort 1. The delimitation of the area of interest was determined by their unique morphology delimitating the cerebral cortex and corpus callosum by the hippocampus (Figure 2.2). The corpus callosum was identified by its fibrous characteristic due to the high number of myelinated axons.

2.5.4 Immunohistochemistry (IHC)

FFPE sections were dewaxed in xylene (5 minutes in two different xylene containers) and rehydrated to water through a graded series of ethanol 100%, 100%, 95%, 70% (5 minutes in each). This protocol used a standard horseradish peroxidase-conjugated avidin-biotin complex (ABC-HRP) IHC technique (Vectastain Elite kit, Vector Laboratories UK) with 3, 3'-diaminobenzidine (DAB) (Vector Laboratories UK) as substrate, using the Vectastain Elite ABC-HRP kits, specific to the species in which the primary antibody was raised. After dewaxing and prior to antigen retrieval, all the sections were immersed for 20 minutes at RT in 3% hydrogen peroxide in methanol (Appendix II). Following pre-treatment (dewaxing, dehydration and the blocking of endogenous peroxidase with hydrogen peroxide) the FFPE sections underwent the optimal antigen retrieval method (Table 2.2).

The sections were placed in a plastic container submerged in tri-sodium citrate (TSC) solution pH 6.5 or ethylenediaminetetraacetic acid (EDTA) pH 8 and heated in a microwave oven on full power (800W) for 10 minutes. For some antibodies an alternative antigen retrieval technique was employed and used high temperature and high pressure in which sections were placed into a plastic container with either pH6 or pH9 antigen retrieval solution from Menapath Access Revelation. The pressure cooker was run with approximately 500ml of dH₂O at 30psi and 125°C for 30 seconds. After antigen retrieval, the slides were rinsed with running tap water and cooled down to RT. All antibodies used in this study were optimised prior to staining of all cohorts. The antibodies that were previously optimised and used in the SITraN Pathology Lab using human tissue, but they were not successfully optimised using mouse tissue, are shown in Table 2.3.

ApoE^{-/-} mouse from the 1st cohort

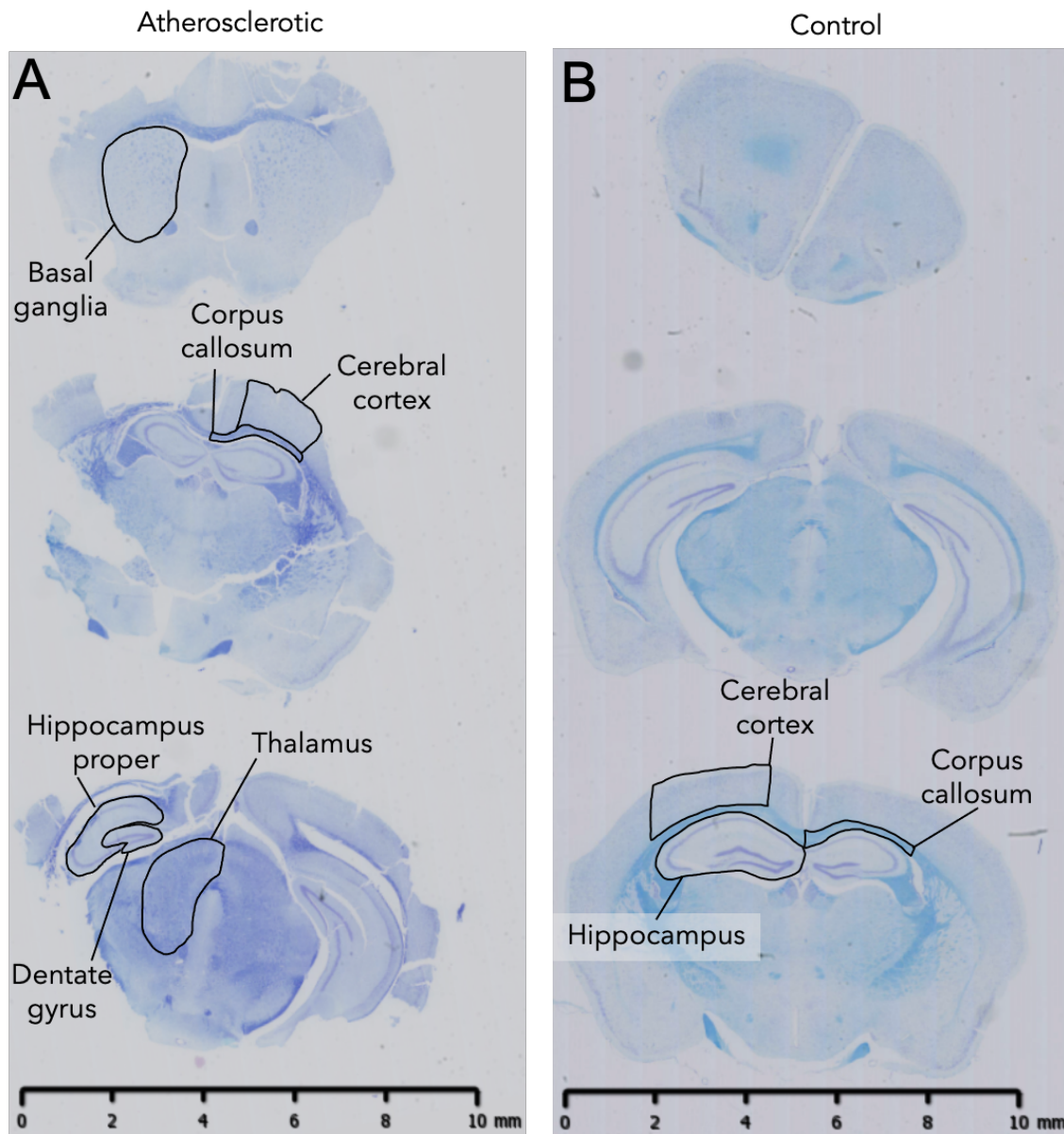


Figure 2.2 Luxol fast blue staining of control and atherosclerotic ApoE^{-/-} mouse brains to identify key regions of interest

ApoE^{-/-} sections were stained with LFB and contrasted with CFV to visualise myelin (blue) and stain the Nissl substance in neurones and cell nuclei (purple). The delineated areas indicate the different brain areas observed on a single section which were used for the initial quantitative analysis in cohort 1 of ApoE^{-/-} mice (A). In ApoE^{-/-} mouse cohort 2 and PCSK9 induced mice only the cerebral cortex above the hippocampus, the corpus callosum above the hippocampus, and the hippocampus were analysed indicated in the representative slides of control ApoE^{-/-} mice (B). Scale bar represents 10mm

Table 2.2. Antibodies used in the IHC study and their optimal conditions

Marker	Primary antibody target	Species	Secondary antibody	Dilution conditions	Antigen retrieval	Supplier	Lot no.
Astrocyte	GFAP	Rabbit polyclonal	Goat anti - rabbit IgG	1:500 1hr, RT	MW TSC buffer, pH 6.5	Dako, UK	200254 80
Microglia	IBA-1	Goat polyclonal	Rabbit anti - goat IgG	1:250 1hr, RT	MW TSC buffer, pH 6.5	Abcam, UK	GR313 212-2
				1:75 1hr, RT			GR187 091-3
Endothelial cell	ICAM-1	Goat polyclonal	Rabbit anti - goat IgG	1:500 1hr, RT	MW TSC buffer, pH 6.5	R&D system, UK	GRG02 17101
				1:250 O/N, RT			GRG34 18306
Pericyte	PDGFR- β	Rabbit polyclonal	Goat anti - rabbit IgG	1:100 O/N, RT	MW TSC buffer, pH 6.5	Abcam, UK	200254 80

Table 2.3 Antibodies tried but not satisfactorily optimised

All antibodies were optimised trying all heat induced antigen retrieval methods available

Primary antibody target	Species	Secondary antibody	Dilution	Incubation	Supplier	Lot number
AQ4	Rabbit polyclonal	Goat anti - rabbit IgG	1:200 1:100 1:50	1hr, RT	Thermofisher, UK	PA5-36521
OCC1	Rabbit polyclonal	Goat anti - rabbit IgG	1:100 1:50 1:25	1hr, RT & O/N, 4°C	Invitrogen, UK	71-1500
CD31	Mouse monoclonal	Horse anti - mouse IgG	1:250 1:500	1hr, RT	Dako, UK	JC70A
COL-IV	Rabbit polyclonal	Goat anti - rabbit IgG	1:500 1:250 1:100	1hr, RT	Abcam, UK	ab19808
MHCII	Mouse monoclonal	Horse anti - mouse IgG	1:1000 1:500 1:250	1hr, RT	Dako, UK	M0746
	Rat monoclonal	Rabbit anti - rat IgG	1:150	1hr, RT & O/N, 4°C	Abcam, UK	ab25333
PS2Y12	Rabbit polyclonal	Goat anti - rabbit IgG	1: 100 1: 50	1hr, RT	Atlas antibodies, UK	HPA014518
hTREM2	Goat polyclonal	Rabbit anti - goat IgG	1:50 1:25 1:10	1hr, RT	R&D systems, UK	AF1828
CD68	Rat monoclonal	Rabbit anti - rat IgG	1:200 1:100 1:50	1hr, RT	BioRad, UK	MCA1957
CD163	Mouse monoclonal	Horse anti - mouse IgG	1:500	1hr, RT	BioRad, UK	MCA1853

After antigen retrieval, the sections were incubated for 30 minutes at RT with 1.5% species specific normal serum in order to minimise the amount of non-specific binding of the secondary antibodies (Table 2.2). All slides were incubated with the primary antibody at the optimal concentration, time, and temperature (Table 2.2). Parallel to this incubation, the primary antibody was omitted from a slide as a negative control, ensuring the staining observed was a result of the antigen being detected and not the reagents used. In addition, a relevant isotype control was also included by incubating a section with the respective antibody IgG (Vector laboratories UK), thereby ensuring that the immunoreactivity observed is specifically due to the primary antibody detecting the antigen. The primary antibody and isotype control were diluted with the appropriate blocking solution and were included in every immune run. The immunoreactive profile was interrogated using primary antibodies to detect GFAP, IBA-1 and ICAM-1 (Table 2.2).

Following incubation in primary antibody, the sections were incubated with the relevant secondary biotinylated antibody for 30 minutes at RT and then incubated with ABC-HRP for 30 minutes at RT. The ABC-HRP was made at least 30 minutes before use. All slides were thoroughly washed between steps with TBS buffer for 5min and tapped to remove excess liquid after each step. The use of the ABC-HRP complex amplifies the signal by increasing the number of binding sites between the secondary antibody and HRP. Then DAB, a colourless chromogen, was added to all the sections and left for approximately 5min until a brown reaction product was observed under a microscope. The enzyme reaction was quenched using tap water. All sections were washed, and counterstained using Harris haematoxylin for 1-2 minutes. The sections were dehydrated in a graded series of alcohol (70%, 95%, 100%, 100%), cleared in

xylene and permanently mounted with DPX mounting media and glass cover slips. An overview of the major steps in the IHC procedure is shown in Figure 2.3.

2.5.5 Immunofluorescence

To assess the co-localisation of ICAM-1 in microglia, dual immunolabelling was performed. Immunostaining for ICAM-1 was performed using ABC-HRP technique with DAB as substrate (see section 2.5.4 and Table 2.2). The DAB-stained section was incubated with avidin/biotin blocking solution (Vector Laboratories, UK) (15 min avidin solution followed by 15 min biotin solution at RT) and then blocked with normal serum (1.5%), followed by incubation with the anti-IBA-1 primary antibody. Sections were washed and incubated with a biotinylated secondary antibody (0.5%) for 30 min at RT, followed by incubation with streptavidin- Alexa fluor 488 complex (0.2%) (Alexa Fluor 488 dye, Thermo Fisher scientific) for 1 hour. Sections were mounted using Fluor mount Mounting Media (Sigma-Aldrich, St Louis, MO, USA).

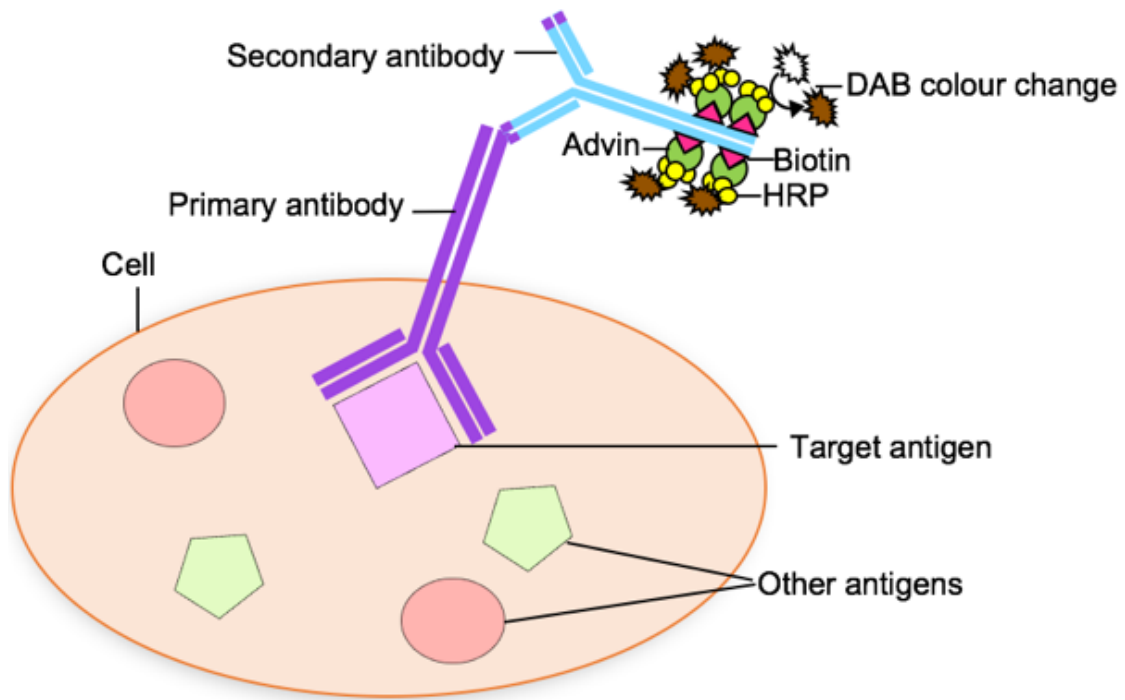


Figure 2.3 Schematic of the immunohistochemistry ABC-HRP process

Immunohistochemistry enables the identification of antigens using specific antibodies. Through antigen retrieval methods the antigen epitopes in the tissue are unmasked thereby allowing the primary antibody to bind to its specific target. A species-specific secondary antibody binds to the primary antibody. The secondary antibody is conjugated with biotin molecules which interact with HRP conjugated avidin, this amplifies the signal. The addition of the enzyme substrate DAB reacts with HRP resulting in a brown reaction product that enables the visualisation and localisation of the target antigen in the tissue section.

2.5.6 Semi-quantitative analysis

The immunoreactive profile of GFAP was semi-quantitatively analysed by capturing 3 random images of the hippocampus, dentate gyrus, cortex, corpus callosum, basal ganglia, and thalamus of control and atherosclerotic *Apoe*^{-/-} cohort 1 cases. These brain regions were selected due to their relevance in relation to dementia and the variability of cellular heterogeneity observed on each of these areas.

Images were taken using a Nikon Eclipse 801i Microscope at a 20x magnification under bright field. Each image was assessed by two independent observers (Dr Julie Simpson and Monica Rebollar), and scored based on the pattern of staining observed: negative or minimal immunoreactivity present (0) (Figure 2.4.A), sparse GFAP⁺ astrocytes present (1) (Figure 2.4B), mild GFAP immunoreactivity throughout (2) (Figure 2.4C), moderate GFAP immunoreactivity throughout (3) (Figure 2.4 D), severe GFAP immunoreactivity throughout (4) (Figure 2.4 E).

2.5.7 Quantitative image analysis

Stained sections were examined using the Nikon Eclipse 801i Microscope, CellR image software system (Olympus, UK), and whole slide scanner (ScanScope CS, Aperio). Images were taken of the complete hippocampus, thalamus, corpus callosum, cerebral cortex and striatum at x20 magnification. Delimitation of the selected neuroanatomical areas was done using the regions of interest tool. The images were analysed using the analySIS[^]D software, which uses size exclusion (pixels) to detect the amount of DAB ('brown') present on the region of interest (Figure 2.5). The percentage (%) immunoreactive area of GFAP, IBA-1 and ICAM-1 was determined. The pixel counting was adjusted to identify all the immunoreactive cells while excluding any background staining. For ICAM-1 images were analysed twice, the first analysis

was performed to identify all immunopositive cells (endothelial cells and microglia) while the second analysis was adjusted to only detect endothelial cells only, as they appeared more immunoreactive than microglia. Percentage (%) area of immunoreactivity for GFAP, IBA-1 and ICAM-1 was used for statistical analysis.

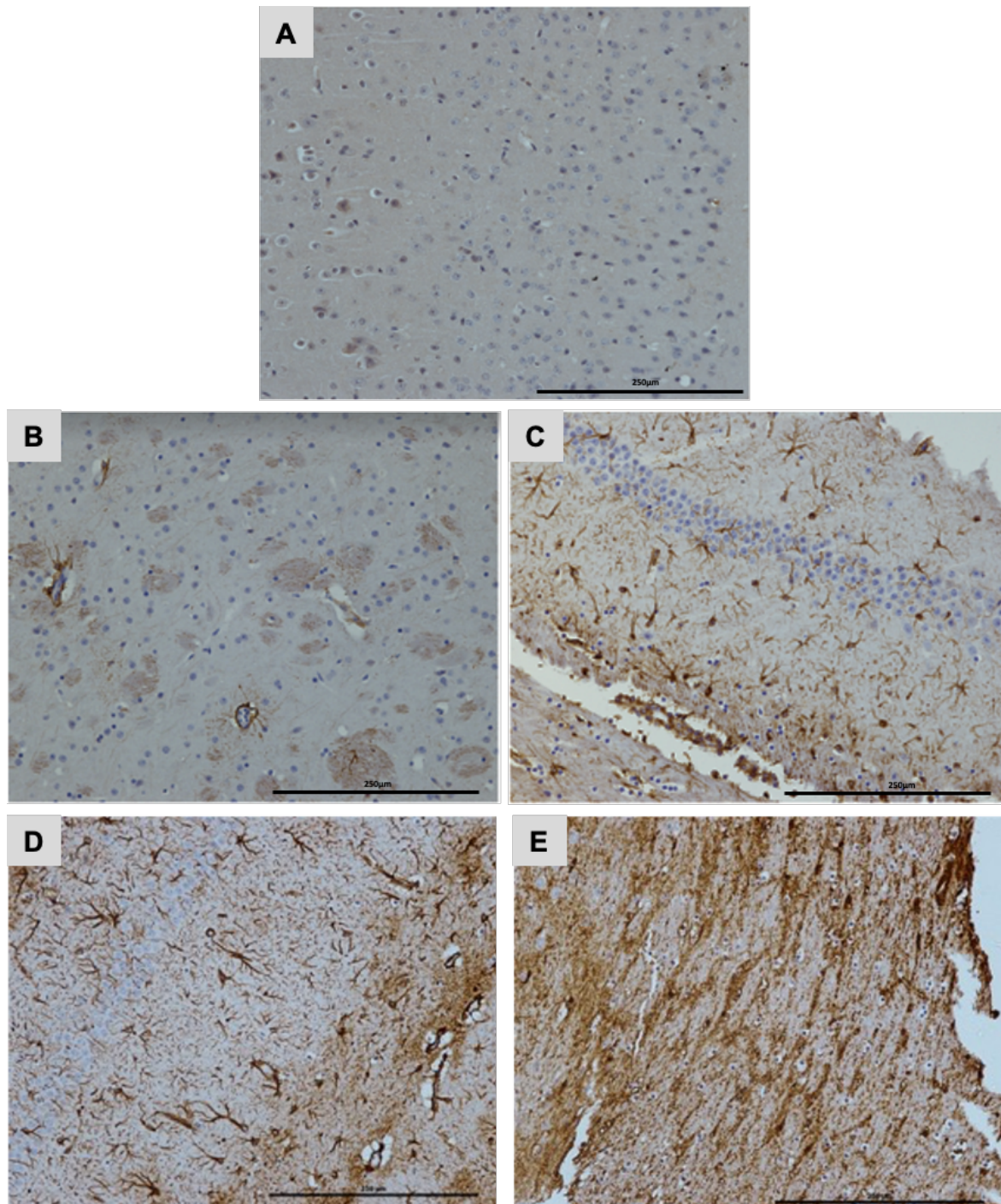


Figure 2.4 Semi-quantitative analysis of GFAP immunostaining

The immunoreactive profile of GFAP was scored according to the staining pattern observed. Representative example of negative or minimal astrocytes present (A), sparse GFAP⁺ astrocytes present (B), mild GFAP immunoreactivity (C), moderate GFAP immunoreactivity throughout (D), severe GFAP immunoreactivity throughout (E).

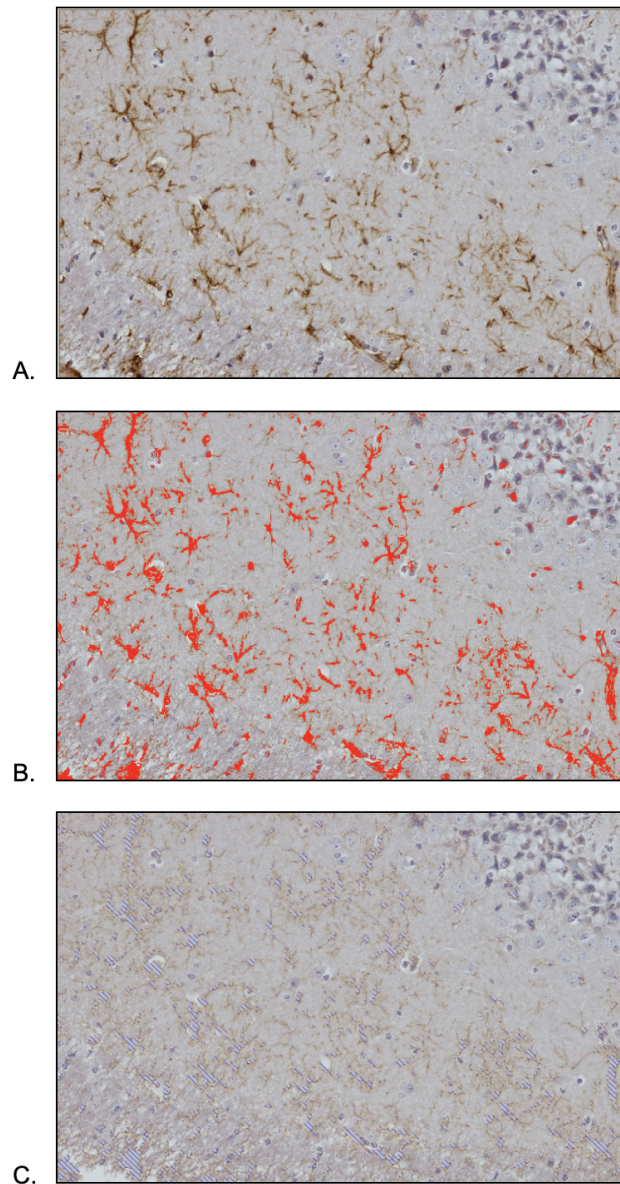


Figure 2.5. Representative image of the percentage (%) area of immunoreactivity quantification

All cases were stained with GFAP and the % area of immunoreactivity was quantitated using analySIS^D image analyser software. (A) the image was uploaded, and the software detected the amount of 'brown' present in the selected area (B). Once detected the selected fields are removed from the image in order to determine if the correct cells are being selected (C). The program was run to detect all the immunoreactivity present in the image and the % area of immunoreactivity calculated.

2.5.8 Statistical analysis

Statistical analysis was performed using SPSS Statistics 27.0 software and graphs were made using GraphPad Prism 9.0 software. The measure of agreement between the two observers of the semi-quantitative analysis, was measured using Cohen's Kappa value. The scores were averaged and analysed using Kurskal-Wallis test.

ApoE^{-/-} mouse cohorts showed different marginal means when plotted; therefore the data was analysed separately. GFAP, IBA-1 and ICAM-1 % area of immunoreactivity in both mouse cohorts and models were not normally distributed and did not show equality of variances using Shapiro-Wilk test and Levene's test respectively. The non-parametric statistical method, Kurskal-Wallis test was applied, followed by Mann-Whitney U test with correction for multiple comparison testing using the Bonferroni method to identify the differences between control and atherosclerotic mice in all brain areas, in all cohorts. For the comparison between the *ApoE*^{-/-} and PCSK9 induced mouse models the average of control mice was use as the baseline and the fold change of each atherosclerotic case was compared to it. The ratio was calculated for each mouse model and followed by a pairwise comparison of the individual brain areas using a Student's t-test and applied Bonferroni correction.

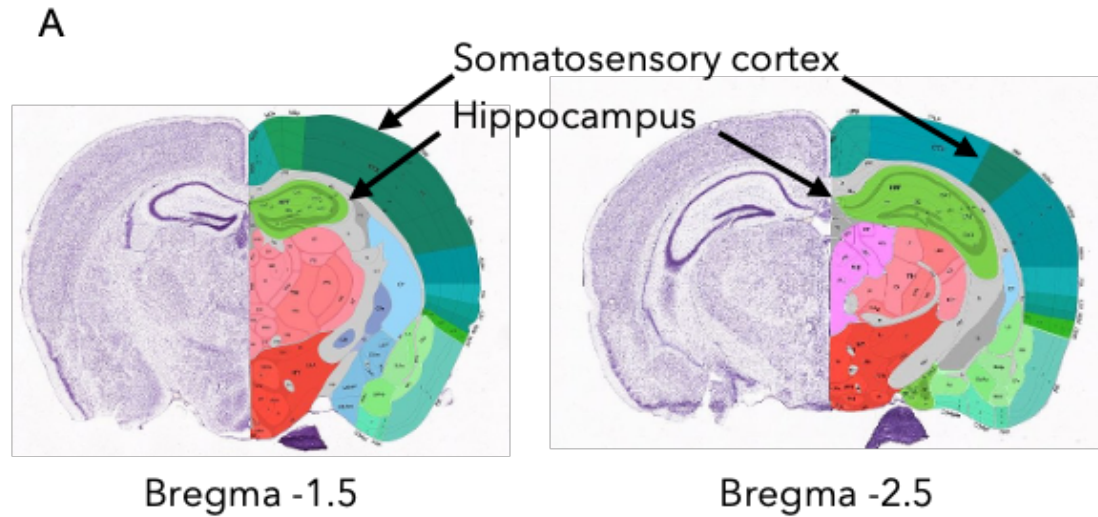
2.6 *Transcriptomics*

2.6.1 Tissue source

Snap frozen tissue used for the transcriptomic work was obtained from cohort 2 of control and atherosclerotic mice (Section 2.4). As the whole left hemisphere was snap frozen, sections were cut from rostral to caudal using the cryostat. Sections were discarded until the somatosensory cortex and the hippocampus were visible, located between Bregma -1.5 and Bregma -2.5 (Figure 2.6 A). While trimming, a 30 μm section was collected into a sterile 0.5 ml Eppendorf tube to assess the quality of RNA of each case prior to LCM. Once trimmed a total of six consecutive sections (7 μm) were placed on individual non-adhesive slides (Leica, UK). Five of these sections were used for LCM and the additional one was for reference of the tissue sections obtained.

2.6.2 LCM sample preparation - Toluidine Blue

LCM was performed on freshly cut cryosections to prevent RNA degradation. Under RNase-free conditions sections were warmed to RT before being fixed in ice-cold acetone for 3 minutes and stained in toluidine blue for 3 minutes at RT. Sections were rinsed in diethylpyrocarbonate (DEPC)-treated water for 30 seconds, dehydrated in a graded series of alcohol (70%, 95%, 100% and 100%) for 15 seconds in each. Sections were cleared in xylene for 5 minutes, before being left to air dry under an air flow hood for 60 minutes. Following the staining protocol, the hippocampus and cerebral cortex of each case were easily identified (Figure 2.6 B).



B Toluidine blue *ApoE*^{-/-} control

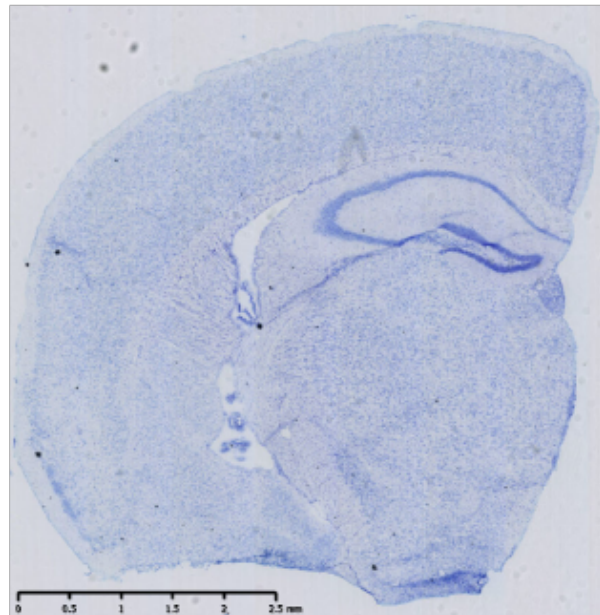


Figure 2.6 Guide images used to obtain the hippocampus and cerebral cortex from frozen mouse brain sections and representative image of toluidine blue *ApoE*^{-/-} control cohort 2 mice for LCM

Mouse brain sections for LCM were collected between Bregma -1.5 and Bregma -2.5 to isolate the hippocampus and the somatosensory cortex (A). Sections were stained with toluidine blue (B) which helps to distinguish the specific target areas under the LCM microscope.

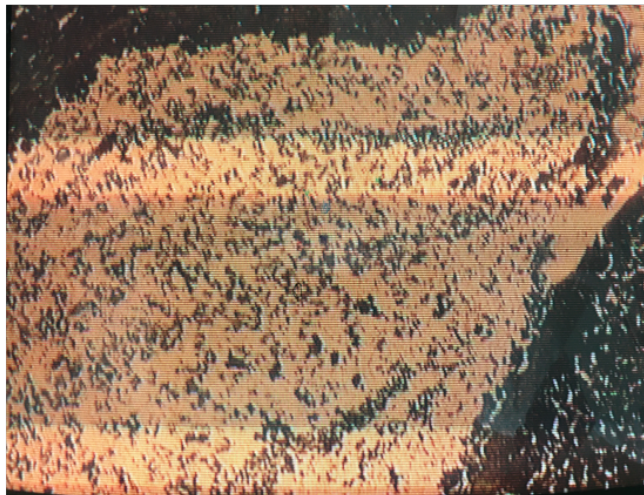
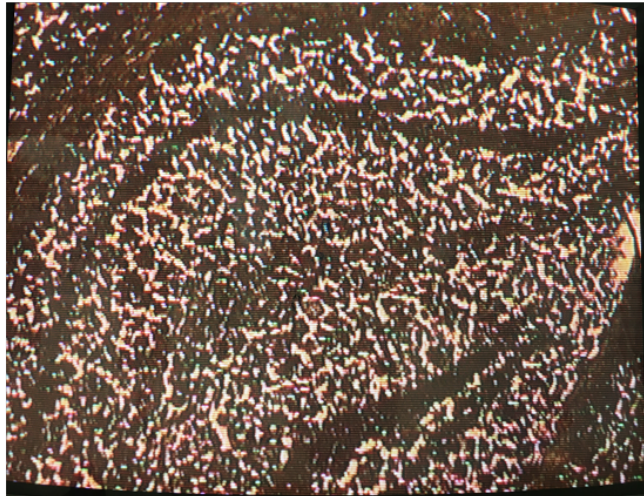
2.6.3 Laser capture microdissection

From the toluidine-stained sections, the hippocampus and the somatosensory cortex were isolated using the PixCell II laser-capture microdissection system (Arcturus Engineering, Mountain View, CA, USA). The dried, stained sections were placed under microscopy and covered with a thermoplastic film cap (CapSure Macro cap Arcturus Engineering, Mountain View, CA). An infrared laser was fired through the cap, melting the film and adhering the selected hippocampus (Figure 2.7). The LCM system was set at; laser spot size 10 μm and power 70-100 mW. Two separate caps were used for the collection of the hippocampus and the somatosensory cortex. After the successful microdissection of five sections per case, the film was removed from the cap and transferred to a sterile 0.5 ml Eppendorf tube for RNA extraction.

2.6.4 Pre-LCM RNA integrity analysis

RNA from each case pre-LCM was extracted under sterile conditions, at RT using the common phase separation method. Each 15 μm cryosection was combined with 500 μl Trizol and 100 μl chloroform. Samples were briefly vortexed, left to incubate for 10 minutes at RT and centrifuged (Sigma centrifuges, UK) at 20,000 $\times g$ at 4°C for 15 minutes. The top aqueous layer was transferred into a sterile 1.5 ml Eppendorf tube and 250 μl isopropanol added and samples left to incubate for 5-10 minutes at RT. Samples were centrifuged at 20,000 $\times g$, at 4°C for 10 minutes and the supernatant was discarded and 1 ml ice-cold 75% ethanol added, samples were vortexed briefly and centrifuged at 15,000 $\times g$, at 4°C for 5 minutes. The residual ethanol was discarded from the samples and the pellet resuspended in 25 μl of sterile dH₂O. The RNA quantity and quality of all samples was analysed using a NanoDrop spectrophotometer and a 2100 Bioanalyzer (Agilent, UK) respectively. The RNA integrity number (RIN) of each case was determined prior to and post LCM.

Mouse hippocampus under LCM microscope



Target area after removal of the mouse hippocampus

Figure 2.7 LCM of the hippocampus of an *ApoE*^{-/-} cohort 2 mice under the microscope

A plastic cap was placed over the toluidine blue stained hippocampus which was easily observed under the LCM microscope (A). An infrared laser was fired on the target areas, causing the film to melt and adhere to the tissue, the cap was lifted to confirm the isolation of the target area (B).

2.6.5 RNA extraction

Total RNA was extracted from the LCM'd hippocampus and somatosensory cortex using the PicoPure RNA isolation kit (Arcturus BioScience, UK) according to the manufacturer's instructions (Figure 2.8). Briefly, 50 μ l extraction buffer was added to each LCM film and incubated in a thermal cycler for 30 minutes at 42°C (G-storm Thermal Cycler, Somerset, UK). The purification column was preconditioned with 250 μ l conditioning buffer for 5 minutes and centrifuged at 13,000 $\times g$ for 1 minute at RT. 50 μ l 70% ethanol was added to each sample and mixed by pipetting up and down. Each sample was transferred to the conditioned purification column. The column was subjected to centrifugation at 300 $\times g$ for 1 minute and then at 13,000 $\times g$ for 1 minute. To purify the extracted RNA bound to the column 100 μ l wash buffer 1 was applied and the column centrifuged at 800 $\times g$ for 1 minute, followed by a second wash with 100 μ l wash buffer 2, and centrifugation at 800 $\times g$ for 1 minute, this second wash step was then repeated. The purification column was transferred to a sterile 1.5 mL Eppendorf tube and 11 μ l elution solution was added to the column. RNA was eluted by subjecting the column to centrifugation at 1,000 $\times g$ for 1 minute and a final centrifugation at 13,000 $\times g$ for 1 minute. Eluted RNA quantity and quality were determined using a NanoDrop 1000 spectrophotometer and a 2100 Bioanalyzer (Agilent, UK), respectively. All RNA samples were stored under sterile conditions at -80°C for future analysis. Due to time constraints the somatosensory cortex was stored and only the hippocampus was used for microarray analysis.

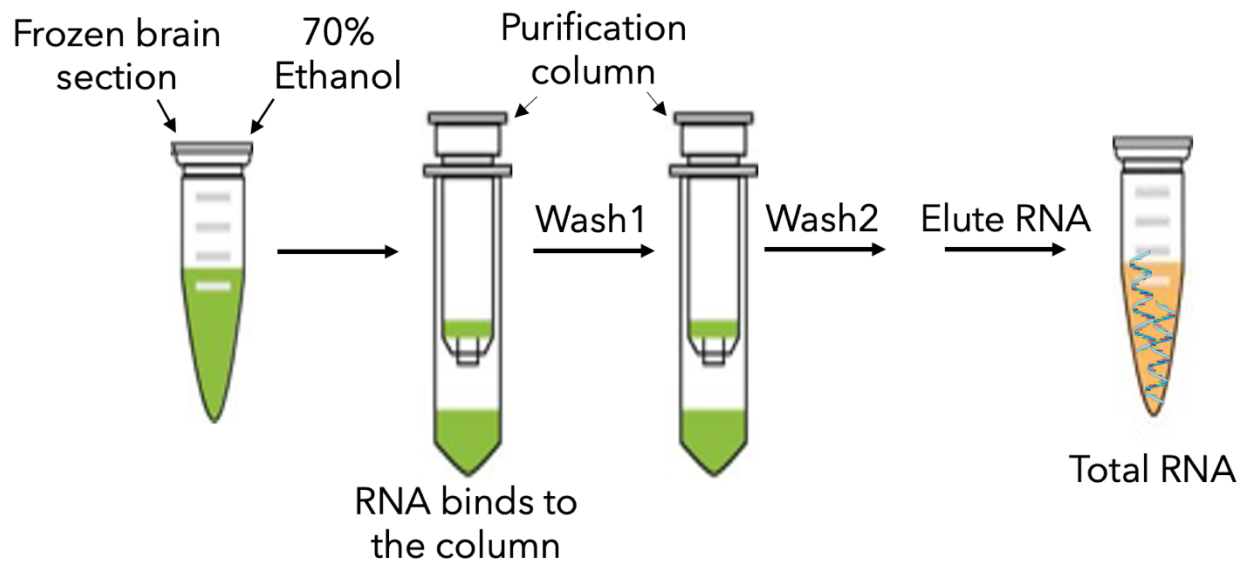


Figure 2.8 PicoPure RNA extraction process from tissue isolated using LCM

RNA from the isolated hippocampus and cerebral cortex tissue obtained from LCM was extracted and purified using reagents, purification columns and a series of centrifugation steps.

2.6.6 RNA extraction quality control

The concentration of extracted RNA was estimated using a NanoDrop ND-1000 spectrophotometer (Thermo Fisher Scientific). This device measures the absorption of light from 230 nm to 340 nm, enabling a close estimate of the quality and quantity of RNA present in each sample. After blanking the spectrophotometer with RNase free water, 1 µl of RNA was placed on the NanoDrop to be analysed.

Using an Agilent RNA 6000 Pico Assay and Agilent 2100 Bioanalyzer (Agilent Technologies Inc., Santa Clara, CA, USA) the quality of RNA pre and post LCM was assessed using the RNA integrity number (RIN), based on the 28S/18S ribosomal peak ratio, with increasing degradation leading to a fall in the ratio and decrease in RIN.

2.6.7 Microarray analysis

Microarrays gene expression analysis was used to identify differentially expressed genes and pathways that could be contributing to disease susceptibility. The Affymetrix (ThermoFisher Scientific) mouse genome 430 2.0 microarray, used in this study, contain 45,000 probe sets representing over 34,000 genes. Different genes are represented by a probe set which are unique 25-mer oligonucleotides located at a designated region on the solid microarray surface. This process measures and compares the expression of every gene simultaneously.

In summary, total RNA isolated from *ApoE* mouse hippocampus (n= 12) was reverse transcribed into cDNA, the cDNA was amplified, fragmented and labelled with a biotin fluorescent dye before being hybridised to the mouse genome 430 2.0 microarray chips. The microarray chips were analysed using a high-resolution laser scanner and the extent of the signal intensity of each spot on the array proportional to the amount of DNA bound to the chip. Significant differentially expressed genes were quantified

and comparisons between normal diet and western diet samples were determined (Chapter 3).

Poly-A control preparation

RNA extracted from each hippocampal sample was processed and amplified using the GeneChip™ whole transcript (WT) pico reagent kit to prepare for gene expression analysis using Affymetrix mouse genome 430 2.0 microarray chips. To monitor the labelling process, poly-A RNA control was added to each sample in a series of dilutions (5 ng RNA, 5 µl poly-A control) The poly-A control consisted of polyadenylated transcripts from *B. subtilis* not present in eukaryotic cells.

2.6.8 Two round linear RNA amplification

First strand cDNA synthesis

Using the GeneChip™ whole transcript (WT) pico reagent kit (Affymetrix, Thermo Fisher Scientific, MA, USA), 50 ng total RNA and poly-A control RNA was reverse transcribed into single-stranded cDNA (ss-DNA) containing a T7 promoter sequence at the 5' end. To each sample, 5 µl of First-Strand master mix was added and mixed thoroughly (4 µl first strand buffer and 1 µl first strand enzyme) before being incubated in a thermal cycler at 25°C for 5 minutes followed by 42°C for 60 minutes and 4°C for 2 minutes. 2 µl WT Pico Cleanup Reagent was added to each sample and mixed thoroughly before incubation at 37°C for 30 minutes, 80°C for 10 minutes and 4°C for 2 minutes.

3' Adapter cDNA Synthesis

A 3'- Adaptor was added to the ss-cDNA to act as a template for the *in vitro* transcription (IVT) reaction. To each first strand cDNA sample (5 µl), 8 µl 3' adapter master mix was added and mixed thoroughly (7 µl 3' adapter buffer and 1 µl 3' adapter

enzyme) before incubating in a thermal cycler at 15°C for 15 minutes, 35°C for 15 minutes, 70°C for 10 minutes and 4°C for 2 minutes. Tubes were centrifuged briefly to collect the samples at the bottom of the tube.

Double-strand cDNA synthesis

Double-stranded cDNA (ds-cDNA) was synthesised using a master mix containing DNA polymerase and RNase H, which incorporated the t7 polymerase promoter into the ds-cDNA while the RNA was broken down by the RNase H.

Preparation of complementary RNA by *in vitro* transcription

The synthesised ds-cDNA served as a template for the *in vitro* transcription (IVT) reaction that synthesised copies of amplified antisense RNA (complementary RNA). The cRNA obtained using IVT technology and t7 RNA polymerase was purified using beads to remove inorganic phosphates, salts, enzymes or unincorporated nucleotides.

Second cycle single-stranded cDNA synthesis

In the second round of amplification, cRNA was reverse transcribed to sense-strand cDNA containing dUTP at a fixed ratio relative to dTTP using random primers and reverse transcriptase. The remaining cRNA was hydrolysed with RNase H resulting in a single-stranded cDNA. The sense-strand cDNA was purified with magnetic purification beads and assessed using the NanoDrop spectrophotometer.

RNA fragmentation, hybridisation and microarray scanning

The sense-strand cDNA was broken at the synthetic dUTP residues by uracil-DNA glycosylase (UDG) and apurinic/apyrimidinic endonuclease 1 (APE 1). Followed by labelling the fragments of cDNA with a DNA labelling that is bonded to biotin using terminal deoxynucleotidyl transferase (TdT). 120 ng fragmented, and labelled ss-DNA was prepared for hybridization using a using a GeneChip® Hybridisation wash and

stain kit. The GeneChip Mouse Gene 2.0 ST Array cartridges were preconditioned with prehybridization mix in a hybridisation oven (Affymetrix, UK) at 45 °C at 60 rpm for 10 min. Samples were added to a hybridization cocktail master mix containing 20x hybridisation controls (bioB, bioC, bioD and cre genes), positive oligonucleotide B2 control (B2 oligo), DMSO, 2x hybridisation mix and nuclease-free water (9.3 µl). The mix was incubated for 5 minutes at 99 °C, followed by 5 minutes at 45 °C, and centrifuged briefly. 73 µl of pre-hybridised samples were injected and hybridized to GeneChip Mouse Gene 2.0 ST Array cartridges at 45 °C for 16 hours, rotating at 60rpm. The hybridisation cocktail was removed from the arrays and the arrays were washed with Wash buffer A to remove any unbound sample before being stained with Affymetrix GeneChip® Command Console Fluidics Control (ThermoFisher Scientific, MA, USA). Scanning of the arrays was performed using a GeneChip® Scanner 3000, and the Affymetrix Expression Console generated the raw signal intensity values (CEL files). This process is summarised in Figure 2.9.

2.6.9 Microarray data analysis and quality control

Affymetrix Gene Expression Console software version 4.0 (Affymetrix, Stickport, UK) was used to assess the quality of the data by looking at the overall signal intensity across the samples alongside the intensity of the labelling (poly-A control) and hybridization controls. Differentially expressed genes were identified using Transcriptome Analysis Console (TAC) software version 4.1.1 (Affymetrix, Stockport, UK) through a two-group comparison of normal diet *ApoE*^{-/-} mice and western diet *ApoE*^{-/-} mice with restrictive settings of $p \leq 0.05$ and a fold change $\geq \pm 1.2$. Qlucore

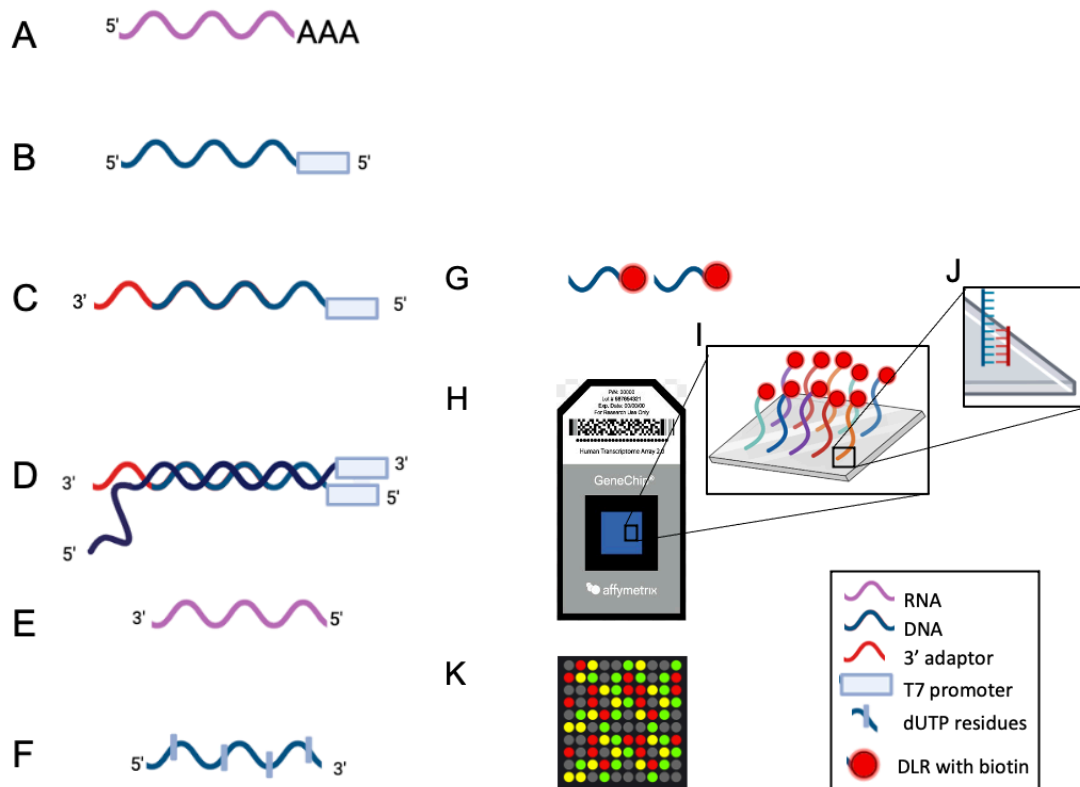


Figure 2.9. Process of two round linear amplification and labelling of RNA obtain from LCM of *ApoE*^{-/-} mouse hippocampus

A poly-A tail is added to the target RNA (A) to initiate reverse transcription and synthesise a single stranded cDNA with a T7 promoter sequence at the 5' end (B). A 3' Adaptor is added to the ss-cDNA (C) and acts as a template for the ds-cDNA synthesis (D). The ds-cDNA also acts as a template for IVT transcription synthesising and amplifying an anti-sense RNA (E). After purifying the cRNA a second ss-cDNA is generated through reverse transcription generating a sense strand cDNA. The sense strand-cDNA is hydrolyse from aRNA leaving a ss-CDNA containing dUTPs (F). This is then fragmented and labelled fluorescently with biotin (G). The oligonucleotide probes on the microchip hybridise with its corresponding fragment of labelled ss-cDNA (H-J) and a scanner detects the fluorescent signal to determine the gene expression in the samples.

Omics Explorer (version 3.0) software (Qlucore, Lund, Sweden) was used to visualise the distribution of the samples using Principal Component Analysis (PCA).

The list of genes showing a significant difference were analysed using the database for annotation, visualisation and integrated discovery (DAVID) Functional Annotation Tool Version 6.8 (National Institute of Allergy and Infection Disease, National Institute of Health, USA) to group the genes based on their biological function and the use of Kyoto Encyclopaedia of Genes and Genomes (KEGG) pathway analysis. The Integrated Molecular Pathway Level Analysis (IMPaLA) a software for integrated pathway-level analysis of transcriptomics (Max Planck Institute for Molecular Genetics, Berlin, Germany) was also used.

2.7 Validation RT-PCR and qRT-PCR

2.7.1 cDNA synthesis for RT-PCR

Using the same method as highlighted in section 2.6.5 RNA was extracted from the mouse hippocampus by LCM (control n=6, atherosclerosis n=6). Total RNA was synthesised to complementary DNA (cDNA) via reverse transcription using qScript cDNA SuperMix (Quanta Biosciences, Gaithersburg, MD, USA). The master mix contained optimised concentrations of qScript reverse transcriptase, magnesium chloride (MgCl₂), deoxyribonucleotide triphosphates (dNTPs), ribonuclease inhibitor protein, and titrated concentrations of pre-blended oligonucleotide (dT) primer, random primers and stabilisers. RNA sample concentrations were equalised to 25ng per µl with RNase-free water based on the NanoDrop 1000 spectrophotometer reading. The volume of cDNA obtained was not enough in 5 samples therefore all samples were diluted in order to have enough volumes to investigate all the target genes through qPCR. The final concentration was 25 ng per µl RNA. Following the manufacturer's

protocol, in a sterile 0.2 ml Eppendorf tube, 25 ng RNA was added to 2 µl qScript and the volume adjusted to 10 µl with sterile RNase free water. Samples were mixed thoroughly by gently vortexing and spun down to collect all liquid at the bottom of the tube. Samples were incubated at 25°C for 5 minutes, 42°C for 30 minutes, and the reaction stopped by heating to 85°C for 5 minutes and the sample was then held at 4°C.

2.7.2 Agarose gel electrophoresis of PCR products

The synthesised cDNA was tested using standard PCR and agarose gel electrophoresis. PCR amplifies a specific cDNA target through thermal cycling in which high heat is applied to denature the cDNA and gene specific primers are annealed to flank the target region of DNA with Taq DNA polymerase used to extend the 3' end of each primer along the template strand DNA. These steps are repeated in a number of cycles to produce exact copies of target DNA. The gene *ACTB*, which encodes the Actin-β (ACTB) protein, part of the microfilaments in the cytoskeleton of all cells, is routinely used as a housekeeping gene (HK) due to its ubiquitous expression and intermediate stability (Penna et al., 2011). PCR was performed using 1.25 ng of cDNA, 1x Firepol green PCR master mix (MM) (Solis BioDyne, UK) and optimised concentrations of forward and reverse *ACTB* primers in a total volume of 20 µl. This primer was optimised by and provided from Dr. Mead's laboratory, purchased from Sigma-Aldrich (Poole, Dorset, UK) to amplify across exons 3 and 4. The forward primer consisted of 20 base pair (bp) (TGCTGGAAGGTGGACAGTGAGG), as did the reverse primer (CATTGCTGACAGGATGCAGAAGG), and produced a 150 bp product.

The PCR was performed using a G-storm Thermal Cycler (G-storm, Somerset, UK) with the following protocol: 10 minutes at 95°C, 40 cycles of 15 seconds at 95°C and

1 minute at 60°C, and finally ten minutes at 75°C. The samples were held at 4°C at the end of the protocol. To check for specificity, a no template control (NTC) was also run alongside the cDNA samples with d.H₂O replacing the cDNA.

All PCR products were analysed on a 3% agarose gel, which separates DNA according to molecular size. In total, 10 µl of PCR product and 2 µl of Hyperladder IV (Bioline, UK) were loaded into individual wells of a 3% (w/v) agarose gel with ethidium bromide (100ng/ml) was run in an electrophoresis tank containing 1x tris-acetate-EDTA buffer at 100 V for 40 minutes. Ethidium bromide intercalates with DNA and acts as a fluorescent tag that can then be visualised upon illumination with UV light (GENi transilluminator, Syngene, Cambridge, UK).

This PCR step was performed to confirmed the presence of the correct sized product and therefore the presence of cDNA in all samples. It also indicated that the same amount of amplified *ACTB* was present in all the samples. All PCR gel electrophoresis included the NTC to ensure that the results were not due to contamination or the formation of primer-dimers.

2.7.3 Quantitative real-time Polymerase Chain Reaction (qRT-PCR)

qRT-PCR was used to validate the gene expression changes identified between the control diet *ApoE*^{-/-} mice and western diet *ApoE*^{-/-} mice. All genes and associated primers used in the validation are listed in table 2.3. The genes of interest were selected based on the results of the transcriptomic analysis and the optimised primers purchased from Integrated DNA Technologies. In this process an amplicon is amplified similar to RT-PCR; however, it produces a fluorescent signal that can be used to detect variations in amplicon concentration over real-time. All primer sets used a 5' to 3' Taq DNA polymerase labelled with a fluorescent reporter dye at one end and a quencher

dye at the other. The proximity of these dyes inhibits their fluorescence, but Taq prime has 5' to 3' exonuclease activity that allows cleavage of the 5' terminal nucleotide. When this polymerase encounters the probe, it cleaves the 5' reporter dye, allowing it to emit a fluorescent signal because it is no longer being quenched, and the signal is detected by the PCR machine.

The HK, glyceraldehyde 3-phosphate dehydrogenase (*GAPDH*) (PrimeTime Std qPCR Assay Integrated DNA Technologies Inc.), was included for comparison and normalisation to the target gene expression. The most suitable HK was determined based on the results from the microarray analysis.

Reactions were performed in triplicate in 384-well PCR plates (Bio-Rad, UK). For each well the reaction contained 0.5 µl of PrimeTime Std qPCR Assay for the target gene, 8.3 ng of cDNA, 5 µl of Luna Universal Probe qPCR Master Mix (New England BioLabs, Ipswich, MA, USA) and adjusted with RNase free deionised H₂O to a final volume of 10 µl. After setting up the reactions a microseal 'C' film (Bio-Rad, UK) was applied to the plate prior centrifugation to ensure that all the components were at the base of each well. All plates included a NTC to serve as a general control for any contamination. All qPCRs were performed using a CFX384 Thermo Cycler (Bio-Rad, Hercules, CA, USA) with the following protocol: 95°C for 3 minutes, and 40 cycles of 95°C for 10 minutes and 60°C for 30 seconds.

2.7.4 qRT-PCR Data Analysis

The qPCR results were analysed using CFX real time system, Maestro Software for Bio-Rad, and the average Ct of the technical triplicates was calculated. Initially for each sample's target and HK all triplicate Ct values were averaged. The average Ct value

of the target gene for a given sample was subtracted from the average Ct value of the relative sample's HK *GAPDH*, providing their delta-Ct (ΔCt).

Table 2.4 PrimeTime ® standard qPCR assays used for validation of the candidate gene expression changes in control and atherosclerotic ApoE -/- mice from the microarray analysis.

Gene	PrimeTime Assay ID	Ref. Seq.	Exon location
Atp2b2	Mm.PT.58.13258897	NM_001036684(2)	8 - 9'
Prkaca	Mm.PT.58.6604755	NM_008854(1)	5 - 6
Adcy8	Mm.PT.58.43742997	NM_009623(1)	5 - 6
Tgfb1	Mm.PT.58.6677268	NM_011577(1)	5 - 6
Gpx3	Mm.PT.58.46354769	NM_008161(1)	3 - 5
Ndufs8	Mm.PT.58.50504206	NM_001271443(3)	5 - 6
Aif1	Mm.PT.58.7014816	NM_019467(1)	5 - 7

An average Ct from all the control samples was used as a reference for the relative gene expression. The ΔCt of each western diet sample was then subtracted from the average ΔCt of the control diet samples. This delta-delta ($\Delta\Delta\text{Ct}$) was multiplied by two to the power of negative $\Delta\Delta\text{Ct}$ ($2^{-\Delta\Delta\text{Ct}}$) to account for the exponential nature of qPCR and provide the relative gene expression in western diet mice compared to control diet mice.

2.7.5 Statistical analysis of qRT-PCR data

Normality was determined via Shapiro-Wilk test and normally distributed data was analysed using an unpaired *t*-test. Differences were considered significant when $p < 0.05$.

**CHAPTER III: NEUROPATHOLOGICAL
CHARACTERIZATION OF THE APOLIPOPROTEIN E
KNOCKOUT MOUSE: A MODEL OF SYSTEMIC
ATHEROSCLEROSIS**

3.1 Introduction

Systemic atherosclerosis contributes to strokes, WMH, dementia and shares common risk factors with diabetes and hypertension which are associated with inflammation. Animal studies have demonstrated that peripheral inflammation can increase neuroinflammatory responses and increase damage in response to injury (Laskowitz et al., 1997). Previous studies have characterised endothelial cells and microglial morphology in the striatum, cerebral cortex, hypothalamus and meninges of ApoE^{-/-} mice fed a high-fat diet (Paigen) demonstrate increased IBA-1 and VCAM-1 immunoreactivity compared to ApoE^{-/-} controls mice fed a normal diet (Chow) (Denes et al., 2012).

Feeding ApoE^{-/-} mice with a high-fat diet leads to accelerated development of atherosclerosis, but it should be noted that they do not develop lesion rupture and consequent thrombosis associated with advanced atherosclerotic plaques. (Civeira et al., 2004; Pendse et al., 2009). ApoE^{-/-} mice fed with a normal diet (Chow) also develop mild atherosclerosis and an increased level of LDL plasma cholesterol compared to wild type mice and humans with familial hypercholesteremia. Therefore this model allows to investigate cellular changes in the CNS and BBB dysfunction in relation to atherosclerosis and neuroinflammation in the absence of occlusion. Furthermore the presence of mild atherosclerosis in ApoE^{-/-} controls provides a more possible comparison to the aging population as most people over the age of 60 present some degree of atherosclerosis (Tuzcu et al., 2001).

Furthermore in lipohyalinosis, a cSVD, the inflammation caused by atherosclerosis results in the accumulation of precipitated plasma proteins in the connective tissue of the blood vessels wall which disrupts their integrity, affecting small WM vessels (Lee, 2020; Saji et al., 2016). The extensive inflammation occurring through the

accumulation of ROS in systemic atherosclerosis could be exacerbated by reactive astrocytes, microglia and oligodendrocytes which produce ROS in their reactive state (Caplan, 2015). The chronic inflammation and vascular dysfunction could damage the BBB and its failure could aggravate neuroinflammation (De Montgolfier et al., 2019; Niu et al., 2019).

In mice, lack of *ApoE* is associated with BBB breakdown with reductions in tight-junction and basement-membrane proteins, pericyte coverage, and regional CBF, which increases progressively with age (Bell et al., 2012; Hafezi-Moghadam et al., 2007). However, to date most of the research on atherosclerosis in relation to the BBB and NVU focuses on endothelial cell changes, and the subsequent neuroinflammation associated with ischaemia. A limited number of studies have assessed the neuropathology associated with systemic atherosclerosis and the detailed histological characterisation of the NVU in the *ApoE*^{-/-} model has not been carried out. Neuroinflammation, is a feature of atherosclerotic *ApoE*^{-/-} mice and the mechanisms that contribute to the inflammation in atherosclerosis and the links to VaD are poorly understood.

3.2 Aims and objectives

To test the hypothesis that systemic atherosclerosis in *ApoE*^{-/-} mice impacts the NVU leading to cerebrovascular dysfunction and neurodegeneration, this study aimed to characterise the changes in the brains of *ApoE*^{-/-} mice fed with a western diet compared to *ApoE*^{-/-} mouse fed with a control diet by investigating the expression of a panel of neurovascular unit (NVU) and neuroinflammatory makers using immunohistochemistry. Objectives:

- Investigate the expression of a panel of cell phenotype markers for astrocytes (GFAP and AQP4), microglia (IBA-1, MHCII, CD11b, CD163, TREM-2), pericytes (PDGFR- β) and vessels (ICAM-1, CD31, Collagen IV), in the hippocampus, cerebral cortex, corpus callosum, striatum and thalamus
- Provide a qualitative description of the staining pattern of this panel of markers.
- Determine regional variation and expression of these markers between brain areas through quantitative analysis.
- Use a second *ApoE*^{-/-} mouse cohort to validate all qualitative findings on the most relevant brain areas.

3.3 Results

3.3.1 Histological assessment of the *ApoE*^{-/-} mouse brain after normal or high-fat diet feeding

The assessment of H&E in cohort 1 controls and atherosclerotic mice showed a regular distribution of the cell nuclei with no visible evidence of perivascular inflammation indicated by inflammatory infiltrates (Figure 3.2 A-B). Luxol fast blue (LFB) enables the visualisation of myelinated axons within brain tissue. The integrity of myelin in cohort 1 controls and atherosclerotic mice was maintained, as indicated by an evenly distribution of LFB throughout the WM. The corpus callosum above the hippocampus seemed to contain considerably fewer cell bodies compared to the cortex. The cell bodies in the WM appear smaller and consistent with neuroglial cell bodies rather than larger nerve cell bodies present in the hippocampus and cerebral cortex (Figure 3.2. C-D).

The pyramidal cell-layer neurons of the hippocampus are uniform in size and evenly arranged with rounded nucleus and prominent nucleolus in both controls and atherosclerotic mice from cohort 1 mice. The molecular layer contains many glial cells among neuronal processes. Layer 1 of cerebral cortex presented fewer cell bodies consistent with small neuroglia appearing as naked nuclei with the cytoplasm being indistinguishable from the nerve fibres that make up most of this layer. The shape of cells on the other layers of the cerebral cortex were of diverse shape and sizes. Investigation of structural differences between atherosclerotic and control *ApoE* mice using conventional morphological and myelin staining revealed no visible differences (Figure 3.2) and the regions of interest were assessed and identified through these tinctorial stains.

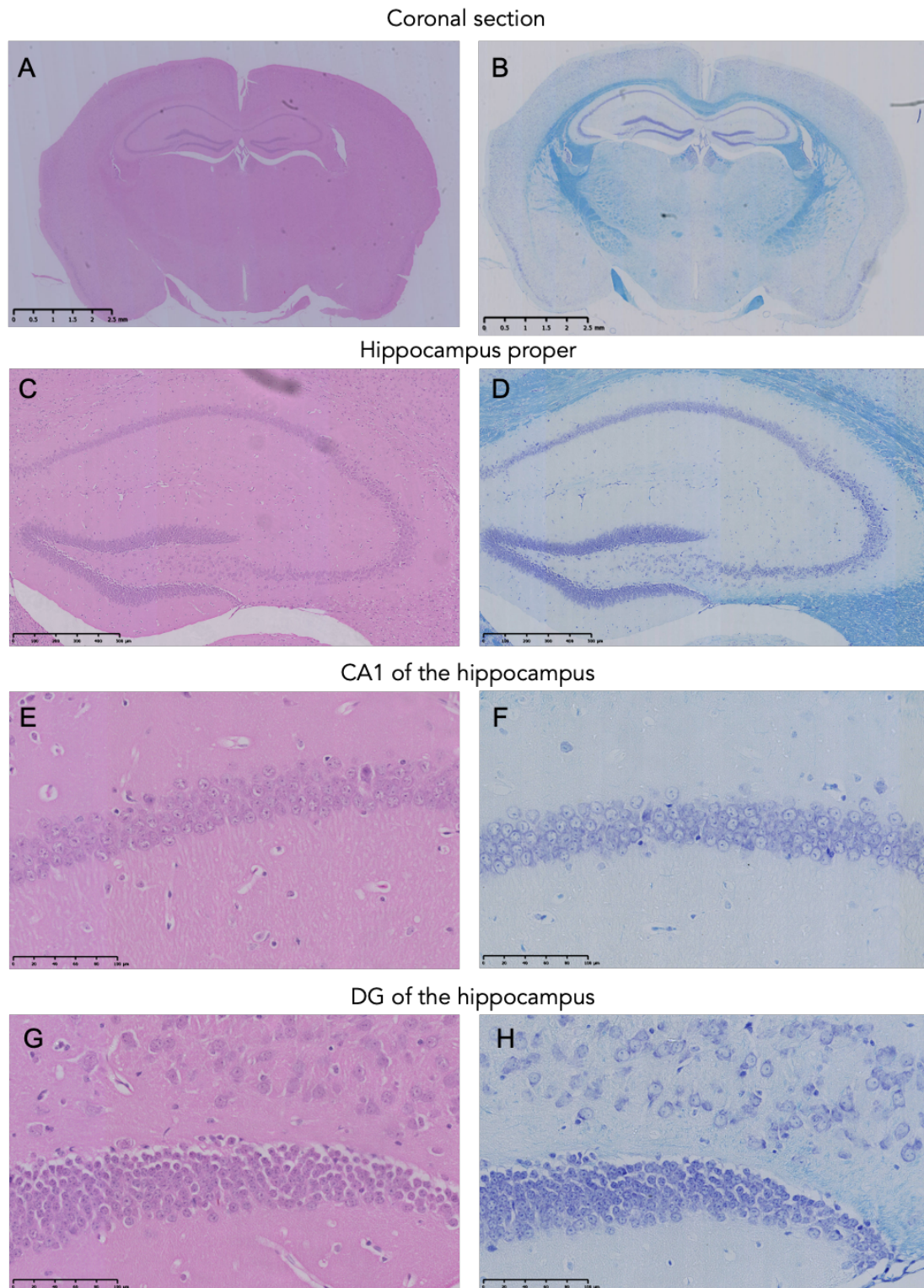


Figure 3.1 Histological characterisation of the hippocampus of an *ApoE*^{-/-} mouse using H&E (left) and LFB (right)

Representative images of a coronal section of a control *ApoE*^{-/-} mouse hippocampus showing a coronal section at a low magnification in which neuroanatomically relevant areas are observed (A & B). The anatomy of the hippocampus was easily identified using H&E (C) and LFB (D). The cellular nucleus are distinguished in these staining allowing to appreciate Cornus Amoris 1 (CA1) (E&F) and the dentate gyrus (DG) (G&H). Scale bar represents 50 μ m and 250 μ m.

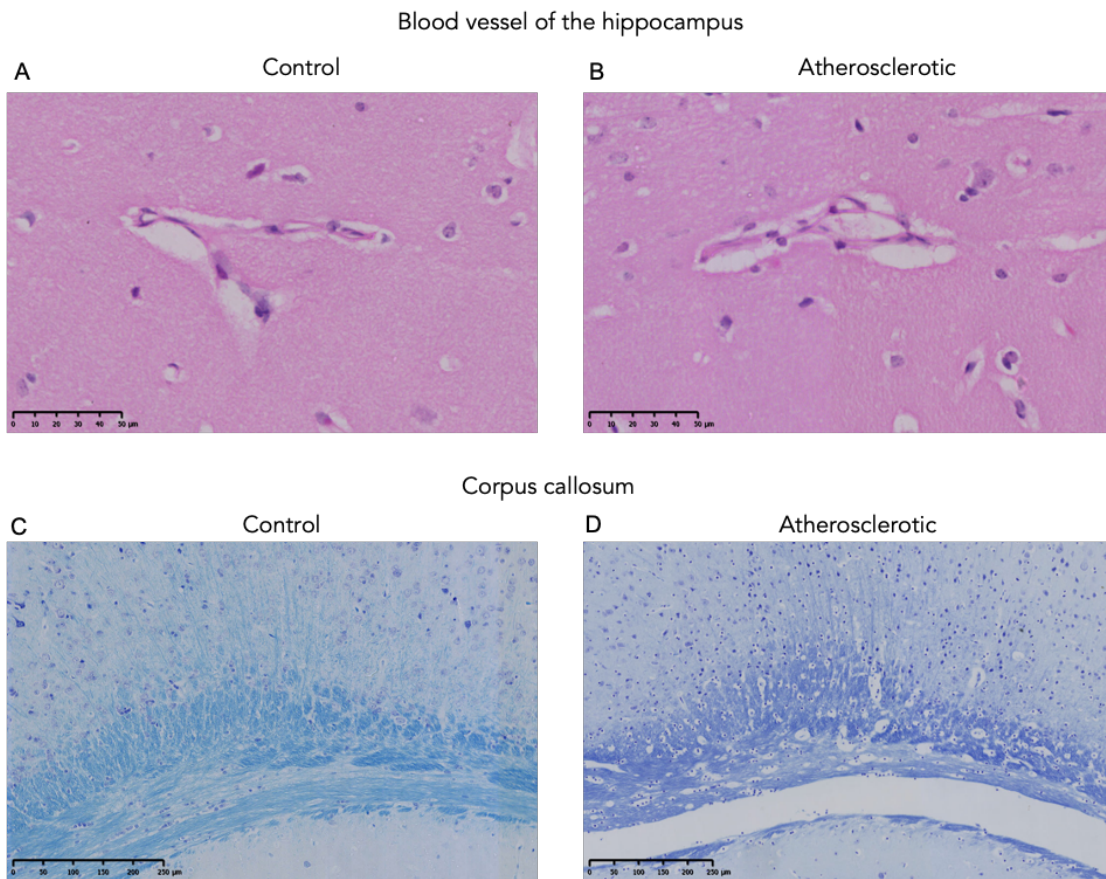


Figure 3.2 Histological comparison of the hippocampus and corpus callosum between control and atherosclerotic *ApoE*^{-/-} mouse model

Representative images of the hippocampus in control (normal diet) (A) and atherosclerotic (high-fat diet) (B) mouse showing blood vessel morphology using H&E. There was no observable change under the microscope and this was not investigated further. LFB showed a regular distribution of WM staining of the corpus callosum above the hippocampus in controls (C) and atherosclerotic (D) mouse. Scale bar represents 50 μm and 250 μm.

3.3.2 Assessment of Cells of the NVU

Changes to cells of the NVU was investigated using IHC to markers of astrocytes (GFAP), microglia (IBA-1) and endothelial activation (ICAM-1). The absence of immunostaining in the no primary antibody and isotype negative control in the control slides confirmed the specificity of the immunoreactive staining pattern detected in the tissue (Figure 3.3). Immunostaining for PDGF-R β and Collagen IV was not consistently reproducible and therefore was not analysed further, whilst extensive investigations with a more comprehensive panel of NVU-related cell markers (AQ4, OCC1, CD31, MHCII, CD31, PS2Y12, TMEM119, hTREM-2, CD68, CD163) failed to produce specific immunostaining profiles (Appendix III).

3.3.3 Increased ionized calcium-binding adaptor molecule 1 (IBA-1)

immunoreactive microglia in atherosclerotic *ApoE*^{-/-} cohort 1 mice

IBA-1 is expressed by both resting and active microglia. In the current study IBA-1 immunoreactive microglia appeared more immunoreactive in atherosclerotic cohort 1 mice compared to controls and presented a heterogeneous pattern of staining across the different brain areas. Control mice presented scarce IBA-1 immunopositive cell bodies that were small and round, surrounded by delicate branching processes. In contrast, atherosclerotic mice presented varied microglial morphologies and a more regular distribution compared to controls. The corpus callosum presented bipolar-appearing processes and a low number of cell bodies (Figure 3.4). These qualitative observations were not quantified. In contrast, the cerebral cortex presented more cell bodies and defined processes towards the edge of the cortex (Figure 3.5) and the IBA-1⁺ microglia cell bodies in the hippocampus were few compared to the intermittent processes (Figure 3.6).

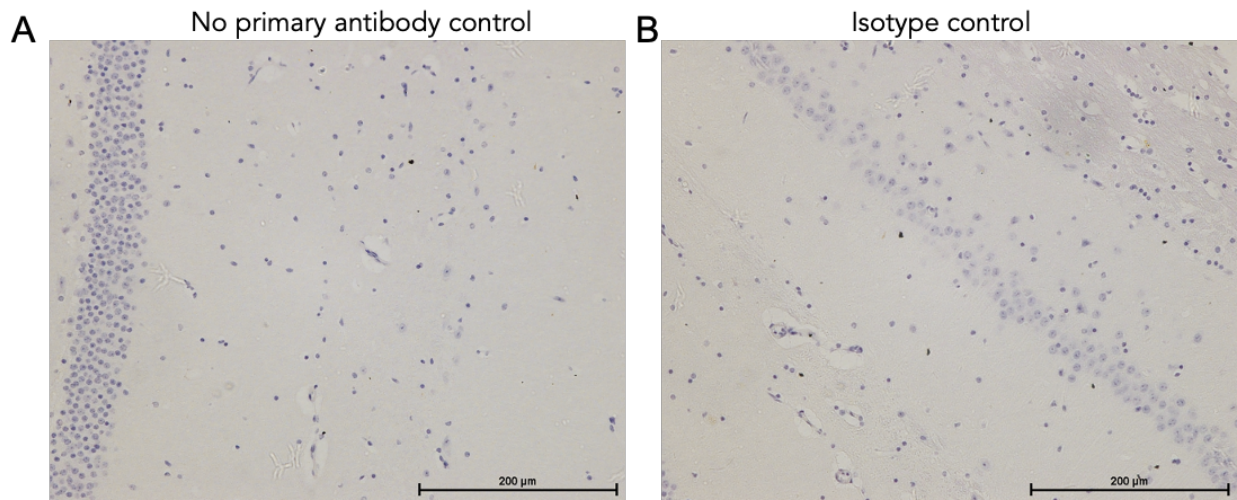


Figure 3.3 Representation of negative controls

Representative figures of negative controls showing haematoxylin counterstain nuclei and no immunoreactivity. The no primary antibody control followed the IHC protocol replacing the primary antibody incubation period for incubation with blocking solution (A) and the isotype control instead of the primary antibody the tissue is incubated with the host species IgG isotype (B). Scale bar represents 200 µm

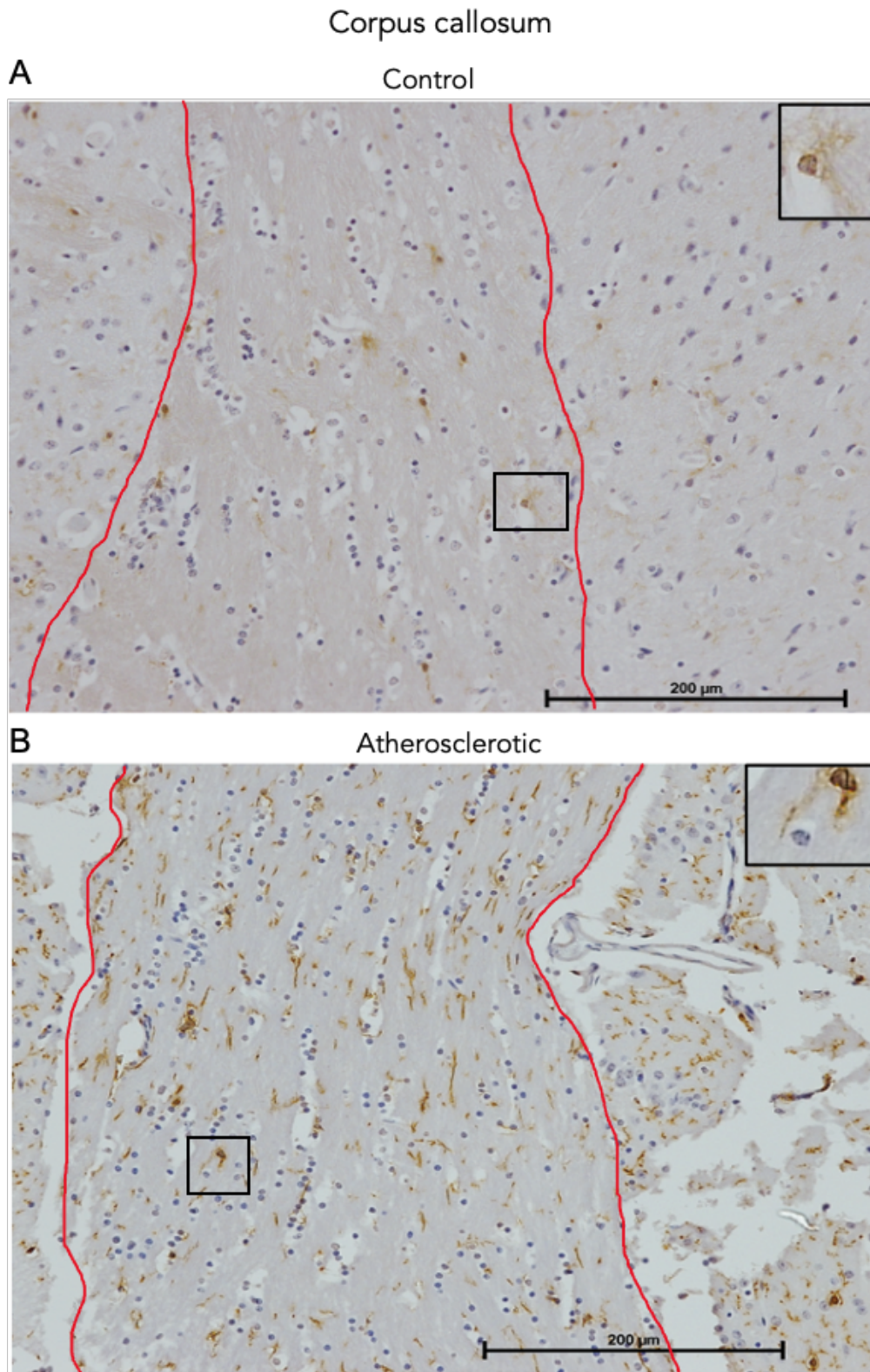


Figure 3.4 Representative images of the corpus callosum showing increased IBA-1 microglia immunoreactivity in *ApoE*^{-/-} cohort 1 atherosclerotic mic

The corpus callosum of *ApoE*^{-/-} cohort 1 control (A) and atherosclerotic (B) mice The corpus callosum (delimited by red lines) showed microglia resembling a bipolar morphology and lower IBA-1⁺ cell bodies in the atherosclerotic mice (B) compared to controls (A). Control n= 7, Atherosclerotic n= 8. Scale bar represents 100 µm (20 µm insert).

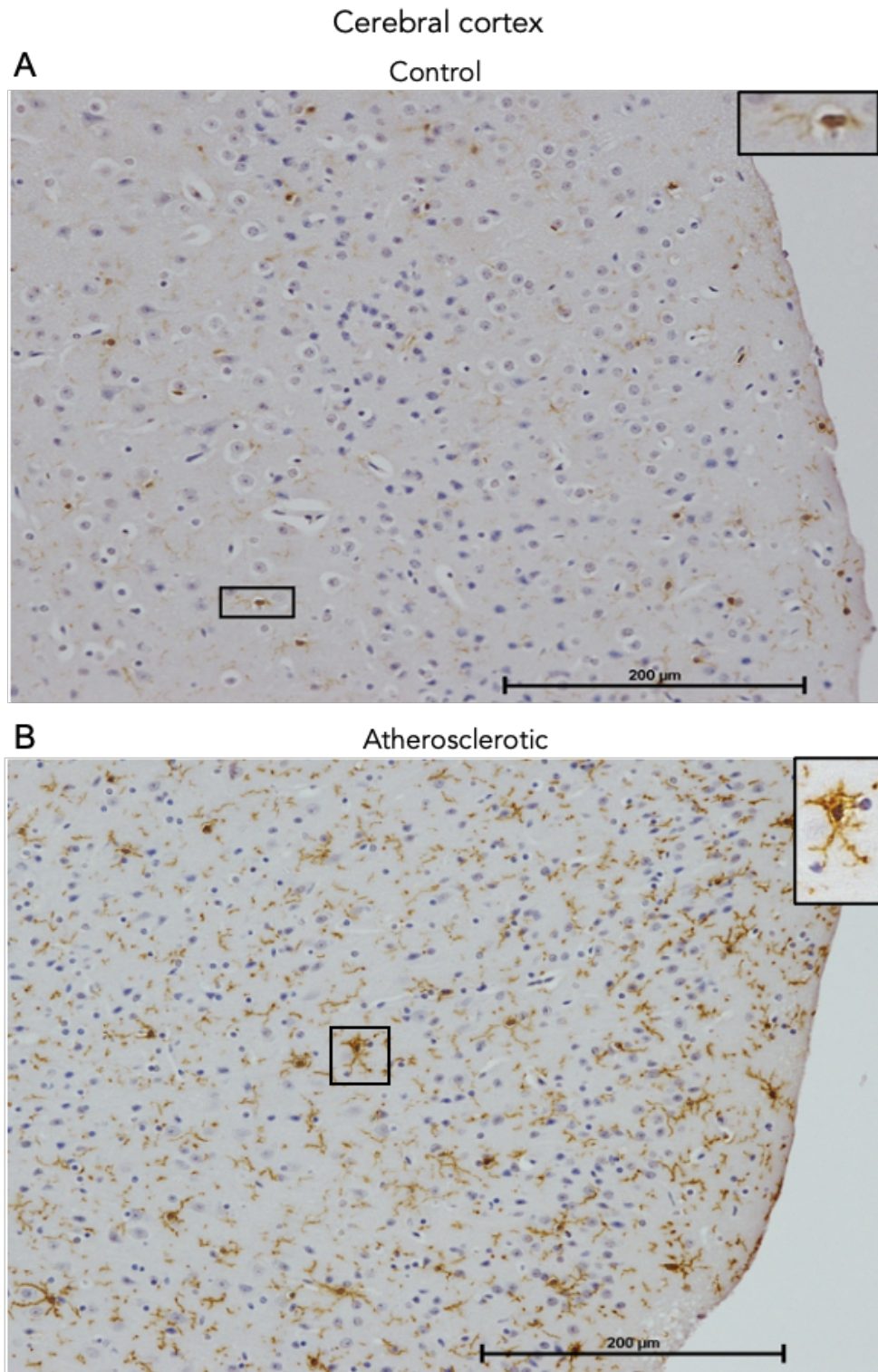


Figure 3.5 Representative images of the cerebral cortex showing increased IBA-1 microglia immunoreactivity in *ApoE*^{-/-} cohort 1 atherosclerotic mice

Representative images of the cerebral cortex of *ApoE*^{-/-} cohort 1 control (A) and atherosclerotic (B) mice. A higher number of IBA-1 immunopositive microglia in atherosclerotic mice (B) compared to controls(A). The cell bodies of microglia seemed larger and more present at the edge of the cortex. The processes in the atherosclerotic microglia were also more visible with thicker processes. Antibody used rabbit anti-goat IBA-1 Abcam (Lot. GR313212-2). Control n= 7, Atherosclerotic n= 8. Scale bar represents 100 μm (20 μm insert).

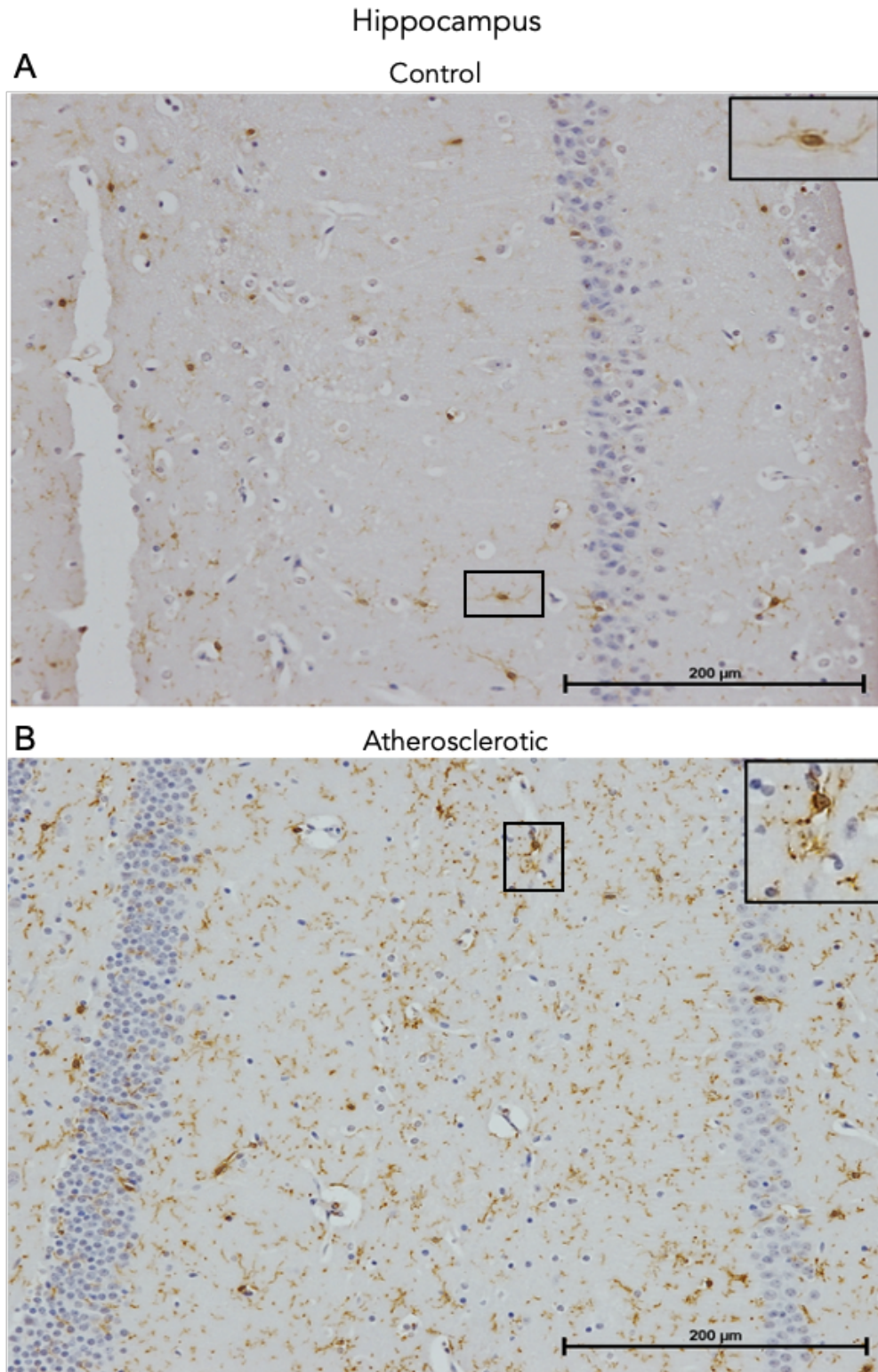


Figure 3.6 Representative images of the hippocampus showing increased IBA-1 microglia immunoreactivity in *ApoE*^{-/-} cohort 1 atherosclerotic mice

Representative images of the hippocampus of *ApoE*^{-/-} cohort 1 control (A) and atherosclerotic (B) mice. The microglia in the hippocampus showed more IBA-1 immunoreactivity in the controls (A) than in the atherosclerotic mice (B), with more microglial processes present. Antibody used rabbit anti-goat IBA-1 Abcam (Lot. GR313212-2). Control n= 7, Atherosclerotic n= 8. Scale bar represents 100 μm (20 μm insert).

The microglia in cerebral cortex, hippocampus and corpus callosum expressed a significantly different % area of immunoreactivity ($H = 0.001$, $p < 0.001$).

Increased immunoreactivity for IBA-1 was greater in atherosclerotic mice compared to controls in all brain areas (Figure 3.7). The cerebral cortex (Controls $M = 0.55$, $SEM = 0.92$; Atherosclerosis $M = 4.95$, $SEM = 1.2$, $p = 0.002$) and the hippocampus (Controls $M = 0.96$, $SEM = 0.25$; Atherosclerosis $M = 5.5$, $SEM = 1.2$, $p = 0.007$) showed a similar level of IBA-1 immunoreactivity. The corpus callosum show the lowest mean difference (Controls, $M = 0.92$, $SEM = 0.26$; Atherosclerotic $M = 3.38$, $SEM = 0.49$, $p = 0.0012$).

3.3.4 The immunoreactive profile of IBA-1 is not consistent across *ApoE*^{-/-} mouse cohorts

Sections from cohort 2 were stained with the same IBA-1 antibody, under the same conditions, as cohort 1. In addition, a section from cohort 1 was used as an inter-run control. While initial assessment of the inter-run control displayed a similar staining pattern to cohort 1, the pattern of staining was more intense (Figure 3.8). In cohort 2 IBA-1 immunoreactivity identified microglia with larger cell bodies and extended processes in control compared to atherosclerotic mice. Also, microglia presented with a different morphology across brain areas with cells showing a low number of processes with a bipolar appearance and a rounded cell body in the corpus callosum (Figure 3.9). The microglia in the cerebral cortex displayed small cell bodies and fine processes with an even distribution (Figure 3.10), while the hippocampus presented a punctate and irregular pattern of staining and ramified microglia with large cell bodies and long processes (Figure 3.11). Overall, the qualitative assessment of IBA-1 expression in control mice from cohort 2 indicated an increased in IBA+ immunopositive microglia compared to atherosclerotic mice from the same cohort (Figure 3.12).

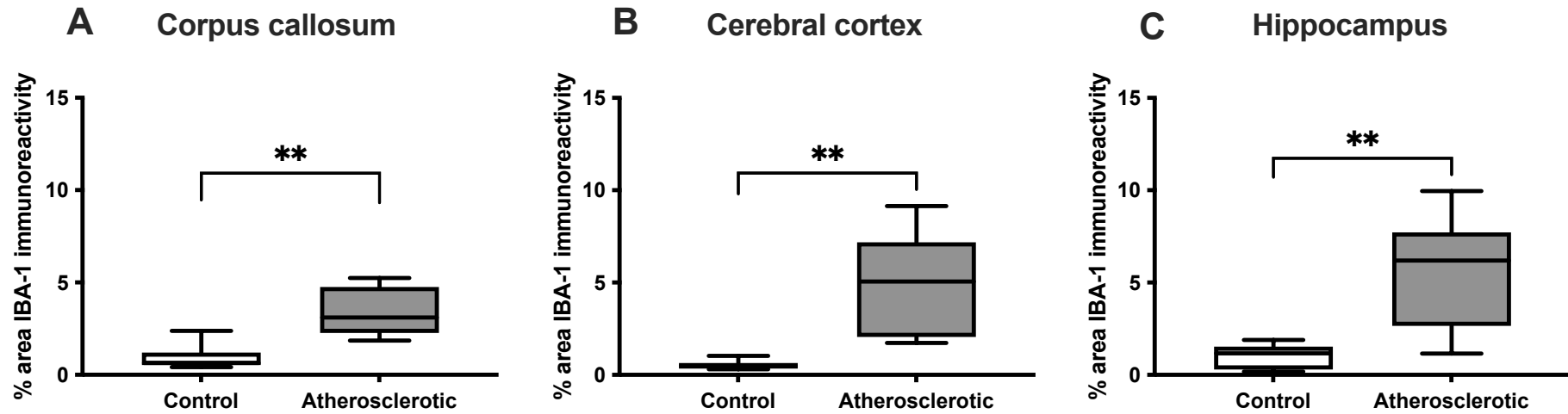


Figure 3.7 Increased percentage (%) area of microglia IBA-1 immunoreactivity the corpus callosum, cerebral cortex and hippocampus of atherosclerotic cohort 1 *ApoE*^{-/-} mice compared to controls

IBA-1 expression was significantly increased in the corpus callosum (A), cerebral cortex (B) or hippocampus (C) of atherosclerotic mice (n=6) compared to controls. (** P<0.01)

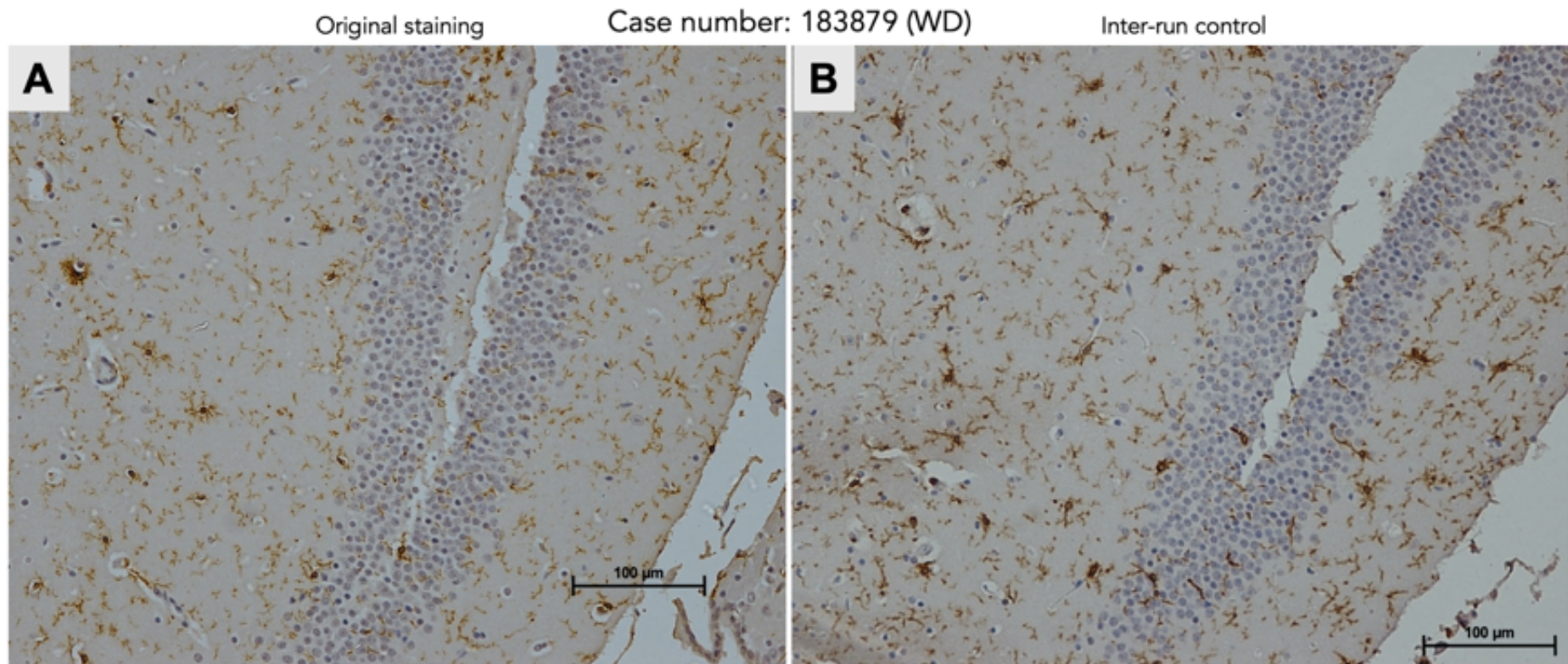


Figure 3.8 Inter-run control of IBA-1 staining comparing *ApoE*^{-/-} cohort one hippocampus of atherosclerotic and control mice

The same case (183879) was used as an inter-run control and displayed a similar pattern of IBA-1 immunoreactivity in both cohorts. The original staining from cohort 1 mice (A). The same case (183879) was later stained at the same time as cohort 2 (B). While the staining was more intense, the immunoreactive profile was similar, showing individual microglia with elongated processes and therefore was evaluated using the same parameters. Scale bar represents 200 µm (A) and 100 µm (B).

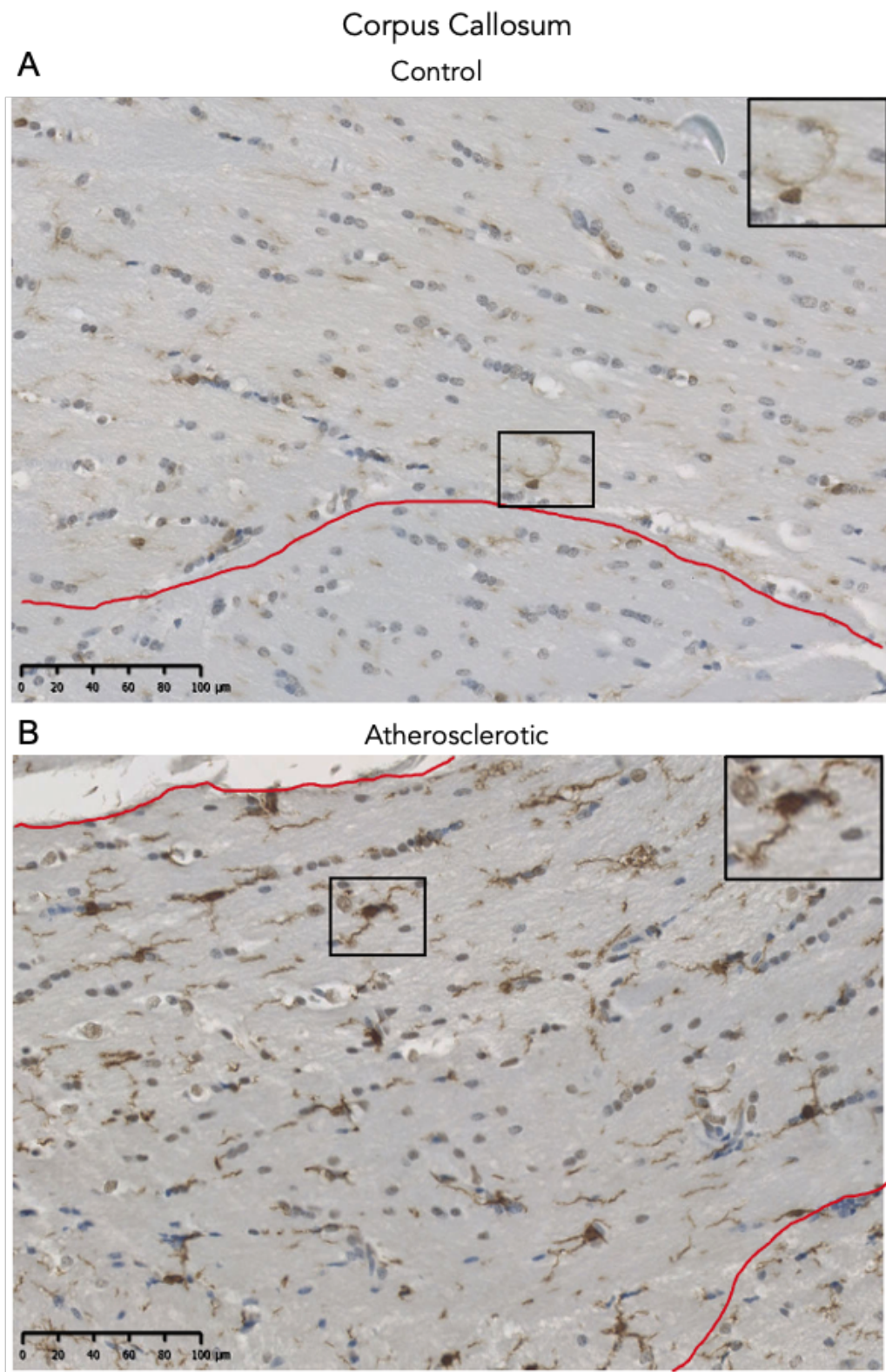


Figure 3.9 Representative images of the corpus callosum showing IBA-1 microglia immunoreactivity in control and atherosclerotic *ApoE*^{-/-} cohort 2 mice

Control mice microglia had longer and denser processes. Corpus callosum (delimited by red lines) showed microglia resembling a bipolar morphology, in control mice (A) more than in atherosclerotic mice (B). Antibody used rabbit anti-goat IBA-1 Abcam (Lot. GR313212-2). Control n= 6, Atherosclerotic n= 6. Scale bar represents 100 μm (20 μm insert).

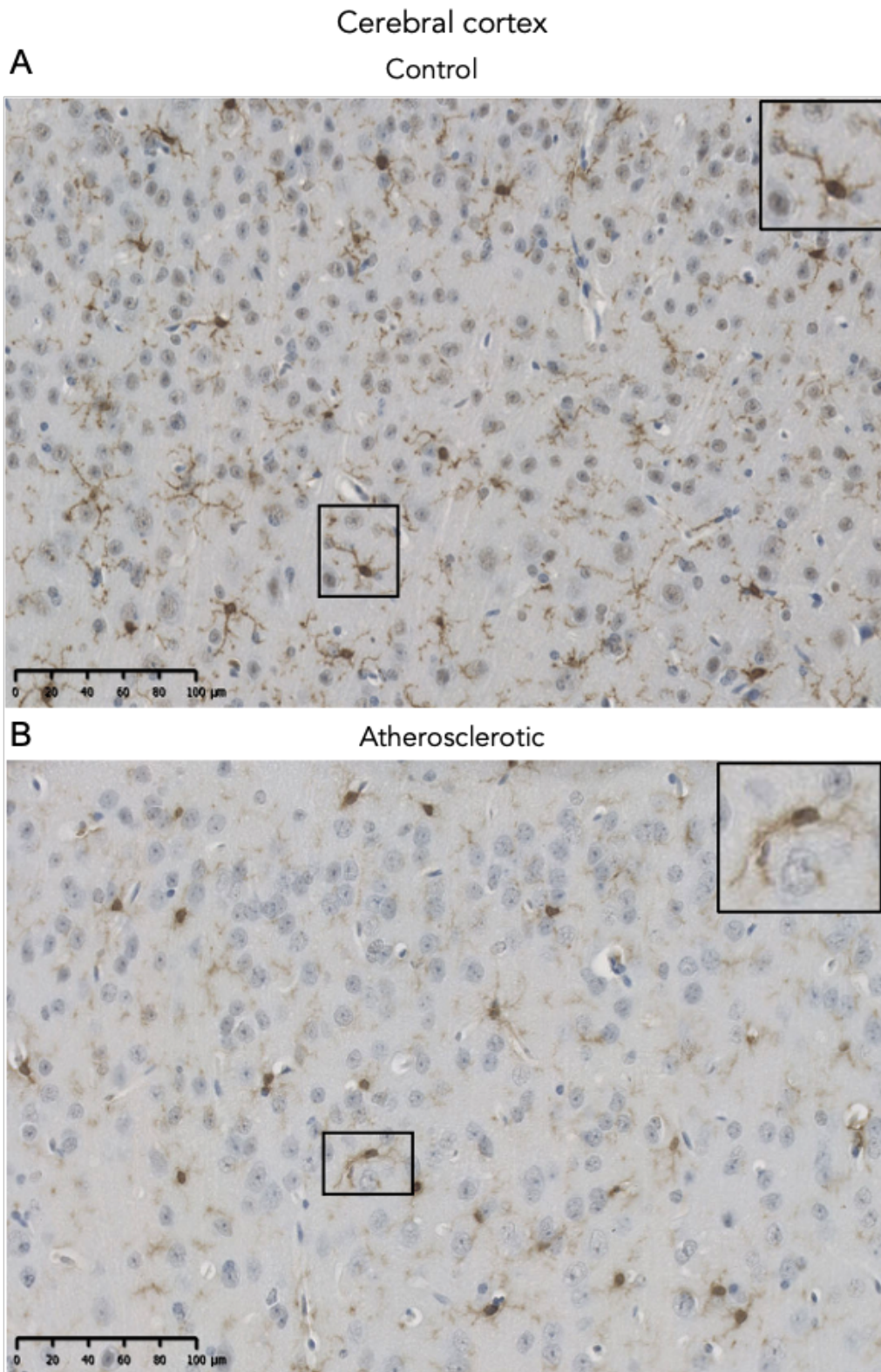


Figure 3.10 Representative images of the cerebral cortex showing IBA-1 microglia immunoreactivity in control and atherosclerotic *ApoE*^{-/-} cohort 2 mice

The cerebral cortex appeared to have a higher number of IBA⁺ microglia present in the controls (A) mice compared to atherosclerotic (B). The microglia cell bodies in the atherosclerotic mice had long and fine branching processes while controls had shorter and thicker processes. Antibody used rabbit anti-goat IBA-1 Abcam (Lot. GR313212-2). Control n= 6, Atherosclerotic n= 6. Scale bar represents 100 μ m (20 μ m insert).

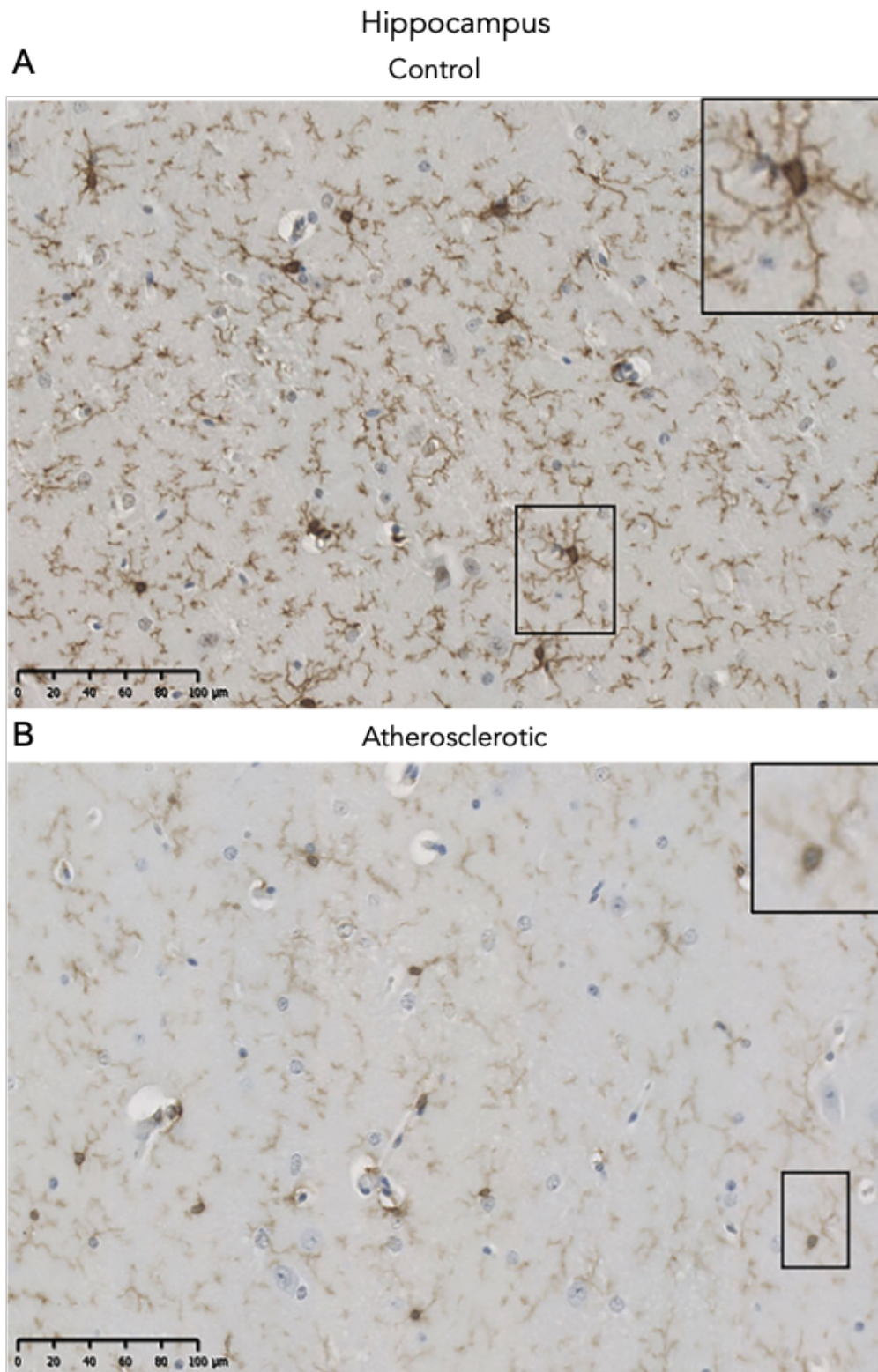


Figure 3.11 Representative images of the hippocampus showing IBA-1 microglia immunoreactivity in control and atherosclerotic *ApoE*^{-/-} cohort 2 mice

Control (A) mice hippocampus displayed a denser IBA-1 immunoreactive microglia population compared to atherosclerotic (B) mice. The microglia cell bodies in the atherosclerotic mice had long and fine branching processes while controls had shorter and thicker processes. Antibody used rabbit anti-goat IBA-1 Abcam (Lot. GR313212-2). Control n= 6, Atherosclerotic n= 6. Scale bar represents 100 μ m (20 μ m insert).

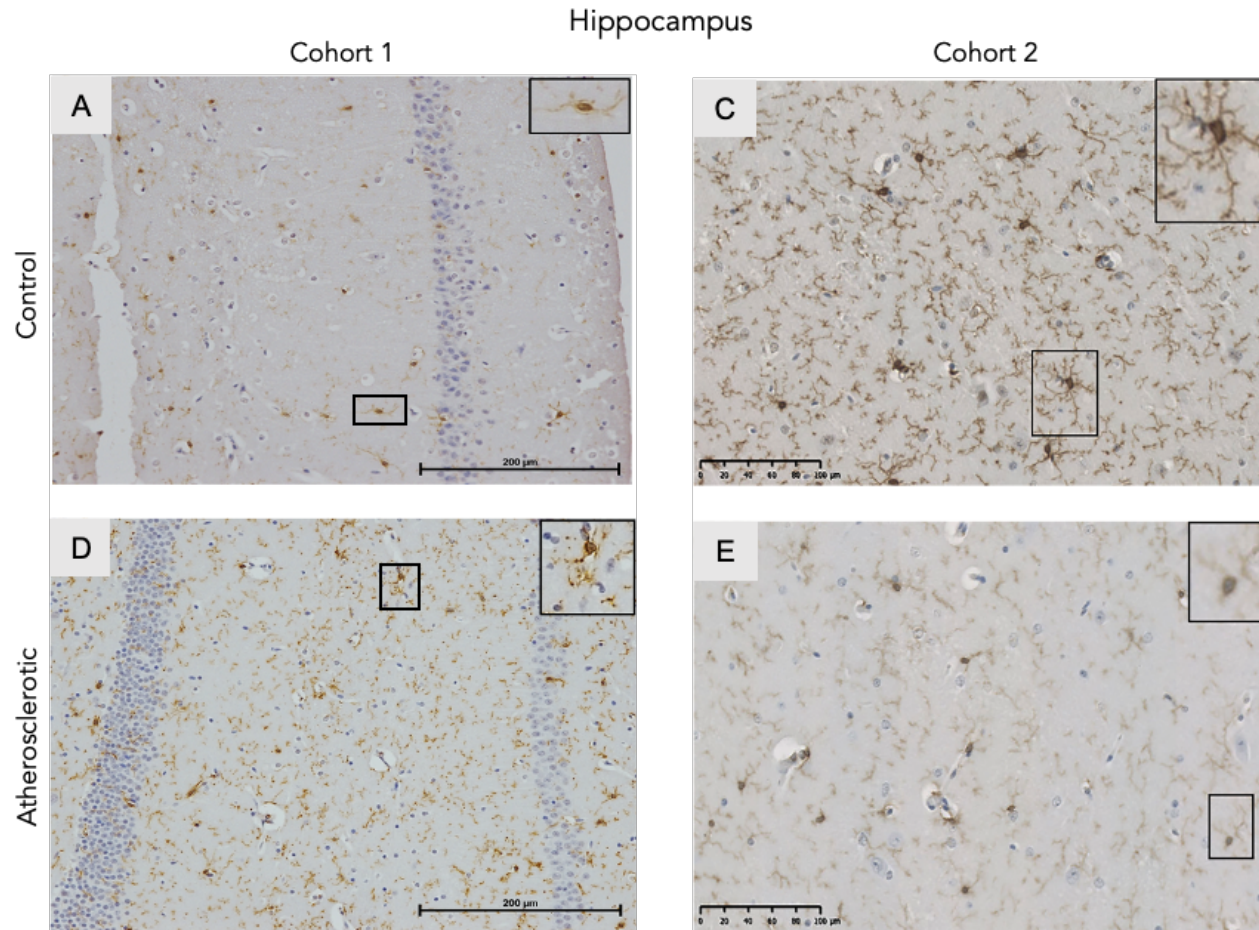


Figure 3.12 Representative images comparing microglial IBA-1 immunoreactivity on the hippocampus of both *ApoE*^{-/-} mouse cohorts stained at different time points

Mouse in cohort 1 (A & D) displayed a different pattern of staining to cohort 2 (C & D). Control mice in cohort one (A) showed a more similar pattern of staining to atherosclerotic mice in cohort 2 (B), while control mice in cohort 2 (E) showed more immunoreactive IBA-1 microglia with thicker and longer processes than atherosclerotic mice in cohort 1 (D). Antibody used rabbit anti-goat IBA-1 Abcam (Lot. GR313212-2). Scale bar represents 100 µm (20 µm insert).

The parameters of Analysis^{AD} were not adjusted between cohorts to avoid variability. Nevertheless, there was a noticeably higher detection rate in cohort 2 compared to the previous cohort. The results from both cohorts were analysed and showed inconsistent trends, therefore the data was not analysed together (Figure 3.13).

Quantification of IBA-1 immunoreactivity in cohort 2 mice did not show any significant difference between any of the brain areas of interest $H = 0.052$. In control mice the corpus callosum (Controls $M = 8.6$, $SEM = 1.0$; Atherosclerotic $M = 6.6$, $SEM = 1.8$, $p > 0.99$), hippocampus (Controls, $M = 9.1$, $SEM = 2.1$; Atherosclerotic $M = 6.1$, $SEM = 2.2$, $p > 0.99$), and cerebral cortex (Controls $M = 8.4$, $SEM = 2.7$; Atherosclerotic $M = 3.4$, $SEM = 1.3$, $p > 0.99$) show similar % area of immunostaining (Figure 3.14).

A new IBA-1 antibody, from the same brand (Abcam) but a different batch, was optimised and all samples from all cohorts and models underwent immunohistochemistry simultaneously, in order to confirm the observed differences between cohorts was not due to differences in the staining performed on different days. The alternative antibody confirmed the pattern of IBA-1 immunoreactivity observed in both cohorts. In cohort 1, atherosclerotic mice have visibly more IBA⁺ ramified microglia than control mice (Figure 3.15). Cohort 2 showed the same microglia morphology, but, the % area of immunohistochemistry was higher in controls than atherosclerotic mice (Figure 3.16). Analysed individually, the results from each mouse cohort resemble previous analysis, however, none of the results were statistically significant. Cohort 1 mice demonstrated higher expression of IBA-1 immunoreactivity in all areas but this was not statistically significant. In cohort 2 mice the difference between the means of control and atherosclerotic mice was less than 0.01 in all brain areas (Figure 3.17).

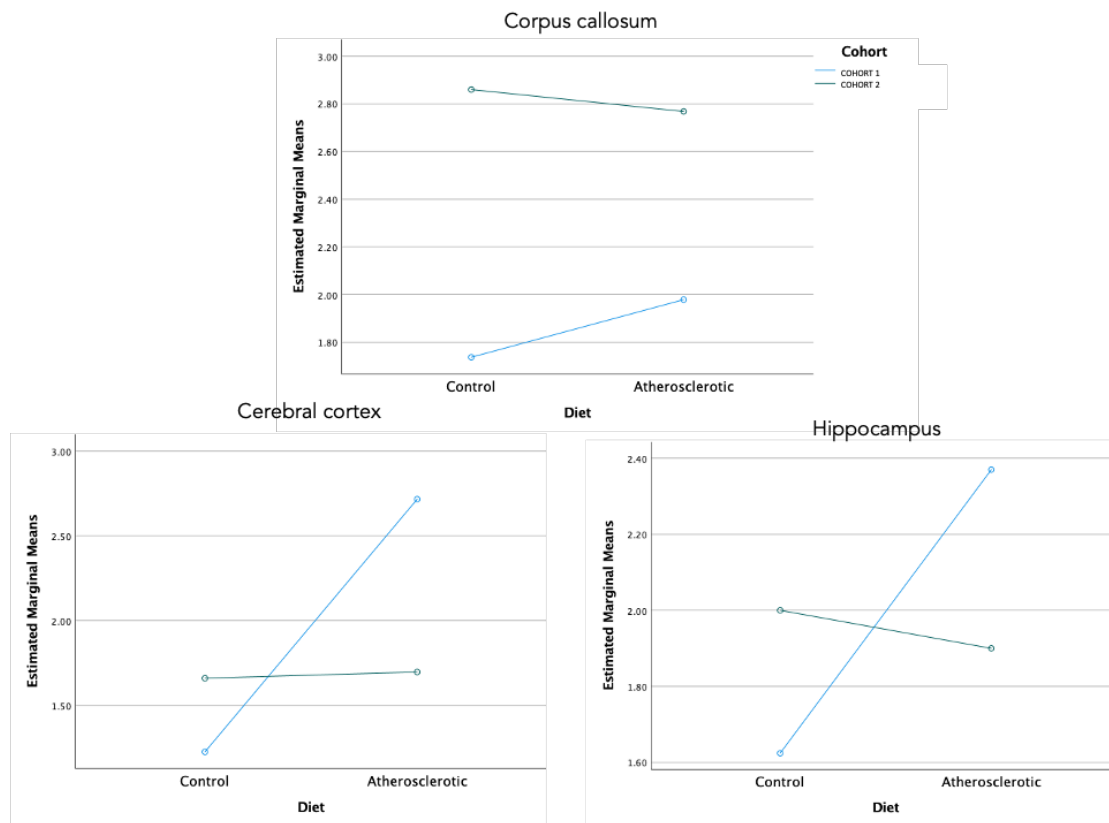


Figure 3.13 IBA-1 immunoreactivity differs between *ApoE*^{-/-} cohorts

The estimated marginal means of cohort 1 and cohort 2 confirms that they had opposite trends in relation to their diet and both cohorts had to be analysed separately.

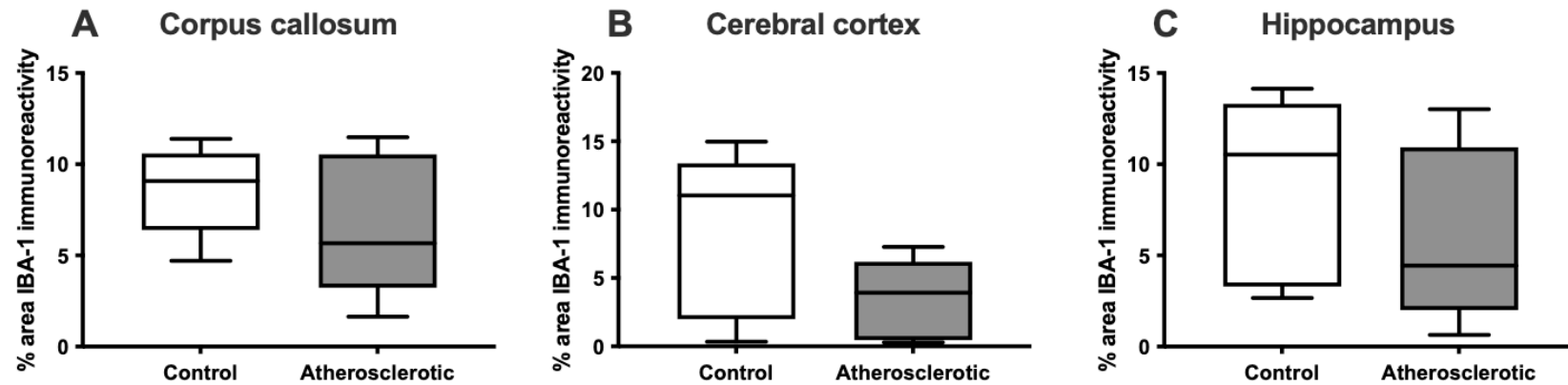


Figure 3.14 Analysis of the percentage (%) area of microglia IBA-1 immunoreactivity the corpus callosum, cerebral cortex and hippocampus of control and atherosclerotic cohort 2 *ApoE*^{-/-} mice

The corpus callosum (A), cerebral cortex (B) or hippocampus (C) of control mice showed a trend of higher % area of IBA-1 immunoreactive microglia compared to atherosclerotic mice, but, the results were not significantly different in any of the investigated areas.

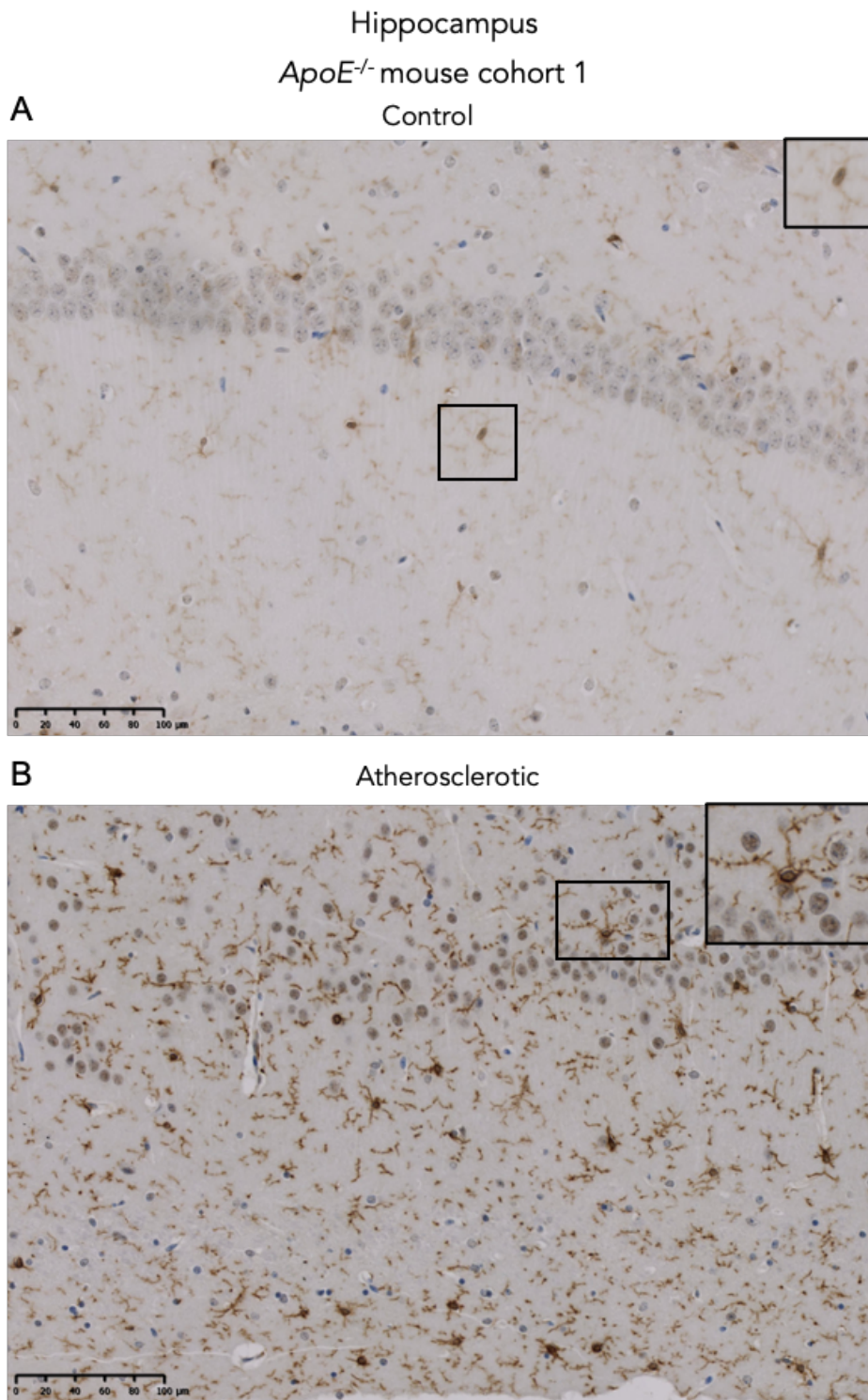


Figure 3.15. Representative image showing IBA-1 microglia immunoreactivity in the hippocampus of cohort 1 *ApoE*^{-/-} mice controls and atherosclerotic mice during simultaneous cohort staining

The microglia in control cases from the first cohort showed less IBA-1 immunoreactivity than atherosclerotic cases, it had the same morphology as stated in the previous analysis. IBA⁺ microglia on the first atherosclerotic mice cohort displayed a bigger cell body and dense ramified processes, with the hippocampus having more easily observed differences. The second cohort showed case variability and microglia with fine processes. Antibody used rabbit anti-goat IBA-1 Abcam (Lot. GR187091-3). Control n= 7, Atherosclerotic n= 8. Scale bar represents 100 μm (20 μm insert).

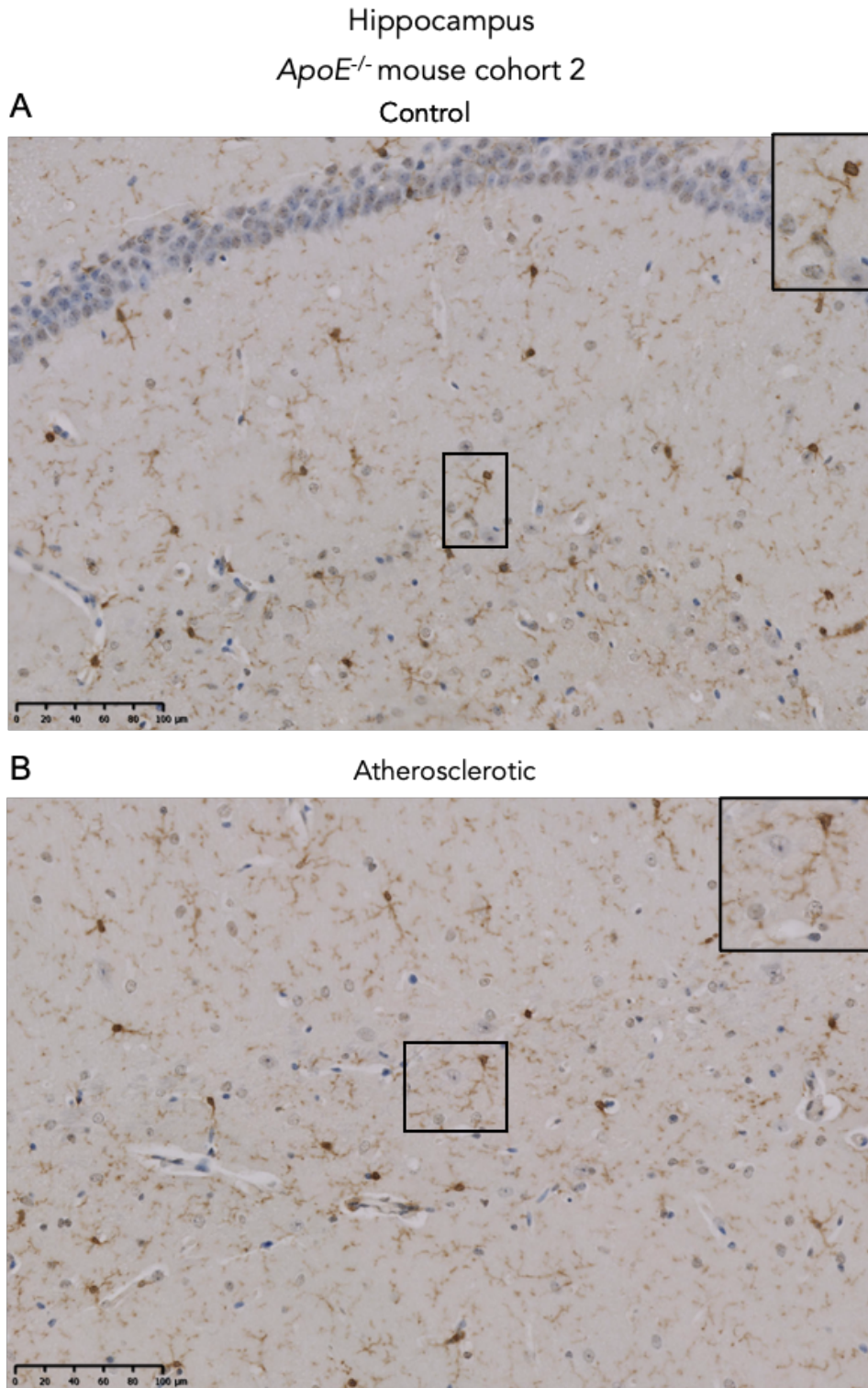


Figure 3.16 Representative image showing IBA-1 microglia immunoreactivity in the hippocampus of cohort 1 ApoE^{-/-} mice controls and atherosclerotic mice during simultaneous cohort staining

On the second cohort, there was no observable differences in the IBA-1 immunoreactivity between control and atherosclerotic mouse brains and atherosclerotic mice brains in the second cohort appear to displayed lower IBA-1 immunoreactive than controls. Antibody used rabbit anti-goat IBA-1 Abcam (Lot. GR187091-3). Control n= 6, Atherosclerotic n= 6. Scale bar represents 100 μm (20 μm insert).

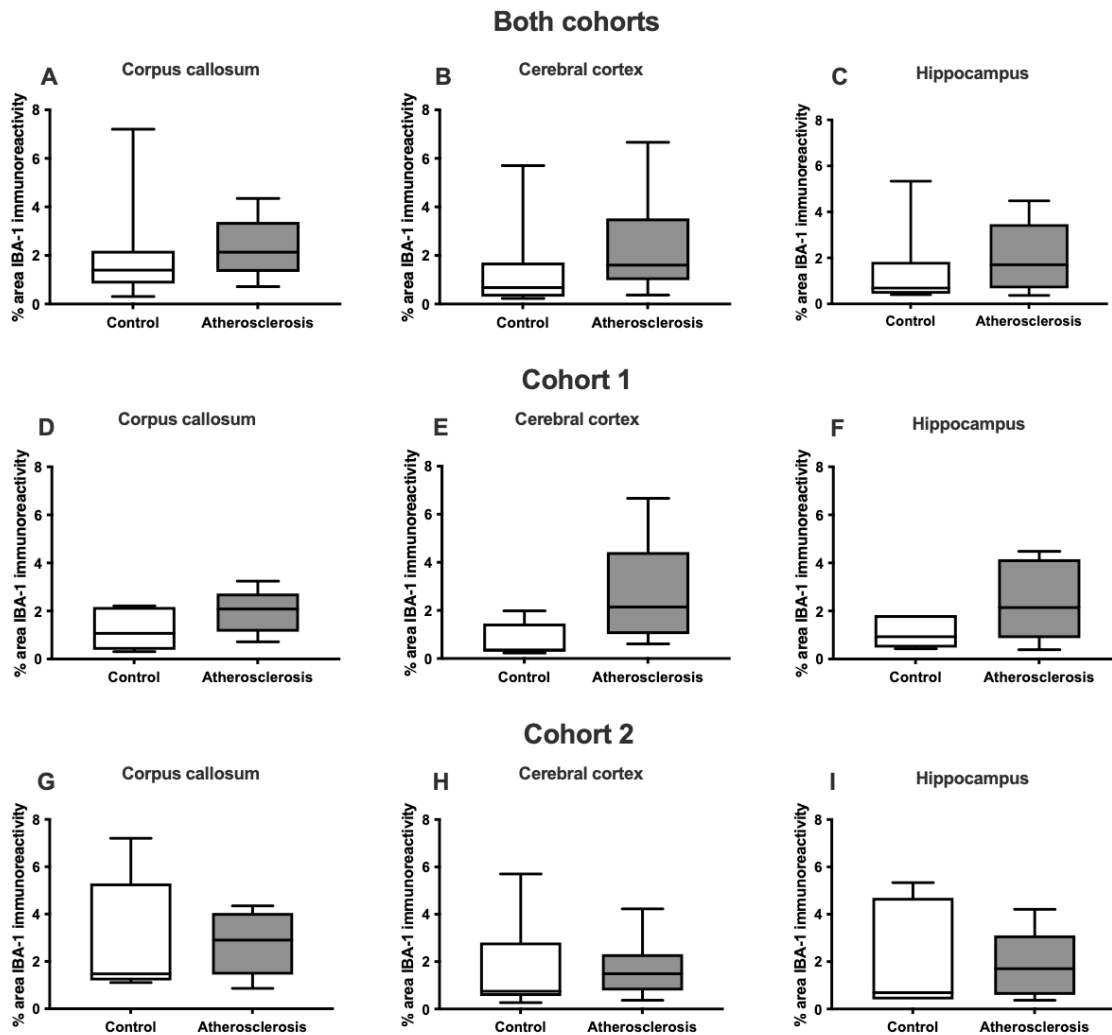


Figure 3.17 Comparison analysis of the percentage (%) area of microglia IBA-1 immunoreactivity the corpus callosum, cerebral cortex and hippocampus of control and atherosclerotic *ApoE*^{-/-} mice cohort 1 and 2 (simultaneous staining)

The corpus callosum (A), cerebral cortex (B) or hippocampus (C) of control mice showed no significant changes in the % area of IBA-1 immunoreactivity of microglia when the cohorts were stacked (A-C) or individually in cohort 1 (D-F) and cohort 2 (G-H). Furthermore, independent analysis of the cohorts did not detect any significant difference in expression of IBA-1.

Cohort 1: CC, Controls $M = 1.2$, $SEM = 0.3$; Atherosclerotic $M = 1.9$, $SEM = 0.3$, $p = 0.32$; HIP, Controls, $M = 1.1$, $SEM = 0.3$; Atherosclerotic $M = 2.4$, $SEM = 0.6$, $p = 0.5$, and COR, Controls $M = 0.7$, $SEM = 0.3$; Atherosclerotic $M = 2.7$, $SEM = 0.7$, $p = 0.9$.

Cohort 2: CC, Controls $M = 2.86$, $SEM = 1.02$; Atherosclerotic $M = 2.77$, $SEM = 0.59$, $p > 0.99$; HIP, Controls, $M = 1.9$, $SEM = 0.92$; Atherosclerotic $M = 1.9$, $SEM = 0.57$, $p > 0.99$, and COR, Controls $M = 1.65$, $SEM = 0.84$; Atherosclerotic $M = 1.69$, $SEM = 0.54$, $p > 0.99$

3.3.5 Regional variation and glial fibrillary acidic protein expression in astrocytes

The semi-quantitative assessment was determined by two independent observers using the criteria in section 2.5.6. The results showed 62.3% agreement with the inter-reliability statistics indicated moderate agreement with Cohen's kappa value $\kappa = 0.47$, $p < 0.001$. The scoring of the corpus callosum was higher on atherosclerotic mice ($M = 2.3$, $SEM = 0.50$) than in controls ($M = 1.9$, $SEM = 0.13$) ($p = 0.002$) while the basal ganglia (Controls $M = 3.3$, $SEM = 0.15$; Atherosclerosis $M = 4.7$, $SEM = 0.18$, $p = 0.13$), cerebral cortex (Controls $M = 1.62$, $SEM = 0.14$; Atherosclerosis $M = 2.16$, $SEM = 0.19$, $p = 0.085$), dentate gyrus of the hippocampus (Controls $M = 3.04$, $SEM = 0.17$; Atherosclerosis $M = 3.67$, $SEM = 0.23$, $p = 0.09$), the hippocampus proper (Controls $M = 3.2$, $SEM = 0.15$; Atherosclerosis $M = 3.5$, $SEM = 0.13$, $p = 0.18$) and thalamus (Controls $M = 1.7$, $SEM = 0.07$; Atherosclerosis $M = 1.8$, $SEM = 0.13$, $p = 0.18$) expressed similar trend of the score values of GFAP expression between control mice and atherosclerotic mice with a higher average score value on atherosclerotic mice areas compared to controls (Figure 3.18).

3.3.6 Glial fibrillary acidic protein is increased in astrocytes in the corpus callosum of atherosclerotic *ApoE*^{-/-} mice

Glial fibrillary acidic protein was used to characterise the astrocyte response in five different brain regions of both control mice and atherosclerotic mice from cohort 1. Control mice showed GFAP immunoreactivity in the cell body and proximal processes of astrocytes. Compared to control mice, the cell bodies of astrocytes in atherosclerotic mice were more rounded and surrounded by finer processes.

Table 3.1. Percentage (%) of agreement of GFAP scores assigned based on the astrocytic pattern of staining between two independent observers

Brain Area	Percentage (%) of agreement
Basal Ganglia	74%
Corpus callosum	38%
Cerebral cortex	74%
Dentate gyrus	55%
Hippocampus	48%
Thalamus	83%
Total	62%

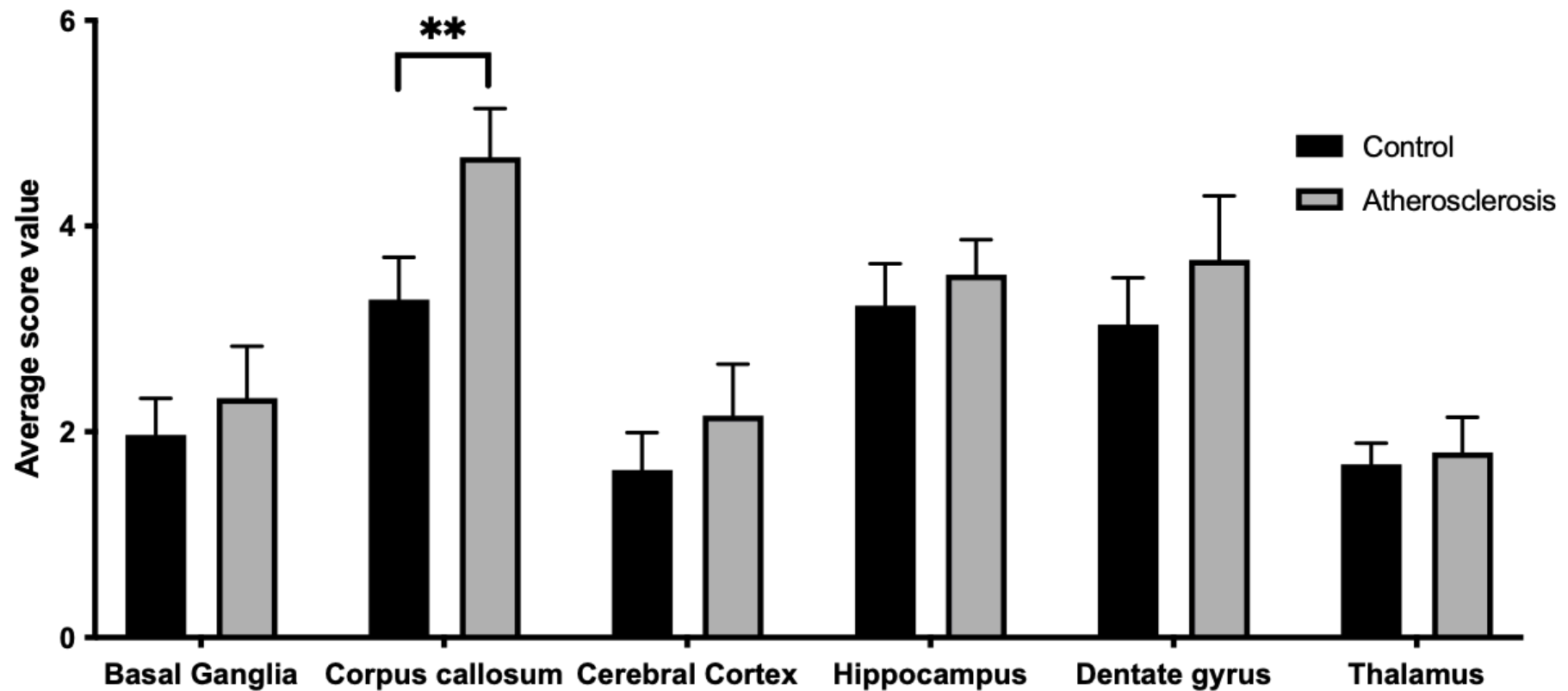


Figure 3.18 Analysis of GFAP⁺ astrocytes histological characterisation of cohort 1 *ApoE*^{-/-} mice

The scoring from two independent blinded observers using the predetermined scoring to evaluate *ApoE*^{-/-} cohort 1 mice resulted in 62.3% moderate agreement allowing to average the score given to each investigated brain area. An increase expression of GFAP in corpus callosum astrocytes of atherosclerotic mice compared to controls. Consistent regional variation was observed in controls and atherosclerotic mice.

The % of agreement between both observers was lower than expected for the corpus callosum and hippocampus and was later agreed that another score would be necessary between score 3 and 4, however a quantitative analysis was the next step which provides more accurate results. Overall, there was a more sparse pattern of GFAP⁺ astrocytes with fewer processes in all brain areas of control mice with blood vessels easily identified by the astrocytic endfeet encompassing them. Initial assessment was done in six brain areas: The corpus callosum, cerebral cortex, hippocampus proper, dentate gyrus, basal ganglia and thalamus (Appendix IV), but further examination including *ApoE*^{-/-} cohort 1 focused on the corpus callosum, the cerebral cortex and the whole hippocampus.

The corpus callosum showed a noticeable difference compared to controls in the distribution pattern with atherosclerotic mice astrocytes, showing dense GFAP immunopositive spherical cell bodies with bipolar processes that were shorter compared to controls (Figure 3.19). In the cerebral cortex there was an uneven distribution of astrocytes, with their increasing towards the edge of the cortex. The GFAP⁺ astrocytes in the control cerebral cortex displayed scarce immunolabelling of GFAP⁺ fine delicate astrocyte processes compared to more extensive and rounded radiation of short-branched processes in the atherosclerotic mice (Figure 3.20).

In contrast to the cerebral cortex, more intense GFAP immunoreactivity was observed in controls and atherosclerotic mice within the hippocampus, with elongated astrocyte cell bodies, and dense proximal processes that do not overlap (Figure 3.21). There were clear differences in the size of astrocytes between control and atherosclerotic mice, with the control mouse hippocampus presenting positively stained small stellate cells with a sparse distribution, while the astrocyte cell bodies in the atherosclerotic mouse hippocampus appeared larger. A separate assessment on cohort 2 of *ApoE*^{-/-}

mice showed a similar pattern of GFAP immunoreactivity to cohort 1 and was shown with an inter-run control (Figure 3.22). Plotting the estimated marginal means (the means for the mouse diet averaged across both cohorts) showed a difference between cohorts therefore they were analysed separately (Figure 3.23).

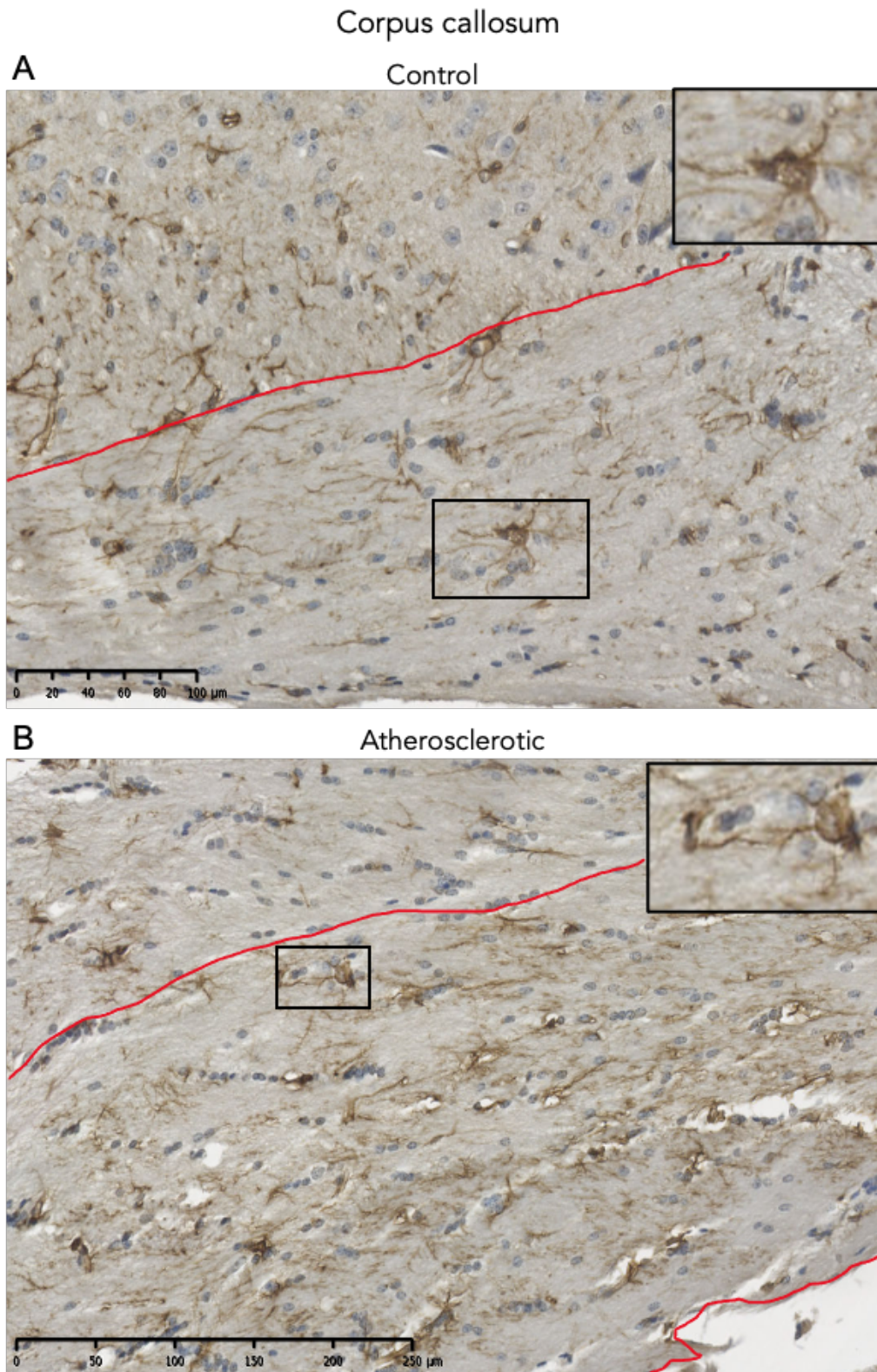


Figure 3.19 Representative image showing astrocyte expression of GFAP immunoreactivity in the corpus callosum of *ApoE*^{-/-} cohort 1 mice

GFAP⁺ astrocytes were prominent in the corpus callosum (delimited with red lines), with atherosclerotic mice (B) showing a higher density of GFAP⁺ astrocytes present compared to controls (A). Control n= 6, Atherosclerotic n= 6. Scale bar represents 100 μm (20 μm insert).

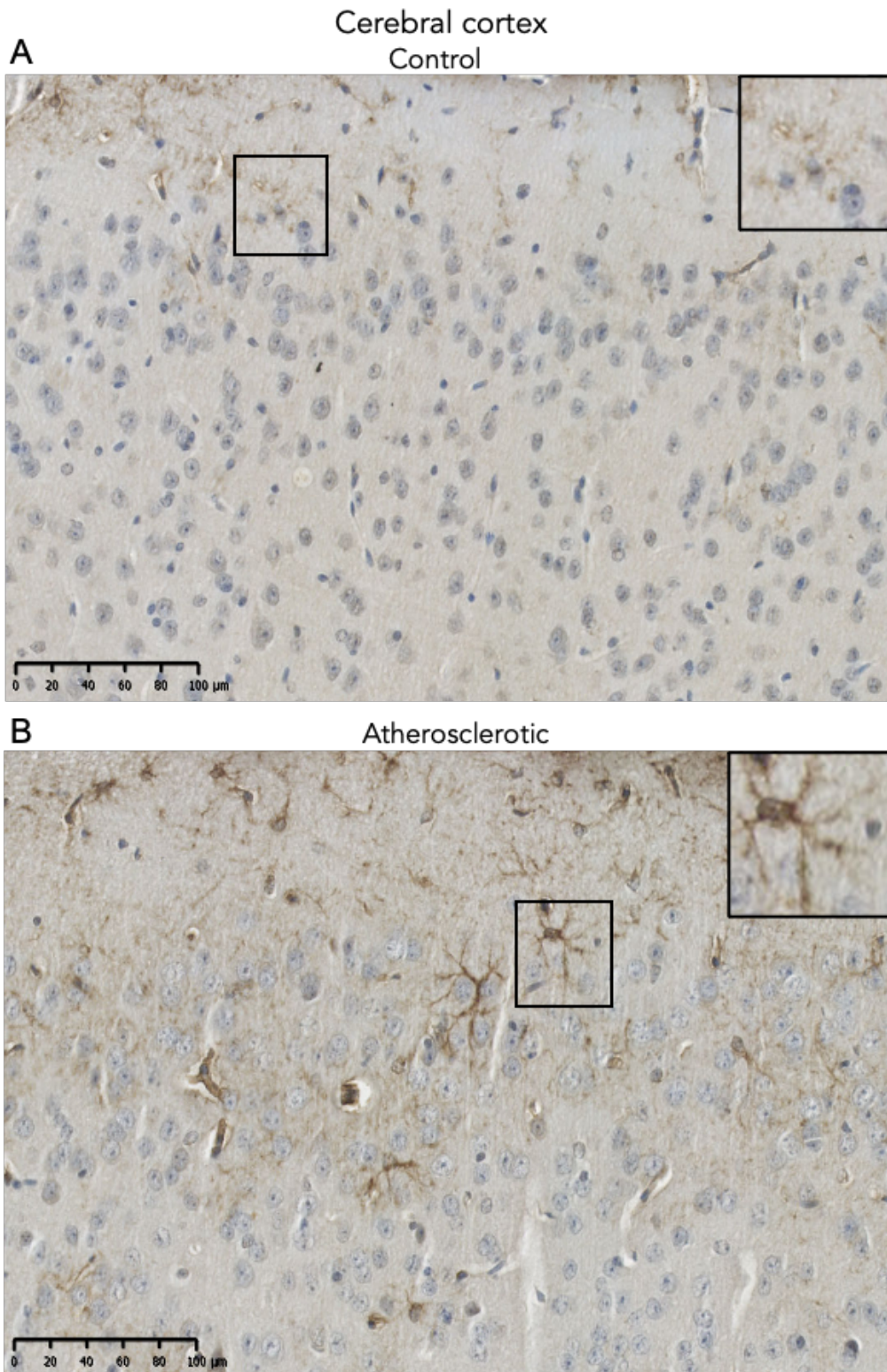


Figure 3.20 Representative image showing astrocyte expression of GFAP immunoreactivity in the cerebral cortex of *ApoE*^{-/-} cohort 1 mice

In the cerebral cortex GFAP immunoreactive astrocytes increased towards the edge of the cortex with sparse astrocytes with delicate processes on control mice (A) compared to atherosclerotic mice (B). In atherosclerotic mice, astrocytes were more easily distinguishable with their individual stellate morphology and longer, thicker processes. Control n= 6, Atherosclerotic n= 6. Scale bar represents 100 μm (20 μm insert).

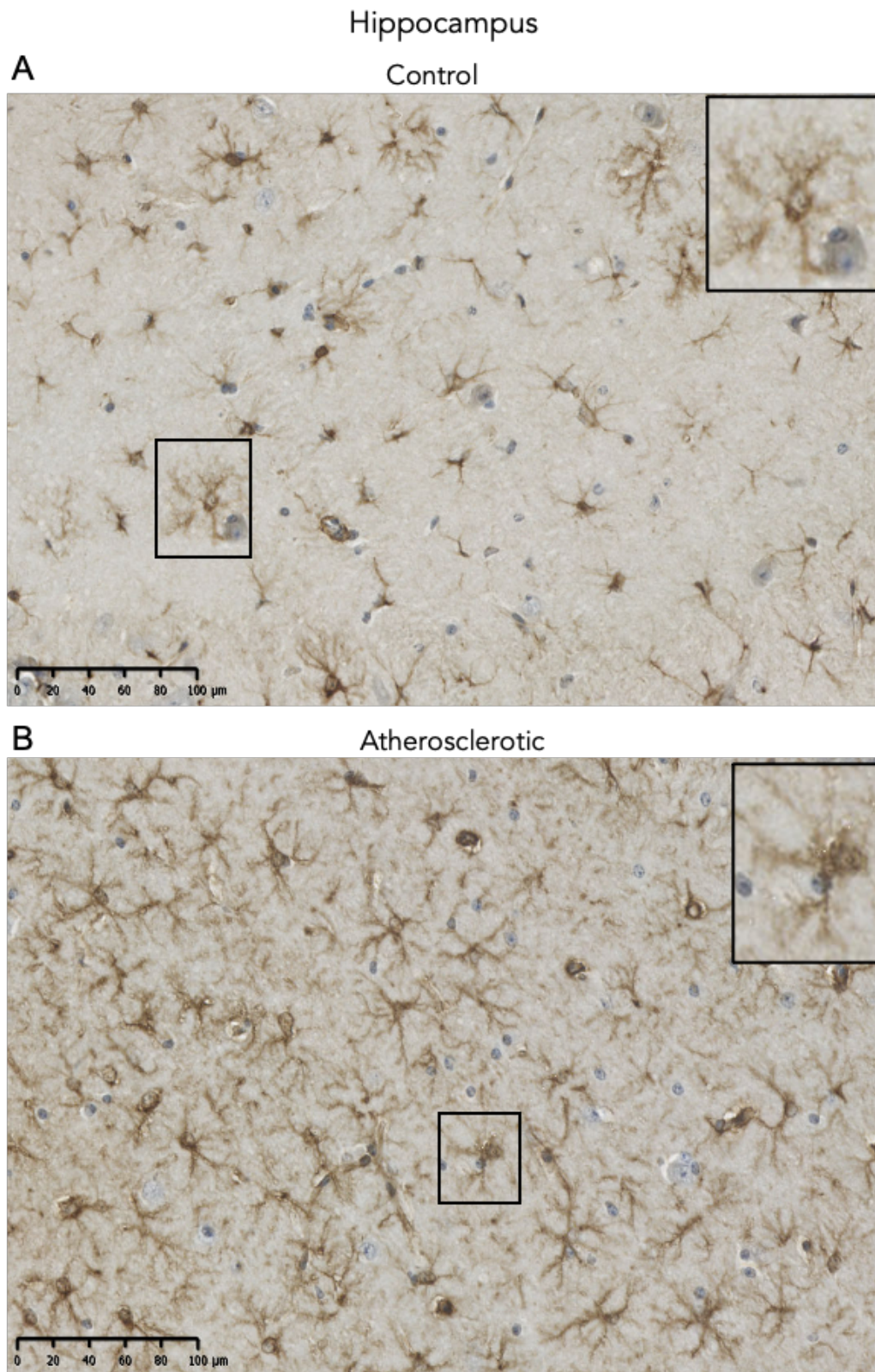


Figure 3.21 Representative image showing astrocyte expression of GFAP immunoreactivity in the hippocampus of *ApoE*^{-/-} cohort 1 mice

The astrocytes in the control hippocampus (A) were dispersed with mostly immunoreactive cell bodies, while in the atherosclerotic hippocampus (B) astrocytes demonstrated a dense distribution with more prominent GFAP⁺ processes. Control n = 6, Atherosclerotic n = 6. Scale bar represents 100 μ m (20 μ m insert).

Case number: 183879 (Atherosclerotic)

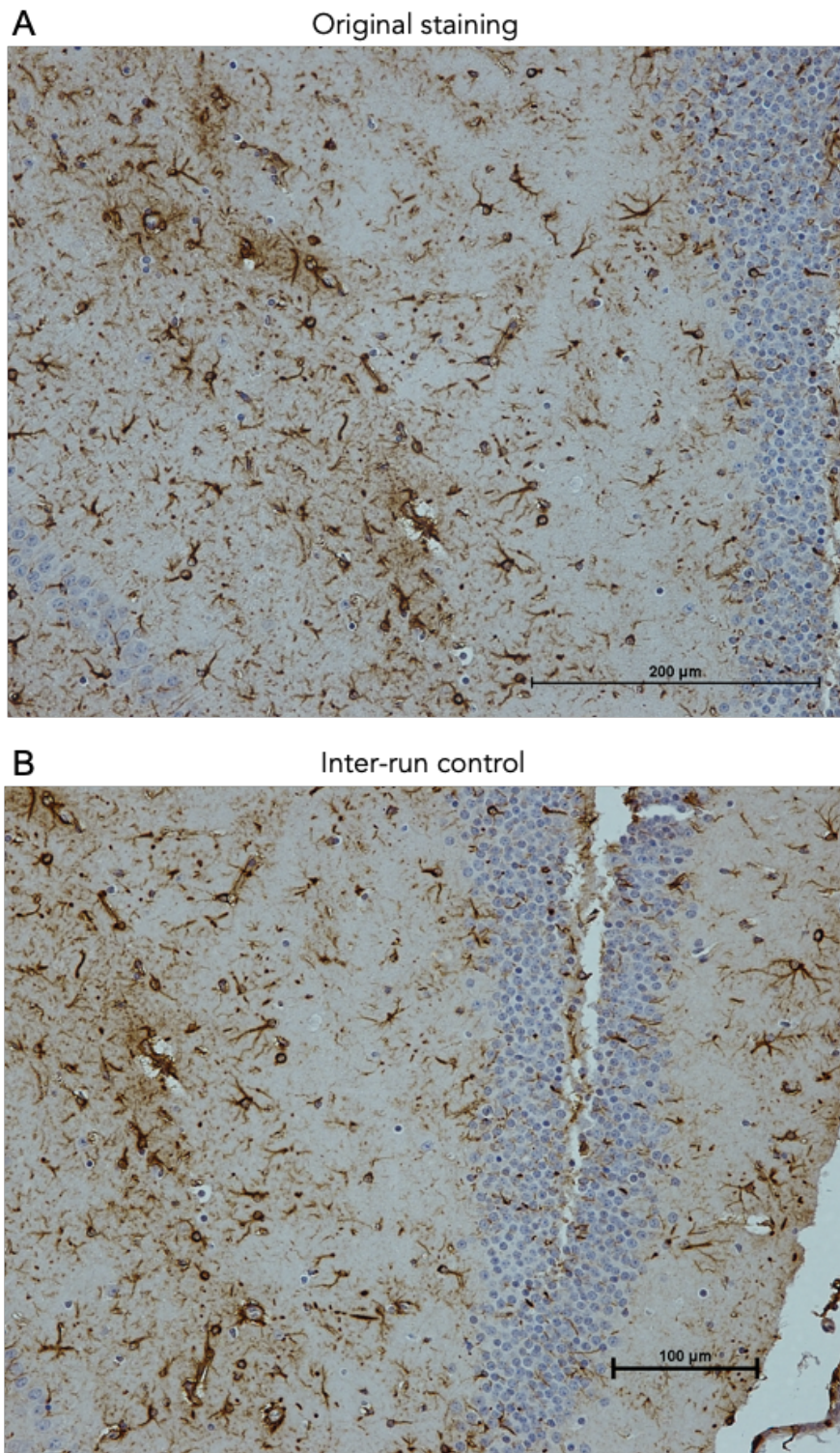


Figure 3.22 Representative image comparing astrocyte GFAP immunoreactivity on the hippocampus of both *ApoE*^{-/-} mouse cohorts stained at different time points

The same case (183879) was used as an inter-run control and displayed the same pattern of GFAP immunoreactivity in both cohort staining runs. The original staining (A) is from cohort 1 mice. The same case (183879) was later stained at the same time as cohort 2 (B). The images showed a similar pattern of staining, and individual astrocytes with dense processes. Scale bar represents 200 μm (A) and 100 μm (B).

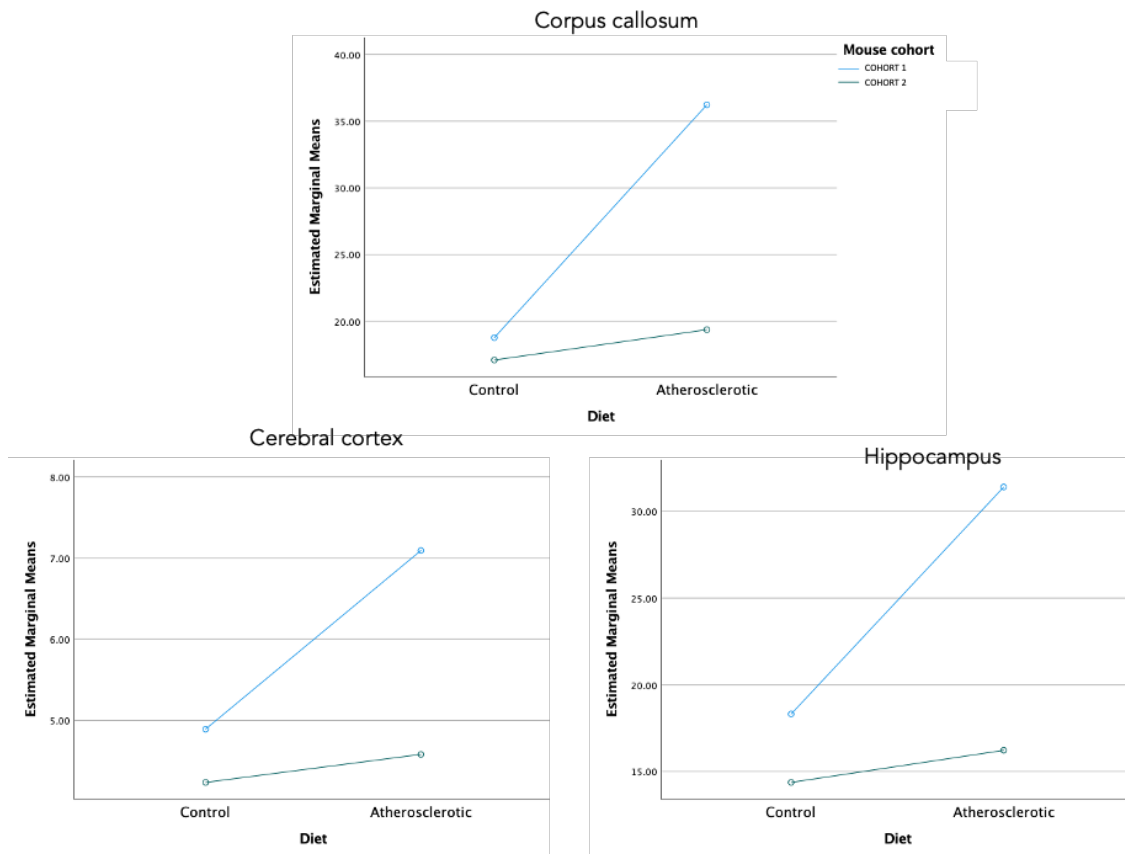


Figure 3.23 GFAP immunoreactivity differs between *ApoE^{-/-}* cohorts

The estimated marginal means of both cohorts has the same trend but the expression of GFAP in atherosclerotic mice could skew the data therefore separate evaluation of the cohorts led to a more reliable analysis.

In cohort 1 the corpus callosum of atherosclerotic mice presented a higher average % area of GFAP immunoreactivity than controls (Mean (M) \pm standard error of the mean (SEM): $M = 39.3$, $SEM = 6.19$) compared to control mice ($M = 18.7$, $SEM = 2.1$, $p = 0.017$). The hippocampus (Controls $M = 18.3$, $SEM = 3.7$; Atherosclerosis $M = 29.0$, $SEM = 7.3$), and the cerebral cortex (Controls $M = 4.9$, $SEM = 1.6$; Atherosclerosis $M = 11.3$, $SEM = 4.6$), both show a trend to higher GFAP in the atherosclerotic mice, but statistical significance was not reached (cerebral cortex, $p = 0.29$; hippocampus, $p = 0.29$). In the $ApoE^{-/-}$ mouse cohort 2 the corpus callosum (Controls $M = 26.8$, $SEM = 2.9$; Atherosclerosis $M = 39.6$, $SEM = 4.8$, $p = 0.06$) and the hippocampus (Controls $M = 29.0$, $SEM = 5.0$; Atherosclerosis $M = 31.8$, $SEM = 2.7$, $p = 0.7$) showed similar levels of immunoreactivity in both control and atherosclerotic mice as the % area of immunoreactivity observed in the atherosclerotic corpus callosum and hippocampus of cohort 1 $ApoE^{-/-}$ mice. In both cohorts the cerebral cortex showed the lowest levels of GFAP immunoreactivity (cohort 1; Control ($M = 4.9$, $SEM = 1.6$; Atherosclerosis $M = 11.3$, $SEM = 4.6$) with the control from cohort 2 being slightly higher than the atherosclerotic mice from the same cohort ($M = 12.42$, $SEM = 1.1$; Atherosclerosis $M = 11.9$, $SEM = 1.1$, $p = 0.07$) (Figure 3.24).

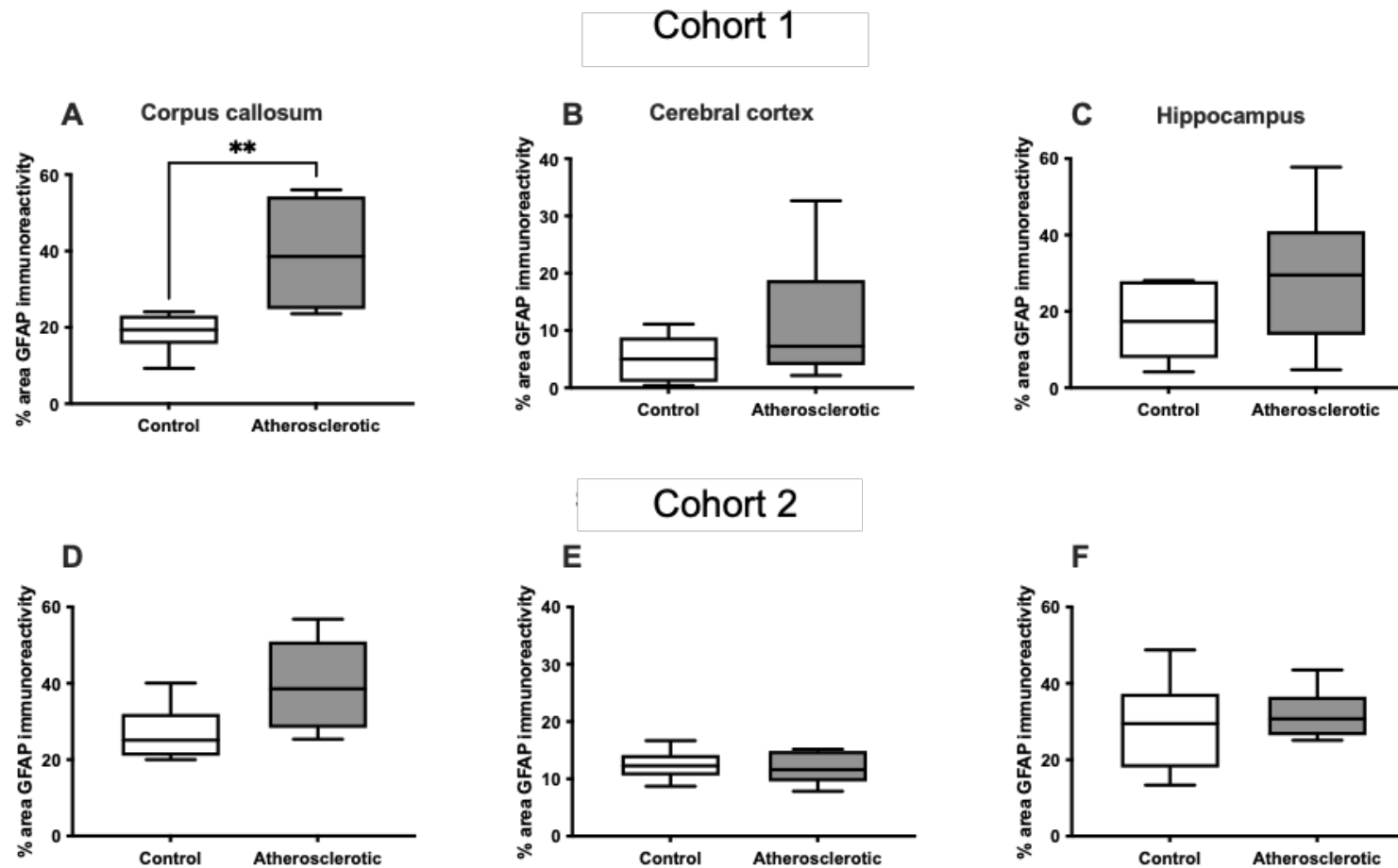


Figure 3.24 Increased percentage (%) area of astrocytes GFAP immunoreactivity in the corpus callosum of atherosclerotic cohort 1 *ApoE*^{-/-} mice compared to controls

The % area GFAP immunoreactivity was significantly increased in the corpus callosum of cohort 1 *ApoE*^{-/-} mice (A). In contrast the cerebral cortex (B) and the hippocampus (C) did not show any significant difference in GFAP immunoreactivity but atherosclerotic mice presented a trend of higher immunoreactivity compared to controls. Cohort 2 of *ApoE*^{-/-} mice did not show significant difference on the % area of immunoreactivity between atherosclerotic and control mice. (** P < 0.01).

3.3.7 Intracellular adhesion molecule -1 (ICAM-1) immunoreactivity

expression in both *ApoE*^{-/-} mice cohorts.

Evaluation of ICAM-1 immunoreactivity in cohort 1 showed ICAM-1⁺ blood vessels but examination detected additional diffuse staining associated with parenchymal cells morphologically resembling microglia. To confirm that the observed ICAM1⁺ parenchymal cells were microglia, dual immunohistochemistry was performed and demonstrated colocalization of ICAM1 with IBA-1, confirming that ICAM-1⁺ parenchymal cells are microglia (Figure 3.25)

Based on the results from previous staining both *ApoE*^{-/-} cohorts were stained together but analysed separately. In cohort 1 the endothelial cells of atherosclerotic mice expressed more ICAM-1 immunoreactivity compared to controls with a diffuse staining pattern surrounding smaller blood vessels. The morphology of endothelial cells was similar across brain areas. However, the distribution of endothelial cells varied; ICAM-1⁺ blood vessels were not easily observed in the corpus callosum of atherosclerotic mice, less so in controls (Figure 3.26). The cerebral cortex contained the large ICAM-1 immunoreactive blood vessels (Figure 3.27). In contrast, the hippocampus presented smaller ICAM-1 immunopositive blood vessels compared to the cerebral cortex, with atherosclerotic mice having a more rounded morphology compared to controls (Figure 3.28). ICAM-1 immunoreactivity was more intense on the endothelial cells than microglial cells. Microglial expression of ICAM-1 in cohort 1 showed higher immunoreactivity in atherosclerotic mice compared to controls, with similar morphology across brain areas. ICAM-1 immunoreactivity was present on microglia cell processes rather than in the cell body. The cell processes were not continuous and the pattern of staining was not distinct/sharp as with IBA-1.

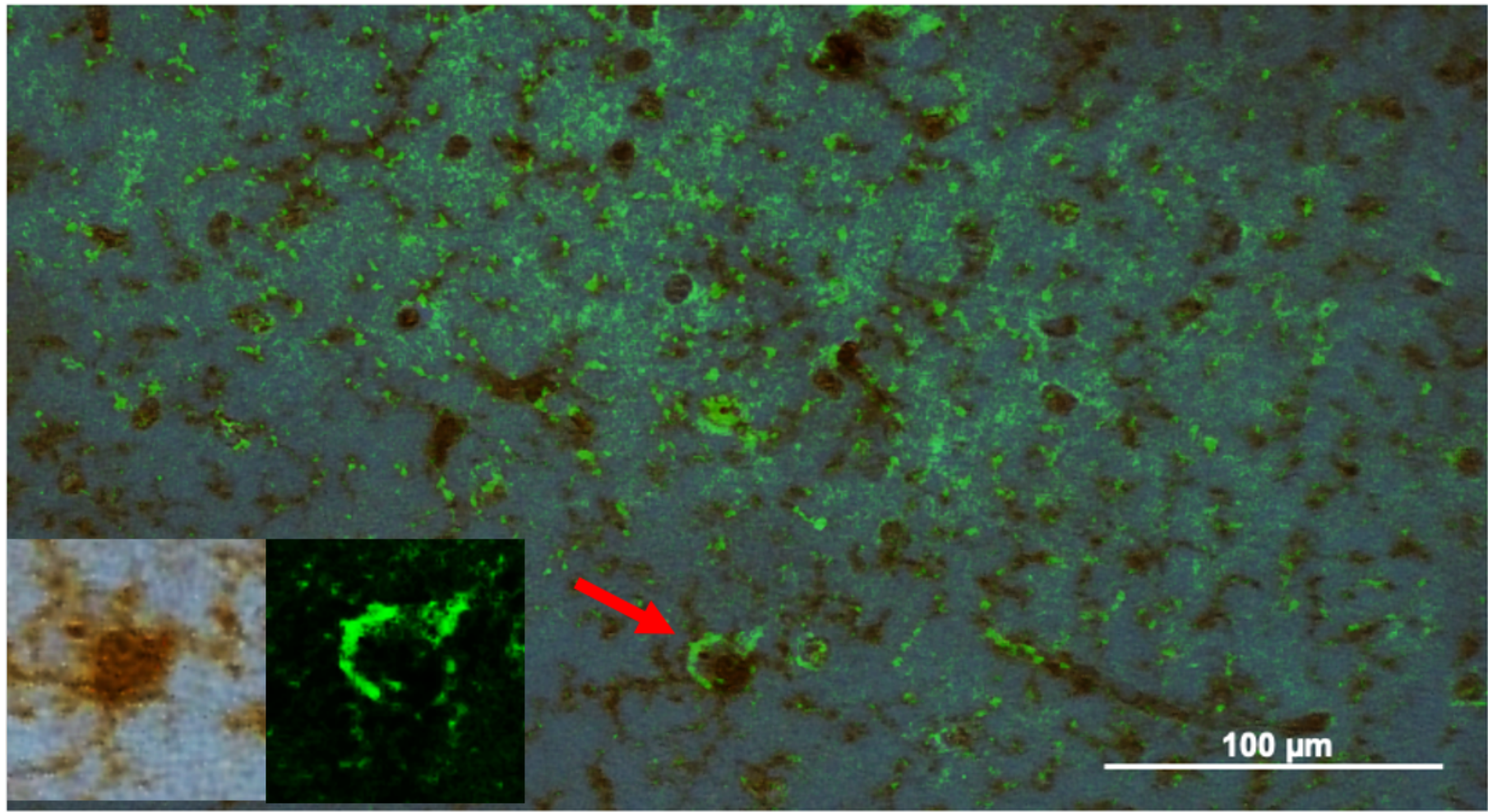


Figure 3.25. Representative image showing co-localisation of ICAM-1 with IBA1⁺ microglial cells

ICAM-1⁺ cells (brown) were also stained for IBA-1 (green) to identify the parenchymal cells resembling microglia. Red arrows indicate examples of co-localisation. Left hand side insert represents ICAM-1 immunoreactive microglia. Right hand side insert represents IBA-1 immunoreactive microglia. Scale bar 100 µm.

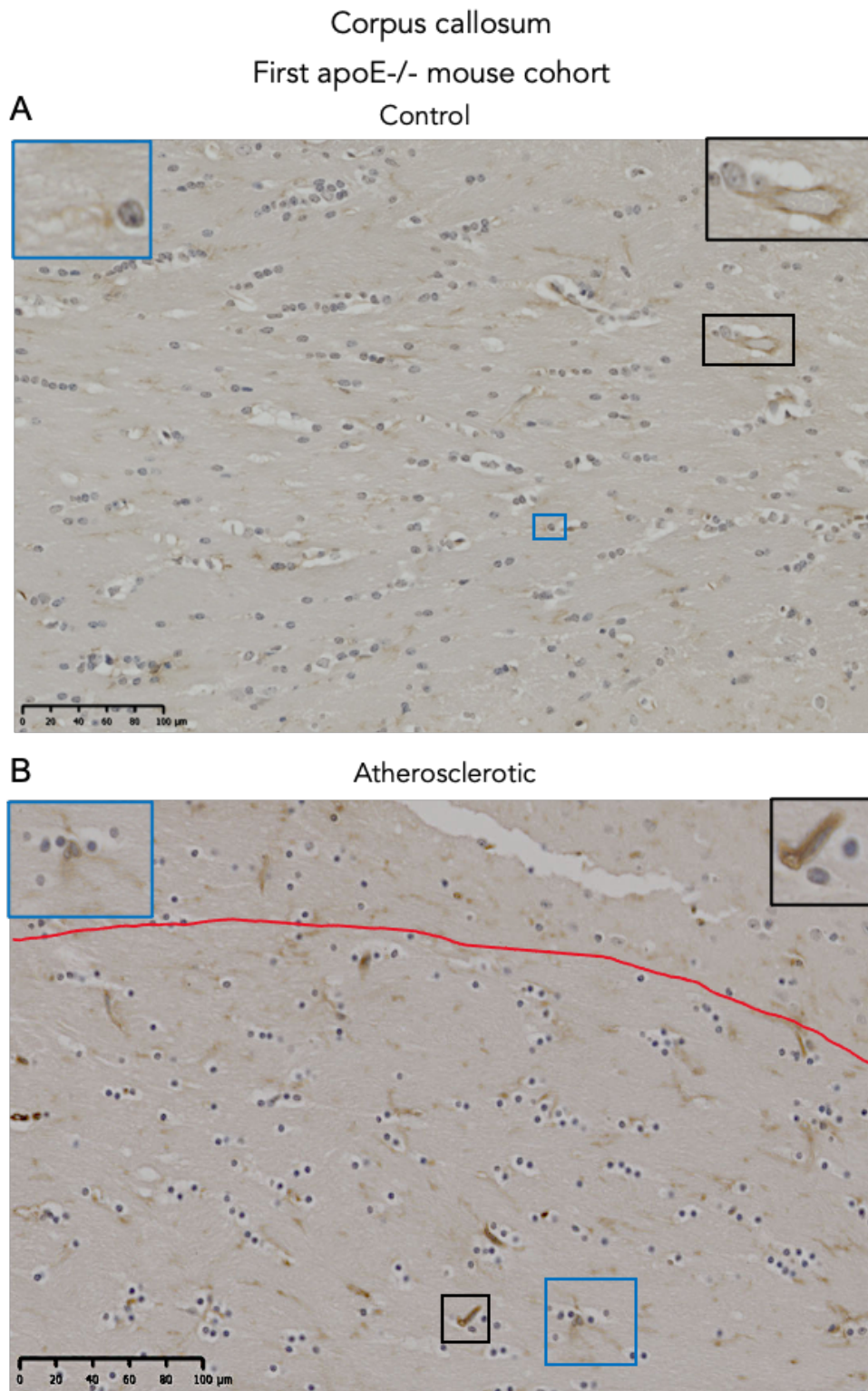


Figure 3.26. Representative image showing endothelial cell and microglia expression of ICAM-1 immunoreactivity in the corpus callosum of *ApoE^{-/-}* cohort 1 mice

Atherosclerotic mice (B) showed higher ICAM-1 immunoreactivity than controls (A) in both endothelial cells and microglia. The endothelial cells in the blood vessels are not easily identified in the corpus callosum with few ICAM+ blood vessels in both diets. There were more ICAM-1 immunoreactive microglia cell bodies and processes in the atherosclerotic mice. Control n= 6, Atherosclerotic n= 6. Scale bar represents 100 μm (20 μm insert of endothelial cell on the right hand side and microglia on the left hand side).

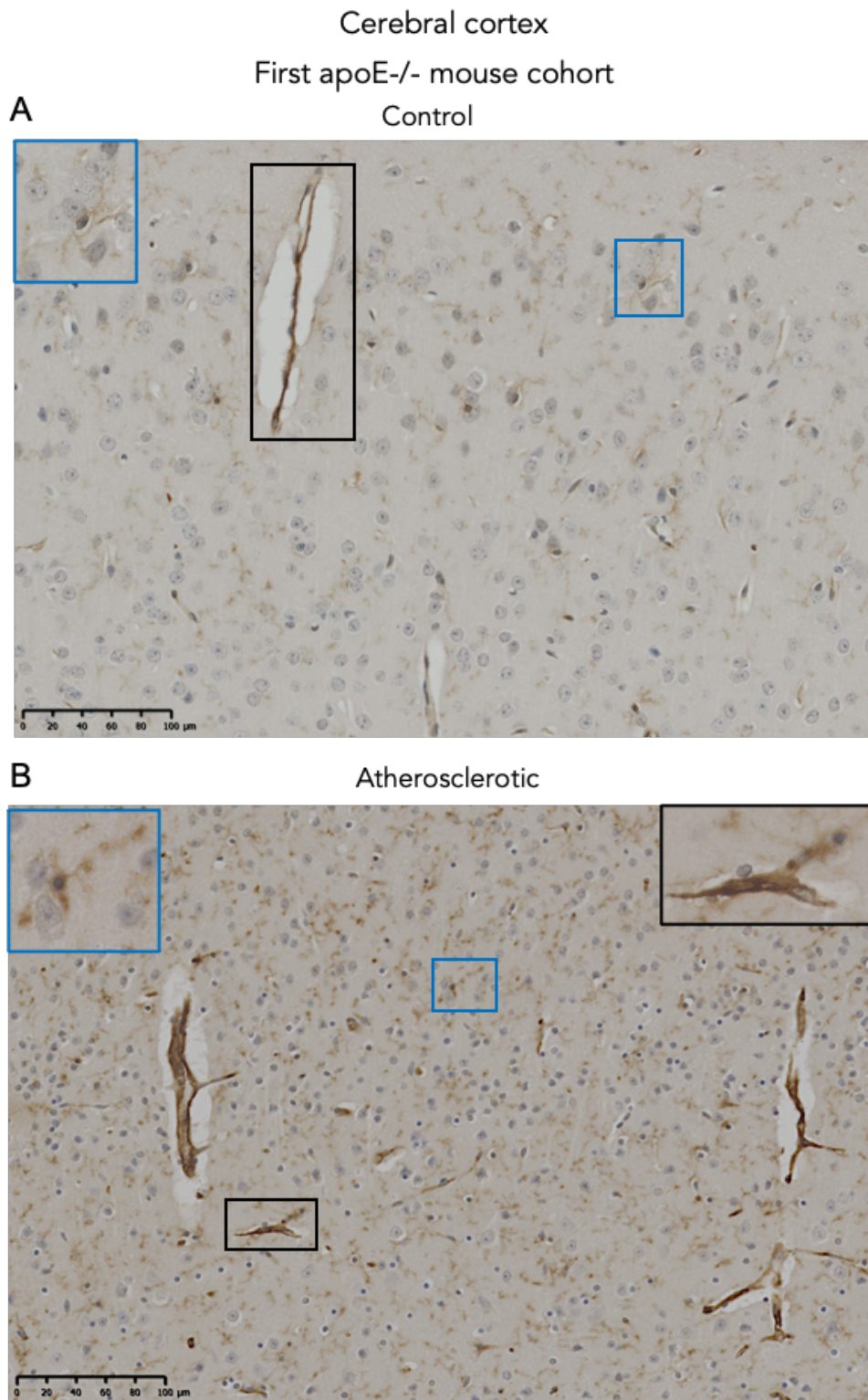


Figure 3.27 Representative image showing endothelial cell and microglia expression of ICAM-1 immunoreactivity in the cerebral cortex of *ApoE*^{-/-} cohort 1 mice

The endothelial cells and microglia in the atherosclerotic mice (B) had a higher level of ICAM-1 immunoreactivity compared to controls (A). Blood vessels appear thicker on atherosclerotic mice. The thicker and discontinued microglia processes were more easily observed in atherosclerotic mice compared to delicate microglial processes in the cerebral cortex of control mice. Control n= 6, Atherosclerotic n= 6. Scale bar represents 100 μ m (20 μ m insert of endothelial cell on the right hand side and microglia on the left hand side).

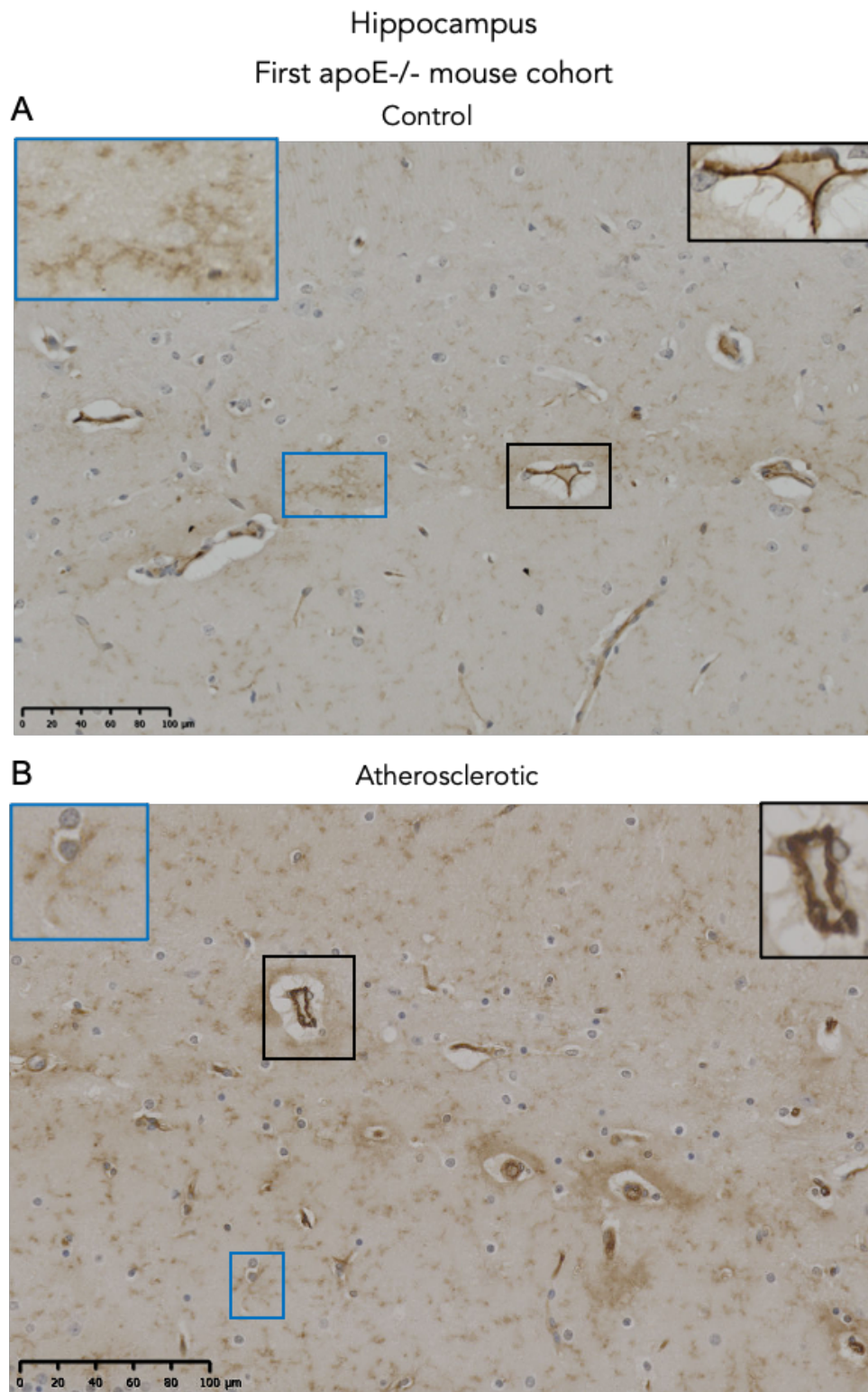


Figure 3.28. Representative image showing endothelial cell and microglia expression of ICAM-1 immunoreactivity in the hippocampus of *ApoE*^{-/-} cohort 1 mice

The blood vessels in the hippocampus appeared smaller compared to the cerebral cortex. The ICAM-1 immunoreactivity of blood vessels seemed higher in atherosclerotic (B) than controls (A). The ICAM-1⁺ microglial cell bodies presented low immunoreactivity in control and atherosclerotic *ApoE*^{-/-} mouse. The microglia processes were thicker and had a discontinued appearance. Control n= 6, Atherosclerotic n= 6. Scale bar represents 100 μ m (20 μ m insert of endothelial cell on the right hand side and microglia on the left hand side).

The control and atherosclerotic mice in *ApoE*^{-/-} cohort 2 presented a similar cellular morphology of blood vessels and microglia as cohort 1 across the corpus callosum (Figure 3.29), cerebral cortex (Figure 3.30) and hippocampus (Figure 3.31). However, the intensity of ICAM-1 immunoreactivity in endothelial cells and microglia was greater in controls than in atherosclerotic mice.

In cohort 1 the corpus callosum showed a significant increase in ICAM-1 immunoreactivity in the endothelium of atherosclerotic mice compared to controls after Bonferroni correction (Controls $M = 0.48$, $SEM = 0.1$; Atherosclerosis $M = 1.8$, $SEM = 0.3$, $p = 0.04$), and non-significant trends to increase in the cerebral cortex (Controls $M = 0.34$, $SEM = 0.1$; Atherosclerosis $M = 2.6$, $SEM = 0.9$, $p = 0.2$) and the hippocampus (Controls $M = 0.55$, $SEM = 0.1$; Atherosclerosis $M = 3.0$, $SEM = 0.95$, $p = 0.06$), which did not replicate in cohort 2 (Figure 3.32). The analysis of *ApoE*^{-/-} mouse cohort 2, displayed an opposite trend to cohort 1 (Corpus callosum, Controls $M = 1.7$, $SEM = 0.35$; Atherosclerosis $M = 1.0$, $SEM = 0.20$, $p = 0.24$; Cerebral cortex; (Controls $M = 1.05$, $SEM = 0.16$; Atherosclerosis $M = 0.56$, $SEM = 0.2$, $p = 0.24$; Hippocampus, (Controls $M = 2.12$, $SEM = 0.38$; Atherosclerosis $M = 0.71$, $SEM = 0.17$, $p = 0.09$) (Figure 3.32).

Corpus callosum
Second apoE^{-/-} mouse cohort

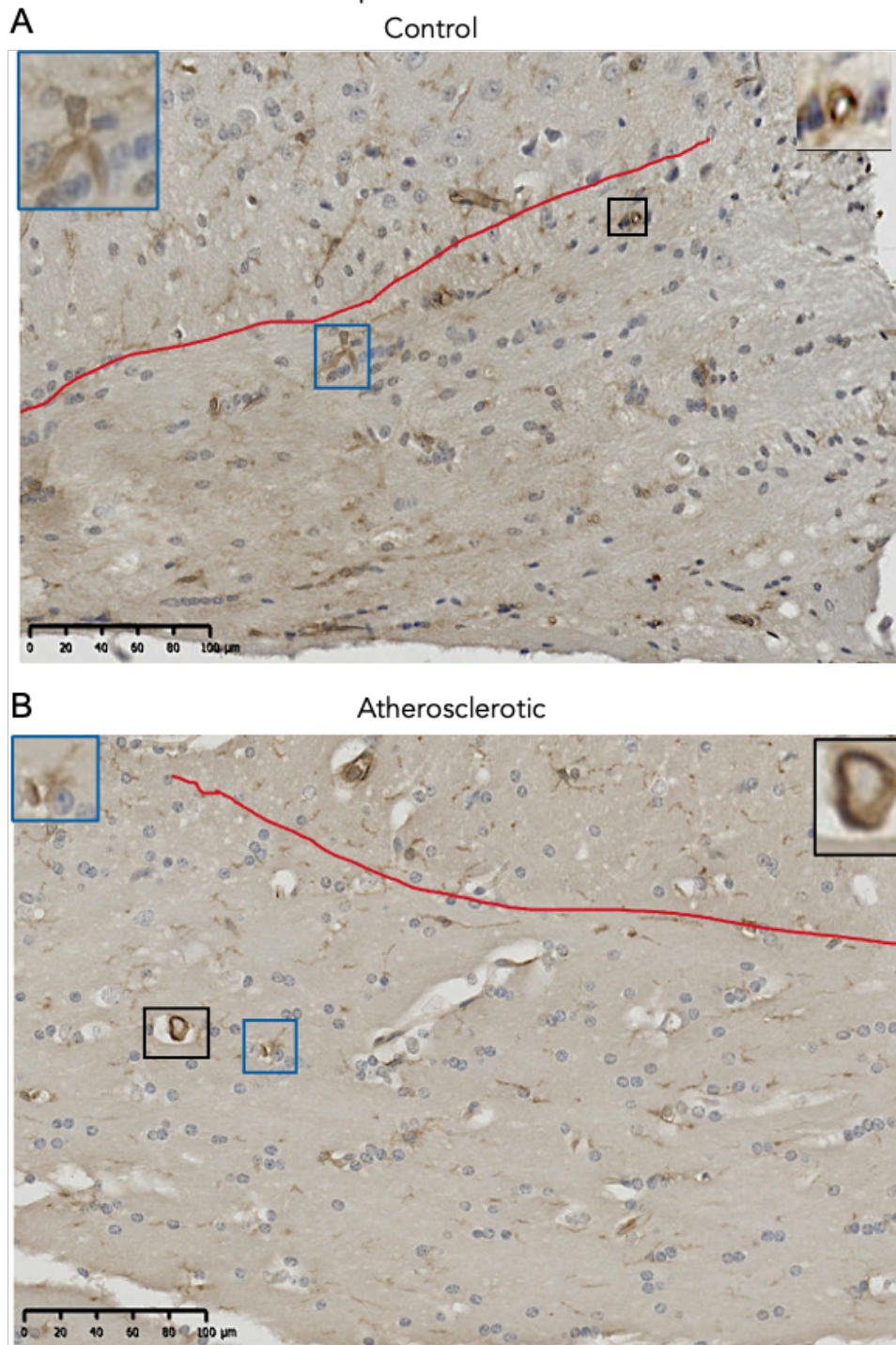


Figure 3.29 Representative image showing endothelial cell and microglia expression of ICAM-1 immunoreactivity in the corpus callosum of *ApoE^{-/-}* cohort 2 mice

Control mice (A) displayed higher ICAM-1 immunoreactivity than atherosclerotic (B) in both endothelial cells and microglia. The endothelial cells in the blood vessels were not easily identified in the corpus callosum with few ICAM⁺ blood vessels in both diets. There were more ICAM-1 immunoreactive microglia cell bodies and processes in the control mice. Control n= 6, Atherosclerotic n= 6. Scale bar represents 100 μm (20 μm insert of endothelial cell on the right hand side and microglia on the left hand side).

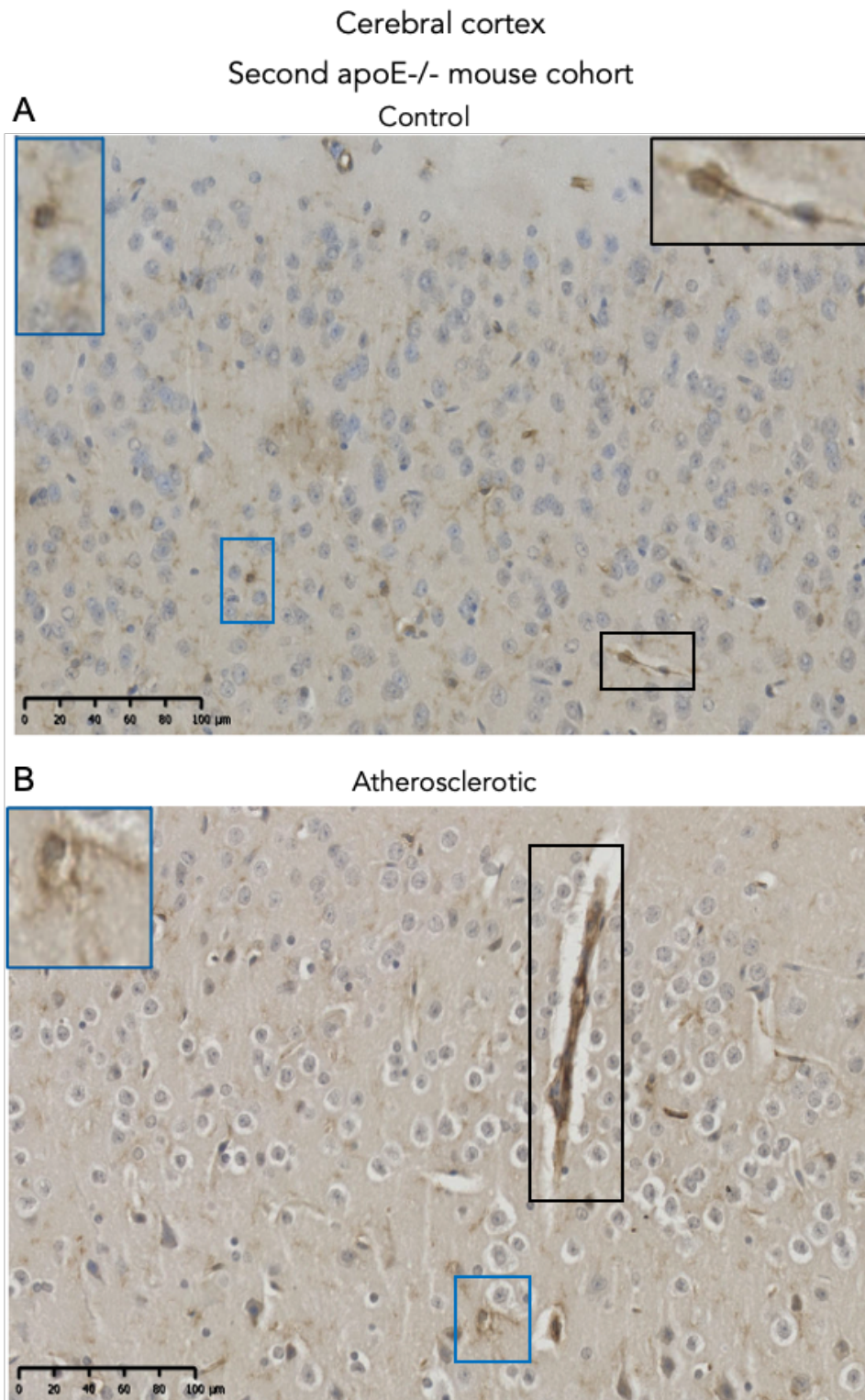


Figure 3.30 Representative image showing endothelial cell and microglia expression of ICAM-1 immunoreactivity in the cerebral cortex of *ApoE*^{-/-} cohort 2 mice

The endothelial cells and microglia in the control mice (A) presented a higher level of ICAM-1 immunoreactivity compared to atherosclerotic (B). The morphology of elongated blood vessels was similar in both diets and cohorts. The thicker and discontinued microglia processes were more easily observed in atherosclerotic mice compared to delicate microglial processes in the cerebral cortex of control mice. Control n= 6, Atherosclerotic n= 6. Scale bar represents 100 μm (20 μm insert of endothelial cell on the right hand side and microglia on the left hand side)..

Hippocampus
Second apoE^{-/-} mouse cohort

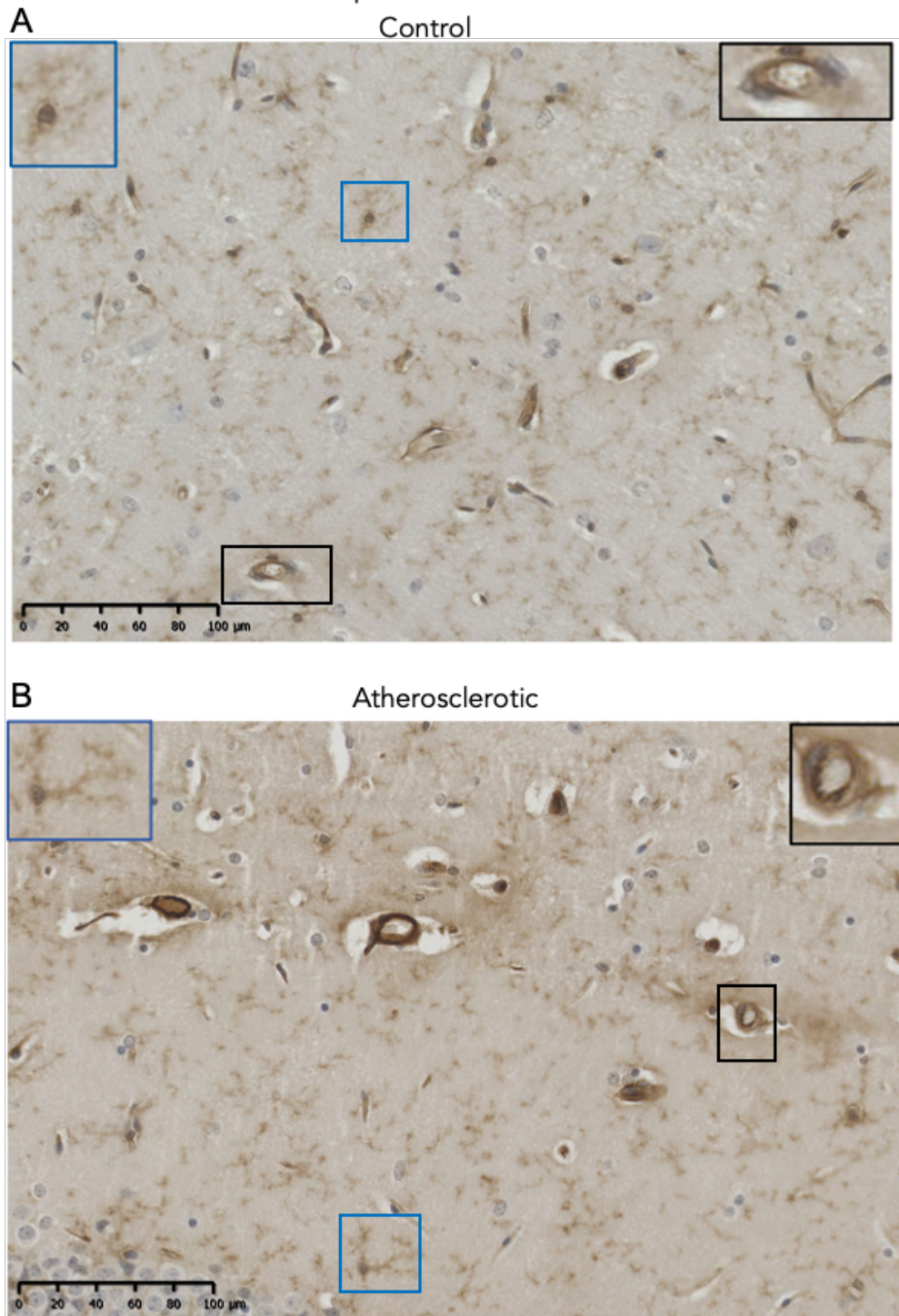


Figure 3.31 Representative image showing endothelial cell and microglia expression of ICAM-1 immunoreactivity in the hippocampus of *ApoE*^{-/-} cohort 2 mice

The hippocampus appeared to present small size vessels compared to the cerebral cortex, with a more rounded morphology in atherosclerotic mice (B) than in controls (A). The ICAM-1⁺ microglial cell bodies was low in the hippocampus of both diets and the microglia processes were thicker and had a discontinued appearance, with the overall ICAM-1 immunoreactivity was lower in controls compared to atherosclerotic mice. Control n= 6, Atherosclerotic n= 6. Scale bar represents 100 µm (20 µm insert of endothelial cell on the right hand side and microglia on the left hand side).

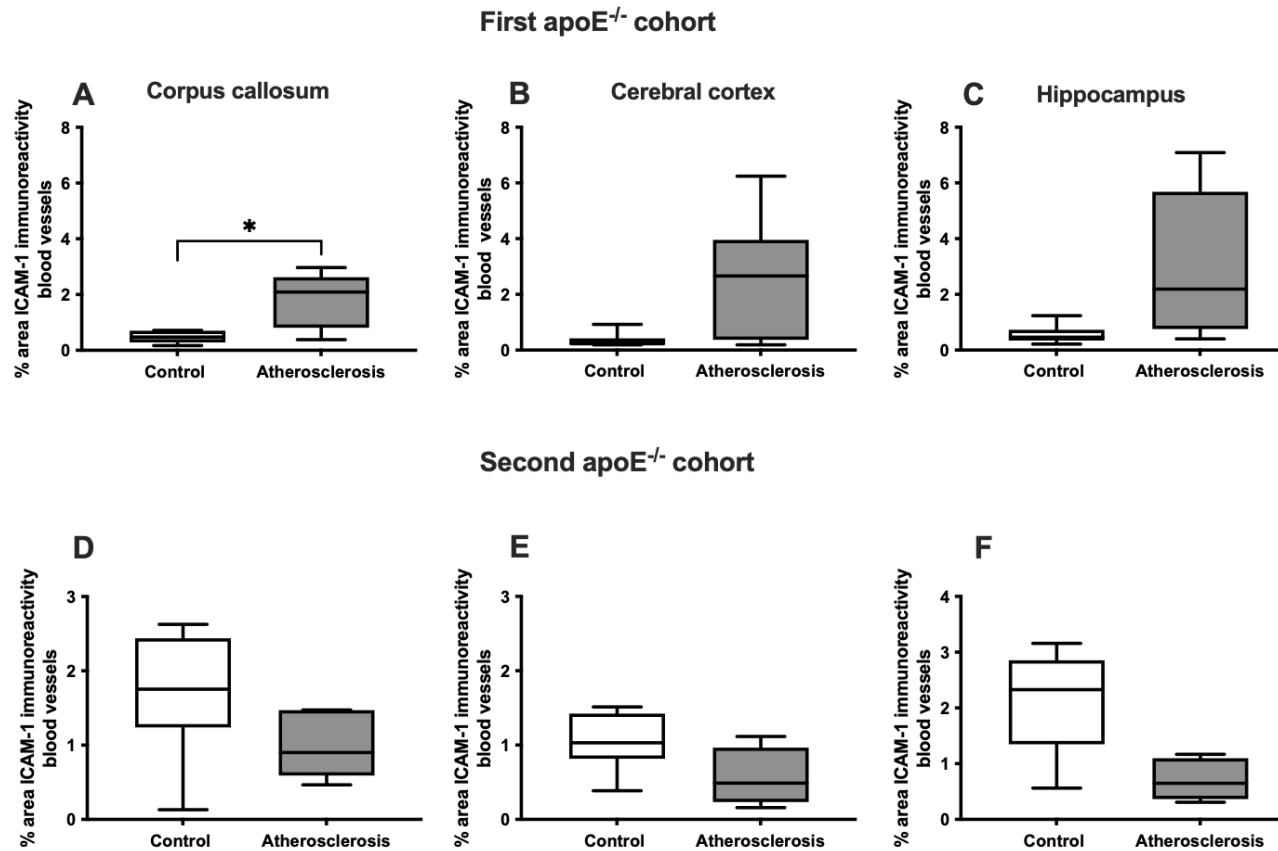


Figure 3.32. Comparison analysis of the percentage (%) area of endothelial cells ICAM-1 immunoreactivity the corpus callosum, cerebral cortex and hippocampus of control and atherosclerotic *ApoE^{-/-}* mice cohort 1 and 2

ICAM-1 expression was increased in the corpus callosum of cohort 1 of atherosclerotic mice compared to controls (A). Cohort 1 of *ApoE^{-/-}* mice (D-F) showed an opposite, not statistically significant, trend with the endothelial cells of controls expressing a higher % of ICAM-1 immunoreactivity than atherosclerotic mice. The statistical differences are marked by an asterisk. (* $P < 0.05$).

Quantitative assessment of ICAM-1 immunoreactive microglia in cohort 1 revealed levels were significantly higher in the corpus callosum (Controls $M = 0.96$, $SEM = 0.15$; Atherosclerosis $M = 3.2$, $SEM = 0.72$, $p = 0.01$), cerebral cortex (Controls $M = 0.49$, $SEM = 0.1$; Atherosclerosis $M = 4.0$, $SEM = 1.1$, $p = 0.045$) and hippocampus, (Controls $M = 0.8$, $SEM = 0.17$; Atherosclerosis $M = 4.7$, $SEM = 1.5$, $p = 0.04$). Cohort 2 showed ICAM⁺ microglia did not replicate this finding and differences between atherosclerotic and control mice did not reach significance in any area. (Corpus callosum, Controls $M = 3.31$, $SEM = 0.69$; Atherosclerosis $M = 1.85$, $SEM = 0.46$, $p = 0.16$; Cerebral cortex; (Controls $M = 2.23$, $SEM = 0.36$; Atherosclerosis $M = 1.1$, $SEM = 0.46$, $p = 0.34$; Hippocampus, (Controls $M = 3.9$, $SEM = 0.95$; Atherosclerosis $M = 7.97$, $SEM = 0.97$, $p = 0.53$) (Figure 3.33).

3.3.8 Inconsistent PDGFR- β staining on FFPE mouse tissue.

PDGFR- β is a widely expressed pericyte marker (Ding et al., 2020). Initial optimisation of the pericyte marker PDGFR- β showed distinct staining of pericytes surrounding blood vessels (Figure 3.34. A). Nevertheless, the pattern of staining was inconsistent and not reproducible. Examination of visible blood vessels showed intense immunoreactivity surrounding some, but not all, blood vessels (Figure 3.34 B, red arrows). Furthermore, PDGFR- β ⁺ parenchymal cells resembling microglia were observed (Figure 3.34 B, blue arrow). Overall, the immunodetection of PDGFR- β in FFPE mouse tissue failed to reproduce the pattern of staining observed in the initial optimisation, therefore this antibody was not included in the overall assessment of pathology in this study

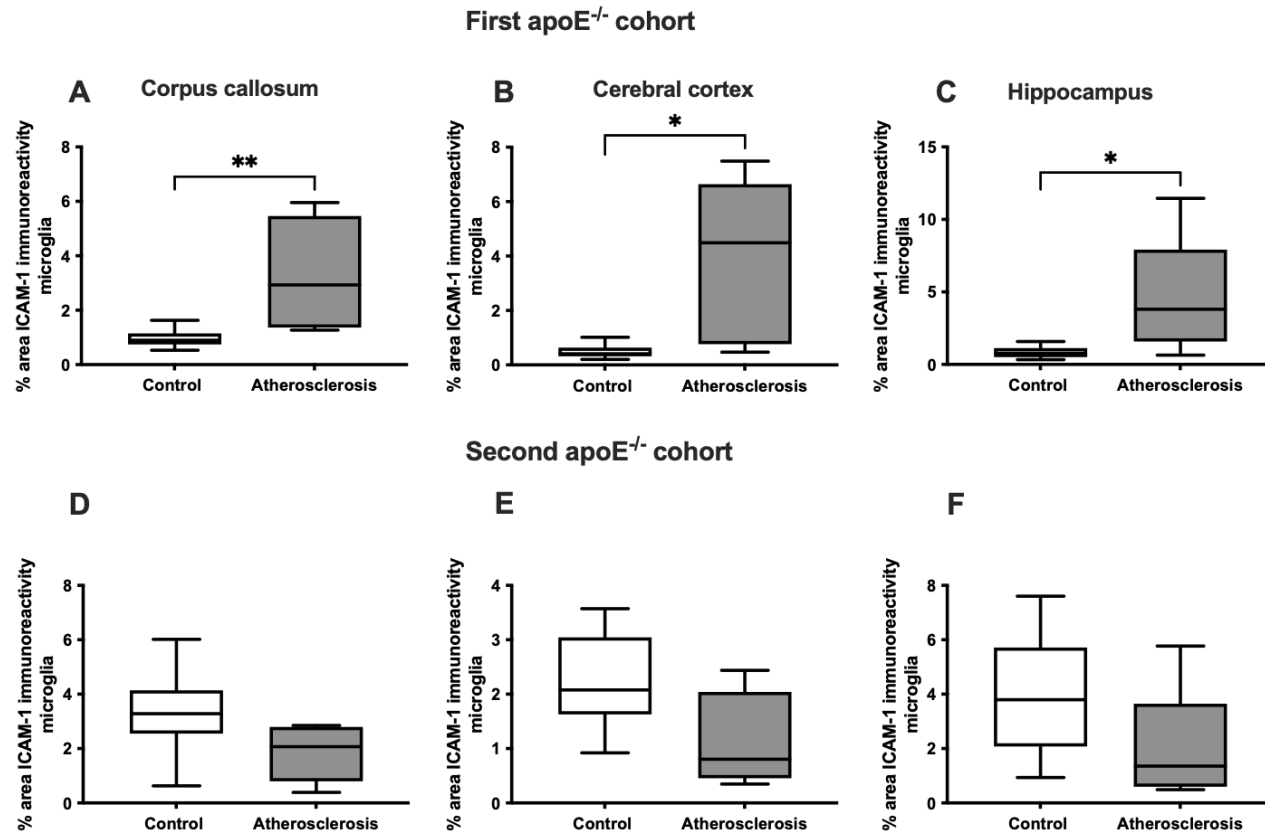


Figure 3.33. Increased percentage (%) area of microglia ICAM-1 immunoreactivity the corpus callosum, cerebral cortex and hippocampus of atherosclerotic cohort 1 *ApoE^{-/-}* mice compared to controls

ICAM-1 expression in the microglia was increased in the corpus callosum (A), cerebral cortex (B) and hippocampus (C) of cohort 1 of atherosclerotic mice compared to controls. Cohort 2 (D-F) showed an opposite, not statistically significant, trend with the endothelial cells of controls expressing a higher % of ICAM-1 immunoreactivity than atherosclerotic mice. The statistical differences are marked by an asterisk. (**P<0.01, *P<0.05).

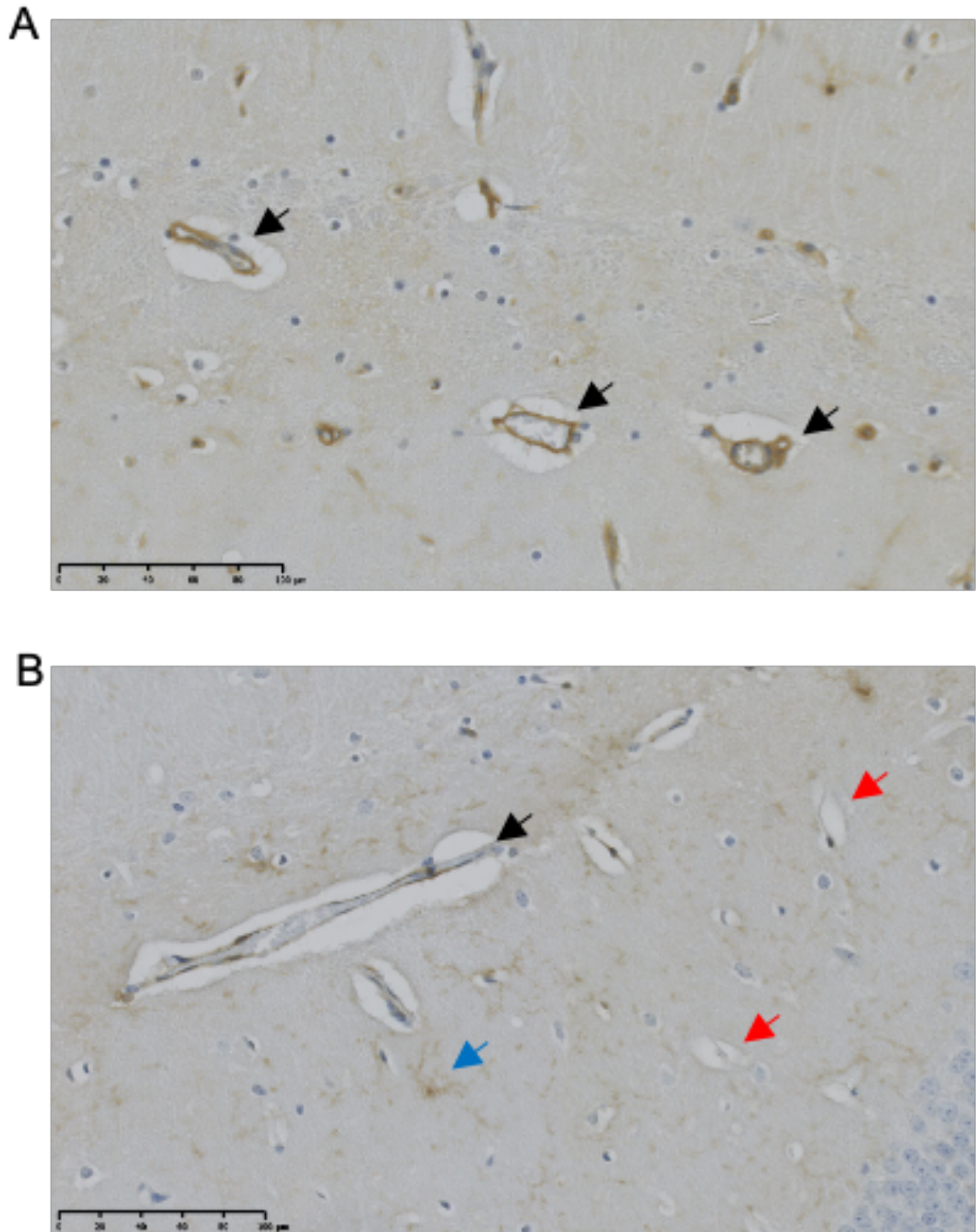


Figure 3.34. Representative image showing pericyte pattern of staining using PDGFR- β revealed different patterns of immunoreactivity between experiments

Representative pictures of scanned slides of PDGFR- β^+ cells in the hippocampus of a same control case. PDGFR- β immunoreactivity was observed surrounding the blood vessels (black arrows) (A) showing a stronger signal compared to later replication (B) of staining. Not all blood vessels showed PDGFR- β immunoreactivity (red arrows) and there was evidence of PDGFR- β^+ resembling microglia (blue arrow). Scale bar of images is 100 μ m.

3.3.9 Summary of *ApoE*^{-/-} control and atherosclerotic mice characterisation

- Microglia % area of IBA-1 and ICAM-1 immunoreactivity was increased in the hippocampus, cerebral cortex and corpus callosum of atherosclerotic mice compared to controls only on cohort 1 mice.
- Astrocytes % area of GFAP immunoreactivity was higher in the corpus callosum of atherosclerotic mice compared to controls only on cohort 1 mice.
- Endothelial cell % area of ICAM-1 immunoreactivity was higher in the corpus callosum of atherosclerotic mice compared to controls in cohort on cohort 1 mice.
- Evidence of co-localization of ICAM-1 and IBA-1 in microglial cells.
- *ApoE*^{-/-} cohort 2 mice, which intended to replicate the results from cohort 1 *ApoE*^{-/-} mice and conduct transcriptomic studies, presented a different pattern of staining with no significance found in IBA-1, GFAP and ICAM-1 markers.

3.4 Discussion

The purpose of this study was to evaluate neuroinflammation in the well characterised atherosclerotic *ApoE*^{-/-} model, which does not present with vessel occlusion or thrombus, in order to determine whether systemic atherosclerosis is associated with remote effects on the brain NVU. This research demonstrates that increased neuroinflammation is a feature of atherosclerotic *ApoE*^{-/-} mice, as evidenced by increased microglial expression of IBA-1 and ICAM-1 in the corpus callosum, cerebral cortex and hippocampus. This is further supported by increased astrogliosis and endothelial activation in the corpus callosum. This well characterised model of atherosclerosis develops spontaneous atheromatous vascular lesions at an accelerated rate, suggesting that any neuroinflammatory response may be related to chronic systemic inflammation or may be driven by metabolic disruption. In addition this study also highlights the importance of reproducibility and replicability in animal research as different cohorts of the same model showed inconsistent findings.

3.4.1 Regional variation in cell activation across atherosclerotic and control mice

The function of glia is highly diverse and dependent on countless factors, such as their neuroanatomical localisation (Miller, 2018). The heterogeneity within specific cell populations indicates how they perform different functions even in the same brain region such as in the different layers of the cortex or the hippocampus. Regional variation in the expression of microglia, astrocyte and endothelial cell markers was observed throughout this study.

Astrocytes and microglia show phenotypical heterogeneity across different regions of the CNS with varying density across brain areas. In wild type mice, previous

immunohistochemical analysis showed microglia and CNS macrophage density to be higher in the hippocampus, basal ganglia and substantia nigra; lower in the cerebellum and fibre tracts; and average in the cerebral cortex, thalamus and hypothalamus (Lawson et al., 1990). The regional heterogeneity was also observed in adult human brains, with higher number of MHCII and CD68 cells in the WM compared to the cerebral grey matter (Mittelbronn et al., 2001). In support of these findings the current study demonstrates microglial heterogeneity, specifically the corpus callosum demonstrated a higher number of IBA-1 immunoreactive microglia than in the cerebral cortex of control mice, however atherosclerotic mice results showed a higher % of IBA-1 active microglia in the cortex than in the corpus callosum.

Microglia plasticity and heterogeneity allows for rapid changes in their morphology and gene expression to react on demand to potential surrounding alterations (Matejuk and Ransohoff, 2020). New transcriptional data in mice indicate a low number of subclasses under homeostatic conditions with high homogeneity, whereas during pathology microglia subtype specification emerges in a region- and disease-stage-specific manner (Lawson et al., 1990). Different microglial clusters with distinct gene expressional profiles have been shown in the cortex of AD and in the whole brain of systemic inflammation mouse models (Sousa et al., 2018). The disease associated microglia (DAM) in an AD model presented high expression levels of *Lpl* (encoding lipoprotein lipase) and *ApoE* in microglia surrounding A β plaques in the cerebral cortex (Duncombe et al., 2017). Furthermore, microglial transition from their homeostatic state to DAM is TREM2 independent while further activation requires TREM2 signalling. On the other hand, microglia from mice mimicking systemic inflammation through peripheral lipopolysaccharide (LPS) injection showed reduced TREM2 (Sousa

et al., 2018). These data suggest complex mechanisms facilitating microglial diversity which should be further investigated in the current model.

Astrocytes were originally described as fibrous and protoplasmic depending on their location in white or grey matter respectively (Andriezen, 1893). Since then, categorisation of astrocytes into different subsets is based on morphologic and molecular characteristics (Matias et al., 2019). Astrocytes in the murine cortex, hippocampus and striatum present transcriptomic profiles that change in an age and region-dependent manner (Clarke et al., 2018). The striatum and hippocampus, areas highly prone to neurodegeneration, display the highest level of diversity. In support, the current study performed on both *ApoE*^{-/-} mouse cohorts showed regional variation in the expression patterns of GFAP between regions. Furthermore, this regional immunoreactive profile was similar between control and atherosclerotic mice in both GFAP analyses.

The vascular supply to different brain regions is also heterogeneous, and large differences in capillary density exist between the cortex and WM. The higher capillary density in the cortex may relate to the higher metabolic demand of neuronal cell bodies and synapses compared to axons (Cavaglia et al., 2001). As with astrocytes, the vascular structures of some brain regions might be more vulnerable to inflammation and stroke than others. In the current study, increased expression of ICAM-1⁺ blood vessels in the cerebral cortex may impact glial cells and consequently neurons. TLR-4 has been shown to activate ICAM-1 and contribute to the inflammatory phenotype of endothelial cells through activation of TLR-4/myeloid differential protein-88 (MyD-88)/nuclear factor- κ B (NF- κ B) pathway (Lee K.M. et al., 2015; Seok et al., 2015). Endogenous ligands of TLR-4 such as oxidized low-density lipoprotein or ROS (Yang et al., 2005). If there is consistency observed between cohort 1 and future mouse

models the elevated levels of ROS such as observed in atherosclerosis increase the activation of NF- κ B which targets genes of pro-inflammatory cytokines (IL-6, IL-1 β ,) associated with microglia and astrocyte reactivity. It also promotes the release of ROS exacerbating the oxidative stress of endothelial cells.

The selective vulnerability of neuronal populations has been reported in the entorhinal cortex, subiculum and CA-1 region of the hippocampus in AD brains, and WM astrocytes are especially sensitive to ischaemic stroke, demonstrating that specific brain regions or group of cells are more vulnerable to an imbalance CNS environment than others (Chen et al., 2016; Stranahan and Mattson, 2010). Despite the observed heterogeneity in the expression of the investigated cellular markers, a general increase expression of inflammatory markers was observed in *ApoE*^{-/-} atherosclerotic mice from cohort 1.

3.4.2 Increased expression of IBA-1 and ICAM-1 by microglia is a feature of murine atherosclerosis (cohort 1).

Microglial surveillance of the CNS allows for their rapid response to local injury, and these resident brain macrophages are the main form of immune defence in the CNS. The role of microglia as an immune cell is demonstrated by their capability to express cytokines/chemokines depending on their interactions with other cells and the environment (Jeong et al., 2013). The current study examined the expression of IBA-1, which is implicated in microglial motility, and demonstrate significantly higher levels of IBA1 expression in the *ApoE*^{-/-} model. These findings, if consistently observed, corroborate the results from previous studies characterising a damage associated microglial morphology in the striatum, cerebral cortex, hypothalamus and meninges of *ApoE*^{-/-} mice which similarly demonstrate increased IBA-1 immunoreactivity compared

to controls (Denes et al., 2012). As microglia have an essential role in immune response, the IBA-1-associated increase in motility observed in the atherosclerotic mice may indicate a neuroinflammatory response in the absence of stroke. Whether this response is neurotoxic or neuroprotective is unknown.

The observed microglia morphology (small cell body with thin and elongated processes) in this study, which was not quantified, is associated with anti-inflammatory microglia. Anti-inflammatory microglia with a morphology of ramified and elongated processes is also known as M2 type, further analysis should include markers to determine if the microglia observed in these microglia also present proteins associated with M2 or M1 microglia phenotype (Gomes-Leal, 2019). Lou et al., (2016), demonstrated the importance of motility for neuroprotective microglia in BBB repair by showing the immediate accumulation of microglial processes closing a laser-injured capillary. In the *ApoE^{-/-}* mouse model the expression of IBA-1 was widespread across all brain areas, not confined to the vessels which could indicate the observed neuroinflammation was not related to BBB damage. Microglia behaviour can be regulated by neuronal activity, such as increased motility observed at increased neuronal activity. The response of microglia is thought to be regulated by neurotransmitter as microglial processes increased physical contact with neurons (Fontainhas et al., 2011). In order to investigate the increase motility of microglial cells in relation to BBB repair and neuronal signalling future studies could examine the expression pattern of P2RY12 in microglia in addition to vascular and neuronal markers, as it could reveal an aggregation of dense processes surrounding vessels in an attempt to close a leakage of the BBB or in close proximity to neurons.

Apolipoprotein E^{-/-} mice fed with a Paigen diet (containing more cholesterol and cholate than the Western diet) showed a similar microglial morphology to the present study but

was associated with an increase in the production of interleukin-1 and other pro-inflammatory cytokines, commonly associated with the M1 type, pro-inflammatory microglia involved in neurodegeneration (Denes et al., 2012). This evidence suggests that microglia could act as neuroinflammatory intermediaries between excess lipids and neurodegeneration. The deposition of lipids in microglia induces the release of proinflammatory cytokines and oxidative stress, contributing to the inflammatory environment in the CNS, causing further dysfunction to the BBB resulting in neuronal damage (Coltman et al., 2011; Marschallinger et al., 2020). Furthermore, hypercholesterolaemia facilitates the accumulation of ROS and atherosclerosis clinically associates with the generation of ROS mediated by nicotinamide adenine dinucleotide phosphate (NADPH) oxidases (NOX). NOX produces free radicals and is a major contributor to oxidative stress in neurological disorders. Although known to regulate neuronal signalling and memory processing, the overproduction of NOX contributes to neurotoxicity and has a crucial impact in chronic CNS degeneration, such as, AD, MS, PD, stroke, and cerebrovascular diseases (Barua et al., 2019)

Increased levels of ICAM-1 immunopositive microglia was also a feature in all brain areas of atherosclerotic mice from cohort 1. Although ICAM-1 is known to be expressed by vascular cells, studies in rodents have shown the presence of membrane-bound and soluble ICAM-1 in microglia, which is associated with their role in the neuroinflammatory response (Colton and Wilcock, 2010; Imamura et al., 2003). Microglial expression of adhesion molecules, such as ICAM-1, might be able to regulate T-cell migration and activation by delivering co-stimulatory signals through their ligands on lymphocytes or increasing the affinity of cell–cell interactions (Francesca et al., 2000). It has also been suggested that microglia protrude through the endothelial cells as a mechanism for T-cell recruitment into the CNS which could

potentially damage the BBB and lead to the accumulation of plasma proteins (Engelhardt et al., 1997). These changes were observed on cohort 1 mice therefore these results need to be replicated to be able to draw relevant conclusions.

A post-mortem study of capillary cerebral amyloid angiopathy, a vessel disease associated with the accumulation of A β , showed evidence of NADPH oxidase-2 (NOX2)-positive activated microglia engulfing the affected capillaries causing major changes to the expression of occludin, ZO-1 and claudin-5 (tight-junction proteins) and disrupting the BBB (Carrano et al., 2012). The increased lipid deposition observed in hypercholesterolemia and atherosclerosis could potentially lead to a similar microglia activation and BBB damage.

The increased expression of IBA-1 and ICAM-1 by microglia in atherosclerotic mice may be an early indicator of microglial activation in response to disturbances in brain homeostasis and suggests a role for microglia in the progression of cerebrovascular dysfunction. However, the current study did not determine the microglia subtypes present in the ApoE^{-/-} mouse brain and these conclusions are drawn from the results obtained from cohort 1. Further research is necessary to determine if the activation of these microglia is aiding in repair and should investigate the presence of anti-inflammatory molecules and genes in microglia such as neurotrophins (nerve growth factor gene family) or norepinephrine. Furthermore, IBA-1 is known to be present in CNS macrophages in lower quantities, therefore the use of IBA-1 in combination with additional specific microglial markers such as TMEM119 to obtain data on more of the microglia population. The P2Y₁₂ microglia marker is highly expressed in processes encompassing capillaries and aids with the repair of the BBB. In mouse models of AD, its expression is reduced, suggesting a decrease of microglia neuroprotective function, as microglia are less responsive towards neuronal injury a possible indicator of

neurodegeneration (Haynes et al., 2006; Keren-Shaul et al., 2017; Li et al., 2020) The elevated expression of ICAM-1 in microglia should be investigated in relation to microphage infiltration and BBB damage because it was not investigated in detail in this research (Section 3.3.1).

3.4.3 Increased endothelial cell activation and astrogliosis in the corpus callosum of murine atherosclerosis (cohort 1).

Endothelial cells

Constitutively low levels of ICAM-1 are predominantly expressed by endothelial cells, but have also been demonstrated in glial cells where the upregulation of this glycoprotein indicates cytokine activation (Greenwood et al., 2011). Increased expression of VCAM-1 and accumulation of leukocytes has previously been shown in the striatum of the *ApoE*^{-/-} model fed with either a Paigen diet or a Western diet (Section 2.3) (Denes et al., 2012). Furthermore, VCAM-1 expression in Western diet mice is significantly lower than Paigen diet (more cholesterol and cholate) mice, but it should be noted that in this report this finding was not compared to any control mice. The upregulation of ICAM-1 in the corpus callosum of *ApoE*^{-/-} mice fed with a western diet has not been previously studied and the current study is the first to demonstrate an increased expression of ICAM-1 in the blood vessels of atherosclerotic mice compared to controls in this brain area. It should be noted that cohort 2 showed a trend in the opposite direction in all the brain areas examined.

Endothelial dysfunction is a feature of atherosclerosis and ICAM-1 has been implicated in the activation of several proinflammatory signalling cascades and might directly contribute to the neuroinflammatory response (Habas and Shang, 2018). ICAM-1⁺ endothelial cells are possible sites of leukocyte extravasation in atherosclerosis (Sluiter

et al., 2021). It has been hypothesised that there is an initial response where T-cells extravasate into the brain parenchyma via the interaction of leukocyte integrins (LFA1) with endothelial adhesion molecules such as VCAM-1 and ICAM-1 (Devine et al., 1996). The recruitment of regulatory T cells into the CNS is crucial for re-establishing homeostasis and dampening neuroinflammation. The current study did not observe infiltrating T cells in the brain of the *ApoE^{-/-}* model, however it should be noted that this was based on H&E staining. Future immunohistological studies using specific T cell markers, such as CD4 or CD3, are required to confirm this observation.

It has been suggested that areas of diffuse ICAM-1 immunopositive staining surrounding blood vessels in *ApoE^{-/-}* mice when fed on a normal diet may also reflect dysfunction of the BBB (Kitagawa et al., 2002). Loss of BBB integrity and subsequent extracellular accumulation of fluid and extravasations of serum proteins (vasogenic oedema) are a common consequence of ischaemia and prolonged hypoperfusion (Yang et al., 2019). Although *ApoE^{-/-}* mice do not develop plaque rupture, the observed inflammation could be a consequence of reduce cerebral blood flow due to narrowing of the arteries providing cerebral circulation. Endothelial cells could potentially be damaged by the inflammatory environment caused through atherosclerosis which would disrupt the CNS and potentially lead to hypoxia (Steyers and Miller, 2014). Cerebral small vessel disease is associated with damaged to the capillaries, more specifically in the WM; inflammation could be a consequence of reduced cerebral blood. Age-associated WM lesions are associated with the reduce information processing speed probably caused by vascular insufficiency and hypoxia, increased of inflammatory markers such as MHCII, CD86, CD68 represent the attempt to prevent lesion formation (Al-Mashhadi et al., 2015; Fadul et al., 2020). Also, levels of intracellular adhesion molecule serum levels are increased in patients with WM lesions

which has been correlated with cell-surface ICAM-1 expression suggesting an upregulation of ICAM-1 in the brain indicating vascular inflammation and pathology (De Leeuw et al., 2002).

Astrocytes

Astrocytes have a major role in cerebrovascular disease as they surround the majority of brain blood vessels with their processes. They control blood–brain barrier permeability and neurovascular coupling, maintaining extracellular homeostasis and making CBF respond timely to neuronal activity (Matias et al., 2019). Astrocytes are located between neurons and endothelial cells and are considered to be crucial in the process of neuronal damage caused by vascular factors.

Brain diseases are characterized by the active inflammatory state of the astrocytes, which is usually described as astrogliosis (Perez-Nievas and Serrano-Pozo, 2018). The present investigation revealed an increased number of GFAP⁺ astrocytes in the corpus callosum of *ApoE*^{-/-} mice from cohort 1 and a cellular morphology resembling astrogliosis. Atherosclerosis is considered a risk factor for vascular dementia due to its relation to ischaemic stroke. These results suggest that the reactive astrocytes present in atherosclerotic mice could be a response to microglia or endothelial cell signalling, disruption of the lipid homeostasis, an indication of early BBB dysfunction or be related to hypercholesterolaemia.

Reactive astrocytes are involved in multiple neurodegenerative disorder and are a commonality of neuroinflammatory processes. The anti-inflammatory (A2) and pro-inflammatory (A1) subtypes of reactive astrocytes are stimulus-specific and distinguished through their transcriptomic profile as they both present similar morphology and cannot be distinguished using GFAP (Sarkar and Biswas, 2021).

A2 is characterised by upregulated expression of anti-inflammatory genes include cytokines (S100 calcium-binding protein a10 (s100a10) IL-6, leukaemia inhibitory factor (LIF) and transglutaminase 1) and neurotrophic factors (Arginase-1 and nuclear factor erythroid 2-related factor 2) (Liddelow and Barres, 2017). A1 phenotype in astrocytes can be triggered by essential cytokines such as TNF- α , IL-1 α and C1q leading to the activation of the NF- κ B pro-inflammatory pathways and genes encoding pro-inflammatory cytokines (Liddelow et al., 2017). These cytokines are commonly involved in the recruitment of immune cells.

During brain injury in mice, microglia regulate the astrocytic response through the releases of cytokines. Microglial release of IL-1 β , TNF- α , and IL-6 cytokines lowers astrocyte P2Y1 receptor to enable tissue remodelling and repair of the CNS, whereas IL-1 α , TNF- α and complement factor Cq1, induces a neurotoxic state in astrocytes associated with A1 subtype (Liddelow et al., 2017). Appropriate astrocyte-microglia cross-talk in disease is necessary for astrocytes to support neuronal survival and function after acute injury. Research in mice suggests that microglia respond first by recruiting other microglia to the site of damage to phagocytose cell and debris. Later this is followed by the activation of astrocytes-microglia crosstalk resulting in the release of inflammatory mediators to recruit macrophages to the site of injury (Matejuk and Ransohoff, 2020).

Cerebrovascular endothelial cell dysfunction activates astrocytes through multiple pathways. Inflamed endothelial cells promote astrogliosis through secretion of vascular endothelial growth factor-1 (VEGF-1). Activated astrocytes are the main source of VEGF in the brain, while the initial activation is provoked by the secretion of VEGF from endothelial cells in inflammation (Mani et al., 2005). The deposition of fibrinogen is associated with a wide range of neurological diseases, but it is only known to occur

if the tight junction proteins in the endothelial cells are disrupted. The damage to tight junction proteins results in leukocytes infiltrating the brain which has been shown to occur in *ApoE^{-/-}* mice with Paigen diet, which would release of TNF- α and IL-1 β triggering astrogliosis (Cui et al., 2011). However, leukocyte infiltration was not observed with H&E staining on this project. Fibrinogen deposition is found in patients with brain small vessel disease, exhibiting a significant positive correlation with an increased risk of dementia (Bridges et al., 2014; Chen A. et al., 2016; Hainsworth et al., 2017).

In the vascular contributions to cognitive impairment and dementia pathologies (VCID) mouse model astrocytic end-feet surrounding blood vessels were reduced but not as a consequence of reduced vessel density. This suggests that the presence of neuroinflammation and blood–brain barrier breakdown, culminating in microhaemorrhages, leads to astrocyte end-feet disruption, which is likely to have significant implications for astrocyte reactivity and neurovascular coupling (Price et al., 2018). Individuals with VD, AD and mixed dementia are reported to have clasmatodendritic astrocytes in WM lesions (Tachibana et al., 2019). These astrocytes are characterised by large swollen bodies and processes having a beaded appearance due to their disintegration and are attributed to hypoxia, ischaemia, and BBB leakage and extravasated serum proteins taken up by glia. The morphological changes in clasmatodendritic astrocytes are an attribute of irreversibly injured astrocytes but their pathophysiological significance remains to be elucidated. This pattern of staining was not observed in the current *ApoE^{-/-}* model cohorts but clasmatodendrosis has been reported in the corpus callosum of mice during chronic cerebral hypoperfusion (Hase et al., 2017).

Previous studies have shown leukocyte infiltration, hardening of vessels and probable atherosclerotic plaques in large cerebral vessels in the *ApoE^{-/-}* model (Moore and Tabas, 2011). The atherosclerotic plaques narrowing the lumen of cerebral arteries could lead to reduced levels of oxygen available to the brain. The resultant energy depletion in neurons leads to the release of glutamate which induces rapid reduction of ATP levels in neurons, but it should be noted that astrocytes are particularly susceptible to glutamate cytotoxicity. Based on the observations of cohort 1 stained with H&E no inflammatory aggregates were detected, but previous studies using *ApoE^{-/-}* mice by Drake et al. (2011) has shown leukocyte aggregation in the choroid plexus of the ventricular space. The mice were from previous study were 18 months of age while the mice used for this study were 6 months old, suggesting that the inflammatory changes observed in the current study appear before the formation of spontaneous atherosclerotic plaques in major cerebral vessels. Future longitudinal studies using a comprehensive panel of markers and investigating the hardening and dilation of the cerebral vessels are required to reveal more information.

Astrocytes have an array of diverse functions, including ion buffering, cholesterol synthesis and immune signalling (Abbott et al., 2006; Halliday et al., 2016; Pekny and Nilsson, 2005). Through Ca^{2+} signals, astrocytes can induce and drive the progression of the inflammatory state in the CNS. They contribute to the altered neuronal activity in several neurodegenerative pathologies and are therefore, considered key mediators of cognitive impairment (Liu et al., 2020). Current research revealed intracellular brain lipid accumulation is associated with astrocyte activation, and involves APOE. This concurs with the essential role of astrocytes in CNS lipid deposition. APOE binds to HDL-like lipoproteins and redistributes lipids in the CNS. Astrocytes are the largest producers of ApoE and therefore astrocyte dysfunction could exacerbate

neuroinflammation. In humans, the APOE4 variant is associated with AD (Riddell et al., 2008). Human stem cell-derived APOE4 astrocytes show impaired endocytosis of lipids and amyloid with a compromised cholesterol efflux. *In vitro* experiments on human astrocytes presenting tau hyperphosphorylation and abnormalities associated with neuronal toxicity, also demonstrated a disruption in their cholesterol metabolism (van der Kant et al., 2019). The disruption of lipid homeostasis in macrophages could exacerbate systemic inflammation and further lipid deposition in astrocytes. Markers for astrocyte activation such as an upregulation of GFAP, oxidative stress or oxidation of fatty-acids might be associated with the accumulation of lipids in astrocytes (Wyss et al., 2011; Fernandez et al., 2019). Additionally, these changes could contribute to endothelial cells activation that disturb the blood-brain barrier (BBB).

The dysfunction of the BBB leaves WM, such as in the corpus callosum, vulnerable, as a loss of lipid components and demyelination have been demonstrated in chronic cerebral damage (Moroni et al., 2018). A compromised BBB may allow the entry of macromolecules such as proteases, immunoglobulins, leukocytes, monocytes, and cytokines into the parenchyma. These serum components may have deleterious effects on the WM myelin directly in addition to activating the phagocytotic properties of microglia (Silberberg et al., 1984). Unrepaired BBB damage could lead to clasmatodendritic astrocytes, which entail a loss of the normal functions of the astrocytes meaning damage to the integrity of the neurovascular unit or absorption/production of cholesterol. Furthermore, it has been proposed that clasmatodendritic cells gain a toxic function further contributing to neuroinflammation (Perez-Nievas and Serrano-Pozo, 2018). WM pallor is associated with disruption of the neurovascular unit and dysfunction of the BBB. The use of LFB on cohort 1 mice showed no evidence of WM pallor, but the increased expression of ICAM-1 in the

endothelial cells of the corpus callosum could be linked to BBB dysfunction. Future studies should be conducted to investigate a comprehensive panel of markers associated with BBB dysfunction, including tight junction proteins (such as OCC-1 which was not successfully optimised for this study, Appendix III) and serum protein accumulation (fibrinogen, albumin).

The inflammatory mechanisms mentioned in this section have been linked to the pathogenesis of dementia and cognitive impairment and are known to increase with age. Increasing evidence suggests that systemic and local neuroinflammation significantly contributes to cerebral SVD, VD and AD. One hypothesis is that chronic systemic inflammation modulates neuroinflammation, leading to degeneration of myelinated fibers. This may not only cause progressive WM damage, but may foster the onset of inflammatory processes.

3.4.4 Limitations and future immunohistochemical studies

This study relied on immunohistochemistry to examine the expression of a panel of key cell phenotype markers in the *ApoE^{-/-}* mouse model. Although IHC is a reliable and commonly used technique, there are a number of limitations. While well characterised and robust antibodies were used in this study, several issues were encountered during the course of work. The antibodies that did not show the anticipated immunoreactivity profile included monoclonal mouse antibodies which could potentially generate high background staining in mouse sections, but most of these antibodies did not show any specific staining. Although monoclonal antibodies only recognise one single epitope on the antigen in question, making them very specific, they may be less reactive to epitopes in FFPE tissue. Polyclonal antibodies are less reliable as there is batch to batch variability and lesser reproducibility (Kim et al., 2016). Consequently, a limitation to this specificity is the vulnerability of FFPE

tissue losing the single epitope as a result of chemical treatment during fixation or during antigen retrieval resulting in IHC failure (Lipman et al 2005). A major problem was that many of the antibodies had not previously been used in FFPE mouse tissue and were mostly characterised in human or frozen mouse tissue. Frozen mouse sections could be used in the future to investigate if the tested antibodies yield more reliable results, but it should be considered that frozen tissue has poor cellular morphology compared to the well-preserved cellular morphology seen in FFPE sections.

Antibodies are prone to physical and chemical degradation during storage. Epitope binding can be impaired due to aggregation or unfolding of the native form of the antibody. This might be the case for PDGFR- β antibody as the immunostaining was inconsistent and may reflect degradation of the antibody. PDGFR- β has a crucial role in the integrity and functionality of the vasculature, and is expressed by pericytes as well as smooth muscle cells (Ding et al., 2020). In the future, pericyte coverage of capillaries could be examined using periodic acid–Schiff (PAS), α -SMA or COLIV which have been used in previous studies as reliable methods to quantify pericytes (Ding et al., 2020; Geranmayeh et al., 2019; Goodall et al., 2018). Throughout this discussion the investigation into the expression of other cell surface markers is suggested, to elucidate the neuroinflammatory response observed in systemic atherosclerosis. In order to achieve a comprehensive panel of neuroinflammatory markers, future research has to include the expression of an extended panel of markers which will assess different aspects of activation and maturation.

No concordance between *ApoE*^{-/-} mice cohorts

The two mouse cohorts showed different results with the controls in cohort 2 expressing a higher % area of immunohistochemistry than atherosclerotic mice in mouse cohort 1. These findings do not support each other, and it was not possible to investigate these changes in a third mouse cohort. Mice in cohort 2 showed high levels of glial activation in the *ApoE* control mice, which could reflect a response to infection present in the animal house. After the diet change in *ApoE*^{-/-} mice there was a report of Rotavirus or epizootic diarrhoea of infant mice (EDIM), which is highly contagious between mice and causes diarrhoea in infant laboratory mice. Clinical signs are not generally detected in adult mice but rotavirus can alter host physiology in multiple ways and alter results of dietary and nutritional studies (Baker, 1998). Rotavirus can cause symptoms beyond the gastrointestinal tract including neurological changes such as encephalopathy. Furthermore, imbalance of the microbiome has been known to play a role in the development of metabolic syndrome and obesity (Barlow et al., 2015). The microbiome could have been altered as the mice were moved to a different location. The importance of microbiota in the brain lays in their interaction through the endocrine system and hormone secretion. The malfunctioning of such signalling pathways has been associated with the dysregulation of physiological conditions of the CNS and gut microbiota (Fernandez-Real et al., 2015; Labus et al., 2017). Evidence in diabetes research shows gut microbiota can impact brain health through immune influences leading to cerebral endothelial dysfunctions, decreased BBB permeability and upregulated TJ proteins promotes neurovascular damage (Hakim, 2019).

The results observed in cohort 1 might be masked in cohort 2 by the presence of other inflammatory drivers such as infection. Furthermore, the changes observed in cohort 1 are aligned with the literature and support previous studies, suggesting the results

from cohort 1 could be reproduced. The observed neuroinflammatory changes, possibly due to infection, observed in cohort 2 controls are not reflected in the controls could be an indication of microglia in atherosclerotic mice becoming non-responsive becoming unable to present an efficient response to infection. In this instance, the reduced activation of astrocytes could be related to a reduction anti-inflammatory signalling from microglia. The inflammatory response would not be amplified as microglia would not be activated and release IL-1 β which is required to induce astrogliosis leading to the secretion of neuro-toxic factors.

Reproducibility in mouse models

Animal studies have shown that thoroughly planned and well-reported protocols do not automatically guarantee reproducibility as results can vary within laboratories. A simultaneous study across three different laboratories, using the same mouse strain to perform the same experiment yielded remarkably different results (Crabbe et al., 1999). The poor reproducibility was attributed to the influence of many uncontrollable environmental background factors that affected the outcome of the experiment differently such as microbiota, noise and/or stress. The unavoidable variation in animal research could be controlled through implementation of multi-laboratory study designs with the purpose of including heterogeneity within the study population. In particular, by mimicking the inevitably existing between-laboratory variation within one study, the representativeness of the study population is enhanced leading to a highly reproduceable study (Voelkl et al., 2020). As multi-laboratory collaboration are logistically challenging and not yet suitable to replace the broad mass of single-laboratory studies, von Kortzfleisch et al. (2020) suggest that systematic and controlled heterogenisation of experimental conditions within single laboratories also increases the reproducibility of research outcomes in comparison to rigorously standardised

experiments. Such experimental design could potentially help reduce the variable results observed in this study and have potential implications in drug discovery by providing a more accurate representation of the population.

The scientific community is increasingly becoming aware that the lack of reproducibility is a growing issue. A Nature publishing group reported a current 'reproducibility crisis' in science with 90% of the interviewed researchers agreeing with this statement (Baker, 2016). Systemic replication fails at an alarming extent with studies estimating that about 50–90% of the published findings are in fact irreproducible (von Kortzfleisch et al., 2020).

The current lack of reproducibility is a growing issue, and efforts have already been made to facilitate replication research, such as establishing conference tracks and journals focusing on publishing replication studies and providing guidelines on how and why to conduct replication research. However effective change will not occur if the perception of replication research remains to be described as mundane (Brendel et al., 2020).

3.4.5 Conclusion

Neuroinflammation, astrogliosis and increased endothelial cell activation in the corpus callosum in *ApoE*^{-/-} mice suggest that systemic atherosclerosis has a direct effect on the CNS regardless of vascular occlusion and ischaemia. These results support the hypothesis that *ApoE*^{-/-} associated systemic inflammation can modulate neuroinflammation, leading to a 'predisposed' inflammatory environment in the brain. Without further examination of the transcriptomic profile of the evaluated cells or investigation of alternative biomarkers, determining the atherosclerotic mechanisms driving neuroinflammation remains challenging. Deciphering the driver of neuroinflammation in systemic atherosclerosis is fundamentally important as it could potentially elucidate therapeutic targets for vascular dementia. One of the proposed mechanisms driving neuroinflammation is malfunction of the cholesterol metabolism driven by ApoE, resulting in accumulation of cholesterol causing chronic neuroinflammation in astrocytes, microglia and endothelial cells. Furthermore, the vulnerability of WM to inflammation is demonstrated by each of the cellular markers used in this study which concurs with the damage in the WM of SVD. The results from this study also highlight the importance of experimental reproducibility and replication in animal models, increased environmental heterogeneity could lead to more reproducible results. Overall, central nervous system inflammation is observed in response to peripheral disease and may itself contribute to the development of vascular diseases and neurodegeneration.

**CHAPTER IV: NEUROINFLAMMATION IN PROPROTEIN
CONVERTASE SUBTILISIN/KEXIN TYPE 9 OVER
EXPRESSING ADENO-ASSOCIATED VIRUS MOUSE
MODEL**

4.1 Introduction

Genetically modified mouse model, *ApoE*^{-/-} is commonly used in the study of atherosclerosis because of the relative ease to induce a broad metabolic dysregulation by feeding mice a high-fat diet (Cheng et al., 2018; Kumar et al., 2017; Zhong et al., 2009). However, the most recent PCSK9 induced mouse model a single dose of AAV PCSK9DY in C57BLJ/6J causes atherosclerosis in mice (Abifadel et al., 2003). Both PCSK9 and APOE directly interact with LDLr and APOE-receptor (ApoER2), however PCSK9 prevents the natural recycling of LDL cholesterol by targeting LDLr for disintegration in the lysosome while ApoE transports cholesterol into the cells through LDLr (Martins et al., 2006; Shapiro and Fazio, 2017).

Unlike the *ApoE*^{-/-} mouse model, PCSK9 induced mice fed with a normal chow diet do not develop atherosclerosis but have shown to present ~700 mg/dL of plasma cholesterol, which is higher than the levels of plasma cholesterol in *ApoE*^{-/-} mice fed a normal diet (400 - 600 mg/dL). Fed with a Western diet, PCSK9 induced mice is a milder model of atherosclerosis and has lower plasma cholesterol (<1000 mg/dL) than *ApoE*^{-/-} mice (1000 mg/dL) (Oppi et al., 2019). Additionally, the PCSK9 induced mouse model expresses normal levels of APOE and has no genetic modifications. Therefore, the PCSK9 induced mouse model enables the assessment of the impact of atherosclerosis on the neurovascular unit without the strong influence of inflammatory processes associated with the *ApoE*^{-/-} model. This is due to the role of APOE in the inhibition of lipoprotein proliferation and involvement in clearance of cellular debris and apoptotic cells and inhibit which are important steps during inflammation (Grainger et al., 2004; Hayek et al., 1994; Hui and Basford, 2005). The anti-atherogenic functions of *ApoE* might contribute to the stronger development of atherosclerosis in *ApoE*^{-/-} mice compared to PCSK9 induced and other models.

In humans, the *PCSK9-D374Y* mutation is associated with an increase in cholesterol with concentrations typically exceeding 500mg/dL, where normal levels would be less than 200mg/dL and pathological levels being above 250mg/dL (Abifadel et al., 2003). Furthermore, possession of the *PCSK9D374Y* mutation is associated with genetic hypercholesterolemia, which is a major risk factor for cerebrovascular dementia and Alzheimer's disease. This is further supported by AD patients presenting higher levels of PCSK9 in their CSF (Zimetti et al., 2017). In the CNS PCSK9 is believed to promote neuroinflammation in rats with cardiac ischaemia/reperfusion injury, where the hippocampus displays increased levels of microglia and astrocyte activation which is reduced by adding a PCSK9 inhibitor (Apaijai et al., 2019). Furthermore, the reduction of PCSK9 is only observed in plasma suggesting that systemic inflammation modulates brain inflammation, and may represent a potential mechanism underlying atherosclerosis-induced neuroinflammation.

Since its discovery, PCSK9 has been highly studied as a treatment for atherosclerosis and PCSK9 monoclonal antibodies have been shown to be successful lowering the plasma serum cholesterol levels in patients. However, patients reported cognitive adverse events due to PCSK9 inhibitors. A randomised trial of 1204 patients for 19 months did not find evidence of the treatment being associated with adverse cognitive effects, and longer follow-up studies are being conducted to confirm these results (Adorni et al., 2019; Giugliano et al., 2017). The brains of PCSK9 induced mice fed with a chow diet have mostly been studied in relation to its role in the apoptotic pathway in neurons (Cunningham et al., 2005) but there are few and controversial data on PCSK9 induced mouse models and AD. However, to the best of my knowledge there is no research characterising the cellular changes in the brain of PCSK9 induced mice fed with Chow or Western diet.

4.2 Aims and objectives

To test the hypothesis that the PCSK9 induced mouse model of atherosclerosis will display a similar, but reduced level of neuroinflammation compared to the *ApoE*^{-/-} model in this study. This different mouse model would further elucidate the importance of APOE in atherosclerosis and neuroinflammation. The aim is to investigate the PCSK9 induced mouse model by characterising the changes in the brains of mice fed with a western diet compared to mice fed with a control diet using immunohistochemistry and the same cellular markers used in *apoE*^{-/-} mice. Specifically, this chapter aims to

- Investigate the expression of cell phenotype markers for astrocytes (GFAP), microglia (IBA-1) and vessels (ICAM-1), in the hippocampus, cerebral cortex and corpus callosum.
- Provide a qualitative description of the staining pattern of this panel of markers.
- Compare the pattern of staining and quantitative analysis of the PCSK9 induced mouse model to both cohorts of the *ApoE*^{-/-} mouse model.

4.3 Results

4.3.1 Astrocytic expression of glial fibrillary acidic protein in the proprotein convertase subtilisin/kexin type 9 (PCSK9) induced mouse model

Astrocytes in both control (n= 3) and atherosclerotic (n= 6) mice appeared to present cell bodies of different sizes with visible processes in all areas with a more sparse distribution of GFAP⁺ astrocytes in control mice and the astrocytic cell bodies of atherosclerotic mice appeared larger and swollen compared to controls in all the examined areas. Astrocytic endfeet encompassing blood vessels were easily identifiable in mice fed with either diet in the cerebral cortex and the hippocampus. In the corpus callosum of atherosclerotic mice, the astrocytes processes had a thick appearance in comparison to the controls which appeared to present sparse GFAP⁺ astrocytes with smaller cell bodies with a lower number of thin processes (Figure 4.1). The cerebral cortex of both control and atherosclerotic mice presented radial astrocytic processes throughout the cortex, with a pattern of immunoreactivity looking more intense in atherosclerotic mice than in controls. Astrocytes in atherosclerotic mice had larger cell bodies than controls with thicker processes (Figure 4.2).

The hippocampus showed increased GFAP immunoreactivity in atherosclerotic mice compared to controls. The cell bodies of the astrocytes appear rounded and of similar size in the controls and atherosclerotic mice. However, the processes in the control mice were longer and thinner in a stellate morphology while atherosclerotic mice presented short processes that were non-continuous and there were more fragments GFAP⁺ present giving it a denser appearance (Figure 4.3). However cell morphology was not quantified.

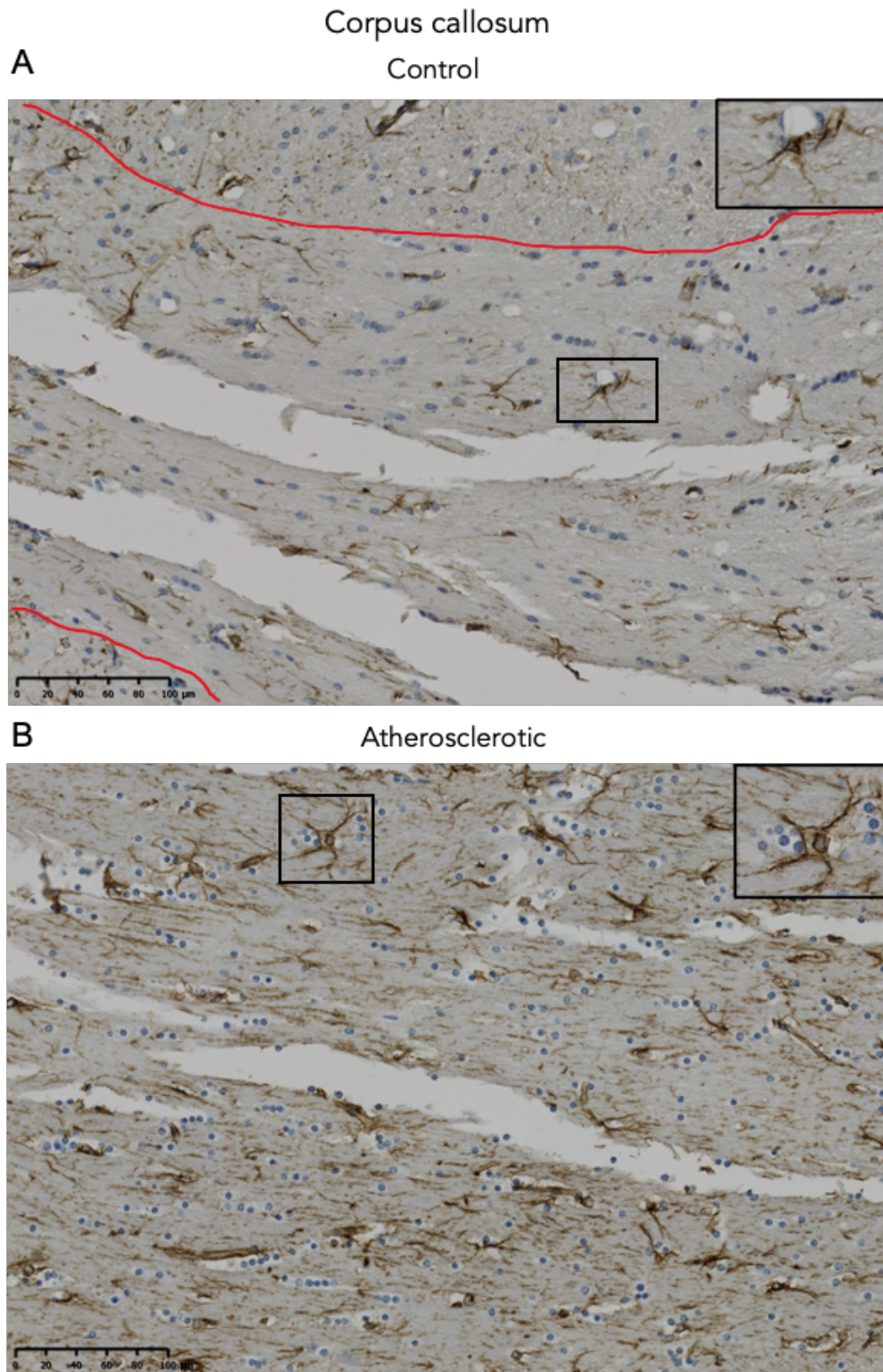


Figure 4.1 Representative image showing astrocyte expression of GFAP immunoreactivity in the corpus callosum of PCSK9 induced mice

GFAP⁺ astrocytes were prominent in the corpus callosum (delimited with red lines), with atherosclerotic mice (B) showing a higher density of GFAP⁺ astrocytes present compared to controls (A). The astrocytes in the controls were thinner and seemed to present less processes than atherosclerotic mice. Control n= 3, Atherosclerotic n= 6. Scale bar represents 100 μ m (20 μ m insert).

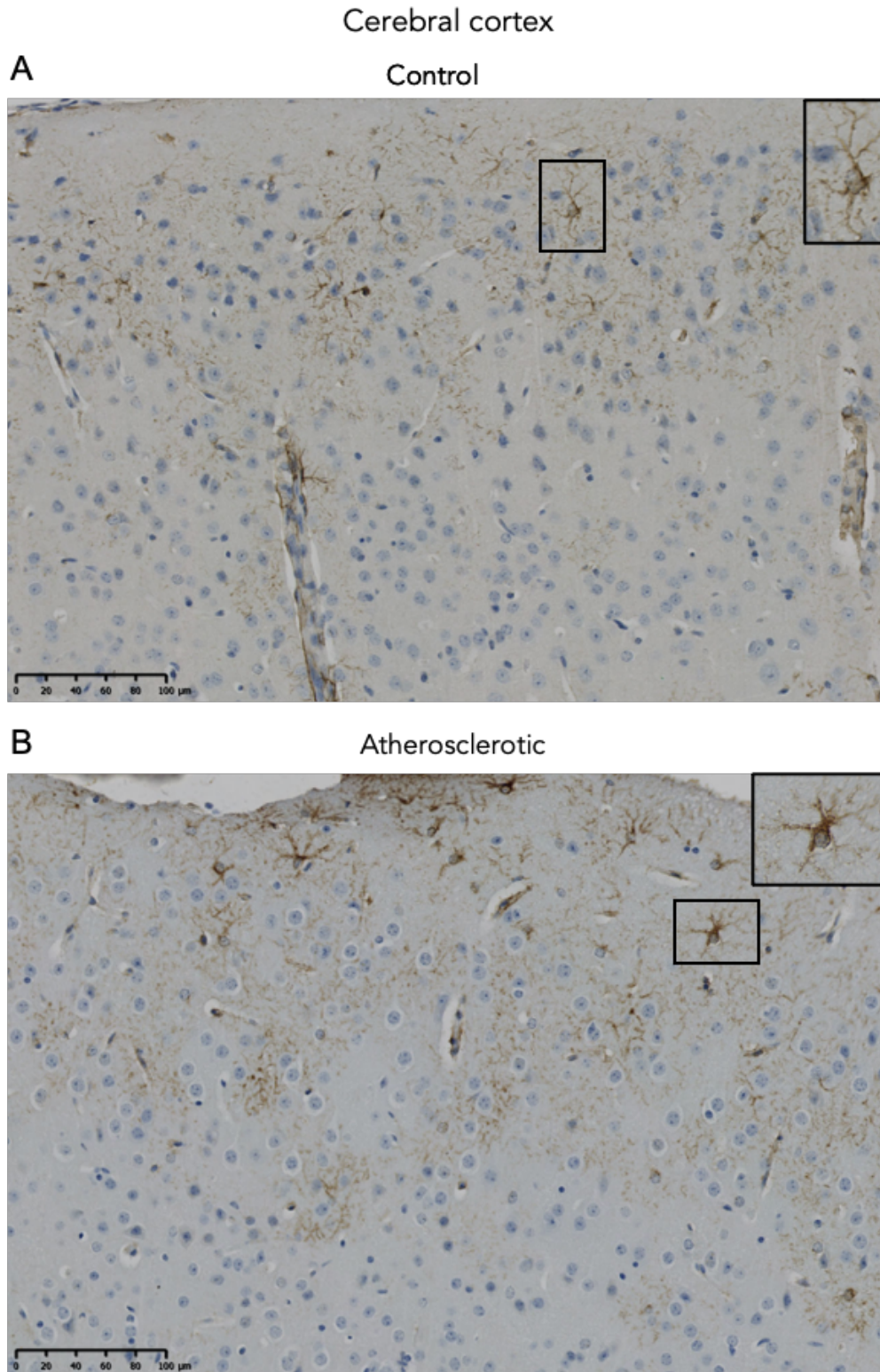


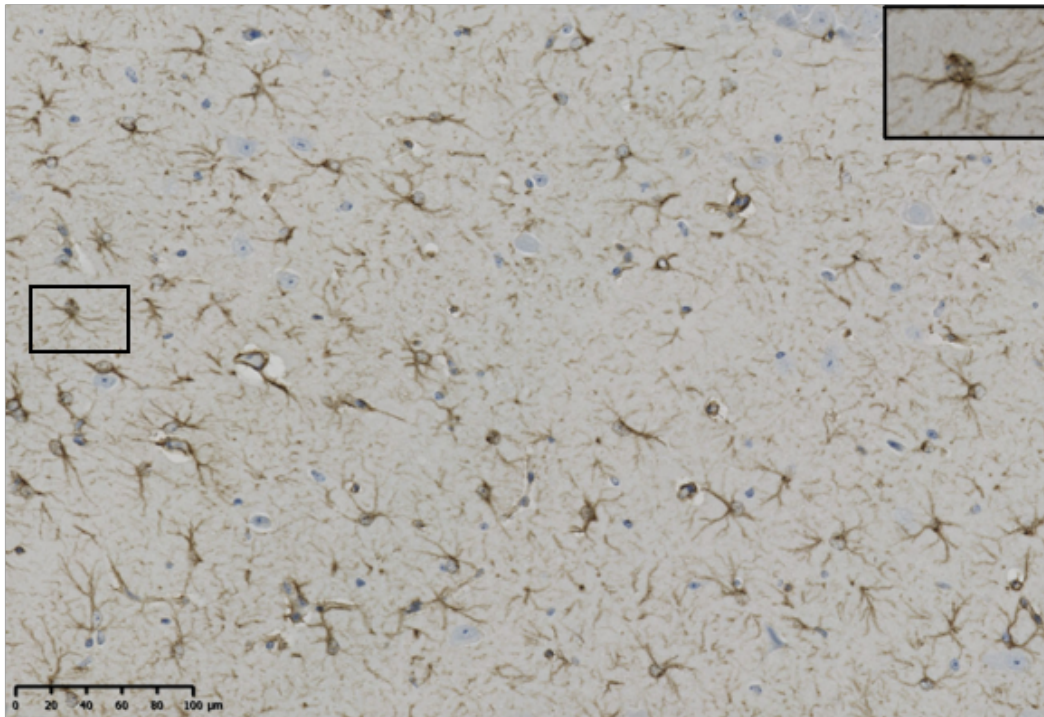
Figure 4.2 Representative image showing astrocyte expression of GFAP immunoreactivity in the cerebral cortex of PCSK9 induced mice

In the cerebral cortex GFAP immunoreactive astrocytes increased towards the more superficial layers of the cortex with sparse astrocytes with thicker processes and enlarged cell bodies in atherosclerotic mice (A) compared to control mice (B). In atherosclerotic mice, astrocytes were more easily distinguished with their individual stellate morphology and shorter processes. Control n= 3, Atherosclerotic n= 6. Scale bar represents 100 μ m (20 μ m insert).

Hippocampus

A

Control



B

Atherosclerotic

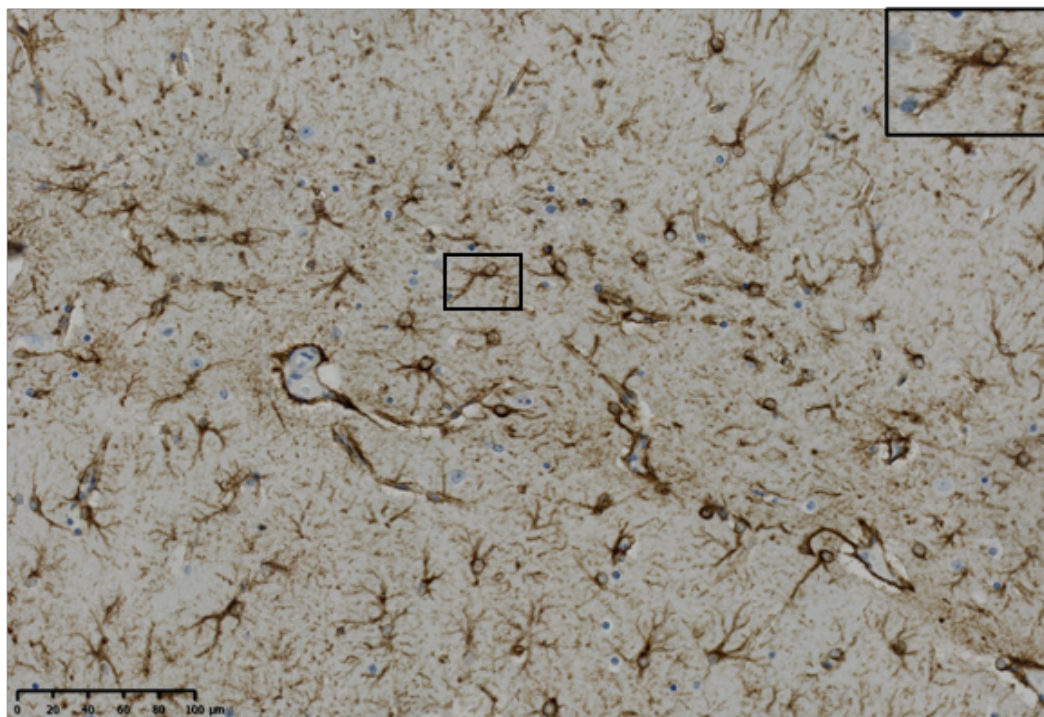


Figure 4.3 Representative image showing astrocyte expression of GFAP immunoreactivity in the hippocampus of PCSK9 induced mice

The hippocampus displaying similar astrocytes cell bodies in the control (A) and atherosclerotic (B) mice. The atherosclerotic mice showed more intense GFAP⁺ astrocytes with shorter and thicker processes. Control n= 3, Atherosclerotic n= 6. Scale bar represents 100 μ m (20 μ m insert).

Quantitative analysis of the % area of GFAP immunoreactivity indicated there was no significant difference in the hippocampus of controls ($M = 12.47$, $SEM = 0.5$) compared to atherosclerotic PCSK9 induced mice ($M = 19.2$, $SEM = 2.0$) ($p = 0.43$). Similarly GFAP immunoreactivity was not significantly different in either the corpus callosum of control ($M = 18.6$, $SEM = 1.8$) and atherosclerotic mice ($M = 23.1$, $SEM = 3.3$) ($p = 0.43$), or and the cerebral cortex (Controls $M = 4.29$, $SEM = 0.6$; Atherosclerosis $M = 9.5$, $SEM = 2.0$, $p < 0.99$) (Figure 4.4).

4.3.2 Expression of ICAM-1 in blood vessels and microglia on PCSK9 induced mouse model of atherosclerosis

Endothelial cells in blood vessels showed a weaker pattern of ICAM-1 immunoreactivity in control PCSK9 induced mice compared to atherosclerotic ones. The morphology of the vessels was conserved across brain areas showing a circular/oval shape or collapsed circle of varied sizes. ICAM-1 immunoreactive blood vessels were not easily recognised by their morphology in the corpus callosum of either control or atherosclerotic mice, but, in both diets (Figure 4.5, ICAM-1⁺ endothelial cells in the cerebral cortex (Figure 4.6) predominantly extended across the cortex and they seemed to be larger than in the corpus callosum and hippocampus. The blood vessels in the hippocampus of PCSK9 induced mice showed some round vessels with a diffuse staining pattern surrounding them. These appeared to have more intense ICAM⁺ immunoreactivity in the atherosclerotic mice compared to controls and seemed smaller than the blood vessels in the cortex (Figure 4.7). However, the morphology was not quantified, only the % area of ICAM-1 immunoreactivity.

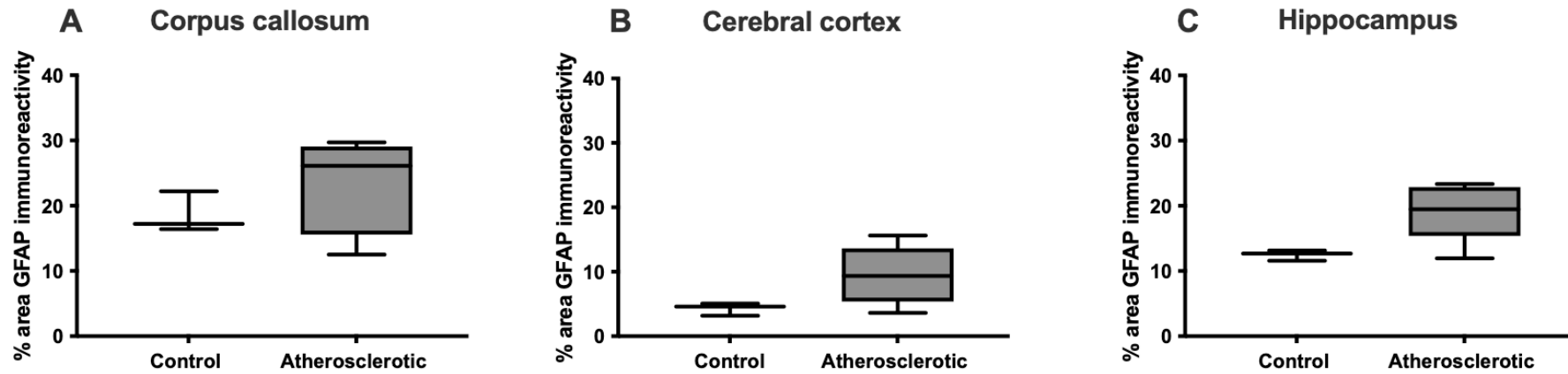


Figure 4.4 Analysis of the percentage (%) area of astrocytes GFAP immunoreactivity the corpus callosum, cerebral cortex and hippocampus of control and atherosclerotic PCSK9 induced mice

The % area GFAP immunoreactivity in the corpus callosum (A), the cerebral cortex (B), and the hippocampus (C). There appears to be larger variation in atherosclerotic mice than in controls but the values did not reach statistical significance. The difference in GFAP immunoreactivity expression between control and atherosclerotic mice was not significant. Control n= 3, Atherosclerotic n= 6.

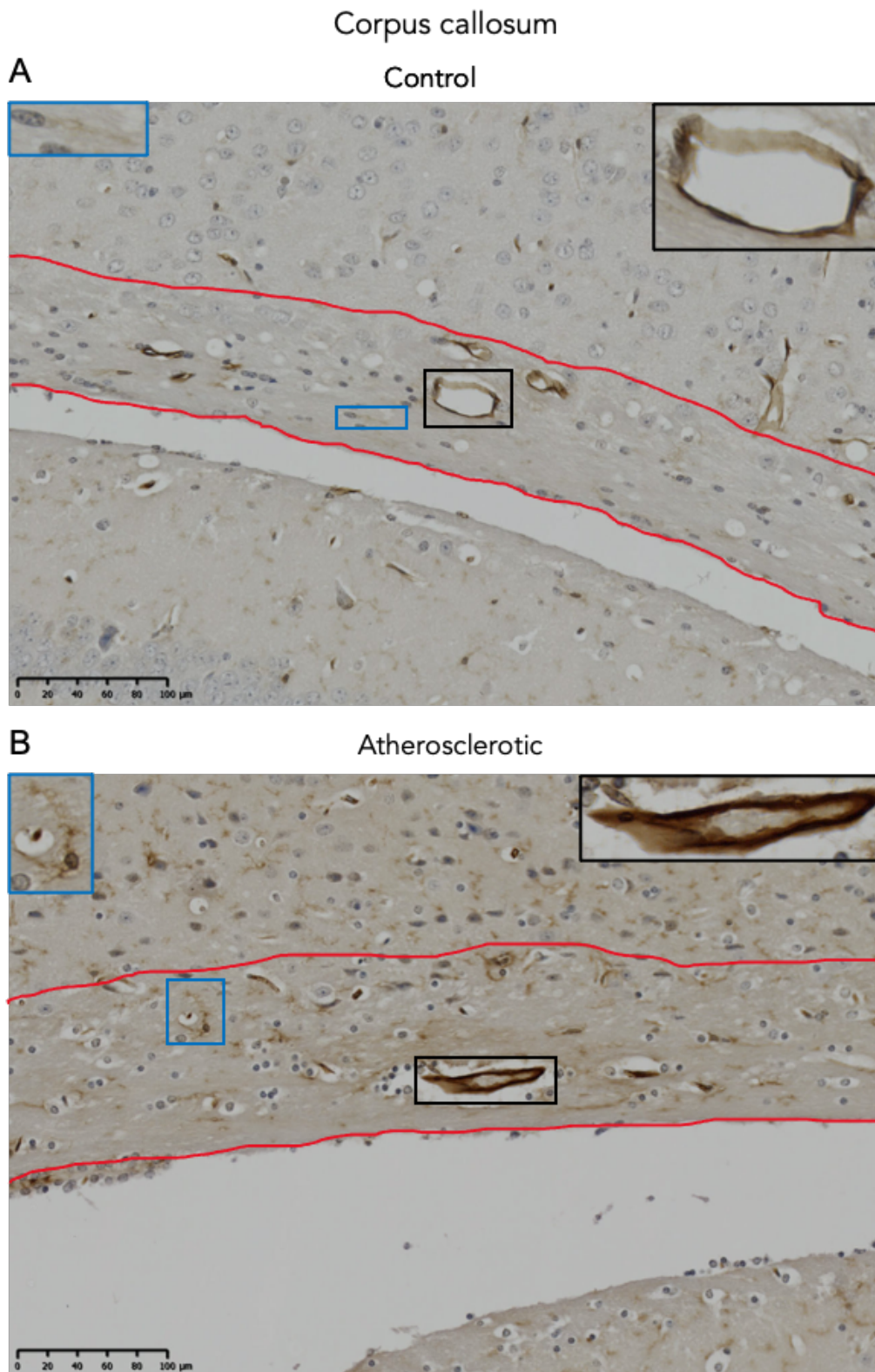


Figure 4.5 Representative image showing endothelial cells and microglia expression of ICAM-1 immunoreactivity in the corpus callosum of PCSK9 induced mice

Atherosclerotic mice seemed to present more intense ICAM⁺ immunoreactivity in microglia and endothelial cells than control mice. Blood vessels can be observed in both mice diets. Atherosclerotic mice appeared to display more microglia nucleus than controls. Control n= 3, Atherosclerotic n= 6 Scale bar represents 100 μm (20 μm insert).

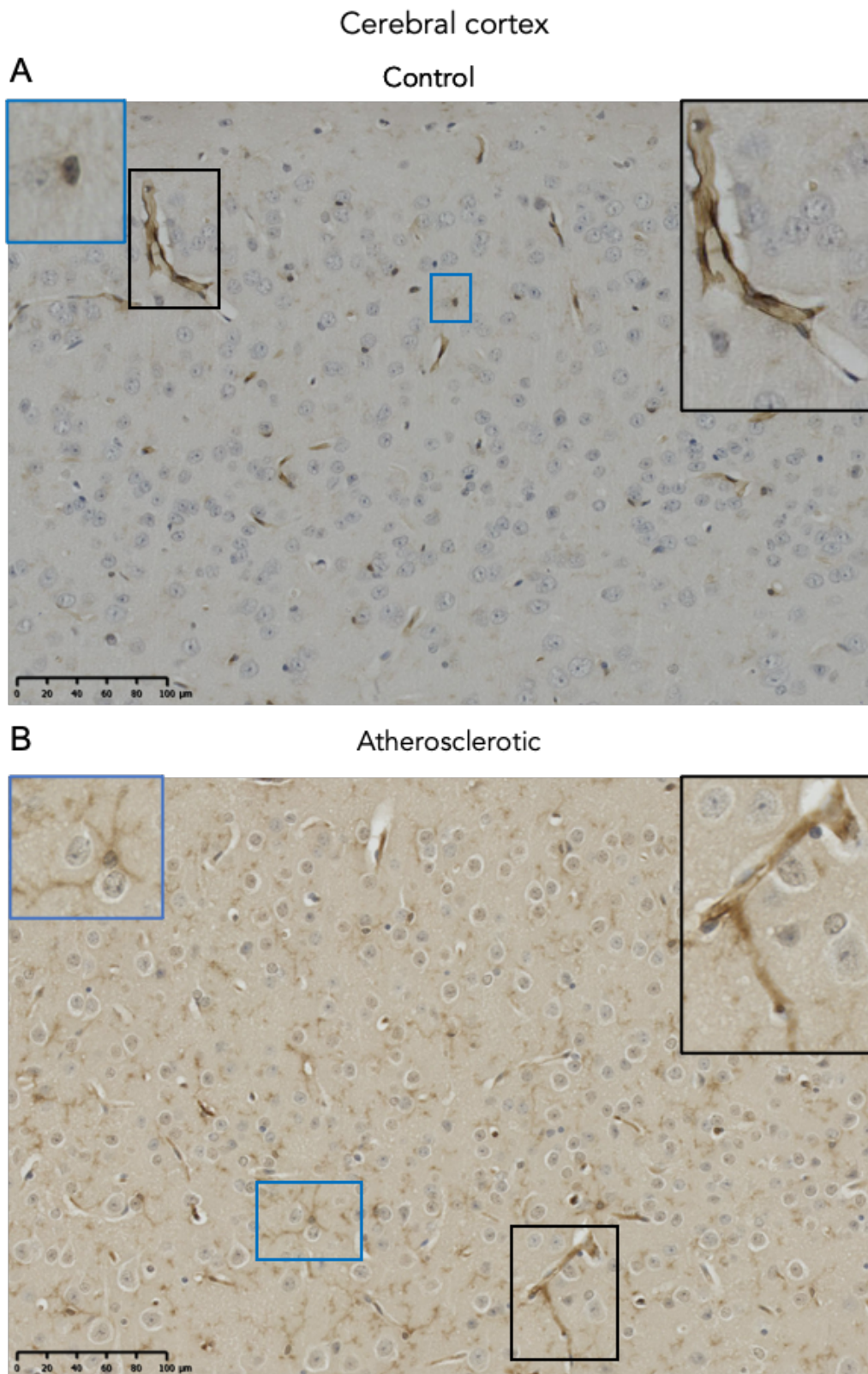


Figure 4.6 Representative image showing endothelial cells and microglia expression of ICAM-1 immunoreactivity in the cerebral cortex of PCSK9 induced transduced mice

The ICAM-1 immunoreactivity of endothelial cells and microglia seemed higher in the atherosclerotic mice compared to controls. The microglial cell bodies appeared to be lower in controls with fading processes compared to atherosclerotic mice. Control n= 3, Atherosclerotic n= 6. Scale bar represents 100 μm (20 μm insert).

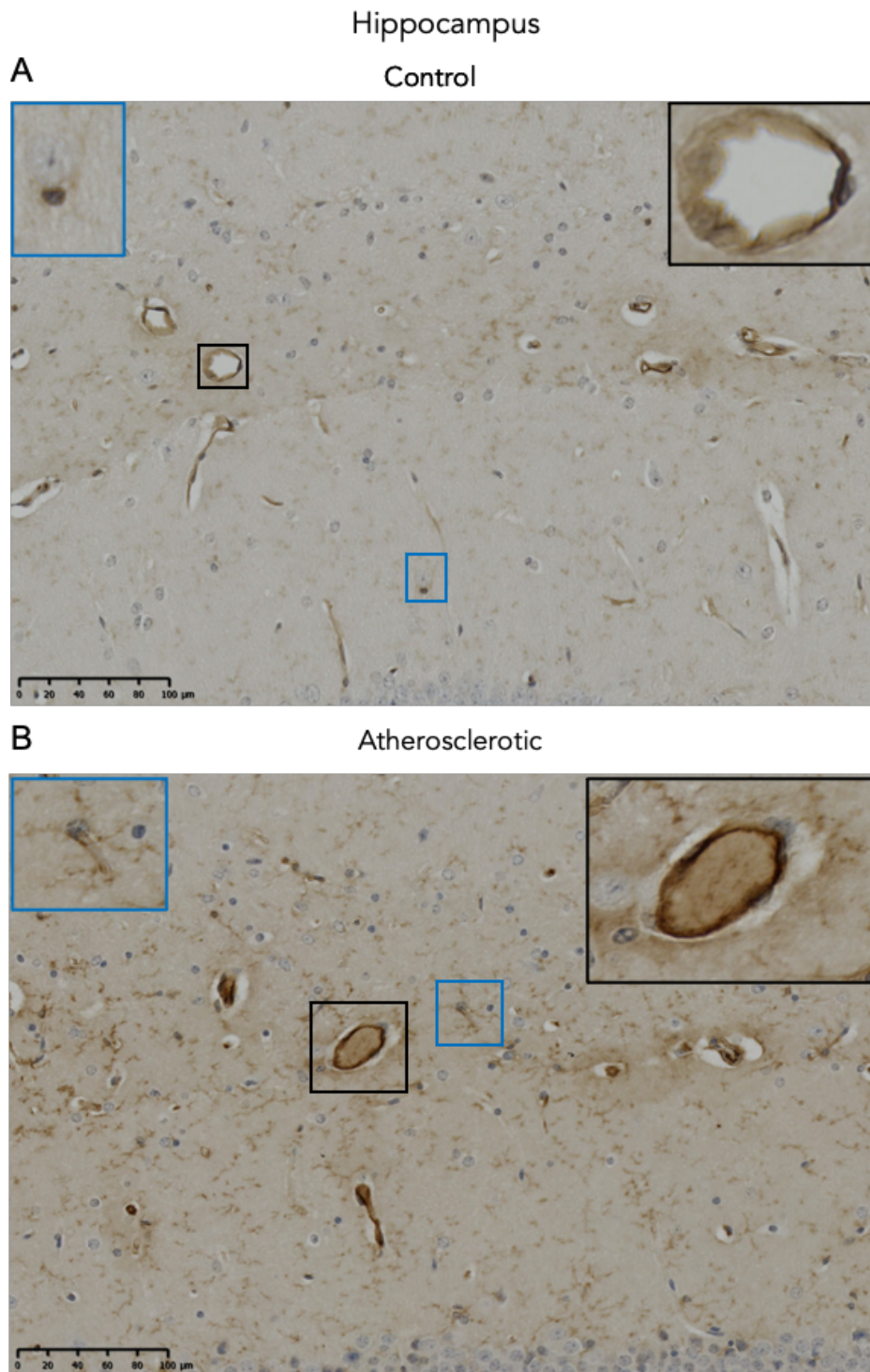


Figure 4.7 Representative image showing endothelial cells and microglia expression of ICAM-1 immunoreactivity in the hippocampus of PCSK9 induced mice

The endothelial cells and microglia immunoreactivity to ICAM-1 seemed higher in atherosclerotic mice than in controls with blood vessels presenting a pattern of diffuse ICAM-1 staining surrounding the blood vessels of mice fed with both diets. The processes of microglia in atherosclerotic mice were more easily identified as there seemed to be more present. The microglia cell bodies presented a similar morphology and size in both conditions, but the processes in atherosclerotic mice were fragmented with some microglia displaying higher ICAM-1 immunoreactivity than others by having more intense processes. Control n= 3, Atherosclerotic n= 6. Scale bar represents 100 µm (20 µm insert).

In addition to ICAM-1⁺ blood vessels in the PCSK9 induced mouse model, ICAM1⁺ microglia were also detected. Both cell types appeared to have a more intense immunoreactivity to ICAM-1 in atherosclerotic mice than in controls and endothelial cells appeared to have more intense immunoreactivity than microglial cells in all brain areas. In the corpus callosum of PCSK9 induced control mice there appeared to be fewer ICAM-1⁺ microglial cell bodies and processes compared to atherosclerotic mice (Figure 4.5). In the cerebral cortex the cell bodies of ICAM⁺ microglial were small and round in both control and atherosclerotic mice, however more processes were visible in the atherosclerotic mice, but they were not easily distinguished as with the IBA-1 staining (Figure 4.6). The hippocampus had ICAM⁺ microglial processes that were more pronounced in atherosclerotic mice and displayed a punctate morphology (Figure 4.7).

The hippocampus displayed the highest mean % of ICAM-1 immunoreactivity in atherosclerotic mice ($M = 6.5$, $SEM = 1.9$, $p = 0.07$) compared to controls ($M = 0.35$, $SEM = 0.1$). Control and atherosclerotic mice showed similar % area of immunoreactivity of ICAM-1⁺ blood vessels in both the corpus callosum (Controls $M = 0.4$, $SEM = 0.1$; Atherosclerosis $M = 3.4$, $SEM = 1.2$, $p = 0.07$) and cerebral cortex (Controls $M = 0.3$, $SEM = 0.1$; Atherosclerosis $M = 3.7$, $SEM = 0.9$, $p = 0.07$) (Figure 4.8 A-C). The assessment of the % area of ICAM-1 immunoreactive microglia revealed that while the average % area is higher in atherosclerotic mice than in controls, the corpus callosum (Controls $M = 0.9$, $SEM = 0.2$; Atherosclerosis $M = 8.6$, $SEM = 2.8$, $p = 0.07$), cerebral cortex (Controls $M = 0.4$, $SEM = 0.1$; Atherosclerosis $M = 4.1$, $SEM = 0.20$, $p = 0.24$) or the hippocampus (Controls $M = 1.7$, $SEM = 0.35$; Atherosclerosis $M = 1.0$, $SEM = 0.20$, $p = 0.24$). This results this did not reach statistical significance (Figure 4.8, D-F).

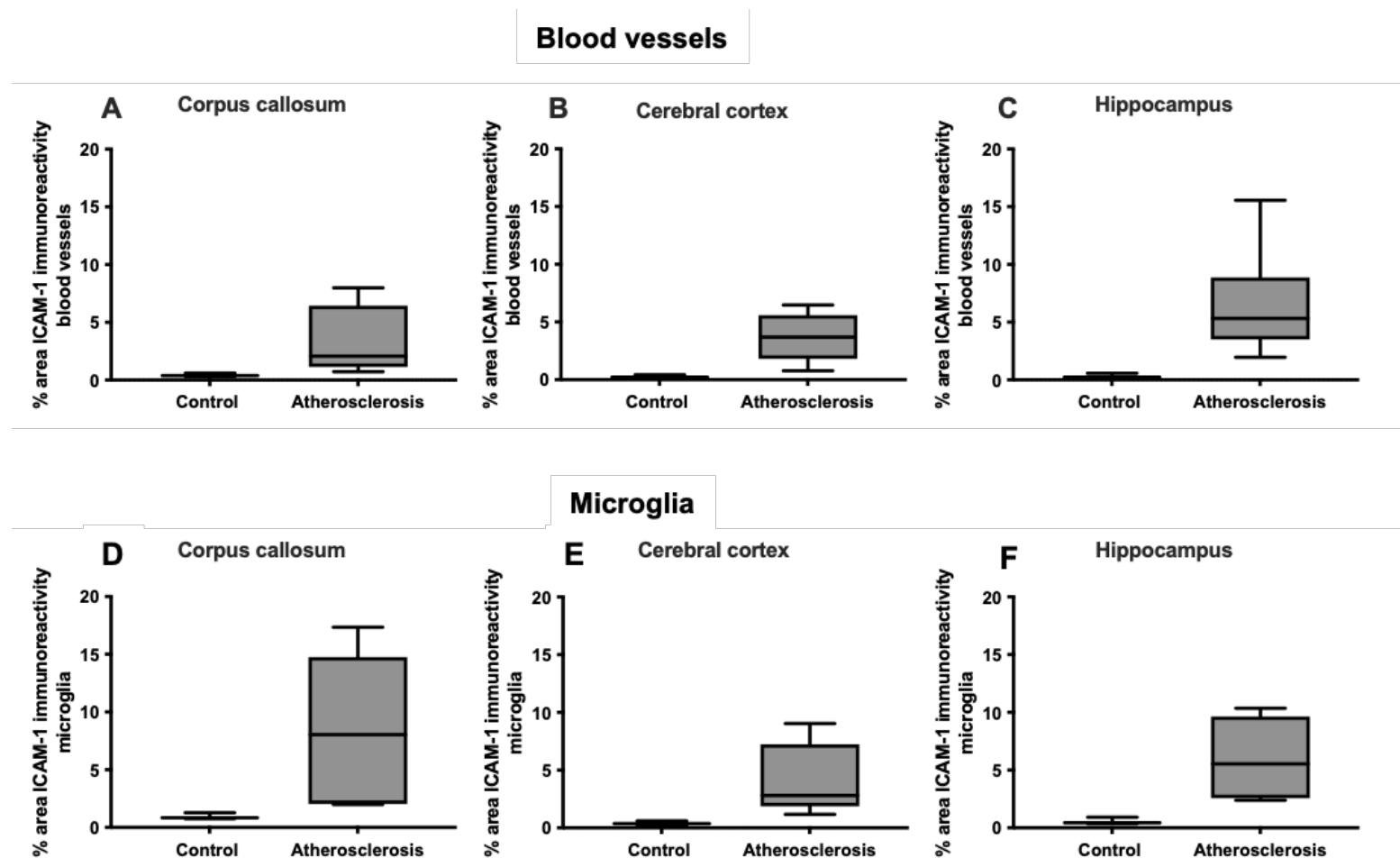


Figure 4.8 Analysis of the percentage (%) area of endothelial cells and microglia ICAM-1 immunoreactivity the corpus callosum, cerebral cortex and hippocampus of control and atherosclerotic PCSK9 induced mice

Mean % area of ICAM-1 expression in the endothelial cells of blood vessels (A-C) and microglia (D-E) appeared higher in atherosclerotic compared to control PCSK9 induced mice in the corpus callosum, cerebral cortex, and hippocampus of the PCSK9 induced mice. However, it was not significantly different. Control n= 3, Atherosclerotic n= 6.

4.3.3 Ionized calcium-binding adaptor molecule 1 (IBA-1)

immunoreactivity in the PCSK9 induced atherosclerotic mouse model

As previously discussed IBA-1 is considered a pan-marker for microglia due to its expression during different stages of microglia activation and morphology. The current study found a heterogeneous pattern of staining across all the investigated brain areas, with atherosclerotic mice microglia appearing to have a more intense IBA-1 immunoreactivity than controls. There appeared to be a fewer number of IBA-1 immunopositive cell bodies in the corpus callosum of control mice compared to atherosclerotic mice. The microglia cell bodies in atherosclerotic mice in the corpus callosum appeared larger with thicker processes that radiate in a bipolar manner, compared to control mice (Figure 4.9). The cell bodies of microglia in the cerebral cortex of atherosclerotic mice also appeared larger and rounder with thicker processes than controls, Processes in control mice also appeared to have more branches and to be thinner than atherosclerotic microglia (Figure 4.10). The hippocampus of control PCSK9 induced mice appeared to have higher immunoreactivity than the corpus callosum or the cerebral cortex. The round microglial cell bodies appeared to be of similar size in controls and atherosclerotic mice, but their processes differ. Atherosclerotic mice presented darker, thicker, and shorter processes that have a punctate morphology compared to controls (Figure 4.11). However, these qualitative observation was not quantified.

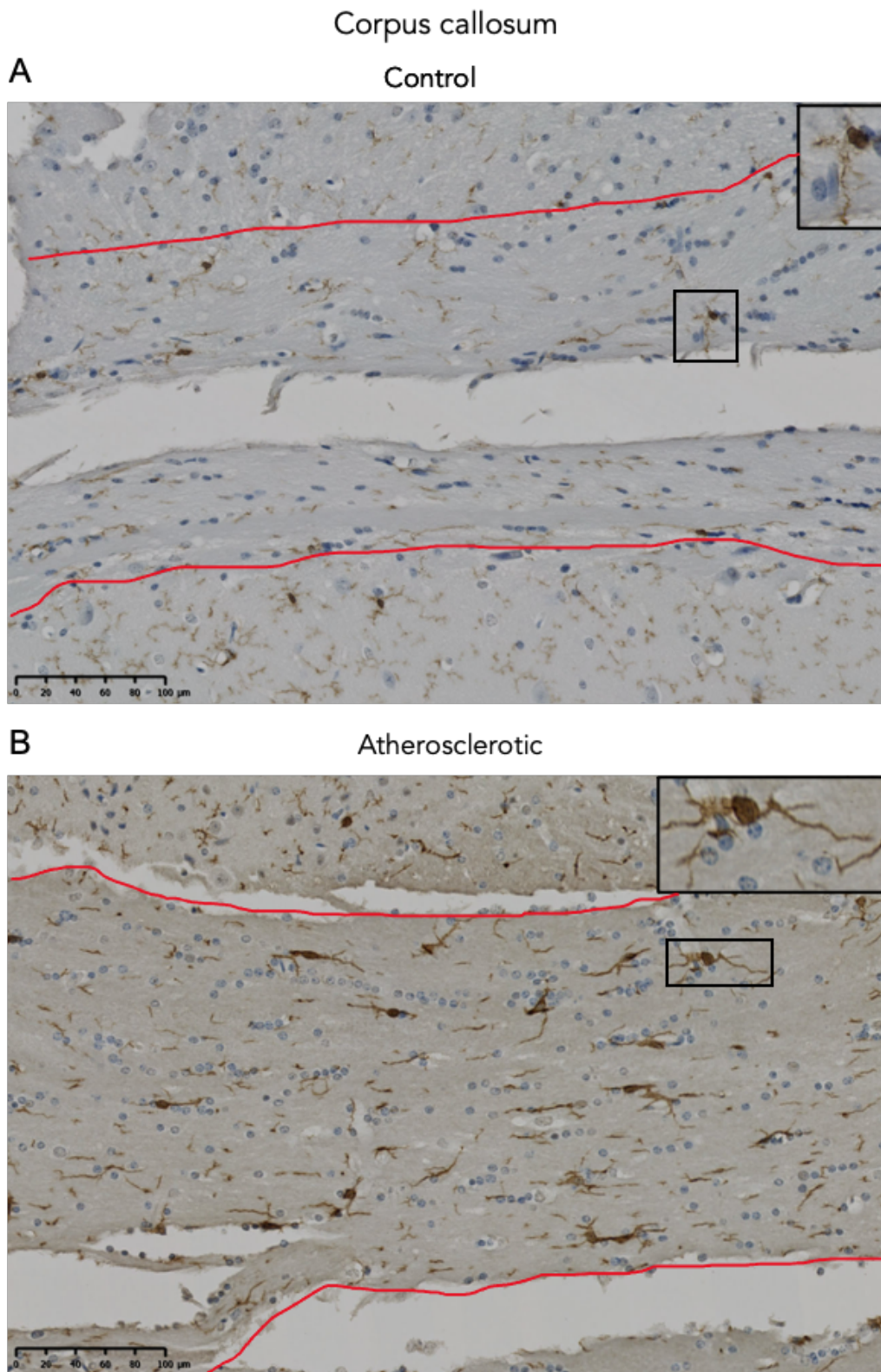


Figure 4.9 Representative image showing microglia expression of IBA-1 immunoreactivity in the corpus callosum of PCSK9 induced mice

The microglia in the corpus callosum (delimited by red lines) appeared to be have a more intense pattern of staining in atherosclerotic mice compared to the controls, with more immunoreactive cell bodies and thicker processes. Control n= 3, Atherosclerotic n= 6. Scale bar represents 100 μ m (20 μ m insert).

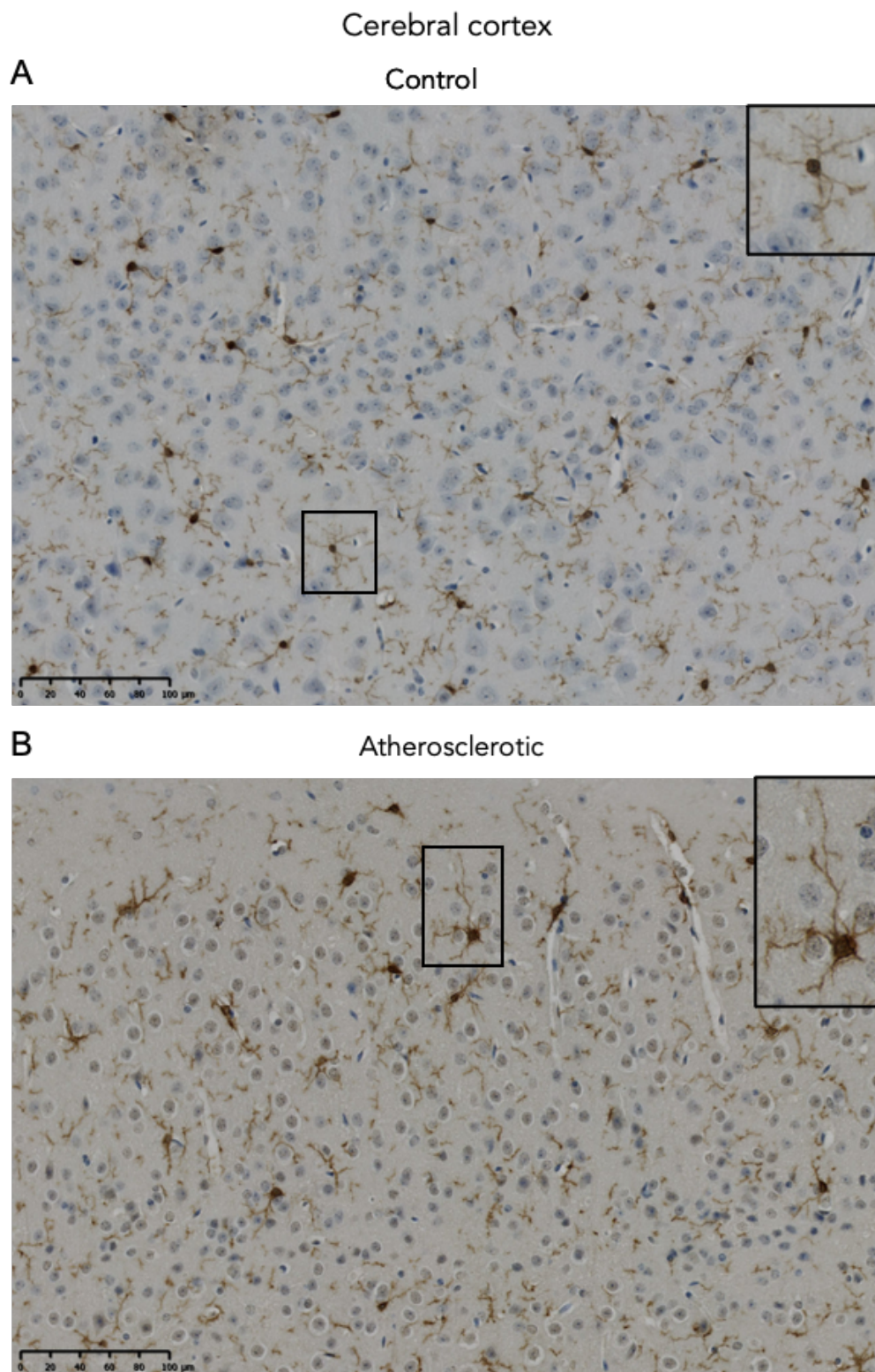


Figure 4.10 Representative image showing microglia expression of IBA-1 immunoreactivity in the cerebral cortex of PCSK9 induced mice

The IBA-1 immunoreactivity seemed more intense on atherosclerotic mice than in control mice. The cell bodies of microglia appeared larger, with longer processes in atherosclerotic mice while controls presented fine processes. Control n= 3, Atherosclerotic n= 6. Scale bar represents 100 μm (20 μm insert).

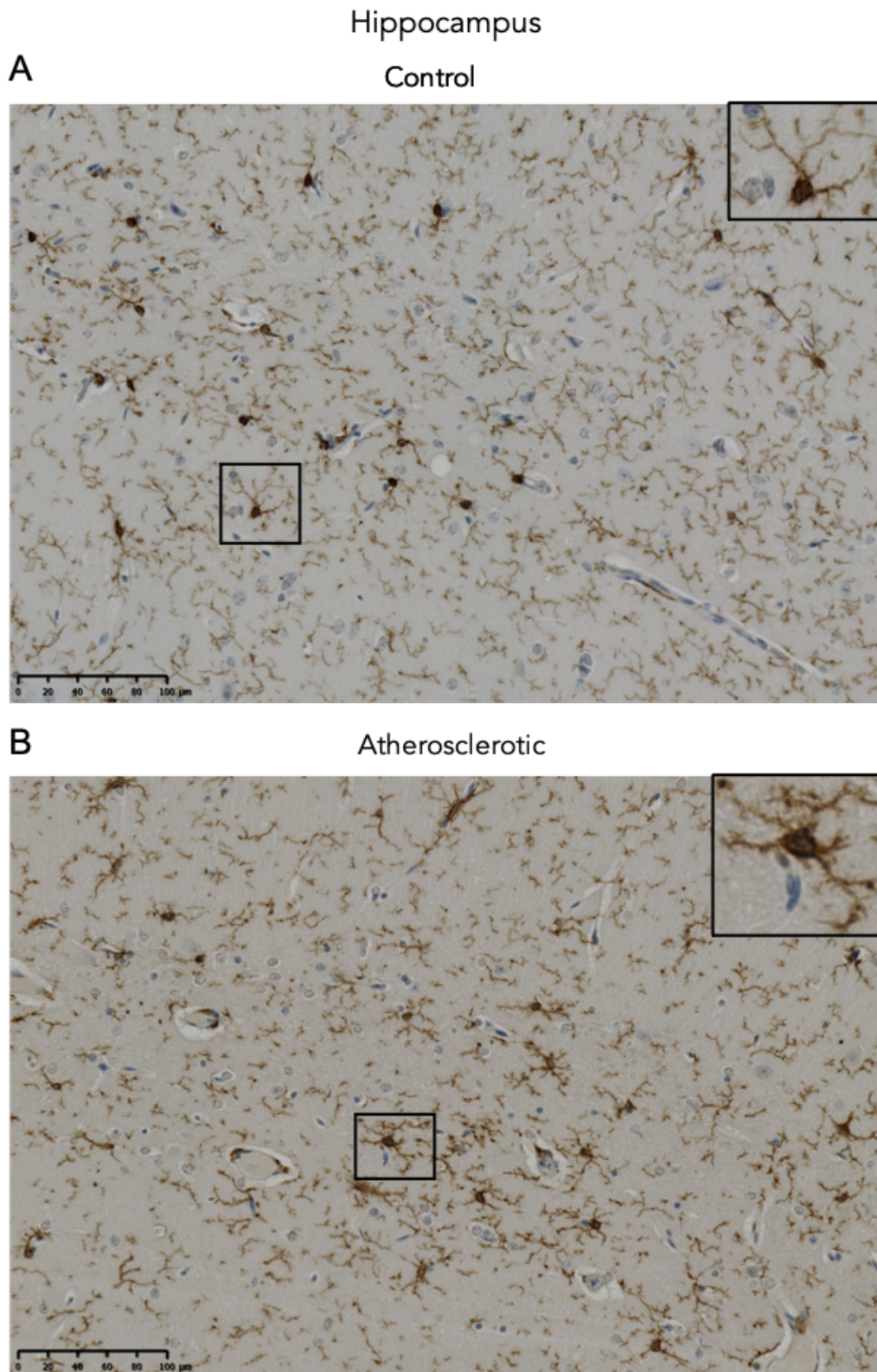


Figure 4.11 Representative image showing microglia expression of IBA-1 immunoreactivity in the cerebral cortex of PCSK9 induced mice

Atherosclerotic mice appeared to have a more intense pattern of IBA-1 immunoreactivity than controls. The microglia cell bodies seemed to be of similar size in both conditions but there were more processes radiating from the microglia in atherosclerotic mice, which are thicker and shorter than in control mice. Control n= 3, Atherosclerotic n= 6. Scale bar represents 100 μm (20 μm insert).

The quantitative analysis of % area of IBA-1 immunoreactivity the cerebral cortex (Controls $M = 0.54$, $SEM = 0.3$; Atherosclerosis $M = 1.0$, $SEM = 0.3$, $p > 0.999$) showing a non-significant difference between both diets. In the hippocampus the difference between controls ($M = 1.23$, $SEM = 0.49$) and atherosclerotic ($M = .28$, $SEM = 0.4$, $p > 0.999$) mice was a minimal. However, the mean % area of IBA-1 immunoreactivity showed the opposite, with the % area of IBA-1 immunoreactivity being higher on the controls of PCSK9 induced mice compared to the corpus callosum of atherosclerotic mice (Controls $M = 1.67$, $SEM = 0.5$; Atherosclerosis $M = 1.5$, $SEM = 0.3$, $p > 0.999$) (Figure 4.12).

4.3.4 Neuroinflammatory response to atherosclerosis in PCSK9 induced mice compared to *ApoE*^{-/-} mice

The PCSK9 induced mouse model was compared to the *ApoE*^{-/-} mouse model to identify neuroinflammatory changes caused by atherosclerosis without the exacerbation of inflammation due to the absence of APOE. As the mice models were obtained at different times, they could not be compared. Therefore, the ratio of change between the average % area of immunohistochemistry in controls was compared to the % area of immunohistochemistry of individual atherosclerosis cases for both mouse models. The fold change of the % area of immunohistochemistry was calculated for GFAP, IBA-1 and ICAM-1.

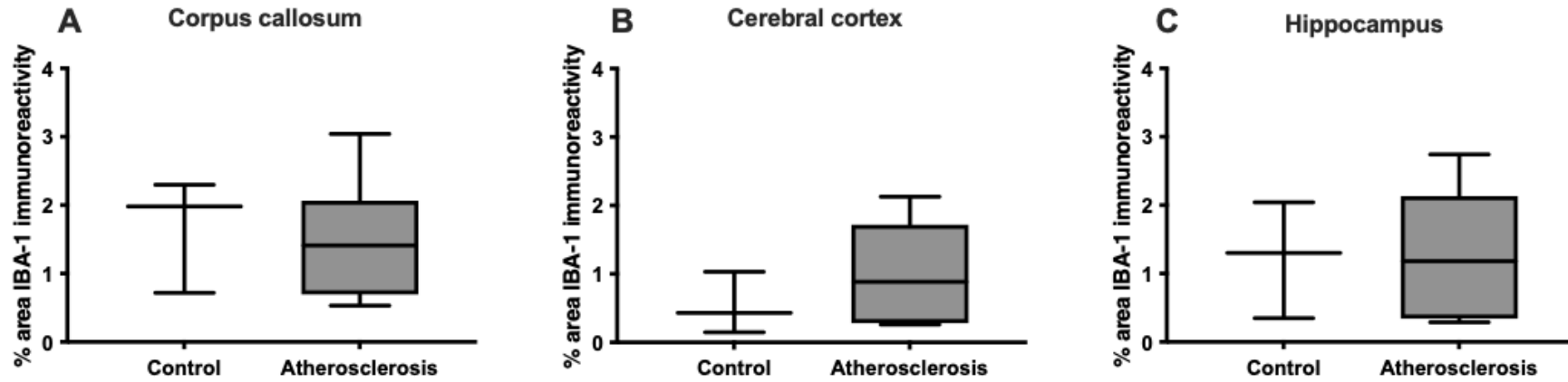


Figure 4.12 Analysis of the percentage (%) area of microglia IBA-1 immunoreactivity the corpus callosum, cerebral cortex and hippocampus of control and atherosclerotic PCSK9 induced mice

IBA-1 expression was not statistically significantly increased in any brain region of PCSK9 induced atherosclerotic mice compared to control mice. The corpus callosum (A) showed the opposite result to the cerebral cortex (B) and hippocampus (C) expressing a slightly higher % of ICAM-1 immunoreactivity in controls than in atherosclerotic mice. Control n= 3, Atherosclerotic n= 6

Endothelial cell activation

The pattern of ICAM-1 immunoreactivity of endothelial cells in the hippocampus (Figure 4.13) and the cerebral cortex (Figure 4.14) in control and atherosclerotic PCSK9 induced mice showed a similar pattern of ICAM-1 immunoreactivity to *ApoE*^{-/-} mice cohort 1. The endothelial cells in the corpus callosum of both controls and atherosclerotic *ApoE*^{-/-} mice cohort 2 appeared to be less immunoreactive to ICAM-1 than PCSK9 induced mice (Figure 4.15). The fold change of control mice against atherosclerotic mice was compared in both mouse models. The statistical analysis revealed that the cerebral cortex of PCSK9 induced mice had a significant increase of 11.58 fold change than *ApoE*^{-/-} cohort 2 mice (Figure 4.16). Overall there was a non-significant trend towards PCSK9 induced mice demonstrating more change compared to both *ApoE*^{-/-} mice cohorts 1 and 2, with cohort 1 showing higher variability than cohort 2 (Table 4.1)

Microglia

PCSK9 induced and *ApoE*^{-/-} controls and atherosclerotic mice brain displayed ICAM⁺ microglia and the distribution of the pattern of staining was similar across mouse models and diets. The hippocampus of atherosclerotic PCSK9 induced mice displayed ICAM⁺ that seem to display thick processes surrounding the immunoreactive cell body. Atherosclerotic *ApoE*^{-/-} mice appeared to have less immunoreactive ICAM-1 microglia than PCSK9 induced atherosclerotic mice. As previously stated *ApoE*^{-/-} cohort 1 presented more immunoreactive ICAM-1 microglia with an inflammatory morphology on atherosclerotic mice while *ApoE*^{-/-} cohort 2 differs by showing a more inflammatory morphology in controls compared to atherosclerotic mice (Figure 4.17).

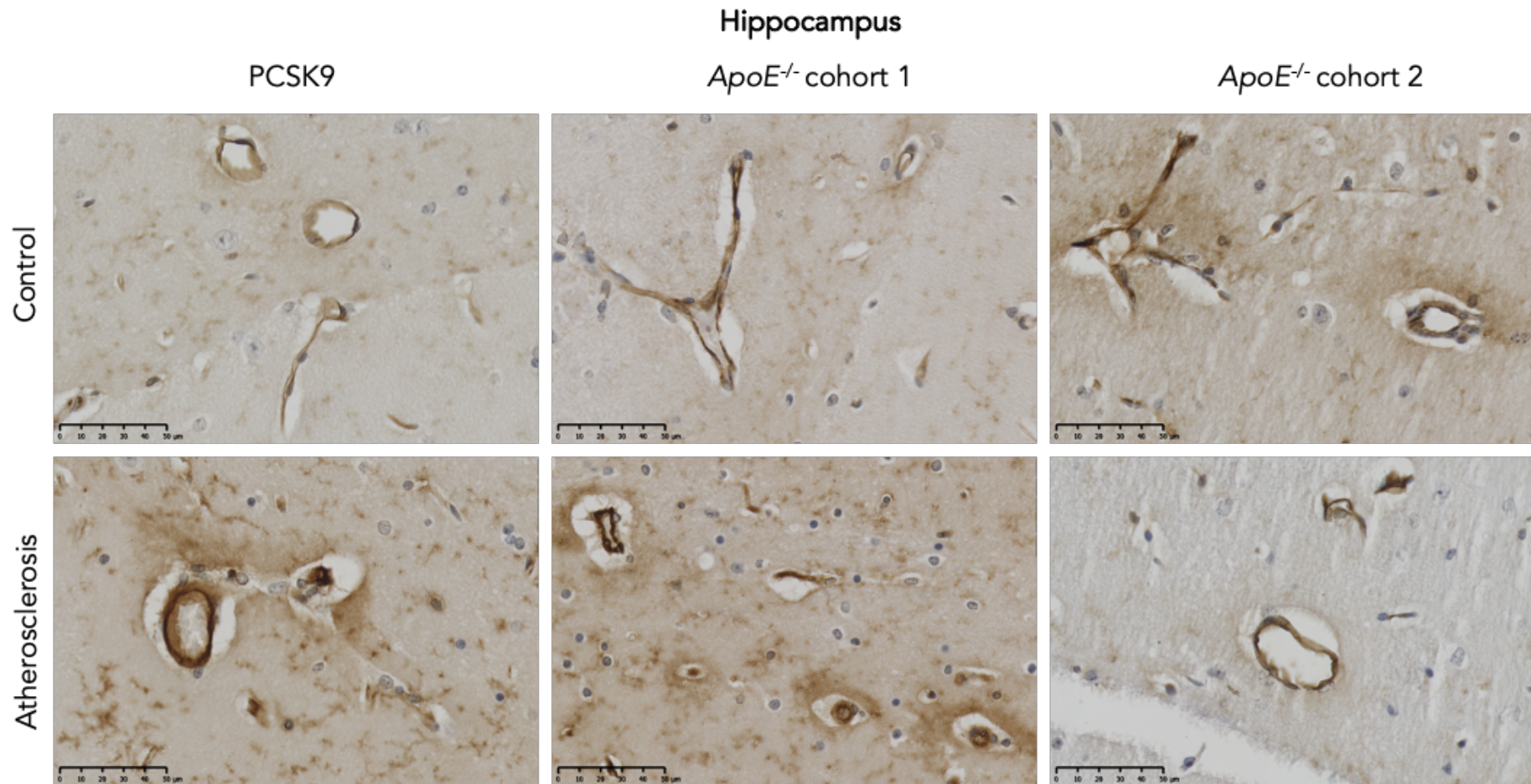


Figure 4.13 Representative image comparing ICAM-1 immunoreactive blood vessels on the hippocampus of controls and atherosclerotic PCSK9 induced mice and *ApoE*^{-/-} cohort 1 and 2

Blood vessels with ICAM-1 immunopositive endothelial cells in the hippocampus of atherosclerotic mice appeared more immunoreactive in PCSK9 induced and *ApoE*^{-/-} cohort 1 mice, while blood vessels in *ApoE*^{-/-} cohort 2 mice hippocampus seemed to be more immunoreactive in controls. There was ICAM-1 immunoreactivity present surrounding the blood vessels of highly immunoreactive cells. PCSK9: Control n= 3, Atherosclerotic n= 6; *ApoE*^{-/-} cohort 1: Control n= 7, Atherosclerotic n= 8; *ApoE*^{-/-} cohort 2: Control n= 6, Atherosclerotic n= 6. Scale bar represents 50 μ m

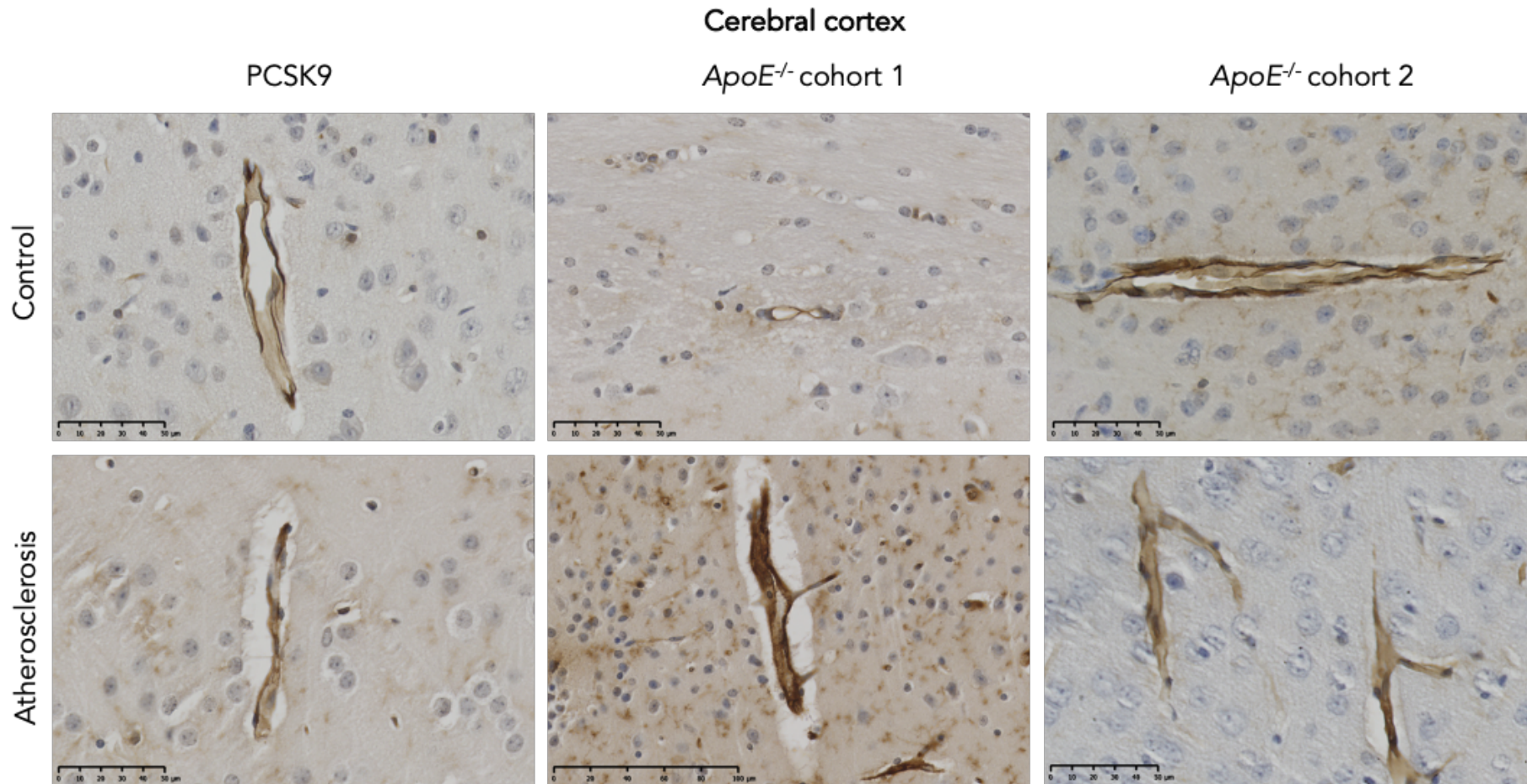


Figure 4.14 Representative image comparing ICAM-1 immunoreactive blood vessels on the cerebral cortex of controls and atherosclerotic PCSK9 induced mice and *ApoE*^{-/-} cohort 1 and 2

Blood vessels with ICAM-1 immunopositive endothelial cells in the cerebral cortex of atherosclerotic mice appeared more immunoreactive in PCSK9 induced and *ApoE*^{-/-} cohort 1 mice, while blood vessels in *ApoE*^{-/-} cohort 2 mice hippocampus seemed to be more immunoreactive in controls. PCSK9: Control n= 3, Atherosclerotic n= 6; *ApoE*^{-/-} cohort 1: Control n= 7, Atherosclerotic n= 8; *ApoE*^{-/-} cohort 2: Control n= 6, Atherosclerotic n= 6. Scale bar represents 50 μm

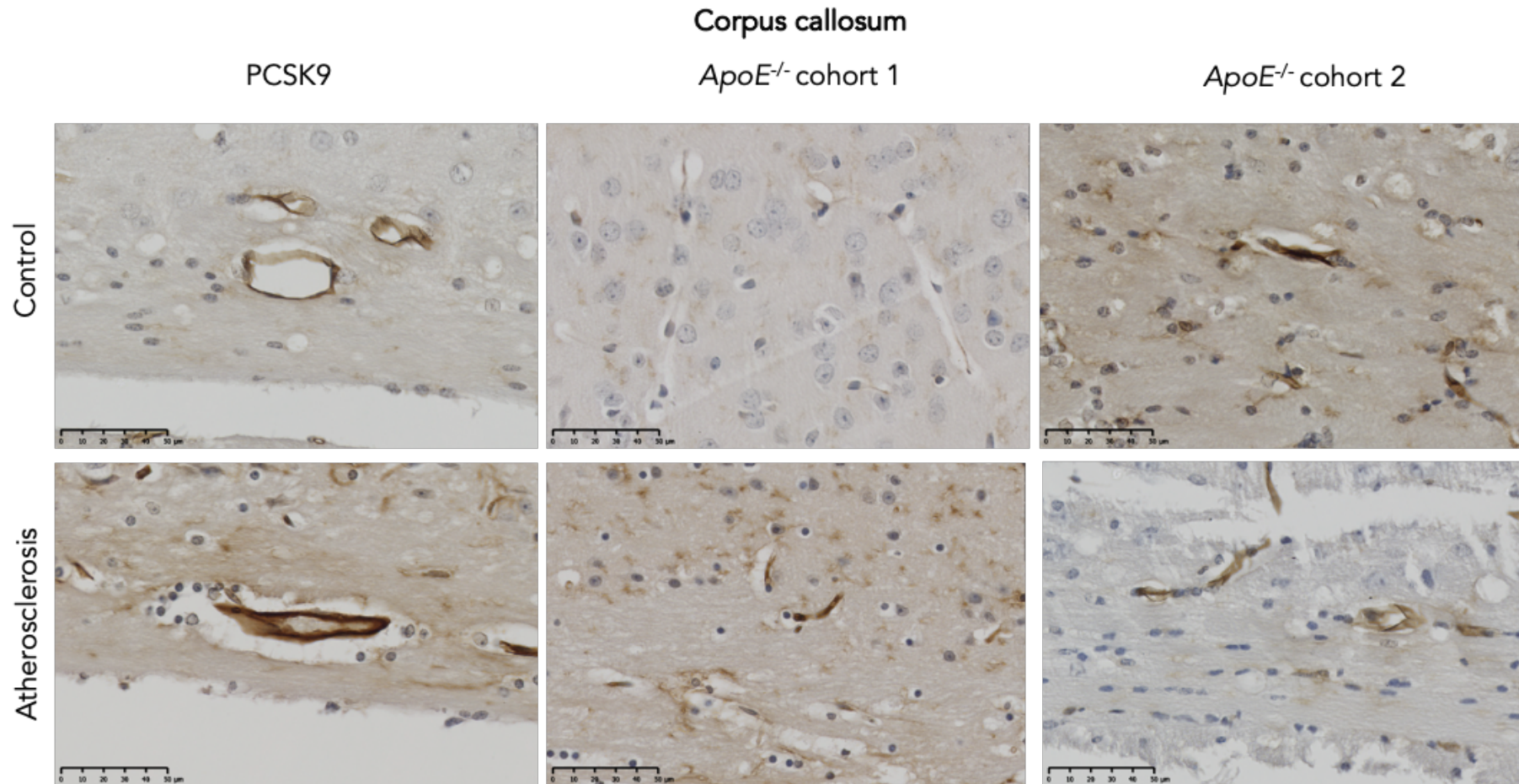


Figure 4.15 Representative image comparing ICAM-1 immunoreactive blood vessels on the hippocampus of controls and atherosclerotic PCSK9 induced mice and *ApoE*^{-/-} cohort 1 and 2

Blood vessels with ICAM-1 immunopositive endothelial cells in the hippocampus of atherosclerotic mice appeared more immunoreactive in PCSK9 induced and *ApoE*^{-/-} cohort 1 mice, while blood vessels in *ApoE*^{-/-} cohort 2 mice hippocampus seemed to be more immunoreactive in controls. PCSK9: Control n= 3, Atherosclerotic n= 6; *ApoE*^{-/-} cohort 1: Control n= 7, Atherosclerotic n= 8; *ApoE*^{-/-} cohort 2: Control n= 6, Atherosclerotic n= 6. Scale bar represents 50 μ m

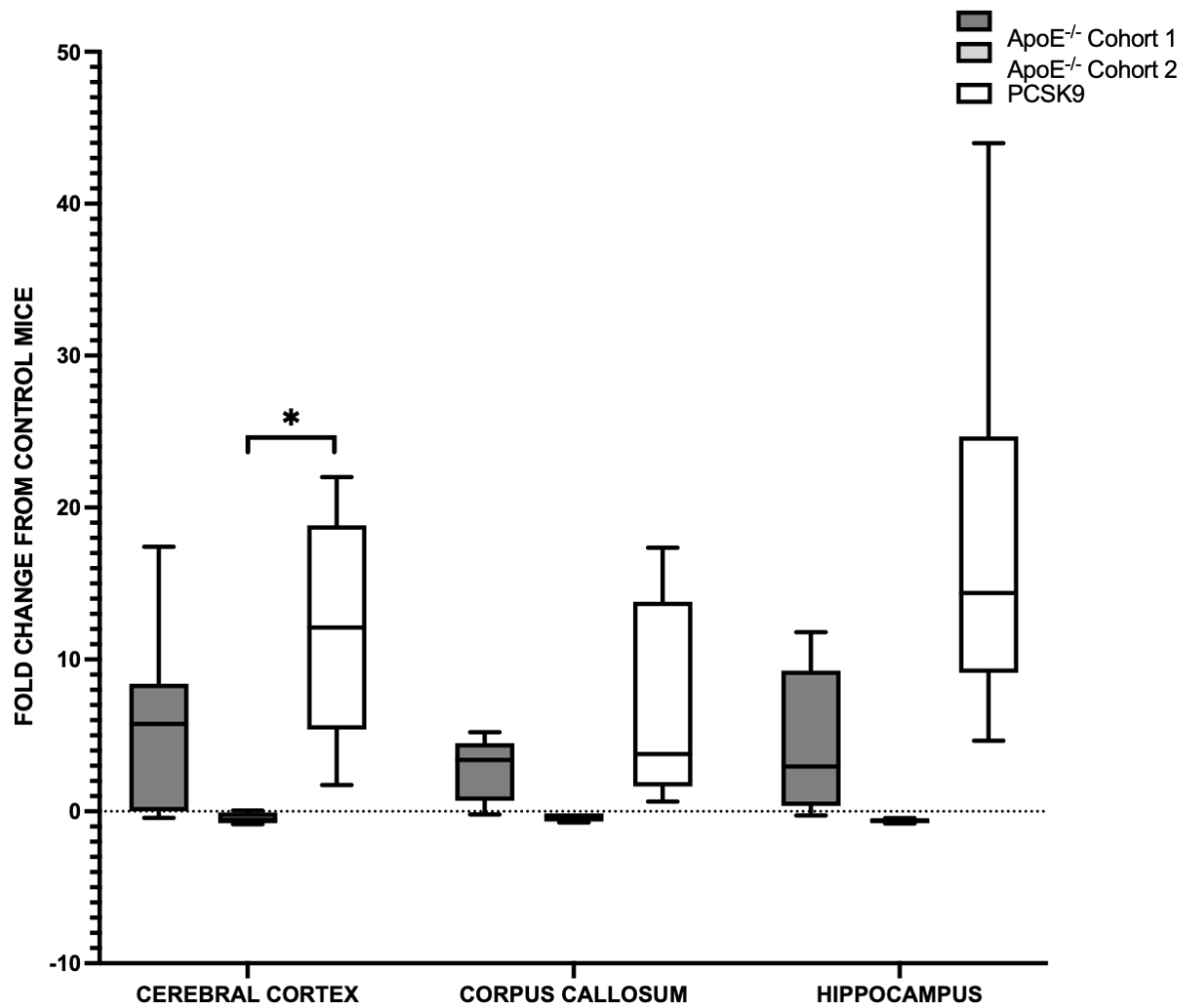


Figure 4.16 Analysis of the fold change between controls and atherosclerotic PCSK9 induced mice express higher change of ICAM-1 immunoreactive endothelial cells than *ApoE^{-/-}* cohort 1 in the cerebral cortex

The PCSK9 induce mice presented a higher difference of the % area of immunoreactivity of ICAM-1 endothelial cells than *ApoE^{-/-}* cohort 2 mice. In all brain areas, PCSK9 induced mice demonstrated a trend indicating more immunoreactive response of endothelial cells on atherosclerotic mice than controls compared to *ApoE^{-/-}* cohort 1 and cohort 2 mice, (* $P < 0.05$).

Table 4.1 Descriptive statistics of ICAM-1 immunoreactive endothelial cells preliminary comparison between PCSK9 induced and *ApoE*^{-/-} mouse models (cohort1 and cohort 2).

Minus numbers represent an average fold change in the opposite direction, therefore controls average is lower than atherosclerotic mice % area of immunoreactivity

ICAM-1 (Blood vessels)						
Cohort 1						
	Cerebral cortex		Corpus callosum		Hippocampus	
	<i>ApoE</i> ^{-/-}	PCSK9	<i>ApoE</i> ^{-/-}	PCSK9	<i>ApoE</i> ^{-/-}	PCSK9
Mean	5.62	12.05	2.94	6.70	4.46	17.71
Median	5.76	12.10	3.40	3.77	2.95	14.38
SEM	2.44	3.14	0.75	2.76	1.72	5.58
P value	0.39		0.56		0.10	

Cohort 2						
	Cerebral cortex		Corpus callosum		Hippocampus	
	<i>ApoE</i> ^{-/-}	PCSK9	<i>ApoE</i> ^{-/-}	PCSK9	<i>ApoE</i> ^{-/-}	PCSK9
Mean	-0.47	12.05	-0.37	6.69	-0.61	17.71
Median	-0.54	12.10	-0.30	3.77	-0.60	14.38
SEM	0.19	3.14	0.14	2.76	0.08	5.58
Sig.	0.04 *		0.22		0.09	

The corpus callosum presented a similar pattern of staining of ICAM-1⁺ microglia in PCSK9 induced and *ApoE*^{-/-} mice, with the microglial processes not being easily identified and appearing to have a low number of small and circular immunopositive microglial cell bodies. The atherosclerotic PCSK9 induce mice corpus callosum seem to present a slightly higher immunoreactivity than all other examined areas (Figure 4.18). In the cortex of PCSK9 induced mice the controls seemed to present lower ICAM⁺ microglial cell bodies and processes with almost no microglia observed. Atherosclerotic PCSK9 induced mice, on the other hand, showed long ICAM-1 immunoreactive microglia processes that appeared less immunoreactive than cohort 2 but more than cohort 1 as in Figure 4.19. The difference between controls and atherosclerotic mice in the % area of ICAM-1 immunopositive microglia was greater on PCSK9 induce mice hippocampus compared to *ApoE*^{-/-} cohort 1 (Table 4.2). The mean difference between the % area of ICAM-1 immunoreactivity of controls and atherosclerotic mice appears higher in all PCSK9 induced mice compared to both cohorts, but it fail to reach statistical significance (Figure 4.20).

The morphological and fold change comparison of IBA-1⁺ microglia in PCSK9 induced mice to both *ApoE*^{-/-} cohorts used the results from the simultaneous staining of all models (Section 3.3.4). The IBA-1 immunoreactive microglia in the cerebral cortex (Figure 4.21) and corpus callosum (Figure 4.22) of control and atherosclerotic PCSK9 induced mice resemble the morphology of control and atherosclerotic *ApoE*^{-/-} mice from cohort 1. However, in the hippocampus of control PCSK9 induced mice appeared to be more IBA-1⁺ microglial cell bodies and processes than in control *ApoE*^{-/-} mice, and atherosclerotic mice from the PCSK9 induced model seem to have more IBA-1 immunoreactive microglial processes radiating from the cell bodies, with longer and more fragmented appearance than in cohort 1 *ApoE*^{-/-} mice microglia (Figure 4.23).

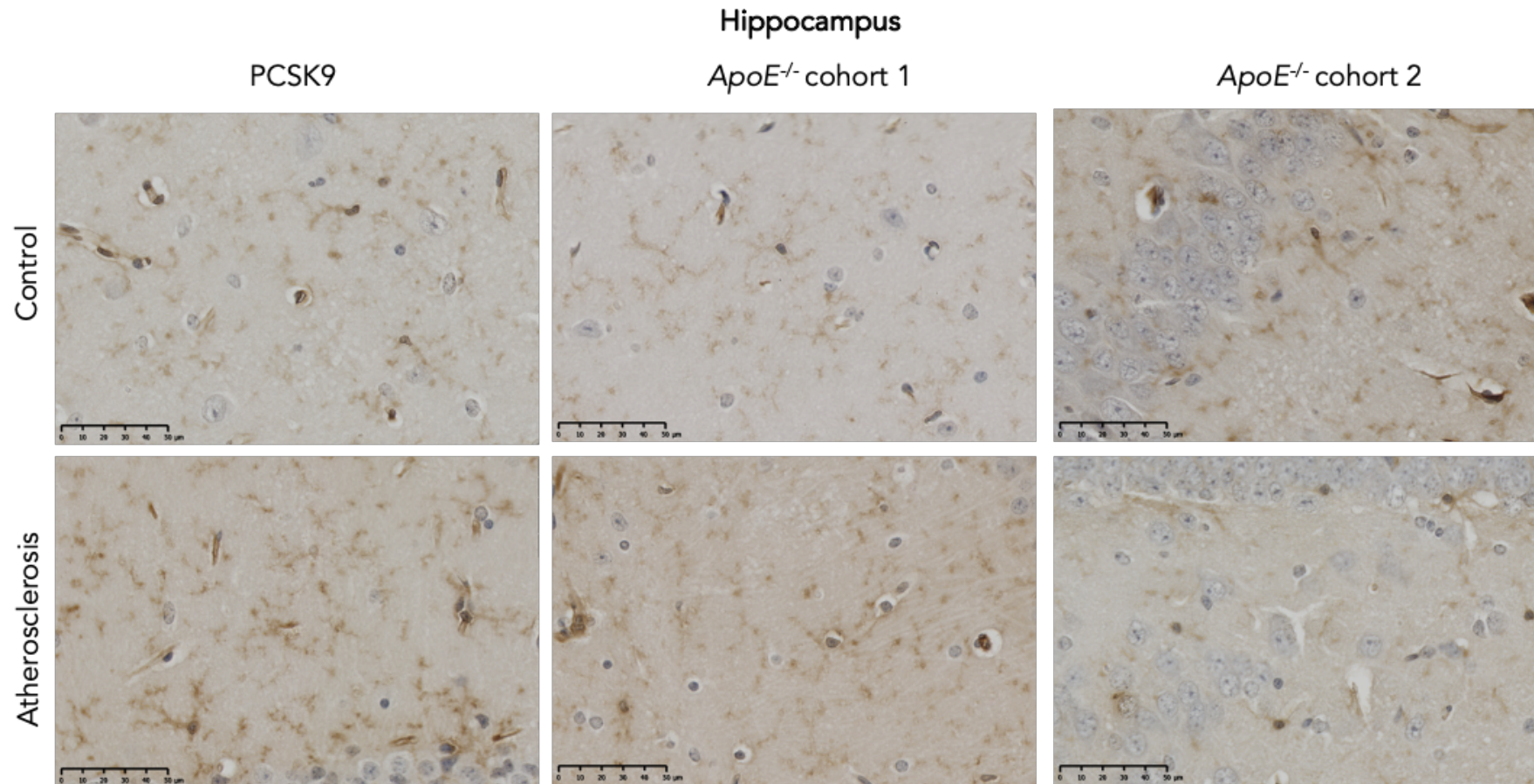


Figure 4.17 Representative image comparing ICAM-1 immunoreactive microglia on the hippocampus of controls and atherosclerotic PCSK9 induced mice and *ApoE*^{-/-} cohort 1 and 2

ICAM-1⁺ microglia in the hippocampus of atherosclerotic mice appeared more immunoreactive in PCSK9 induced and *ApoE*^{-/-} cohort 1 mice, while blood vessels in *ApoE*^{-/-} cohort 2 mice hippocampus seemed to be more immunoreactive in controls. The microglia in atherosclerotic PCSK9 induced and *ApoE*^{-/-} cohort 1 hippocampus appeared to have thicker and more immunoreactive processes than controls. In *ApoE*^{-/-} cohort 2 only a few ICAM-1 immunopositive cell bodies with almost no processes were visible. PCSK9: Control n= 3, Atherosclerotic n= 6; *ApoE*^{-/-} cohort 1: Control n= 7, Atherosclerotic n= 8; *ApoE*^{-/-} cohort 2: Control n= 6, Atherosclerotic n= 6. Scale bar represents 50 μm

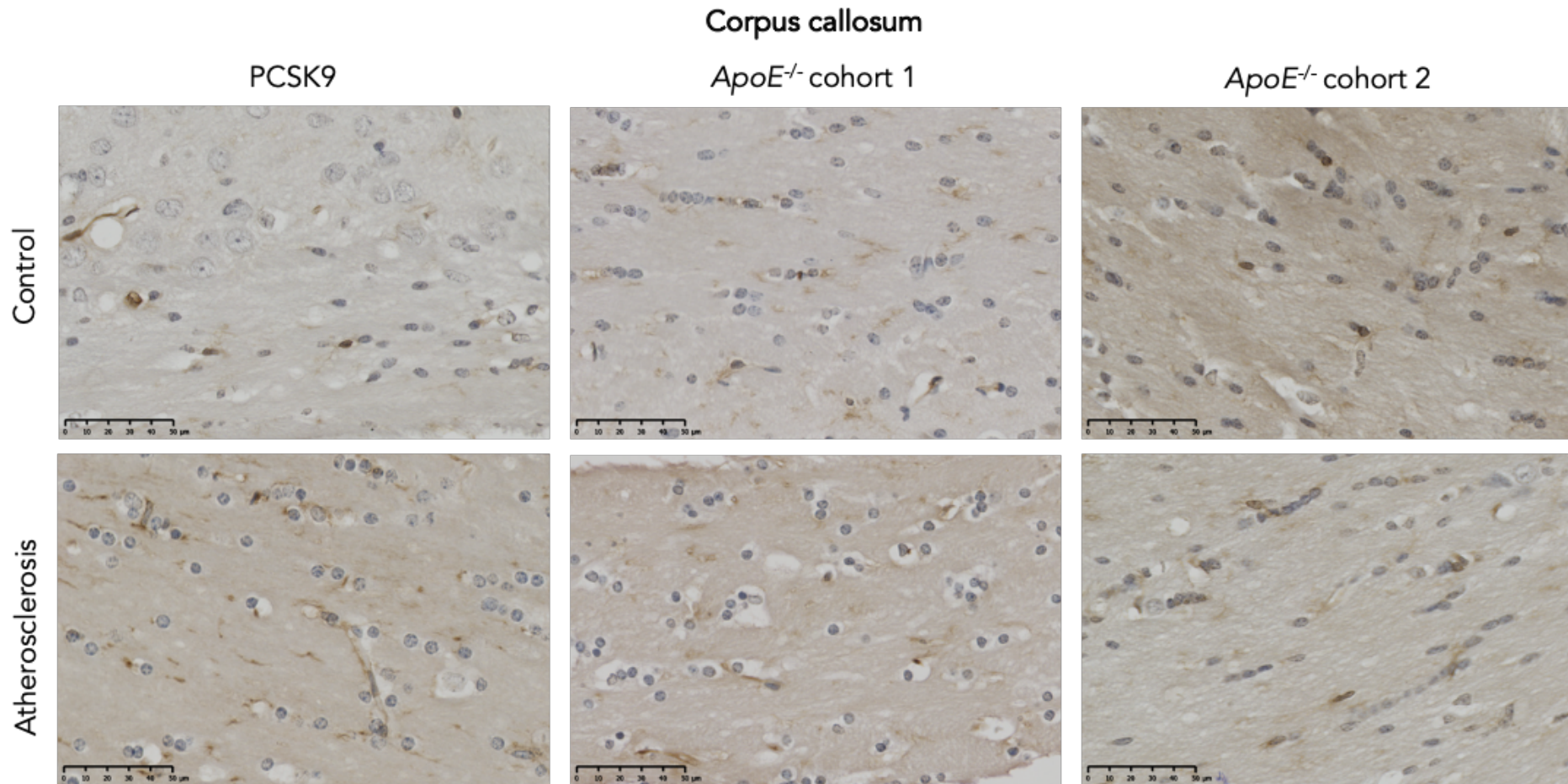


Figure 4.18 Representative image comparing ICAM-1 immunoreactive microglia on the corpus callosum of controls and atherosclerotic PCSK9 induced mice and *ApoE*^{-/-} cohort 1 and 2

In the corpus callosum of atherosclerotic mice ICAM-1⁺ microglia appeared to present similar levels of immunoreactivity with ICAM-1 immunoreactive microglia cell bodies being appreciated. Atherosclerotic PCSK9 induced mice seemed to present the more distinguishable difference between all models and diets with microglial processes being easier to identify. PCSK9: Control n= 3, Atherosclerotic n= 6; *ApoE*^{-/-} cohort 1: Control n= 7, Atherosclerotic n= 8; *ApoE*^{-/-} cohort 2: Control n= 6, Atherosclerotic n= 6. Scale bar represents 50 μm.

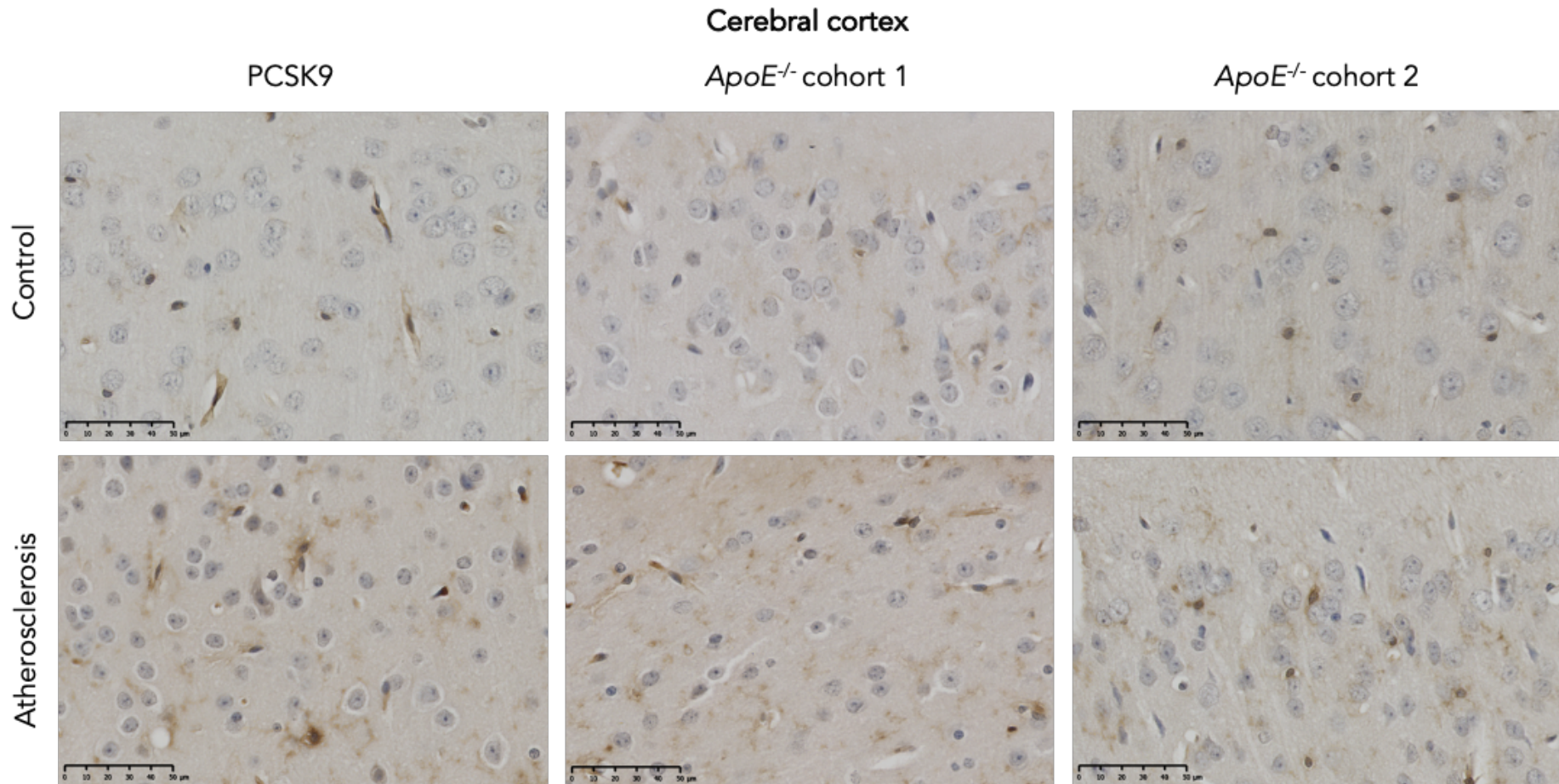


Figure 4.19 Representative image comparing ICAM-1 immunoreactive microglia on the cerebral cortex of controls and atherosclerotic PCSK9 induced mice and *ApoE*^{-/-} cohort 1 and 2

In the cerebral cortex of PCSK9 induced and *ApoE*^{-/-} mice, ICAM-1⁺ microglia appeared to present similar levels of immunoreactivity with ICAM-1 immunoreactive microglia cell bodies being appreciated. Atherosclerotic PCSK9 induced mice seemed to present the more distinguishable different between all models and diets with seemingly larger cell bodies and more processes being visible. PCSK9: Control n= 3, Atherosclerotic n= 6; *ApoE*^{-/-} cohort 1: Control n= 7, Atherosclerotic n= 8; *ApoE*^{-/-} cohort 2: Control n= 6, Atherosclerotic n= 6. Scale bar represents 50 μm.

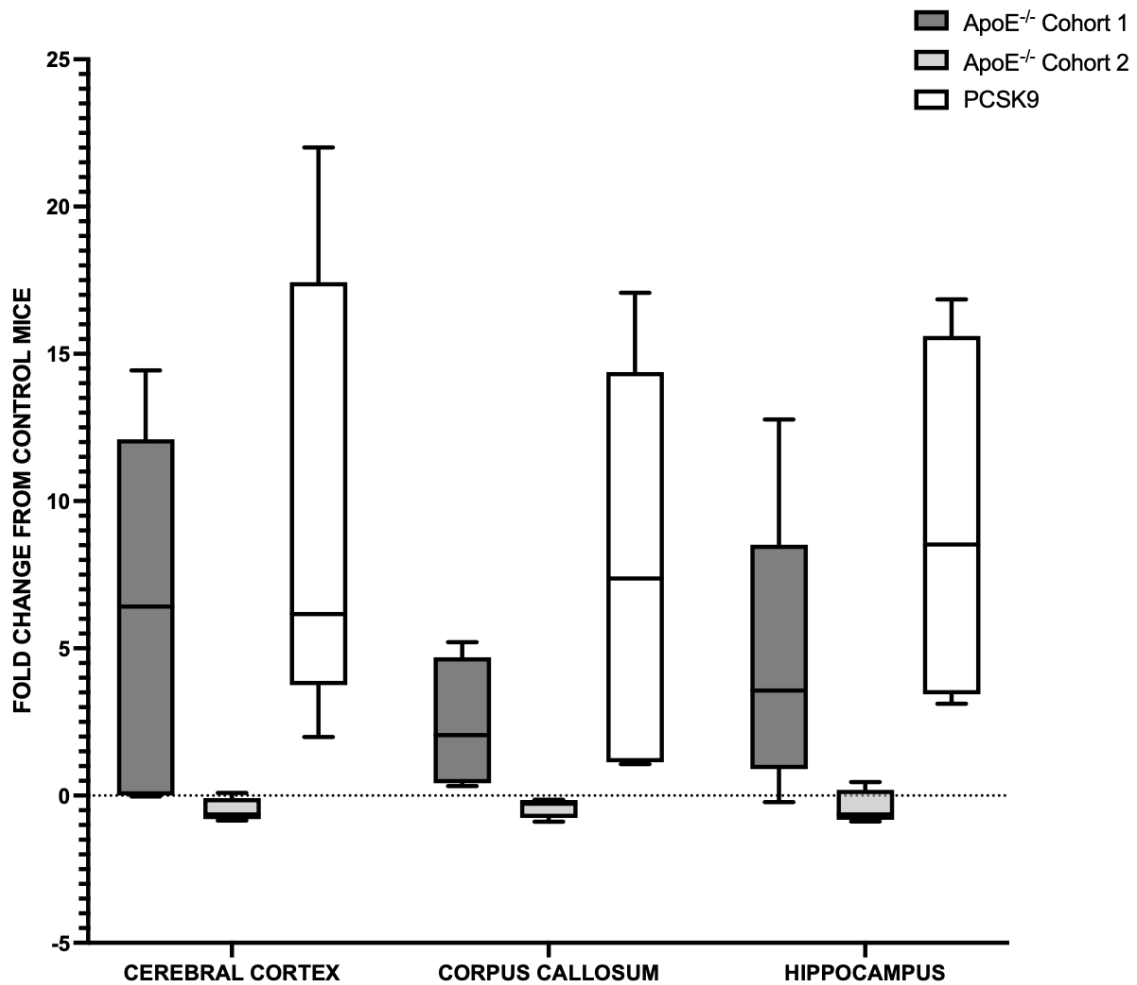


Figure 4.20 Analysis of the fold change between controls and atherosclerotic of PCSK9 induced, *ApoE*^{-/-} cohort 1 and cohort 2 in the cerebral cortex, corpus callosum and hippocampus.

The PCSK9 induced mouse model presented a higher difference of the % area of immunoreactivity of ICAM-1 endothelial cells in the hippocampus than *ApoE*^{-/-} cohort 2 mice. All brain areas showed a similar trend but did not reach statistical significance

Table 4.2 Descriptive statistics of ICAM-1 immunoreactive microglia preliminary comparison between PCSK9 induced and *ApoE*^{-/-} mouse models (cohort1 and cohort 2).

Minus numbers represent an average fold change in the opposite direction, therefore controls average is lower than atherosclerotic mice % area of immunoreactivity

ICAM-1 (Microglia)						
Cohort 1						
	Cerebral cortex		Corpus callosum		Hippocampus	
	<i>ApoE</i> ^{-/-}	PCSK9	<i>ApoE</i> ^{-/-}	PCSK9	<i>ApoE</i> ^{-/-}	PCSK9
Mean	6.26	9.43	2.36	7.92	4.64	9.30
Median	6.42	6.16	2.05	7.38	3.57	8.53
SEM	2.31	3.18	0.75	2.90	1.78	2.49
P value	>0.99		0.54		0.70	

Cohort 2						
	Cerebral cortex		Corpus callosum		Hippocampus	
	<i>ApoE</i> ^{-/-}	PCSK9	<i>ApoE</i> ^{-/-}	PCSK9	<i>ApoE</i> ^{-/-}	PCSK9
Mean	-0.51	9.43	-0.39	7.92	-0.42	9.30
Median	-0.64	6.16	-0.28	7.38	-0.64	8.53
SEM	0.21	3.18	0.17	2.90	0.30	2.49
P value	0.11		0.15		0.04*	

In comparison to cohort 2 of *ApoE*^{-/-} mice, PCSK9 induced mice seemed present a higher level of IBA-1 immunoreactivity in the cerebral cortex and hippocampus in both controls and atherosclerotic mice. In the corpus callosum of PCSK9 induced controls appeared to have more prominent processes but a similar number of microglia cell bodies compared to *ApoE*^{-/-} mice.

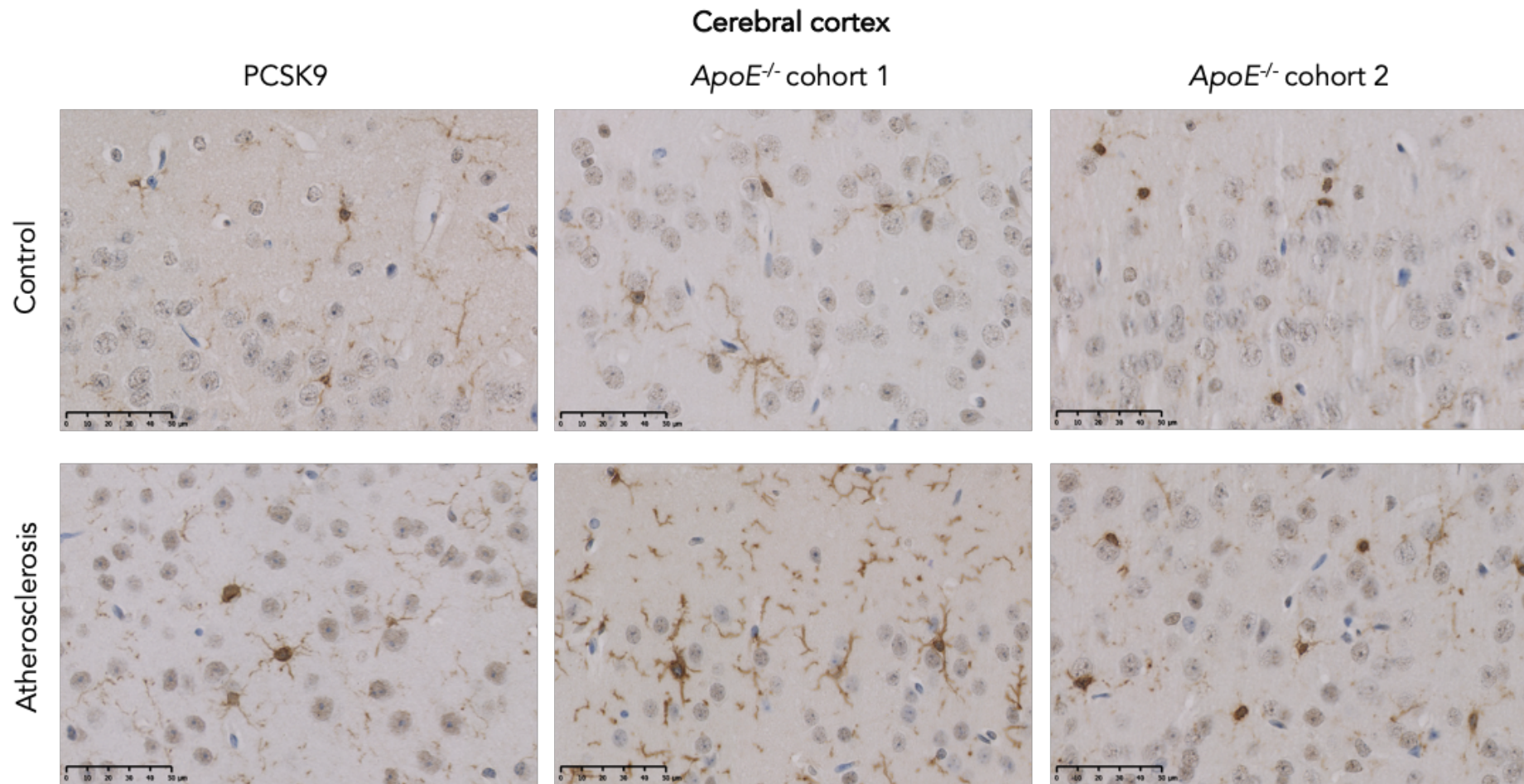


Figure 4.21 Representative image comparing IBA-1 immunoreactive microglia on the cerebral cortex of controls and atherosclerotic PCSK9 induced mice and *ApoE*^{-/-} cohort 1 and 2

IBA-1 immunoreactive microglia present different morphologies with PCSK9 induced and *ApoE*^{-/-} controls appearing to have a low number of microglia cell bodies with long and thin processes. The microglia present in the hippocampus of *ApoE*^{-/-} mice cohort 1 appear more immunoreactive than atherosclerotic PCSK9 induced and *ApoE*^{-/-} 2 cohort. PCSK9: Control n= 3, Atherosclerotic n= 6; *ApoE*^{-/-} cohort 1: Control n= 7, Atherosclerotic n= 8; *ApoE*^{-/-} cohort 2: Control n= 6, Atherosclerotic n= 6. Scale bar represents 50 μ m.

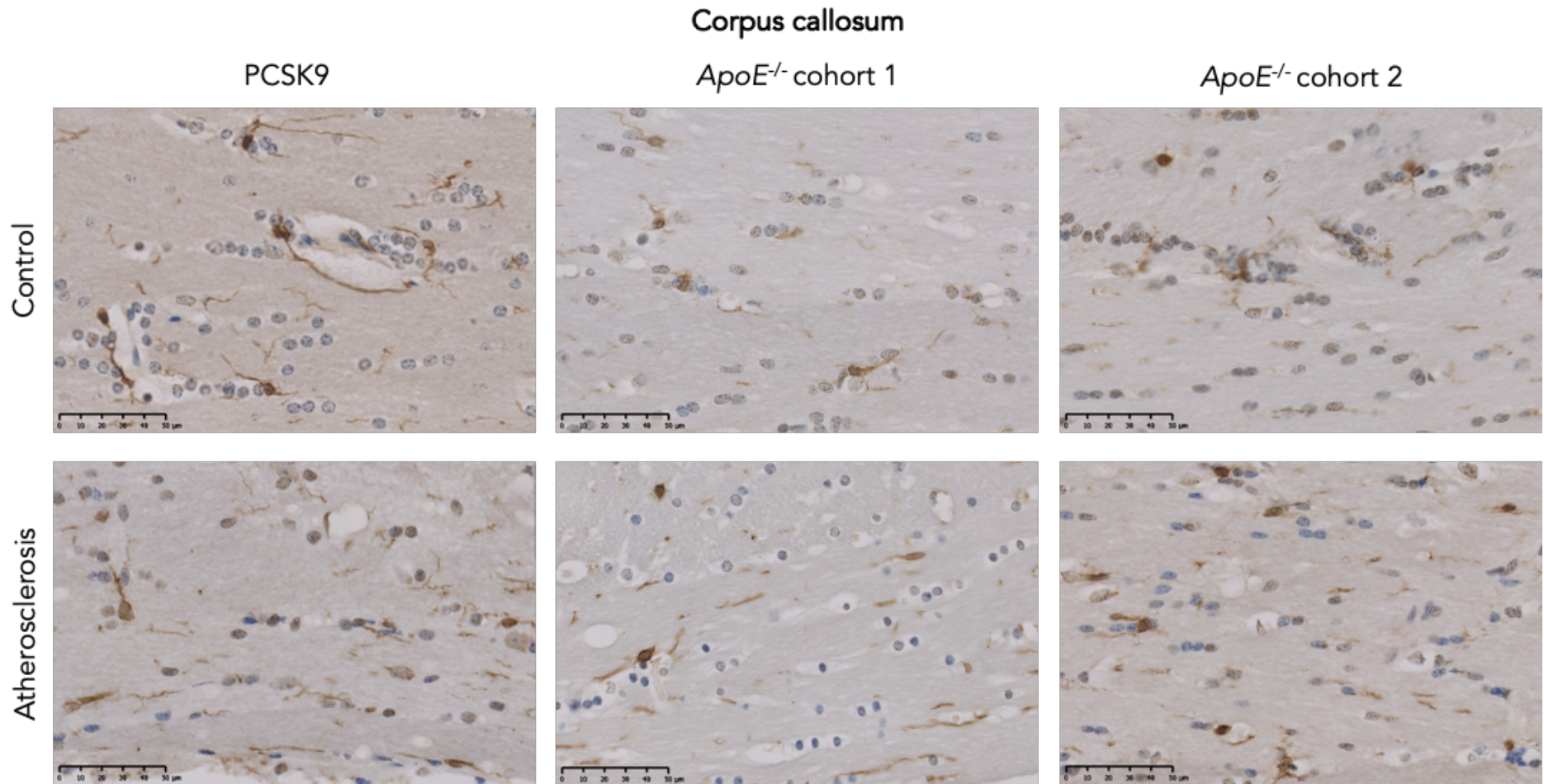


Figure 4.22 Representative image comparing IBA-1 immunoreactive microglia on the corpus callosum of controls and atherosclerotic PCSK9 induced mice and *ApoE*^{-/-} cohort 1 and 2

IBA-1 immunoreactive microglia present similar morphologies with PCSK9 induced control appearing slightly more immunoreactive than *ApoE*^{-/-} cohorts controls. The microglia present in the hippocampus of PCSK9 induced microglia present thin longer processes than *ApoE*^{-/-} control cohorts. PCSK9: Control n= 3, Atherosclerotic n= 6; *ApoE*^{-/-} cohort 1: Control n= 7, Atherosclerotic n= 8; *ApoE*^{-/-} cohort 2: Control n= 6, Atherosclerotic n= 6. Scale bar represents 50 μm.

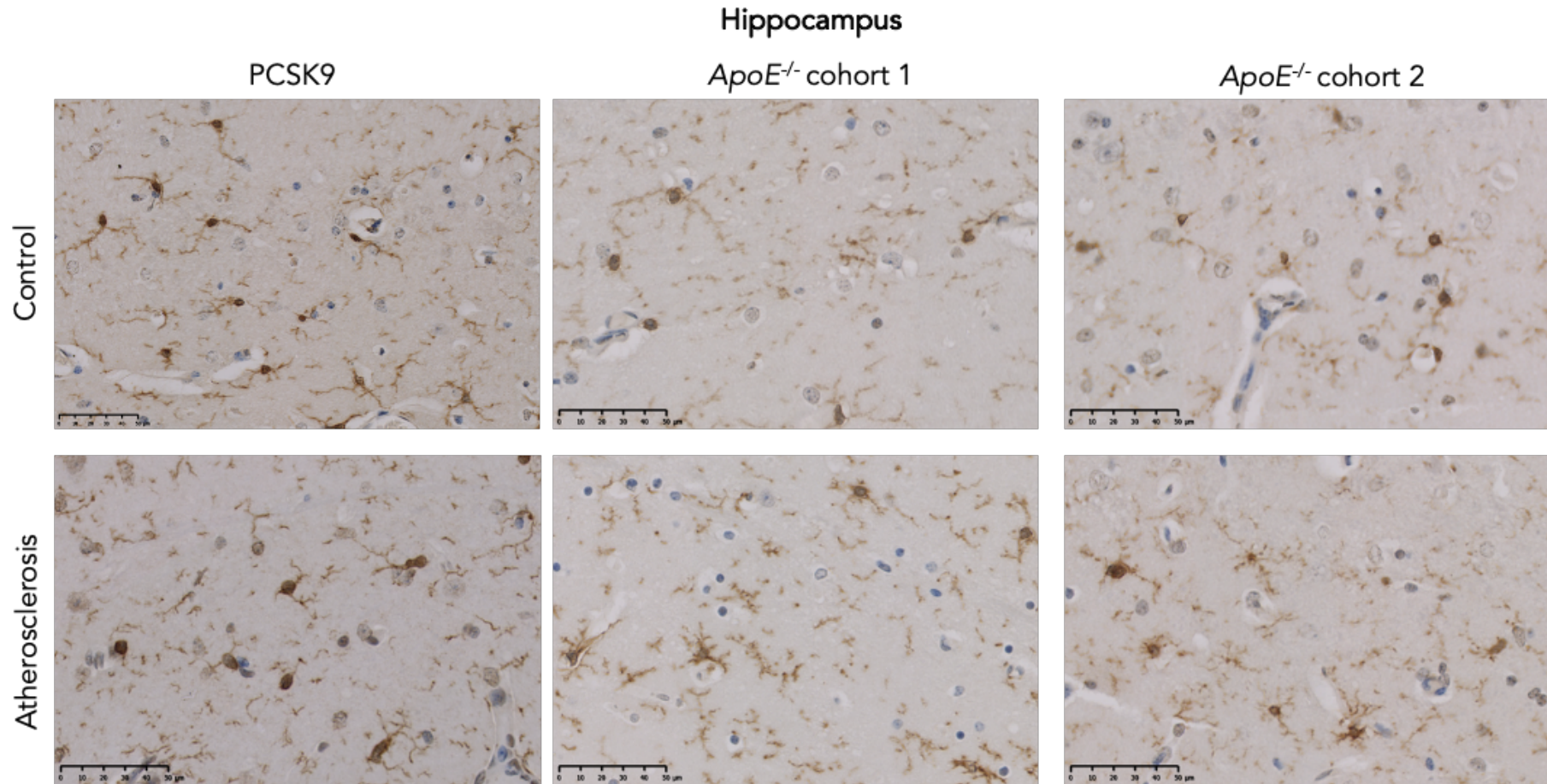


Figure 4.23 Representative image comparing IBA-1 immunoreactive microglia on the hippocampus of controls and atherosclerotic PCSK9 induced mice and *ApoE*^{-/-} cohort 1 and 2

IBA-1 immunoreactive microglia present different morphologies with PCSK9 induced and *ApoE*^{-/-} controls presenting long and thin processes with small rounded cell bodies. The microglia present in the hippocampus of PCSK9 induced appear more immunoreactive than the controls of the other mouse models. Atherosclerotic IBA⁺ microglia of PCSK9 induced mice show similar level of immunoreactivity to *ApoE*^{-/-} cohorts but the processes of *ApoE*^{-/-} mice appear shorter and thicker. PCSK9: Control n= 3, Atherosclerotic n= 6; *ApoE*^{-/-} cohort 1: Control n= 7, Atherosclerotic n= 8; *ApoE*^{-/-} cohort 2: Control n= 6, Atherosclerotic n= 6. Scale bar represents 50 μm.

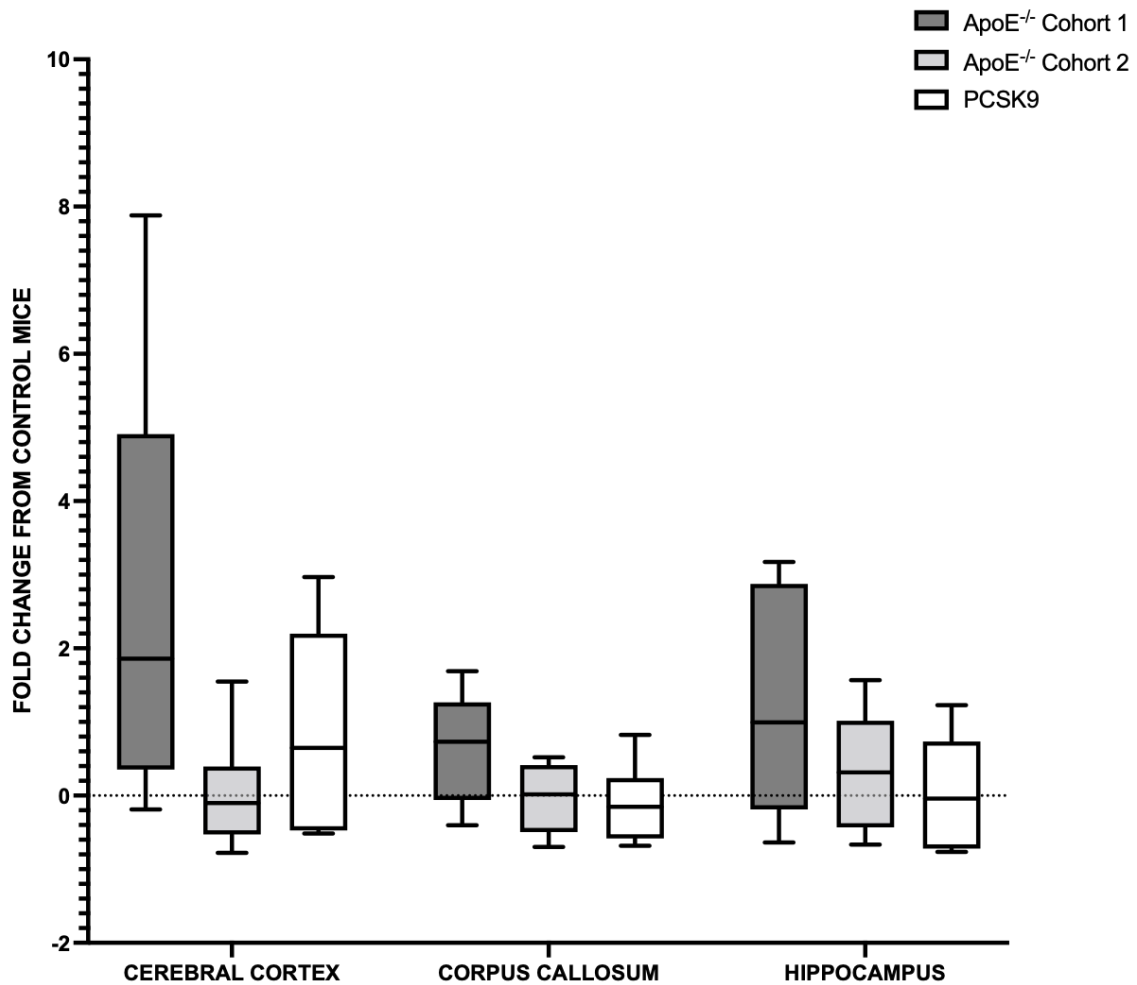


Figure 4.24 Analysis of the fold change between controls and atherosclerotic of PCSK9 induced, *ApoE*^{-/-} cohort 1 and cohort 2 in the cerebral cortex, corpus callosum and hippocampus

The difference of IBA-1 immunoreactivity between controls and atherosclerotic mice seemed greater on *ApoE*^{-/-} cohort 1 mice than PCSK9 induced mice but these results did not reach statistical significance. Compared to *ApoE*^{-/-} cohort 2, PCSK9 induced mice showed a similar level of % area of IBA-1 immunoreactivity.

Table 4.3 Descriptive statistics of IBA-1 immunoreactive microglia preliminary comparison between PCSK9 induced and *ApoE*^{-/-} mouse models (cohort1 and cohort 2).

Minus numbers represent an average fold change in the opposite direction, therefore controls average is lower than atherosclerotic mice % area of immunoreactivity

IBA-1						
Cohort 1						
	Cerebral cortex		Corpus callosum		Hippocampus	
	<i>ApoE</i> ^{-/-}	PCSK9	<i>ApoE</i> ^{-/-}	PCSK9	<i>ApoE</i> ^{-/-}	PCSK9
Mean	2.62	0.87	0.64	-0.11	1.21	0.04
Median	1.86	0.65	0.73	-0.54	0.99	0.04
SEM	1.00	0.57	0.26	0.22	0.53	0.32
P value	0.57		0.17		0.33	

Cohort 2						
	Cerebral cortex		Corpus callosum		Hippocampus	
	<i>ApoE</i> ^{-/-}	PCSK9	<i>ApoE</i> ^{-/-}	PCSK9	<i>ApoE</i> ^{-/-}	PCSK9
Mean	0.02	0.87	-0.03	-0.11	0.34	0.04
Median	-0.10	0.65	0.02	-0.54	0.32	0.04
SEM	0.33	0.57	0.21	0.22	0.33	0.32
P value	0.67		2.39		1.61	

Astrocytes

In the corpus callosum of atherosclerotic PCSK9 induced mice, the GFAP immunopositive cell bodies of astrocytes visually appear to be larger and more easily observed that in the atherosclerotic *ApoE*^{-/-} mice, while controls of PCSK9 induced mice appeared to display less GFAP immunoreactivity than *ApoE*^{-/-} mice controls. Astrocytes in the cerebral cortex of PCSK9 induced mice resembled the GFAP immunoreactive astrocytes in the cerebral cortex of *ApoE*^{-/-} mice, showing an uneven distribution with the number of astrocytes increasing towards the edge of the cortex. Also, GFAP⁺ astrocytes in the control cerebral cortex of PCSK9 induced mice were more abundant with more fine delicate astrocyte processes compared to controls of *ApoE*^{-/-} mice. The astrocytes of atherosclerotic mice from the cerebral cortex of PCSK9 induced and *ApoE*^{-/-} mice showed a similar pattern of staining with the astrocytes in PCSK9 induced model appearing to have weaker GFAP immunoreactivity. The astrocytes of PCSK9 induced control mice hippocampus appeared to have larger cell nucleus and more discontinued processes compared to controls of *ApoE*^{-/-} mice. On the other hand, atherosclerotic PCSK9 induced mice on appeared to have shorter processes with more GFAP immunoreactive astrocytes than *ApoE*^{-/-} atherosclerotic mice.

The fold change describing the quantity of change between the % area of GFAP immunoreactivity of control and atherosclerotic mice showed a non-significant trend to lower change on PCSK9 induced mice compared to *ApoE*^{-/-} in the corpus callosum (Figure 4.28). The cerebral cortex and the hippocampus showed similar values of the means but the medians revealed a non-significant higher fold change in PCSK9 induced mice than in *ApoE*^{-/-} mice (Table 4.4)

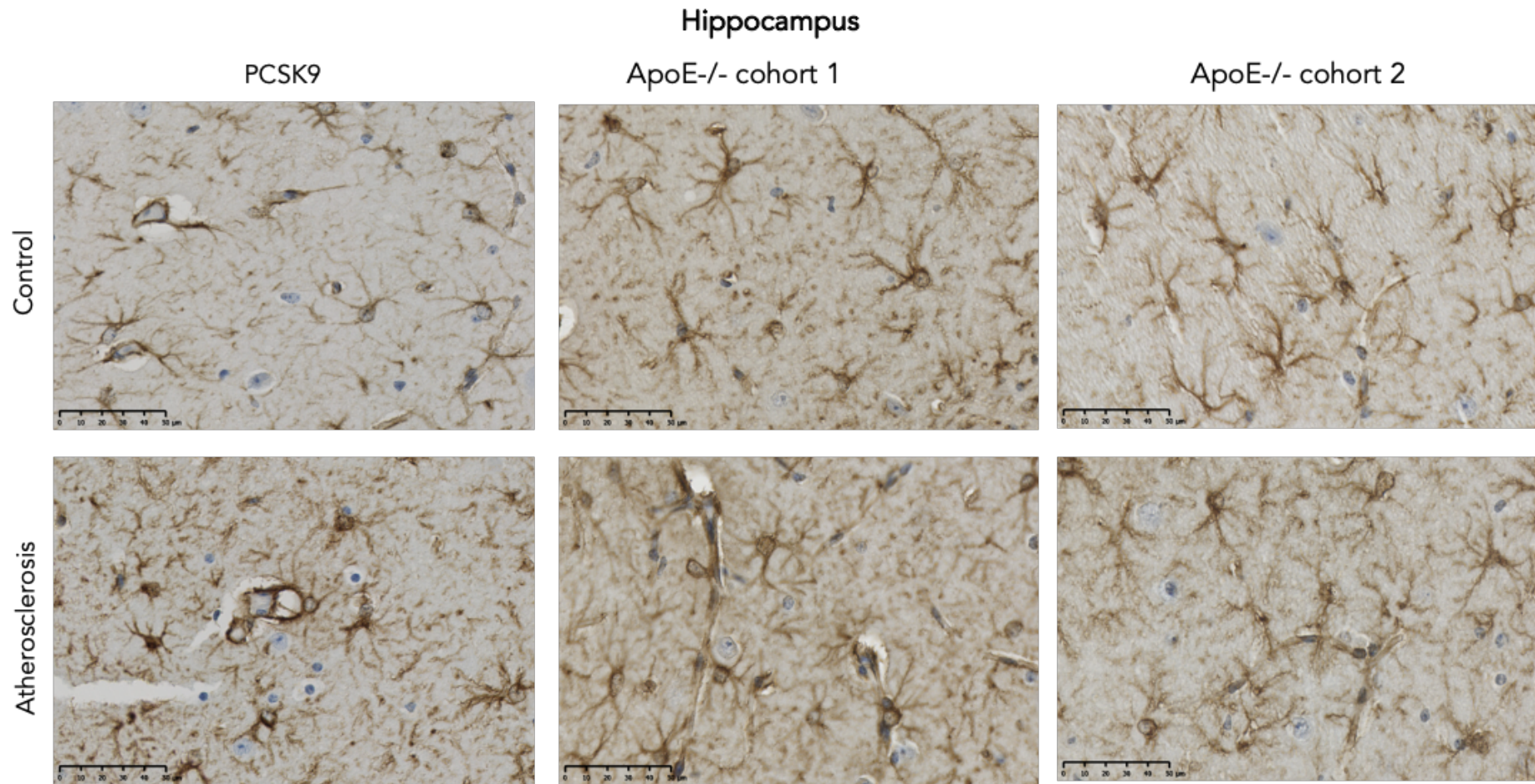


Figure 4.25 Representative image comparing GFAP immunoreactive astrocytes on the hippocampus of controls and atherosclerotic PCSK9 induced mice and *ApoE^{-/-}* cohort 1 and 2

The expression of GFAP in hippocampal astrocytes appeared similar in both *ApoE^{-/-}* cohorts. PCSK9 induced mice seemed to present lower GFAP immunoreactivity in both controls and atherosclerotic mice compared to *ApoE^{-/-}* cohorts. PCSK9: Control n= 3, Atherosclerotic n= 6; *ApoE^{-/-}* cohort 1: Control n= 7, Atherosclerotic n= 8; *ApoE^{-/-}* cohort 2: Control n= 6, Atherosclerotic n= 6. Scale bar represents 50 μ m.

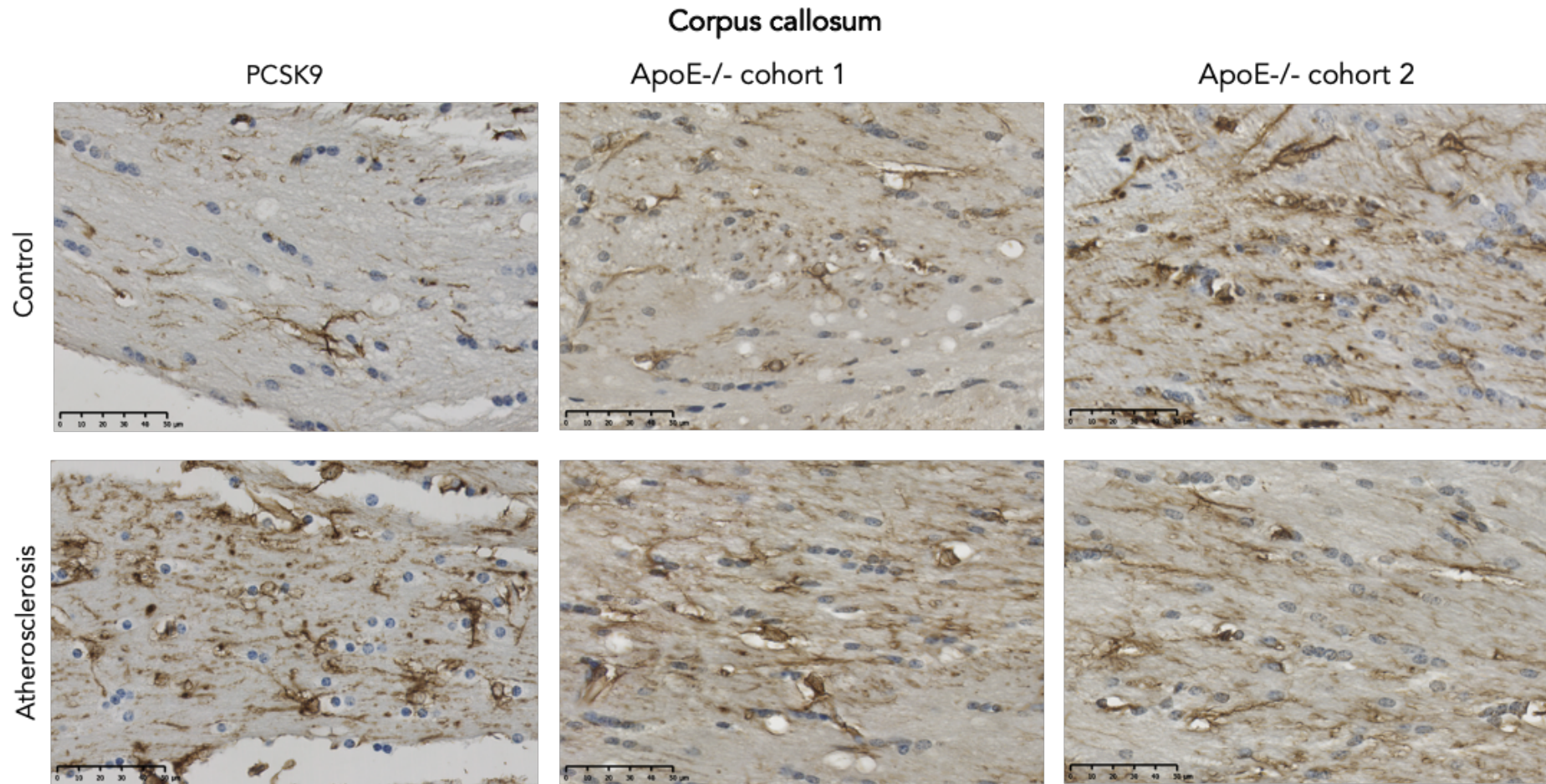


Figure 4.26 Representative image comparing GFAP immunoreactive astrocytes on the corpus callosum of controls and atherosclerotic PCSK9 induced mice and *ApoE^{-/-}* cohort 1 and 2

In the corpus callosum of atherosclerotic PCSK9 induced mice, GFAP immunopositive astrocytes seemed to display larger cell bodies of than in the atherosclerotic *ApoE^{-/-}* mice. Controls appeared to present less GFAP immunoreactivity in PCSK9 induced mice that in both *ApoE^{-/-}* mice cohort controls. PCSK9: Control n= 3, Atherosclerotic n= 6; *ApoE^{-/-}* cohort 1: Control n= 7, Atherosclerotic n= 8; *ApoE^{-/-}* cohort 2: Control n= 6, Atherosclerotic n= 6. Scale bar represents 50 μ m.

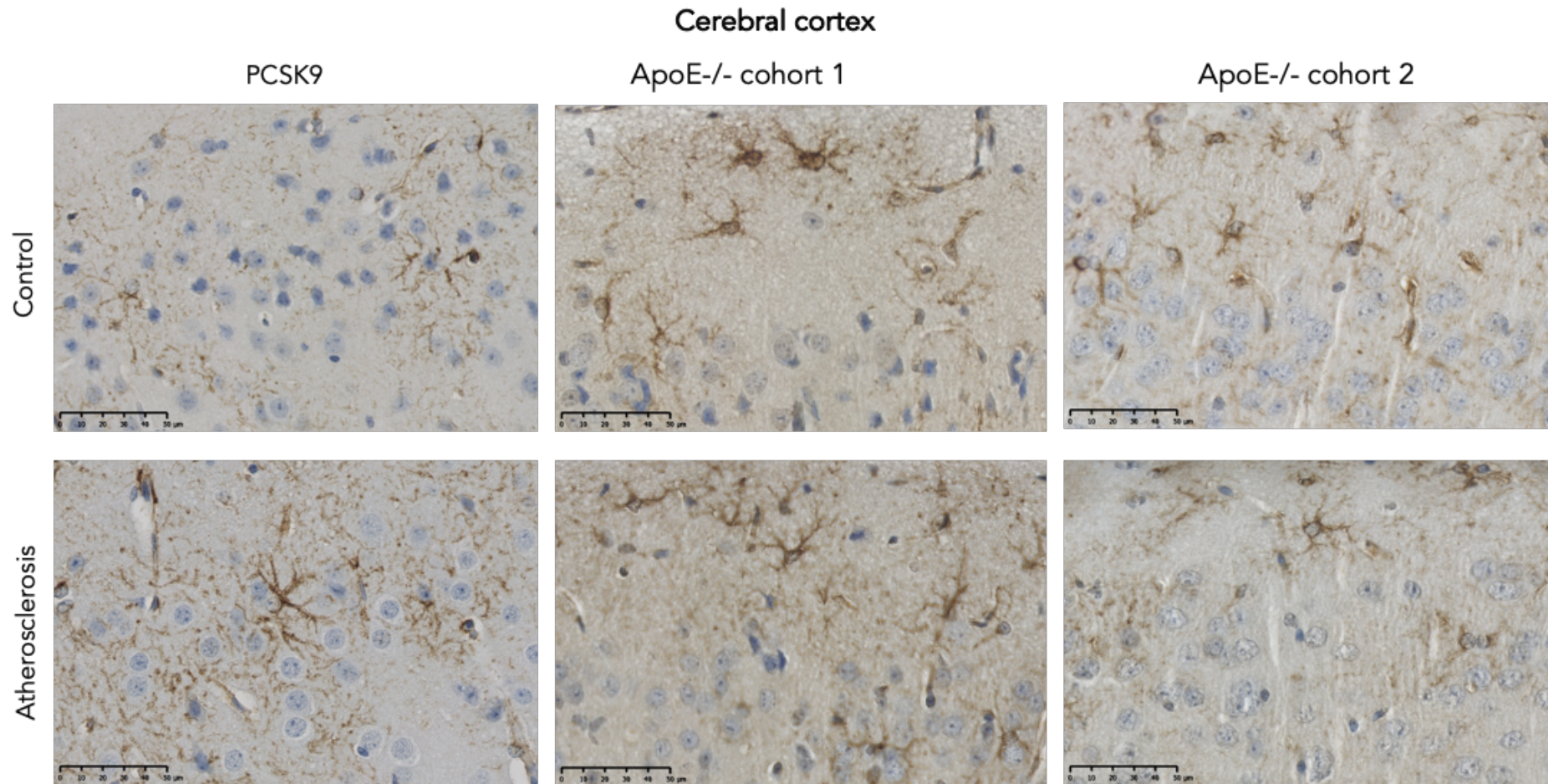


Figure 4.27 Representative image comparing GFAP immunoreactive astrocytes on the cerebral cortex of controls and atherosclerotic PCSK9 induced mice and *ApoE^{-/-}* cohort 1 and 2

GFAP⁺ astrocytes in the control cerebral cortex of PCSK9 induced mice displayed more fine astrocyte processes compared to controls of *ApoE^{-/-}* mice cohorts. The astrocytes of atherosclerotic mice from the cerebral cortex of PCSK9 induced and *ApoE^{-/-}* mice showed a similar pattern of staining with the astrocytes in PCSK9 induced mice appearing to have weaker GFAP immunoreactivity. PCSK9: Control n= 3, Atherosclerotic n= 6; *ApoE^{-/-}* cohort 1: Control n= 7, Atherosclerotic n= 8; *ApoE^{-/-}* cohort 2: Control n= 6, Atherosclerotic n= 6. Scale bar represents 50 μ m.

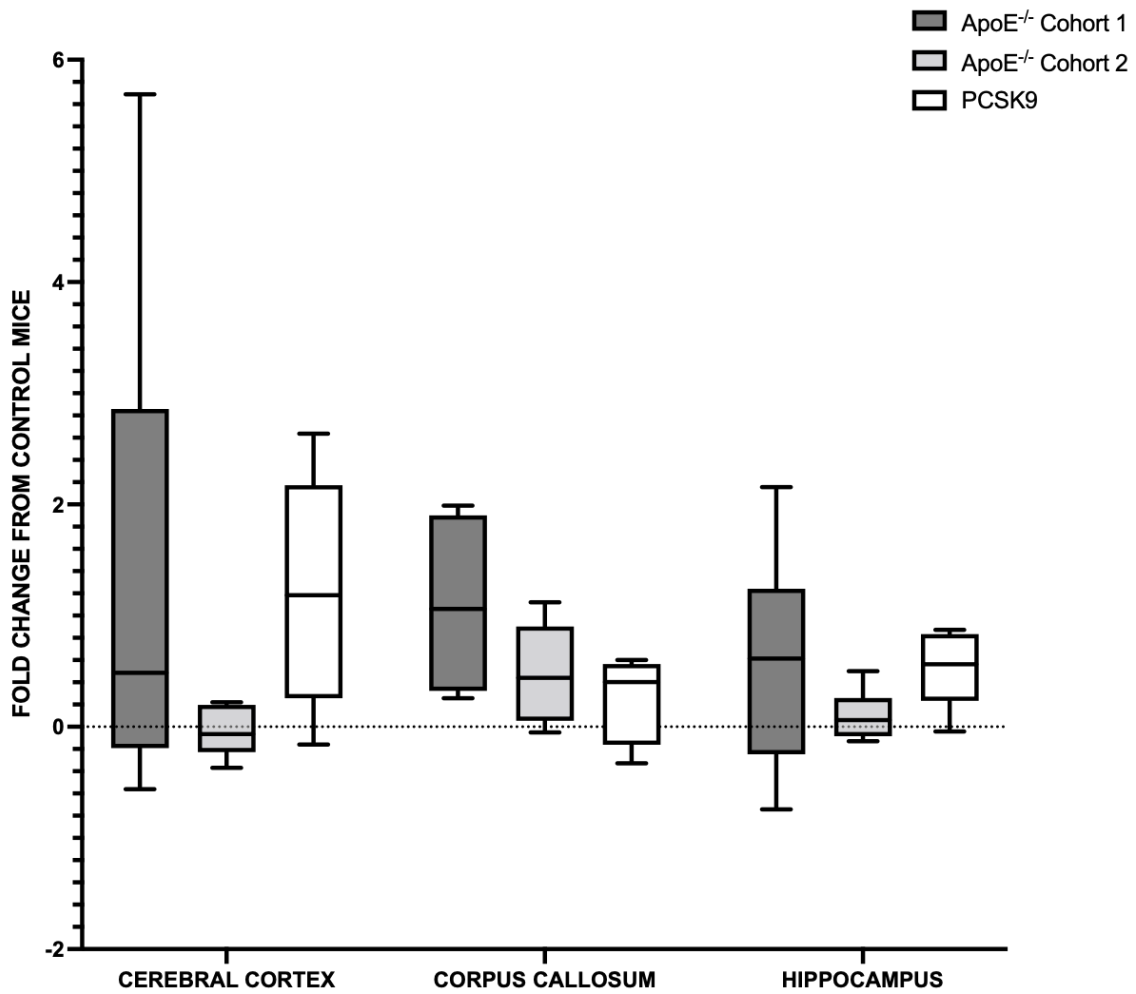


Figure 4.28 Comparison between GFAP fold change of control mice to atherosclerosis in PCSK9 induced and *ApoE*^{-/-} mice

PCSK9 induced mouse model showed no significant difference between the fold change of control to atherosclerotic mice compared to *ApoE*^{-/-} mice. The cerebral cortex expressed the greatest variability values in both models and the hippocampus of *ApoE*^{-/-} also showed high variability.

Table 4.4 Descriptive statistics of GFAP immunoreactive astrocytes preliminary comparison between PCSK9 induced and *ApoE*^{-/-} mouse models (cohort1 and cohort 2).

Minus numbers represent an average fold change in the opposite direction, therefore controls average is lower than atherosclerotic mice % area of immunoreactivity

GFAP						
Cohort 1						
	Cerebral cortex		Corpus callosum		Hippocampus	
	<i>ApoE</i> ^{-/-}	PCSK9	<i>ApoE</i> ^{-/-}	PCSK9	<i>ApoE</i> ^{-/-}	PCSK9
Mean	1.32	1.21	1.10	0.24	0.58	0.54
Median	0.48	1.18	1.06	0.40	0.61	0.56
SEM	0.94	0.47	0.33	0.18	0.40	0.16
Sig.	2.76		0.18		2.78	

Cohort 2						
	Cerebral cortex		Corpus callosum		Hippocampus	
	<i>ApoE</i> ^{-/-}	PCSK9	<i>ApoE</i> ^{-/-}	PCSK9	<i>ApoE</i> ^{-/-}	PCSK9
Mean	-0.05	1.21	0.47	0.24	0.34	0.54
Median	-0.06	1.18	0.44	0.40	0.32	0.56
SEM	0.09	0.47	0.18	0.18	0.33	0.16
P value	0.67		2.39		1.61	

4.3.5 Summary of PCSK9 induced control and atherosclerotic mice characterisation

- Atherosclerotic PCSK9 induced mice were not significantly higher than controls but there was a trend towards higher % area of ICAM-1 immunoreactivity in endothelial cells and microglia and GFAP in astrocytes in all brain areas.
- ICAM-1 immunoreactive blood vessels in the cerebral cortex of PCSK9 induced controls to atherosclerotic fold change was significantly higher than *ApoE*^{-/-} cohort 2 mice
- ICAM-1 immunoreactive microglia in the hippocampus of PCSK9 induced controls to atherosclerotic fold change was significantly higher than *ApoE*^{-/-} cohort 2 mice
- Endothelial cells ICAM-1 immunoreactivity trends towards higher fold change on PCSK9 induced mice than in both *ApoE*^{-/-} mouse cohorts in the corpus callosum, cerebral cortex and hippocampus.
- The fold change of IBA-1⁺ microglia trend towards higher change in *ApoE*^{-/-} cohort 1 compared to PCSK9 induced mice in the corpus callosum, cerebral cortex and hippocampus.

4.4 Discussion

This study aimed to determine whether neuroinflammation in the newer atherosclerotic PCSK9 induced mouse model, which is considered to be a milder model of atherosclerosis and to mimic human atherosclerosis more accurately than other models. The study aimed to determine whether the neuroinflammatory changes observed in the *ApoE*^{-/-} mouse model were replicated, to a lesser extent, in the PCSK9 induced mouse model.

The results demonstrated that, although PCSK9 induced mouse model might be considered a milder model of atherosclerosis, some cellular changes are increased in this model compared to *ApoE*^{-/-} mice. This was evidenced by the increased ratio of atherosclerotic to controls % area of ICAM-1 immunoreactivity in endothelial cells of PCSK9 induced mice compared to *ApoE*^{-/-} cohort 2 mice. Although not significant the fold change of endothelial cell ICAM-1 immunoreactivity appeared higher in all the brain areas of PCSK9 induced mice compared to both *ApoE*^{-/-} mouse cohorts.

The morphology of astrocytes, blood vessels and microglia in atherosclerotic PCSK9 induced mice was consistent with neuroinflammation being present, but, statistical analysis revealed the data did not reach significance. The most recently characterised model of atherosclerosis PCSK9 induced mice, is ideal to study neuroinflammation with functional APOE protein. The current research suggests that the absence of APOE anti-inflammatory properties and involvement of lipoprotein metabolism potentially exacerbates the neuroinflammation observed in *ApoE*^{-/-} mice which is not observed to such extent in all brain areas of the PCSK9 induced mouse model. Additionally, this study highlights that the cellular changes observed in *ApoE*^{-/-} mice are similar on PCSK9 induced mice, endothelial cells, astrocytes and microglia, to a slightly lesser extent which might be associated with APOE anti-inflammatory role.

4.4.1 Comparison of neuroinflammation in the PCSK9 induced and *ApoE*^{-/-} mouse models of atherosclerosis.

PCSK9 and APOE are both involved in cholesterol metabolism but have different mechanisms of actions. APOE function is complex and has been studied for longer. The PCSK9 induced mouse model is a newly characterised model of atherosclerosis and, as such, research has focused on its effect on the liver and peripheral absorption of lipoproteins. PCSK9 binds to LDLR and induces its degradation, reducing the clearance of LDL from the plasma leading to increased serum LDL-cholesterol (Lagace, 2014). This has led to a new single lipid-lowering intervention involving PCSK9 inhibitors as injectable antibodies to PCSK9. However, this has potential adverse effects in cognition, and while these results were considered inconclusive, further research is being conducted to investigate the potential effect of PCSK9 in relation to neurocognitive decline (Apaijai et al., 2019). If such an effect were to be observed it could be due to the potential impact of lowering lipid levels to a threshold where harm could occur, having an effect on PCSK9 in the brain and disrupting the functions of the CNS. As a result, more research is focusing on the role PCSK9 on the brain and its potential involvement in CNS disease.

PCSK9 is highly expressed in the developing mouse brain and in varying concentrations in adult mouse brain, while in humans PCSK9 has been found in the CSF and primary cerebellar neurons (Seidah et al., 2003). In an adult mouse brain PCSK9 does not affect LDLR protein levels under homeostasis but during brain injury (caused by ischaemic stroke) PCSK9 levels are upregulated and reduced LDLR protein levels have been observed in the lesioned dentate gyrus (Rousselet et al., 2011). The reduced LDLR during injury could exacerbate the damage, as PCSK9 interacts with LDLR, VLDLR and APOER2 to transport cholesterol into neurons (Adorni

et al., 2019). Furthermore, the reduced levels of LDLR due to an increased PCSK9 would lead to increase of LDL cholesterol in the circulation and has been linked to increase A β plaque formation by weakening of the BBB through inflammatory mechanisms (Reed et al., 2014)

Increased serum cholesterol on the other hand, also has a detrimental effect on the BBB. De Oliveira et al. (2020) found a positive correlation between plasma cholesterol levels and BBB permeability in the hippocampus of mice, which was also associated with a lack of spatial habituation.

4.4.2 Endothelial cell activation in the cerebral cortex of PCSK9 induced mice is higher than in *ApoE*^{-/-} mice cohort 2

Discrepancies observed between *in vitro* and *in vivo* results in the adult human and mouse brain has been speculated to be due to the role of PCSK9 in cholesterol regulation being cell- and/or tissue-specific. Endothelial cells in blood vessels of the brain showed a trend towards increased expression of ICAM-1 immunoreactivity. This could potentially indicate that the inflammation caused by systemic atherosclerosis in this model is directly related to these changes. While the changes observed *ApoE*^{-/-} mouse cohort 1 higher neuroinflammation associated with microglia, blood vessels endothelial cells might trigger the inflammatory response in the CNS. Potentially the microglia activation is exacerbated by the lack of APOE anti-inflammatory and lipid metabolic functions.

In humans, carotid atherosclerosis is characterised by swelling and expression of adhesion molecules (ICAM-1 and VCAM-1) on endothelial cells and is associated with early cognitive impairment, attributed to cerebral microvascular dysfunction in the frontal and temporal lobes (Matsumoto et al., 2018).

4.4.3 The effect of atherosclerosis on PCSK9 induced mouse brain.

PCSK9 induced atherosclerotic mice presented astrocytes and microglia with an activated morphology, however the % area of immunoreactivity of each of the markers was not significantly different compared to their control littermates. These reactive astrocytes and microglia could potentially damage neurons and lead to a reduction in the number of synapses or neurons. A previous study on atherosclerotic PCSK9 induced mice showed similar microglia morphology to that observed in this study, and furthermore demonstrated it was associated with a reduced neuronal count in the cortex (Shabir et al., 2020b).

Astrocytes are necessary for successful neurovascular coupling and neurovascular coupling is essential for normal metabolic functioning of neurons and the CNS. Astrocytic end-feet facilitate neurovascular coupling and contribute to BBB integrity. Astrocytic end-feet are sensitive to basal Ca^{2+} changes which elicits astrocytes to influence arteriolar tone, without neuronal influence and provide the resting brain with a steady blood flow. It has been shown that a temporary loss of oxygen and glucose (such as in ischemic stroke) causes excitotoxicity in neurons leading to delayed neuronal death (Liu et al., 2020). At the centre of this excitotoxicity is the degradation of mitochondria from astrocyte end-feet, leading to a toxic increase in intracellular calcium Ca^{2+} and glutamatergic activation, leading to neuronal death. It is therefore assumed that astrocyte dysfunction is key to the breakdown of neurovascular coupling and therefore many neurological conditions including neurovascular dysfunction.

Research on the atherosclerotic PCSK9 induced mouse model has shown a reduced vasodilation in the somatosensory cortex during sensory stimulation of the mice whiskers, in association with increased neuroinflammation (changes in microglia

morphology, increased IL-1 β and TNF α) and impaired neurovascular coupling (Shabir et al., 2020a).

4.4.4 Possible link between atherosclerotic PCSK9 induced mice and neuroinflammation

Neurodegeneration due to vascular causes involves multiple factors and complex interactions. The presence of APOE protein enables investigation of the link between cholesterol load with atherosclerosis, APOE and VCID. In the PCSK9 induced mice model, APOE protein is present, and its anti-inflammatory effects are not silent, in contrast to the *ApoE*^{-/-} mouse model, and as such, the results from this research present cellular morphology resembling neuroinflammation which elucidates the effect of systemic atherosclerosis in neurovascular and glial changes more accurately. In PCSK9 induced atherosclerotic mice a possibility is that an increase in cholesterol levels might induce dysfunction of glial cells, the NVU and other supportive elements in the brain causing neuronal damage. Furthermore, LDLR, is also responsible for clearing APOE, a protein known to influence the accumulation of A β a driver of AD. Downregulation of LDLR due to increased cholesterol also serves as one possible explanation for the increased incidence of dementia in patients with atherosclerosis and hypercholesterolaemia. Strikingly, numerous dementia-associated genes (i.e., *APOE*, *ABCA1*, *ABCA7*, *CLU*, *PLC γ 2*, *TREM2*) are critical to lipid homeostasis and are also expressed in microglia and astrocytes (Verheijen and Sleegers, 2018). Studies in mouse models demonstrate that deficiency of either APOE or TREM2 impairs phagocytosis, abrogates clearance of myelin-derived lipids, and promotes CE build-up (Nugent et al., 2020).

4.4.5 Limitations

The sample size in the control was $n = 3$ mice which reduces the statistical power of the test. A small sample size makes it difficult to determine if the results from the analysis are a true finding and the null hypothesis might be incorrectly accepted. In order to increase the statistical power of this experiment a $n = 11$ in both controls and atherosclerotic mice is necessary.

Genetically altered mice have been used to recapitulate human disease, including heart disease, cancer, diabetes and AD, partly because of the ease and success of genetic manipulation. However, despite the genetic similarities between murine models and humans, they are criticised due to their failure to accurately mimic all aspects of human disease phenotypes. The mouse model used in this study counteracts the disadvantages of a knock-out model, and greatly improves the understanding of systemic atherosclerosis and its progression, proving a useful tool for discovering targets for therapeutic drugs. The use of AAVs appears safe and without pathogenicity, however one might still consider a possible anti-viral host immune response of mice (Daya and Berns, 2008). Other studies are required to further investigate the effect of PCSK9 in cognition, and to investigate if the changes observed are in relation to an increase hypercholesterolemia and atherosclerosis as a result of the gain of function PCSK9 or other functions that PCSK9 might be involved in, such as cholesterol dysregulation on astrocytes. Although previous studies have shown cell-mediated immune responses to AAV vectors in response to interperitoneally and intravenous administration only, further investigation would benefit from showing that the changes observed in glial morphology are a response to atherosclerosis and not a potent immune response to AAV. PCSK9 in the CNS is still

poorly understood and further research is necessary to understand the long term effect it might have in inflammation, immunity and cognition.

4.4.6 Conclusion

Systemic atherosclerosis is associated with cognitive decline and cerebrovascular disease, but the mechanisms underlying the pathogenesis are unknown. The current study interrogated the morphology and expression of astrocytes, microglia and endothelial cells in controls and atherosclerotic mice to identify the presence of neuroinflammation and its association with systemic atherosclerosis.

The PCSK9 induced mouse model seems to be a milder model of atherosclerosis including its effects on neuroinflammation. While ApoE mice model is better to study more advanced atherosclerosis and investigate the potential molecular factors involved in plaque formation and neuroinflammation.

***CHAPTER V: MICROARRAY ANALYSIS OF THE
HIPPOCAMPUS TRANSCRIPTOME IN APOLIPOPROTEIN
E KNOCKOUT MOUSE MODEL OF ATHEROSCLEROSIS***

5.1 Introduction

In Chapter 3, the morphological and quantitative characterisation of atherosclerotic *ApoE*^{-/-} mice revealed an increase in IBA-1 and ICAM-1 immunoreactivity in microglia in cohort 1, also reflected by the observed morphological changes in all the investigated areas, with the corpus callosum also showing increased immunoreactivity of GFAP in astrocytes and ICAM-1 in endothelial cells associated with astrogliosis and inflamed blood vessels respectively. The assessment of these mice suggested a neuroinflammatory response present in atherosclerotic *ApoE*^{-/-} mice. Potentially the brains of *ApoE*^{-/-} mice fed with a high-fat diet could present a different transcriptomic profile to *ApoE*^{-/-} mice fed with a control diet. To identify any gene expression changes, microarray analysis was used to assess differences in the transcriptome of control and atherosclerotic *ApoE*^{-/-} mice hippocampus.

Microarrays enable analysis of gene expression patterns of thousands of genes in a single experiment, making them a powerful large-scale gene expression analysis method (Gwon et al., 2019). Transcription profiling has been applied in atherosclerosis research using animal models, cell cultures and human samples (Tuomisto et al., 2005). Although *ApoE*^{-/-} mouse model has been previously investigated in relation to obesity, aging and oxidised phospholipids, studies focused on blood, adipose, liver or arterial (mainly aortic) tissue (Csiszar et al., 2004; Furnkranz et al., 2005; Gwon et al., 2019; Han et al., 2013; Lee et al., 2004; Takahashi et al., 2003). Previous microarray studies have linked vascular changes and atherosclerosis to risk factors and associated pathologies such as increasing age and hypertension. A transcriptomic analysis using mice fed with a high fat diet that present impaired performance of cognitive task revealed dysregulation of genes associated with neuronal signalling and oligodendrocyte dysfunction in the cortex (Yoon et al., 2019)

While microarray analysis has provided valuable information about changes in the expression of mRNA transcripts, and pathways involved in atherosclerosis and its risk factors, to date, gene expression microarray studies have not investigated systemic atherosclerosis associated transcriptomic changes in the brains of *ApoE*^{-/-} mice or in relation to neuroinflammation. The exact inductors and mechanisms by which systemic atherosclerosis elicits a response in the CNS have not been investigated. Furthermore, the expression and composition of a neuroinflammatory phenotype in *ApoE*^{-/-} mice brain has not been described in detail. Possibly, the pathways that modulate the neuroinflammatory response and endothelial cell activation in systemic atherosclerosis are present in the CNS. Therefore, the current research used microarray profiling approach to detect changes in atherosclerotic mice, focusing on the hippocampus due to its importance in cognitive impairment. Analysis of the array data focused on identifying genes of interest and pathways linked to neuroinflammation, neurovascular dysfunction and changes in lipid metabolism as a downregulation of receptors regulating metabolic pathways could potentially indicate an increase LDL accumulation driving the neuroinflammatory changes.

5.2 Aims and objectives

The aim of the experiments presented in this chapter was to perform a detailed characterisation of the transcriptomic profile of *ApoE*^{-/-} mouse hippocampus and identify relevant gene expression changes in response to atherosclerosis due to high fat diet consumption. The hypothesis is that systemic atherosclerosis without vascular occlusion leads to changes in gene expression in the brain.

This was achieved by:

- Isolating the hippocampus from frozen *ApoE*^{-/-} mice brain sections using LCM and obtaining quality RNA to use in transcriptomic analysis.
- Performing a detailed transcriptomic analysis of cohort 2 *ApoE*^{-/-} mice hippocampus and identifying biologically relevant gene expression changes in response to high-fat diet known to cause atherosclerosis, using microarray analysis.
- Performing pathway functional grouping analysis of the microarray results to identify candidate genes and specific pathways linked to atherosclerosis and high-fat diet.
- Validating the expression of selected gene candidates that are biologically relevant by quantitative polymerase chain reaction (qRT-PCR) and interrogating the expression of these genes in the cerebral cortex of the same mice.

5.3 Results

5.3.1 Characterisation and isolation of the *ApoE*^{-/-} mouse hippocampus for gene expression analysis

RNA integrity from frozen *ApoE*^{-/-} mice hippocampus

The left half of the brain from twelve mice from *ApoE*^{-/-} cohort 2 were snap frozen to study the transcriptomic profile of the atherosclerotic hippocampus. The hippocampus from controls (n=6) and the atherosclerosis (n=6) cases were isolated using LCM and RNA extraction of each case carried out. The RNA quality of the samples pre- and post-LCM was determined for all the samples, to assess the impact of the LCM procedure on the quality of the mRNA obtained from the hippocampus (Figure 5.1). The mean of the samples pre-LCM RIN was 4.58 (range 2.7 – 6.3) in controls and 3.72 (2.9 – 5.2) in atherosclerotic mice. Representative electropherograms of the pre-LCM profile for cases with a high and low RIN number are shown in Figure 5.1.

Following LCM, the RNA quantity and quality of each sample were assessed. On average, 5.13 ng/μl (range 3.16 – 5.23 ng/μl) RNA was extracted from the hippocampus of control samples, with an average RIN of 3.7 (range 3.1 – 4.4). From the atherosclerotic cases on average 1.86 ng/ul (range 0.15 – 4.79 ng/μl) RNA was extracted from the hippocampus with an average RIN of 1.86 (0.15 – 4.79). However, the RIN of two control samples (control 2 and 5) and one atherosclerotic sample (atherosclerotic 2) were not detectable (Table 5.1).

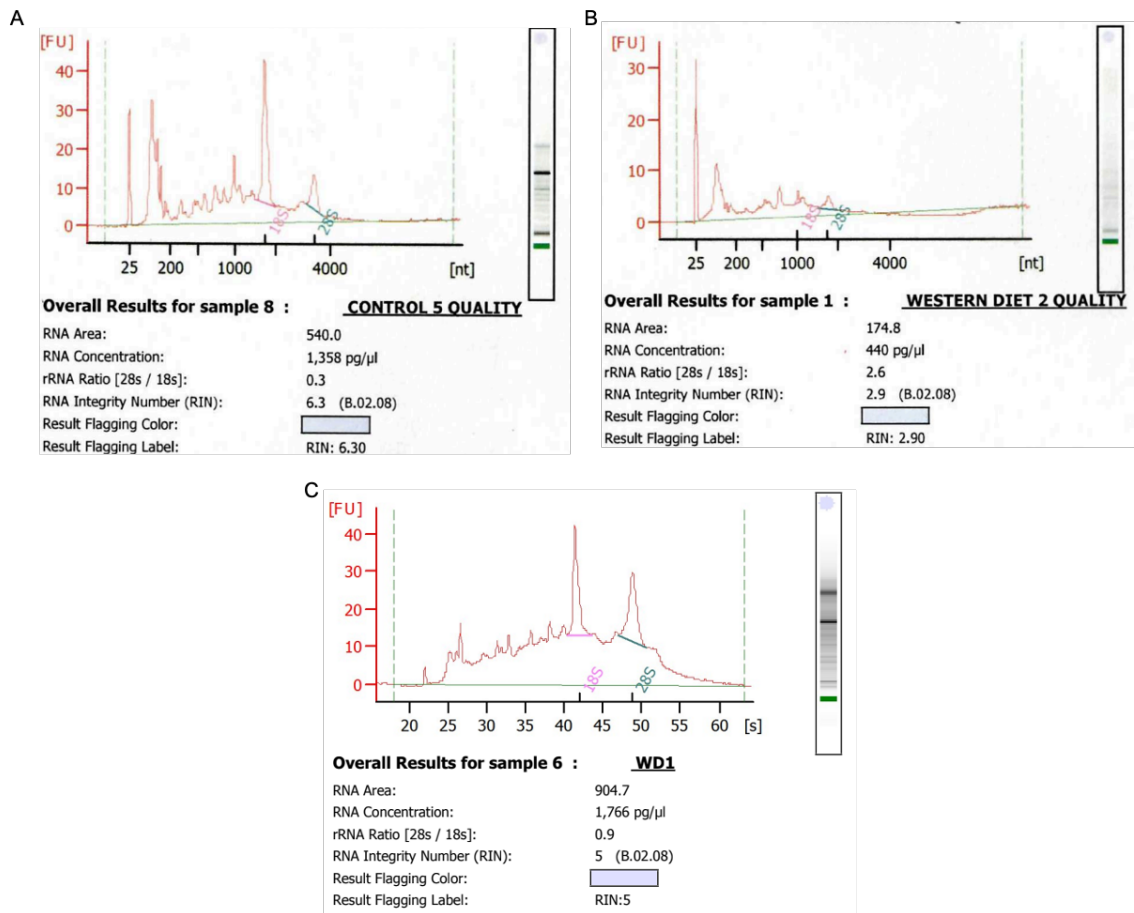


Figure 5.1 RNA integrity of pre- and post- LCM RNA profile

The quality of RNA extracted from each case of the *ApoE*^{-/-} cohort was analysed on an Agilent Bioanalyzer. An example of a high RIN sample prior to LCM (A) and lower RIN sample (B). Representation of the electropherogram profile from LCM-ed *ApoE*^{-/-} mouse hippocampus. Labelled peaks illustrated in the figures represent 18S and 28S ribosomal RNA. (FU: fluorescence unit).

Table 5.1 *ApoE*^{-/-} and Control hippocampal RNA quality and quantity

RNA quality, pre- and post-LCM and the concentration of extracted RNA from each *ApoE*^{-/-} hippocampal brain sample.

Diet group	Case	Pre-LCM RIN	Post-LCM RIN	RNA concentration (ng/μL)
Normal diet	Control 1	ND	3.1	6.57
	Control 2	2.7	ND	5.23
	Control 3	4.7	4.4	6.39
	Control 4	4.7	4.1	3.16
	Control 5	6.3	ND	5.00
	Control 6	4.5	3.2	4.41
	Mean (Range)	4.58 (2.7 - 6.3)	3.7 (3.1- 4.4)	5.13 (3.16 - 5.23)
Western diet	Atherosclerotic 1	3.3	3.4	1.80
	Atherosclerotic 2	2.9	ND	0.83
	Atherosclerotic 3	3.8	2.7	0.40
	Atherosclerotic 4	5.2	3.4	3.20
	Atherosclerotic 5	ND	3.2	0.15
	Atherosclerotic 6	3.4	3.5	4.79
	Mean (Range)	3.72 (2.9 - 5.2)	3.24 (2.7- 3.5)	1.86 (0.15 - 4.79)

However, while the RIN is a good indicator of RNA integrity, the RNA profile should also be considered, and in all cases (even those where a RIN was not available) the RNA profile indicated that the RNA extracted from the cases was comparable between cases and of suitable quality for downstream transcriptomic profiling. A representative electropherogram post -LCM profile is shown in Figure 5.1C

RNA preparation for microarray analysis

The yield of cRNA from the RNA intended to be used for microarray analysis, was measured with a NanoDrop 1000 followed by the purification of ss-cDNA (Table 5.2). Then, 16 µl of cRNA was reverse transcribed for the synthesis of ss-cDNA, and the yield measured using spectrophotometry (Figure 5.1).

5.3.2 Microarray quality control measures

Labelling controls

As mentioned in the methods section, poly-A controls were used to monitor the efficiency of cRNA labelling and TAC was used to analyse the data quality. These controls are derived from *Bacillus Subtilis* (*Dap*, *Thr*, *Phe*, *Lys*) and were spiked into the RNA samples at different concentrations in the following order: *Lys*, *Phe*, *Thr* and *Dap* (1:100,000, 1:50,000, 1:25,000 and 1:6,667, respectively). In this study the patterns of labelling efficiency differed for the Poly-A RNA controls across the samples. The labelling controls do not follow the stepwise expected with the decreasing concentrations but, almost all of the samples showed similar pattern except for two samples (atherosclerotic 4 and atherosclerotic 5) (Figure 5.2).

Table 5.2 Concentrations of cRNA after ss-cDNA synthesis and of ss-cDNA obtained after the second amplification cycle

Condition	Case	cRNA concentration (ng/ μ L)	ss-cDNA concentration (ng/ μ L)
Normal diet	Control 1	3438	823
	Control 2	3481	819
	Control 3	3576	874
	Control 4	3762	1064
	Control 5	3662	845
	Control 6	3710	822
Western diet	Atherosclerotic 1	3451	753
	Atherosclerotic 2	3744	876
	Atherosclerotic 3	3617	794
	Atherosclerotic 4	1457	472
	Atherosclerotic 5	741	311
	Atherosclerotic 6	3717	934
	Mean	3196.40	782.25
	\pm SD	955.30	193.10

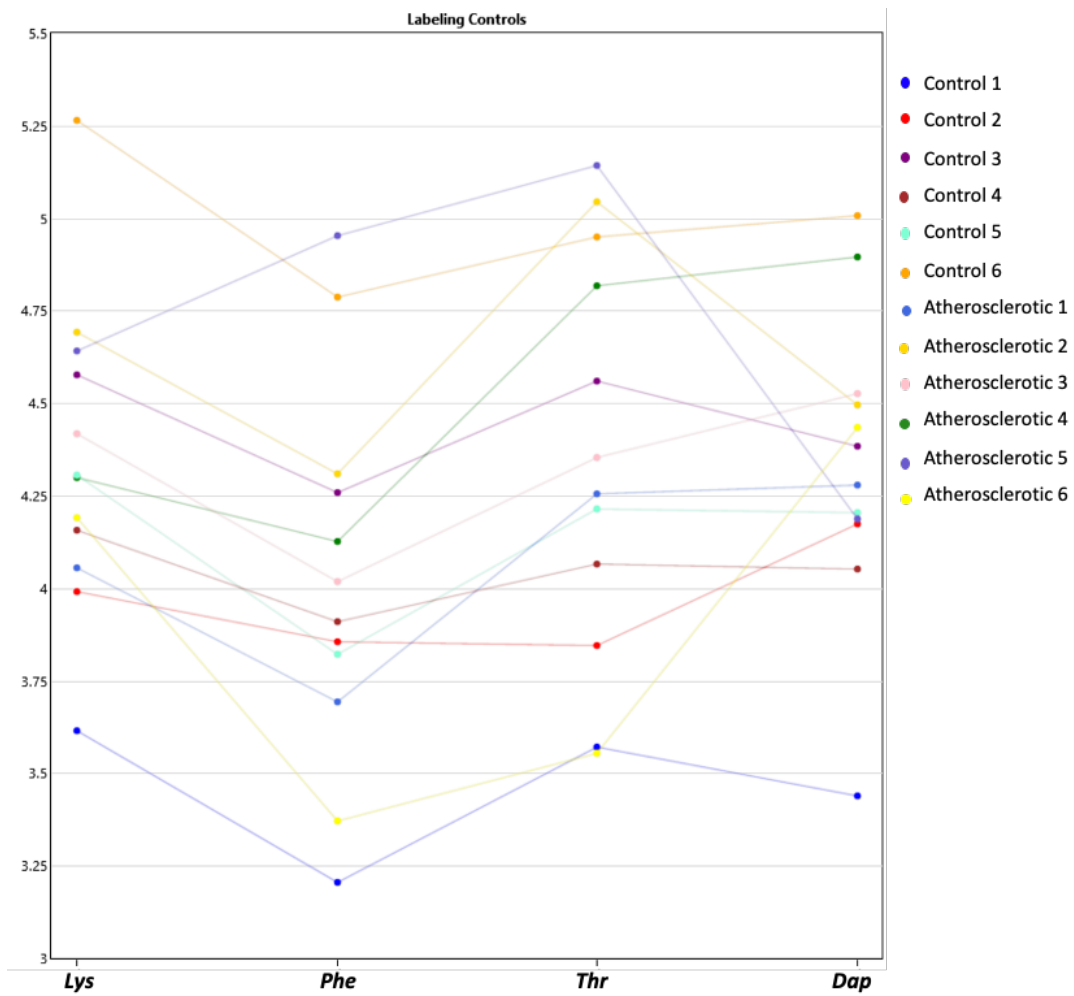


Figure 5.2 Poly-A RNA spike-in controls

Signal intensities plot depicting the mean signal intensities of Poly-A controls (*Lys*, *Phe*, *Thr* and *Dap*) which were added to all samples.

Hybridisation and signal quality

In this assessment, the eukaryotic hybridisation controls were added into the hybridisation mix, which were composed of biotin-labelled cRNA transcripts from *E. Coli* (*BioB*, *bioC*, *bioD*) and the P1 bacteriophage (*Cre*) in a concentration of 1.5 pM, 5 pM, 25 pM and 100 pM, respectively. The hybridization controls (*BioB*, *BioC*, *BioD*, and *Cre* biotin-labeled transcripts) were spiked into the hybridization cocktail. They were used to align the grid and assess the efficiency of hybridization, washing and staining.

Analysed microarray signals for all hybridisation revealed an increasing signal intensity concentration in all samples from *BioB* to *Cre*, except for atherosclerotic 4 and atherosclerotic 5 samples which were removed from the analysis (Figure 5.3).

Signal intensities across the arrays

Affymetrix Expression Console Software enables the assessment of signal intensities generated from microarrays which can be plotted as a histogram. In this data, the signals from the arrays were comparable across 10 samples, with two samples showing higher signal intensity (Figure 5.4). The MicroArray Suite (MAS) 5.0 software was also used to compare of signal intensity detected for each probe set in the arrays against the median signal value across all arrays, the calculation method is known as Relative Log Expression (RLE). These data were represented as a plot to assess the spread of data across the samples. The mouse hippocampus samples showed a similar spread of RLE in 10 of the arrays with two samples presenting a different result (Figure 5.5). Based on these quality control tests, atherosclerotic sample 4 and 5 were not included in any further analysis.

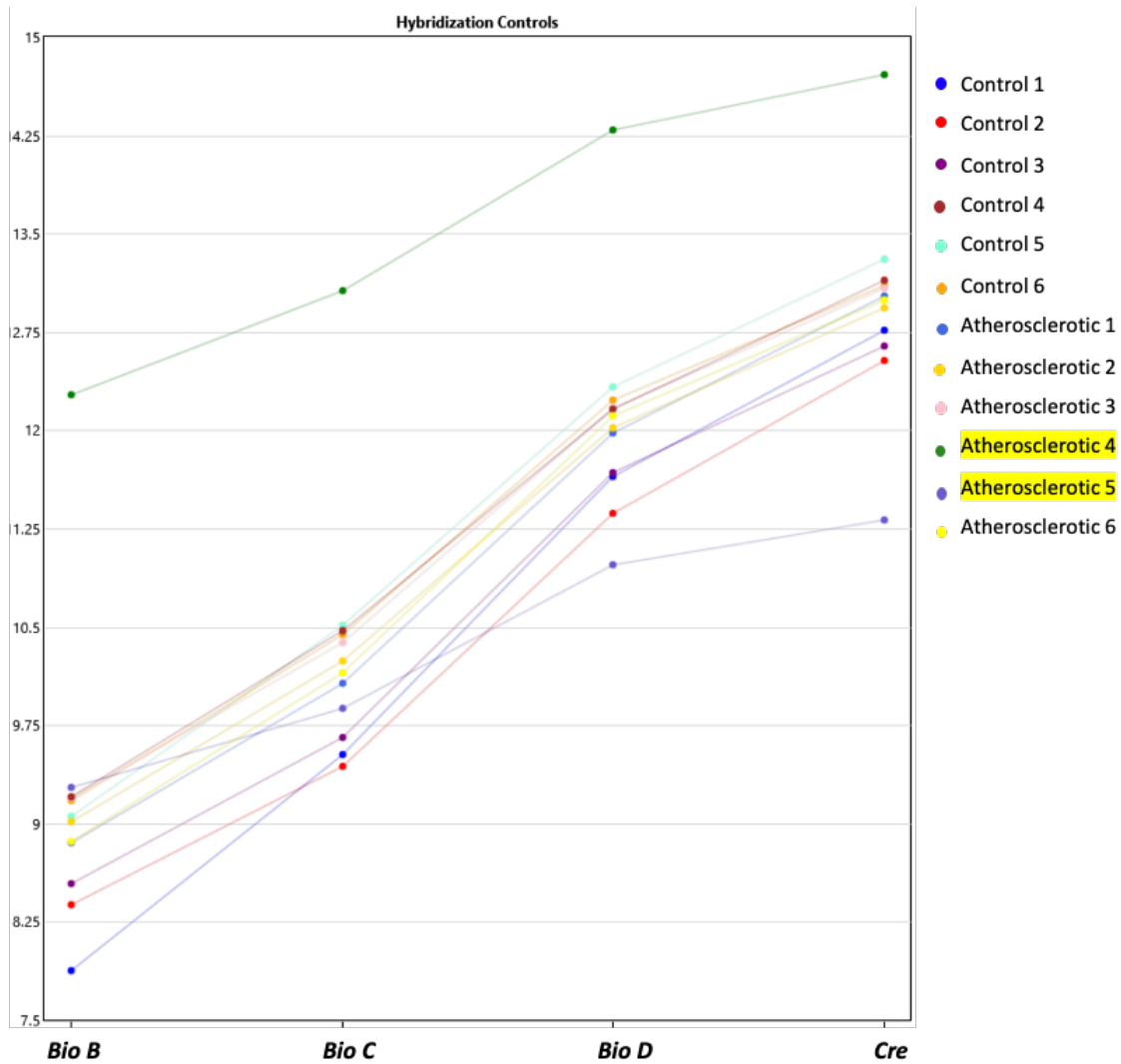


Figure 5.3 Hybridisation control assessments for the hippocampus of controls and atherosclerotic mice.

The mean signal intensity of hybridisation controls (BioB, BioC, BioD, and Cre), showed an appropriate increase of signal intensity (y-axis) in all control, and four atherosclerotic mouse hippocampus samples. Yellow: outlier samples.

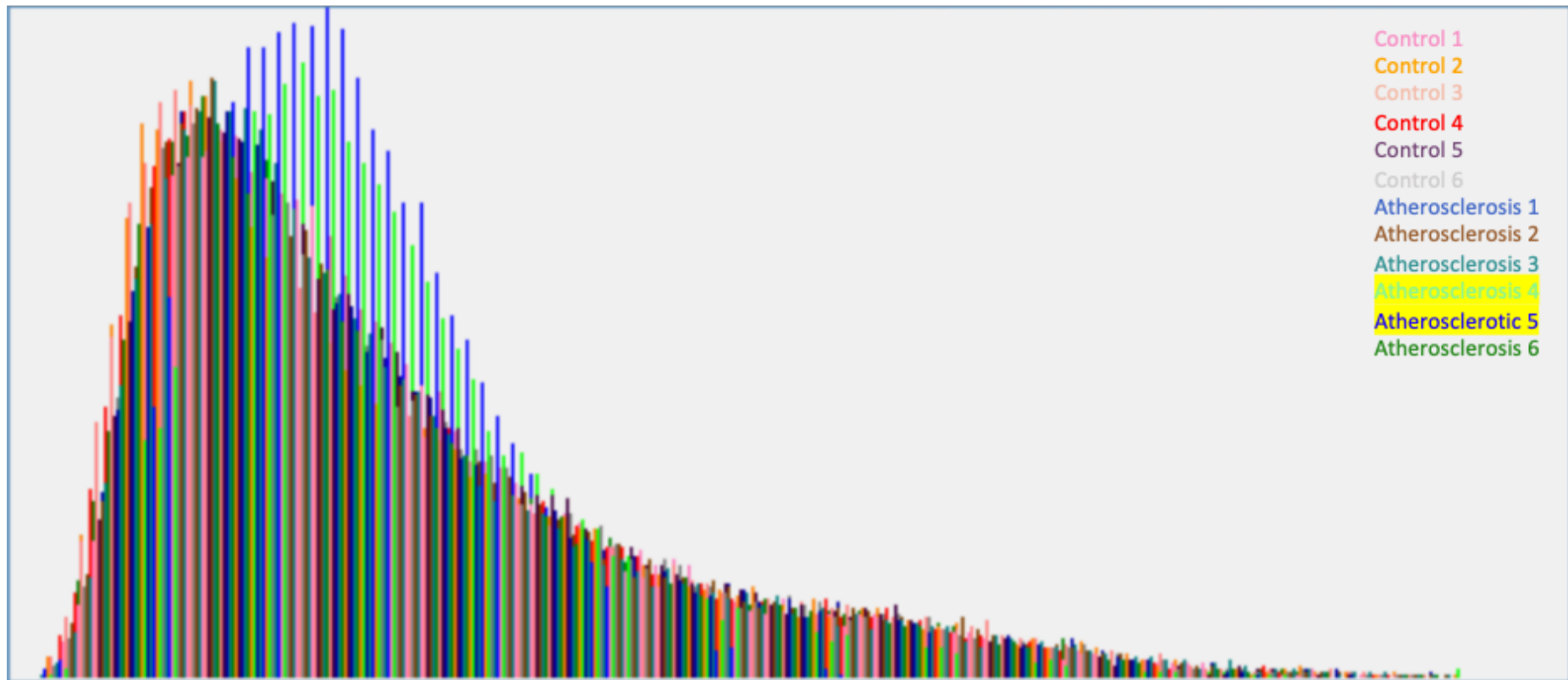


Figure 5.4 Overall signal intensities histogram for the periventricular microarrays

Signal histogram illustrating the signal intensities of the probe sets in the selected 12 samples. While 10 signals from the arrays were the same across all the samples while 2 samples (highlighted in yellow) showed a different pattern of expression. Samples Atherosclerosis 4 and Atherosclerosis 5 were excluded from the analysis.

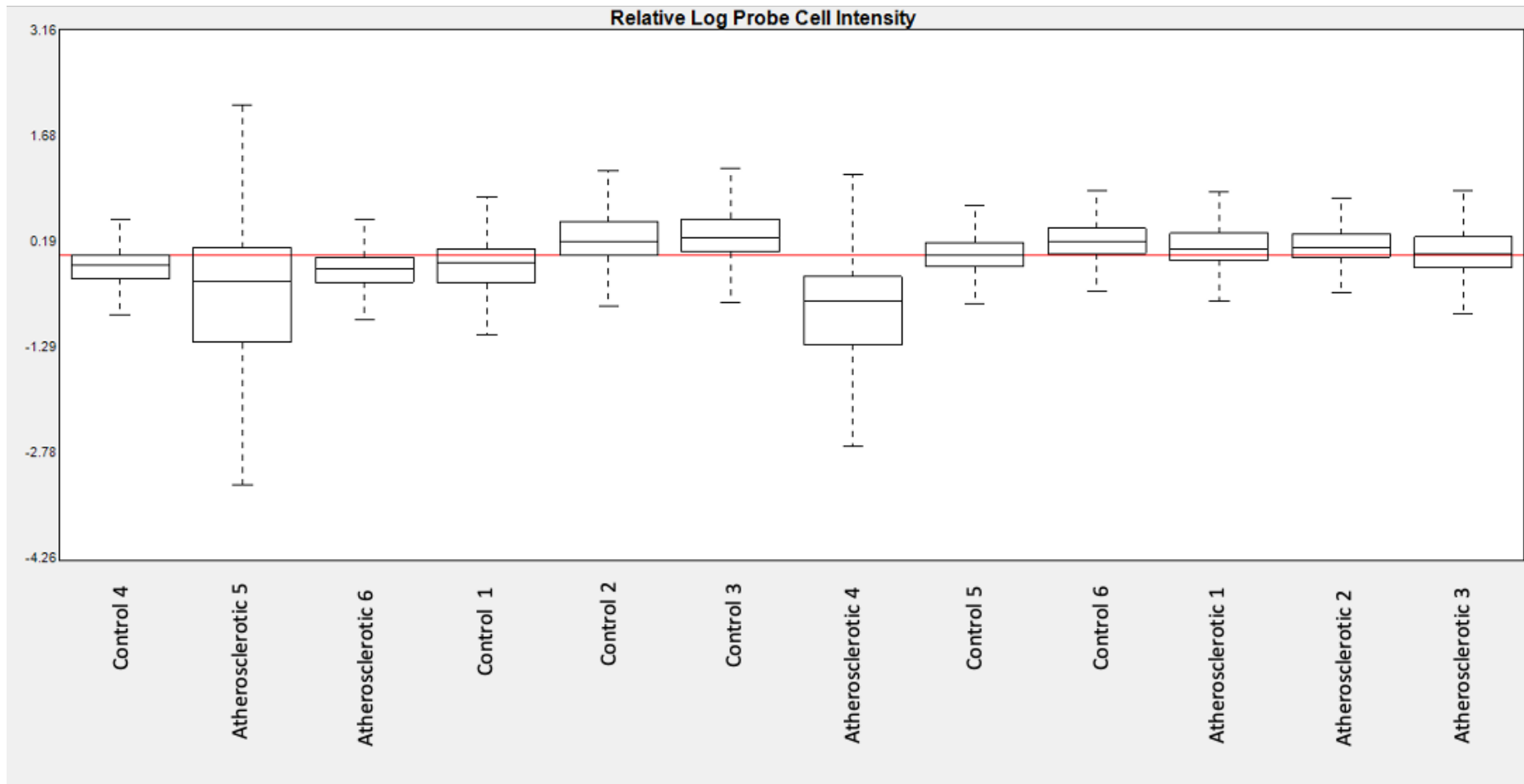


Figure 5.5 Relative log expression (RLE) box plots for the hippocampus arrays

Box plot representation of the median gene expression in all 12 microarrays. Relative log expression signal (y-axis) for all the 12 samples (X-axis).

5.3.3 Microarray analysis

Transcriptomic analysis and comparison of the gene expression

Transcriptomic analysis of the hippocampus was conducted using the mouse genome 430 2.0 microarray, which contained 45,000 probe sets representing over 34,000 genes. Genes were considered significantly differentially expressed if they had a minimum fold change (FC) of ≥ 1.2 and a p-value ≤ 0.05 . A total of 1377 genes were differentially expressed in control and atherosclerotic mice with 612 genes being up-regulated and 765 down-regulated. The UP-REGULATED and DOWN-REGULATED genes with the highest fold change are identified on Table 5.3 and Table 5.4 respectively.

Candidate analysis

Previous to the enrichment analysis, the lists of differentially expressed transcripts were examined for the presence of dysregulated transcripts from common neuroinflammatory, atherosclerosis and neurodegeneration markers, shown in Table 5.5. The atherosclerotic mice presented UP-regulation of inflammatory marker IBA-1 (*Aif1*), TGF- β 1 (*Tgfb1*), TREM2 (*Trem2*) and AD risk markers ACE (*Ace3*) and DOWN-regulation of SLC16a13 (*Slc16a13*) and vascular markers LDLRAD4 and LDLRAD3 (*Ldlrad4* and *Ldlrad3*), LRP8 (*Lrp8*), APOL8 (*ApoL8*), ABCG2 (*Abcg2*) (Table 5.5). However the other inflammatory genes investigated GFAP (*GFAP*), MHCII (*MHCII*), IL-6 (*IL6*), IL-1 (*IL1*) and/or IL-8 (*CXCL8*), TNF α (*TNF α*), VLDLR (*Vldlr*) were not significantly altered in *ApoE*^{-/-} atherosclerotic mice against control mice fed a chow diet. A functional annotation analysis was then performed to identify dysregulated pathways in the controls and atherosclerotic *ApoE*^{-/-} mouse hippocampus that could be related to the development of neuroinflammation and neurovascular unit damage.

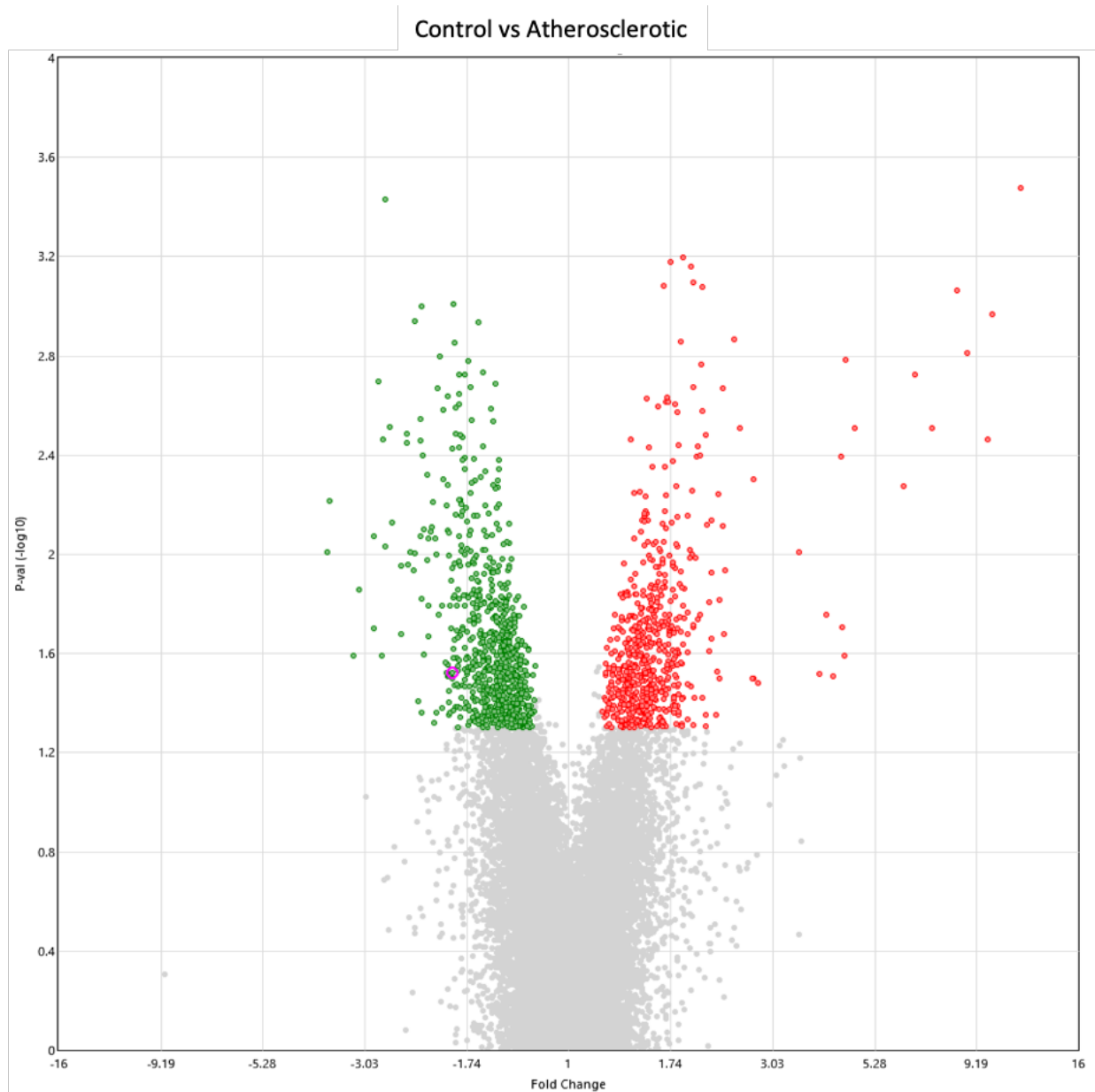


Figure 5.6 Volcano plot of differential gene expression of control and atherosclerotic *ApoE*^{-/-} cohort 2 mice hippocampus

Volcano plot representing the differentially expressed genes in control mice compared to atherosclerotic mice. A total of 1,377 genes were identified with 612 genes UP-REGULATED (red), whilst 765 genes were DOWN-REGULATED (green).

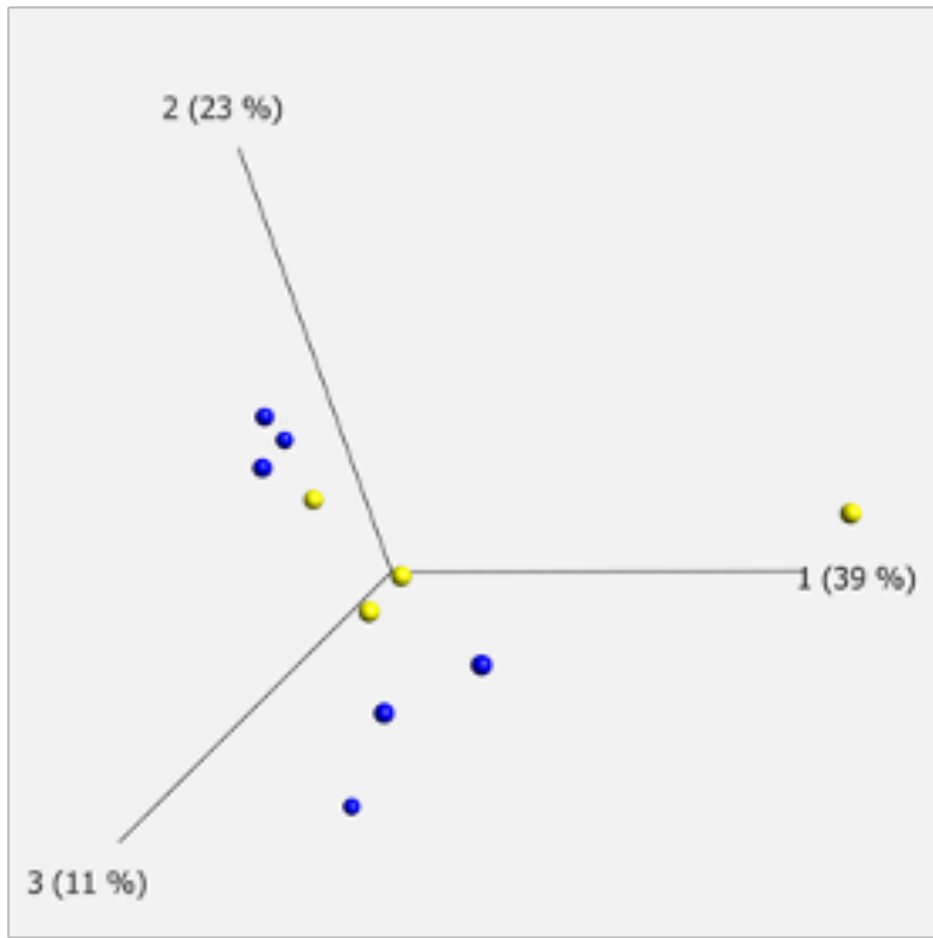


Figure 5.7 PCA Plot

The principal component analysis (PCA) plot of control (blue) and atherosclerotic (yellow) showing no clear separation of differentially expressed genes between the two groups.

Table 5.3 DOWN-REGULATED genes with the highest fold change

Probe set ID	P-value	Fold Change	Gene Symbol	Description
TC0400001502	0.0016	4.49	Phc2	polyhomeotic-like 2 (Drosophila)
TC0900000086	0.0257	4.49	Phxr4	per-hexamer repeat gene 4
TC1600000647	0.0197	4.43	Ccdc191	coiled-coil domain containing 191
TC0300002939	0.0098	3.5	Sec24b	Sec24 related gene family, member B (S. cerevisiae)
TC1300002453	0.0331	2.8	Pde8b	phosphodiesterase 8B

Table 5.4 UP-REGULATED genes with the highest fold change

Probe set ID	P-value	Fold Change	Gene Symbol	Description
TC1100002649	0.0097	-3.73	Tgtp2	T cell specific GTPase 2
TC0400000555	0.0257	-3.24	Rnf20	ring finger protein 20
TC1200001281	0.0139	-3.13	Crip2	cysteine rich protein 2
TC1600000088	0.0084	-2.88	Mettl22	methyltransferase like 22
TC0600002575	0.0198	-2.88	Stampb	STAM binding protein

Table 5.5 Analysis of candidate genes related to inflammation and lipid metabolism

Probe set ID	P-value	Fold Change	Gene Symbol	Description
TC0400001135	0.0034	1.4	<i>Lrp8</i>	low density lipoprotein receptor-related protein 8, apolipoprotein e receptor
TC1800000714	0.0089	1.53	<i>Ldlrad4</i>	low density lipoprotein receptor class A domain containing 4
TC0200004207	0.02	1.73	<i>Ldlrad3</i>	low density lipoprotein receptor class A domain containing 3
TC1500001818	0.0121	1.69	<i>ApoB</i>	apolipoprotein B 100
TC1400002714	0.0192	1.97	<i>Abcc4</i>	ATP-binding cassette, sub-family C (CFTR/MRP), member 4
TC0600000711	0.0348	1.55	<i>Abcg2</i>	ATP-binding cassette, sub-family G (WHITE), member 2
TC1100003086	0.0488	1.39	<i>Slc16a13</i>	solute carrier family 16 (monocarboxylic acid transporters), member 13
TC1700000937	0.0146	-1.62	<i>Trem2</i>	triggering receptor expressed on myeloid cells 2
TC1100001768	0.0177	-1.49	<i>Ace3</i>	Angiotensin I converting enzyme (peptidyl-dipeptidase A)3
TC1700001952	0.0299	-1.89	<i>Aif1</i>	allograft inflammatory factor 1 also known as ionised calcium-binding adaptor molecule (IBA-1)
TC0700000424	0.0046	-1.57	<i>Tgfb1</i>	transforming growth factor, beta 1

Assessment of dysregulated genes prior to enrichment pathway analysis found genes associated with neuroinflammatory and atherosclerosis.

5.3.4 Functional Enrichment Analysis using DAVID bioinformatics tool

The lists of probe IDs from the total number of differentially expressed transcripts for the comparison of controls and atherosclerotic *ApoE*^{-/-} mouse hippocampus computed by TAC were entered into DAVID (Database for annotation, Visualization and Integrated Discovery) Bioinformatics Tool (version 6.7). To identify dysregulated pathways changing in the same direction, the lists of up and down-regulated transcripts were inputted independently. Results from the DAVID Functional Enrichment Analysis are summarised in Table 5.6, Table 5.7 and Table 5.8.

The dysregulated pathways identified by DAVID in the Atherosclerotic vs control included ion transport, oxidative phosphorylation, metabolic pathways, calcium signalling pathways and natural killer cell cytotoxicity. Kyoto encyclopaedia of genes and genomes (KEGG) pathway analysis in DAVID identified 11 significantly (Bonferroni p-value) dysregulated pathways, including metabolic and calcium signalling pathways (Table 5.6). All the KEGG pathways have very high FDR values. This suggests that a high % of the genes may be incorrectly identified as differentially expressed and subsequent validation experiments could be significantly affected.

Analysis of the UP-REGULATED transcripts (Table 5.7) resulted in the identification of enrichment of mitochondrial respiratory chain and natural killer cell mediated cytotoxicity pathways in atherosclerotic vs control *ApoE*^{-/-} mouse hippocampus. Only oxidative phosphorylation and metabolic pathways were significant and had a low FDR value.

Analysis of the DOWN-REGULATED transcripts (Table 5.8) showed enrichment of genes linked to ATP-binding, calcium signalling and protein processing in the endoplasmic reticulum (ER). All of these pathways presented high FDR values.

The analysis focused on pathways that are potentially involved in mitochondrial dysfunction and oxidative phosphorylation in relation to atherosclerosis.

5.3.5 Pathway enrichment analysis using IMPaLA

The lists of gene symbols of the differentially expressed genes from the comparison of controls and atherosclerosis of *ApoE*^{-/-} hippocampus processed in TAC were also entered into IMPaLA (Integrated Molecular Pathway Level Analysis, version 13). As with the DAVID analysis, the total number of differentially expressed genes, as well as the separate lists of UP and DOWN-REGULATED transcripts were analysed and presented high FDA values on most pathways, they are presented in Table 5.9, Table 5.10 and Table 5.11. Analysis of the total number of dysregulated transcripts (Table 5.9) revealed, as the DAVID analysis. that all pathways had very high FDR values, suggesting a large % of incorrectly identified genes in the atherosclerotic and controls *ApoE*^{-/-} mouse hippocampus.

Analysis of the UP-REGULATED transcripts (Table 5.10) resulted in the identification of enrichment of genes involved in electron transport, mitochondrial function more specifically Complex I in atherosclerotic compared to control *ApoE*^{-/-} mouse hippocampus.

Analysis of the DOWN-REGULATED transcripts (Table 5.11) showed enrichment of genes linked to cell signalling in the CNS, metabolism of phospholipids and molecular transport. The pathways highlighted in blue were further analysed in relation to oxidative phosphorylation and metabolism shown to be altered BBB dysfunction or associated with atherosclerosis and had low FDA values.

Table 5.6 DAVID analysis of atherosclerotic hippocampus transcriptomic datasets.

Functional group	DEG	P-Value (Bonferroni)	FDR Value
Mitochondrion	93	8.90E-05	0.01
Transit peptide	49	8.30E-04	0.04
Metal-binding	244	3.40E-04	0.03
Ion transport	58	4.90E-04	0.03
Voltage-gated channel	19	9.80E-04	0.04
Calcium transport	15	9.90E-04	0.04
KEEG Pathway name	DEG	P-Value (Bonferroni)	FDR Value
Oxidative phosphorylation	19	0.0013	0.37
Metabolic pathways	97	0.0048	0.65
Dilated cardiomyopathy	11	0.024	1.00
Synaptic vesicle cycle	9	0.029	1.00
Oxytocin signalling pathway	16	0.032	1.00
Alzheimer's disease	18	0.032	1.00
Pyrimidine metabolism	12	0.034	1.00
Calcium signalling pathway	18	0.037	1.00
Chemical carcinogenesis	11	0.044	1.00
Natural killer cell mediated cytotoxicity	12	0.045	1.00
Glycerophospholipid metabolism	11	0.05	1.00

DEG: Differentially expressed genes; FDR: False discovery rate; KEGG: Kyoto Encyclopaedia of Genes and Genomes

Table 5.7 DAVID functional and pathway enrichment analysis of UP-REGULATED genes

Functional group	DEG	P-Value (Bonferroni)	FDR Value
Mitochondrion	63	6.4E-6	0.0022
T cell mediated cytotoxicity	6	3.4E-5	0.0660
Oxidative phosphorylation	16	2.2E-5	0.0053
KEEG Pathway name	DEG	P-Value (Bonferroni)	FDR Value
Oxidative phosphorylation	16	2.20E-05	0.0053
Metabolic pathways	63	8.40E-05	0.0099
Natural killer cell mediated cytotoxicity	11	0.0014	0.11
Pyrimidine metabolism	10	0.0036	0.21
Glutathione metabolism	7	0.0066	0.27
Chemical carcinogenesis	9	0.0073	0.27
Huntington's disease	14	0.0080	0.27
Metabolism of xenobiotics by cytochrome P450	7	0.014	0.41
Parkinson's disease	11	0.017	0.44
Alzheimer's disease	12	0.021	0.49
Peroxisome	7	0.042	0.92

DEG: Differentially expressed genes; FDR: False discovery rate; KEGG: Kyoto Encyclopaedia of Genes and Genomes

Table 5.8 DAVID functional and pathway enrichment analysis of DOWN-REGULATED genes

Functional group	DEG	P-Value (Bonferroni)	FDR Value
Ion channel activity	22	1.60E-08	1.10E-05
Voltage-gated ion channel activity	14	5.20E-05	0.0012
Transmembrane helix	64	1.50E-06	7.20E-05
Synapse	12	2.00E-06	2.20E-04
Cell junction	14	0.0041	0.032
Calcium transport	11	2.80E-05	6.70E-04
Sodium transport	6	6.90E-04	0.0078
KEEG Pathway name	DEG	P-Value (Bonferroni)	FDR Value
cAMP signalling pathway	15	0.0013	0.18
Calcium signalling pathway	14	0.0017	0.18
Protein processing in endoplasmic reticulum	13	0.0028	0.20
Salivary secretion	8	0.0058	0.32
Thyroid hormone synthesis	7	0.014	0.60
cGMP-PKG signalling pathway	11	0.017	0.61
Dilated cardiomyopathy	7	0.029	0.82
Synaptic vesicle cycle	6	0.03	0.82
Insulin secretion	7	0.034	0.83

Yellow: significant pathways of interest; DEG: Differentially expressed genes; FDR: False discovery rate; KEGG: Kyoto Encyclopaedia of Genes and Genomes

Table 5.9 IMPaLA Pathway Analysis of the total number of differentially expressed transcripts in atherosclerotic *ApoE*^{-/-} mouse hippocampus

Pathway name	Pathway source	DEG	P-Value	FDR Value
Protein localization	Reactome	23	1.50E-05	0.0708
Neuronal System	Reactome	39	7.46E-05	0.0902
Retrograde endocannabinoid signalling	KEGG	19	0.000247	0.0902
Cardiac conduction	Reactome	15	3.42E-04	0.0902
Ion homeostasis	Reactome	9	3.68E-05	0.0902
Glycerophospholipid biosynthesis	Reactome	17	0.000414	0.0902
Complex I biogenesis	KEGG	10	0.000645	0.0902
Metabolism	Reactome	132	0.000733	0.0902
Translation of structural proteins	Reactome	6	0.000922	0.0902
Ion channel transport	Reactome	19	0.000969	0.0902
Metabolism of lipids	Reactome	52	0.00111	0.0902

All the pathways have very high FDR values (DEG: differentially expressed genes, FDR: fold change).

Table 5.10 IMPaLA Pathway Analysis of the UP-REGULATED transcripts in atherosclerotic *ApoE*^{-/-} mouse hippocampus

Pathway name	Pathway source	DEG	P-Value	FDR Value
Complex I biogenesis	Reactome	10	2.09E-06	0.00979
Oxidative phosphorylation	KEGG	13	5.04E-05	0.118
Mitochondrial translation termination	Reactome	10	0.000106	0.136
Respiratory electron transport	Reactome	10	0.000116	0.136
Mitochondrial translation	Reactome	10	0.000184	0.149
Oxidative phosphorylation	Wikipathways	8	0.000191	0.149
Glutathione conjugation	Reactome	6	0.00038	0.186
Methylation	Reactome	4	0.000389	0.186
Electron Transport Chain (OXPHOS system in mitochondria)	Wikipathways	10	0.00039	0.186
Metabolism	Reactome	75	0.000422	0.186
Protein localization	Reactome	13	0.00044	0.186
Mitochondrial translation initiation	Reactome	9	0.000516	0.186
Mitochondrial translation elongation	Reactome	9	0.000516	0.186
Glutathione metabolism	KEGG	7	0.00072	0.198
Pyrimidine metabolism	Wikipathways	8	0.00167	0.391
Microglia Pathogen Phagocytosis Pathway	Wikipathways	5	0.00386	0.699

Blue: significant pathways of interest; DEG: differentially expressed genes, FDR: false discovery rate.

Table 5.11 IMPaLA Pathway Analysis of the DOWN-REGULATED transcripts in atherosclerotic *ApoE*^{-/-} mouse hippocampus

Pathway name	Pathway source	DEG	P-Value	FDR Value
Neuronal System	Reactome	29	3.02E-07	0.00141
Reduction of cytosolic Ca ⁺⁺ levels	Reactome	4	7.94E-05	0.0136
Ion channel transport	Reactome	14	9.08E-05	0.0136
Voltage gated Potassium channels	Reactome	7	0.000101	0.0136
Ion homeostasis	Reactome	7	0.000117	0.0136
Nervous system development	Reactome	23	0.000124	0.0136
Phospholipid metabolism	Reactome	16	0.000124	0.0136
Axon guidance	Reactome	22	0.000134	0.0136
cAMP signalling pathway	KEGG	16	0.000146	0.0136
Dilated cardiomyopathy	KEGG	10	0.00016	0.0136
Disruption of postsynaptic signalling by CNV	Wikipathways	6	0.000169	0.0141
Signalling by Hedgehog	Reactome	9	0.000185	0.0147
Transport of small molecules	Reactome	31	0.000538	0.0381
Glycerophospholipid biosynthesis	Reactome	11	0.000521	0.0381

Blue: significant pathways of interest; DEG: differentially expressed genes, FDR: false discovery rate.

5.3.6 Pathways of interest

Several pathways were identified as being dysregulated by the analysis performed using DAVID and IMPaLA in the controls and atherosclerosis hippocampus of *ApoE*^{-/-} mice. Both DAVID and IMPaLA suggested changes in oxidative phosphorylation and mitochondria but IMPaLA also detected alteration in Ca²⁺ signalling. A more detailed examination of the genes involved in these pathways is described in the following sections.

Mitochondrial dysfunction

IMPaLA and DAVID analysis suggested upregulation in the mitochondrial electron transport chain in atherosclerotic mice hippocampus. The differentially expressed transcripts code for proteins in Complex I (*Ndufa10, Ndufa7, Ndubf5, Ndubf8, Ndubf2, Ndufs8, Ndufs6, Ndufs8, Ndufv3*), Complex IV (*Cox17, Cox15, Cox7A12l*) and Complex V (*Atp 5g1, Atp5j, Atp5s, Atp6v1f, Atp6v1g3, Ppa2*) genes. The only down-regulated genes was detected were *Cox15, Cox7A12l* (Table 5.12). Other pathways activated to reactive oxygen species including Nrf2 pathway were also detected (*Tgfb1, Gstm1, Mgst3, Abcc5, Gsto1, Gpx3*).

Cell signalling pathways and ion transport

DAVID identified down-regulation in cell signalling pathways in atherosclerotic mice hippocampus. The differentially expressed genes in the calcium and cAMP signalling pathways are presented in Table 5.13. Dysregulation of cell signalling related transcripts The majority of the transcripts were linked to ion channel transport *Cacna1b, Cacna1e, Cacna1h, Abcc4, Atp2b2, Atp1b2, Atp2a2* in atherosclerotic hippocampus.

Table 5.12 Genes involved in electron transport chain in control and atherosclerotic *ApoE*^{-/-} mice hippocampus

Gene symbol	Gene name	FC	P-Value
Atp5g1	ATP synthase, H+ transporting, mitochondrial F0 complex, subunit C1 (subunit 9)	-1.33	0.0283
Atp5j	ATP synthase, H+ transporting, mitochondrial F0 complex, subunit F	-1.56	0.0169
Atp5s	ATP synthase, H+ transporting, mitochondrial F0 complex, subunit S	-2.12	0.0081
Atp6v1f	ATPase, H+ transporting, lysosomal V1 subunit F	-1.27	0.0456
Atp6v1g3	ATPase, H+ transporting, lysosomal V1 subunit G3	-1.43	0.0396
Ndufa10	NADH dehydrogenase (ubiquinone) 1 alpha subcomplex 10	-1.4	0.0116
Ndufa7	NADH dehydrogenase (ubiquinone) 1 alpha subcomplex, 7 (B14.5a)	-1.68	0.0216
Ndufb5	NADH dehydrogenase (ubiquinone) 1 beta subcomplex, 5	-1.43	0.048
Ndufb8	NADH dehydrogenase (ubiquinone) 1 beta subcomplex 8	-1.31	0.0221
Ndufb2	NADH dehydrogenase (ubiquinone) 1 beta subcomplex, 2	-1.22	0.0429
Ndufs6	NADH dehydrogenase (ubiquinone) Fe-S protein 6	-1.27	0.0341
Ndufs8	NADH dehydrogenase (ubiquinone) Fe-S protein 8	-2.1	0.0078
Ndufv3	NADH dehydrogenase (ubiquinone) flavoprotein 3	-1.89	0.0198
Cox17	cytochrome c oxidase assembly protein 17	-1.43	0.0265
Cox15	cytochrome c oxidase assembly protein 15	1.73	0.0212
Cox7a2l	cytochrome c oxidase subunit VIIa polypeptide 2-like	1.77	0.0436
Pp2	pyrophosphatase (inorganic) 2	-2.22	0.0432

Transcripts linked to mitochondria complex I, IV and V were up-regulated but also down-regulated in complex IV in atherosclerotic mice compared to controls. (Green: UP-REGULATED, Red: DOWN-REGULATED, FC: fold change).

Table 5.13 Genes involved in calcium and cell signalling in control and atherosclerotic *ApoE*^{-/-} mice hippocampus

Gene symbol	Gene name	FC	P-Value
Htr1a	5-hydroxytryptamine (serotonin) receptor 1A(Htr1a)	1.61	0.0112
Abcc4	ATP-binding cassette, sub-family C (CFTR/MRP), member 4(Abcc4)	1.97	0.0192
Atp2b2	ATPase, Ca ⁺⁺ transporting, plasma membrane 2(Atp2b2)	2.34	0.0116
Atp1b2	ATPase, Na ⁺ /K ⁺ transporting, beta 2 polypeptide(Atp1b2)	1.66	0.0465
Rock1	Rho-associated coiled-coil containing protein kinase 1(Rock1)	1.55	0.02
Adcy8	adenylate cyclase 8(Adcy8)	1.45	0.0157
Adcyap1r1	adenylate cyclase activating polypeptide 1 receptor 1(Adcyap1r1)	1.43	0.0472
Pik3r1	phosphatidylinositol 3-kinase, regulatory subunit, polypeptide 1 (p85 alpha)(Pik3r1)	1.54	0.0233
Pde4a	phosphodiesterase 4A, cAMP specific(Pde4a)	1.76	0.0281
Prkaca	protein kinase, cAMP dependent, catalytic, alpha(Prkaca)	2.25	0.0057
Ryr2	ryanodine receptor 2, cardiac(Ryr2)	1.62	0.02
Sstr2	somatostatin receptor 2(Sstr2)	1.3	0.0456
Sucnr1	succinate receptor 1(Sucnr1)	1.5	0.0372
Htr5a	5-hydroxytryptamine (serotonin) receptor 5A(Htr5a)	1.48	0.0204
Atp2a2	ATPase, Ca ⁺⁺ transporting, cardiac muscle, slow twitch 2(Atp2a2)	1.28	0.0176
Adra1d	adrenergic receptor, alpha 1d(Adra1d)	1.48	0.0189
Cacna1b	calcium channel, voltage-dependent, N type, alpha 1B subunit(Cacna1b)	1.78	0.0258
Cacna1e	calcium channel, voltage-dependent, R type, alpha 1E subunit(Cacna1e)	1.83	0.0132
Cacna1h	calcium channel, voltage-dependent, T type, alpha 1H subunit(Cacna1h)	1.5	0.0068
Gtf2i	general transcription factor II I(Gtf2i)	1.46	0.0207

Transcripts linked to calcium and cAMP signalling pathways were DOWN-REGULATED in atherosclerotic hippocampus. (Green: UP-REGULATED, Red: DOWN-REGULATED, FC: fold change).

Inflammation and immune response

There were several transcripts annotated to immune-like response pathways Table 5.14. There were 4 transcripts up-regulated in atherosclerotic mice hippocampus (*Fer1g*, *Aif1*, *Tgfb1*, *Sos2*), and 8 genes were down-regulated (*Pik3r4*, *Rock1*, *Canx*, *Itgb1*, *App*, *Tmem63a*, *Tmem106a*, *Abcc4*). These genes have a role in the immune response and are related to production of and proinflammatory cytokines.

5.3.7 Validation of microarray candidate gene expression by qRT-PCR

Overall, the enrichment analysis detected dysregulation of genes involved in cell signalling, oxidative phosphorylation, and inflammation, in atherosclerotic *ApoE*^{-/-} mouse hippocampus (Table 5.15). The genes selected for validation as a result of this analysis are listed in Table 5.16. They were selected due to their relation to atherosclerosis, inflammation and NVU disruption.

Housekeeping gene selection

Based on analysis of the original microarray data, one probe sets for β -actin and one probe sets for GAPDH were represented in all 12 of the control samples used in the microarray study. The signal intensity across both probe sets was similar, but, β -actin probes showed higher variability to the GAPDH probes (Table 5.17), therefore GAPDH was used as the HK control in qPCR experiments.

Validation of inflammatory and oxidative phosphorylation response

Validation of the chosen genes was conducted on RNA extracts obtained from the same cohort 2 *ApoE*^{-/-} mouse hippocampus for the microarray analysis. qRT-PCR validation failed to replicate these microarray findings in the technical validation (Figure 5.8). The expression of *Ndusf8* in the hippocampus was down-regulated in atherosclerotic mice compared to controls, opposing the findings from the microarray analysis.

Table 5.14 Genes involved in immune and inflammatory response in atherosclerotic ApoE^{-/-} mice hippocampus

Gene symbol	Gene name	FC	P-Value
Fcer1g	Fc receptor, IgE, high affinity I, gamma polypeptide	-1.51	0.0369
Pik3r4	phosphatidylinositol 3 kinase, regulatory subunit, polypeptide 4, p150	1.67	0.0106
Rock1	Rho-associated coiled-coil containing protein kinase 1	1.55	0.02
Aif1	Allograft inflammatory factor 1	-1.89	0.0299
Canx	calnexin	1.86	0.0379
Itgb5	integrin beta 5	1.55	0.0472
App	amyloid beta (A4) precursor protein	1.38	0.0274
Tmem63a	transmembrane protein 63a	1.69	0.0129
Tmem106a	transmembrane protein 106A	1.49	0.0369
Abcc4	ATP-binding cassette, sub-family C (CFTR/MRP), member 4	1.97	0.0192
Il16	interleukin 16	-1.58	0.0362
Il2ra	interleukin 2 receptor, alpha chain	-1.54	0.0449
Tgfb1	transforming growth factor, beta 1	-1.57	0.0046
Sos2	Son of sevenless homolog 2	-1.79	0.038

Transcripts related to cytokine production, integrin and TGF- β signalling were down-regulated in atherosclerotic mice hippocampus. (Green: UP-REGULATED, Red: DOWN-REGULATED, FC: fold change).

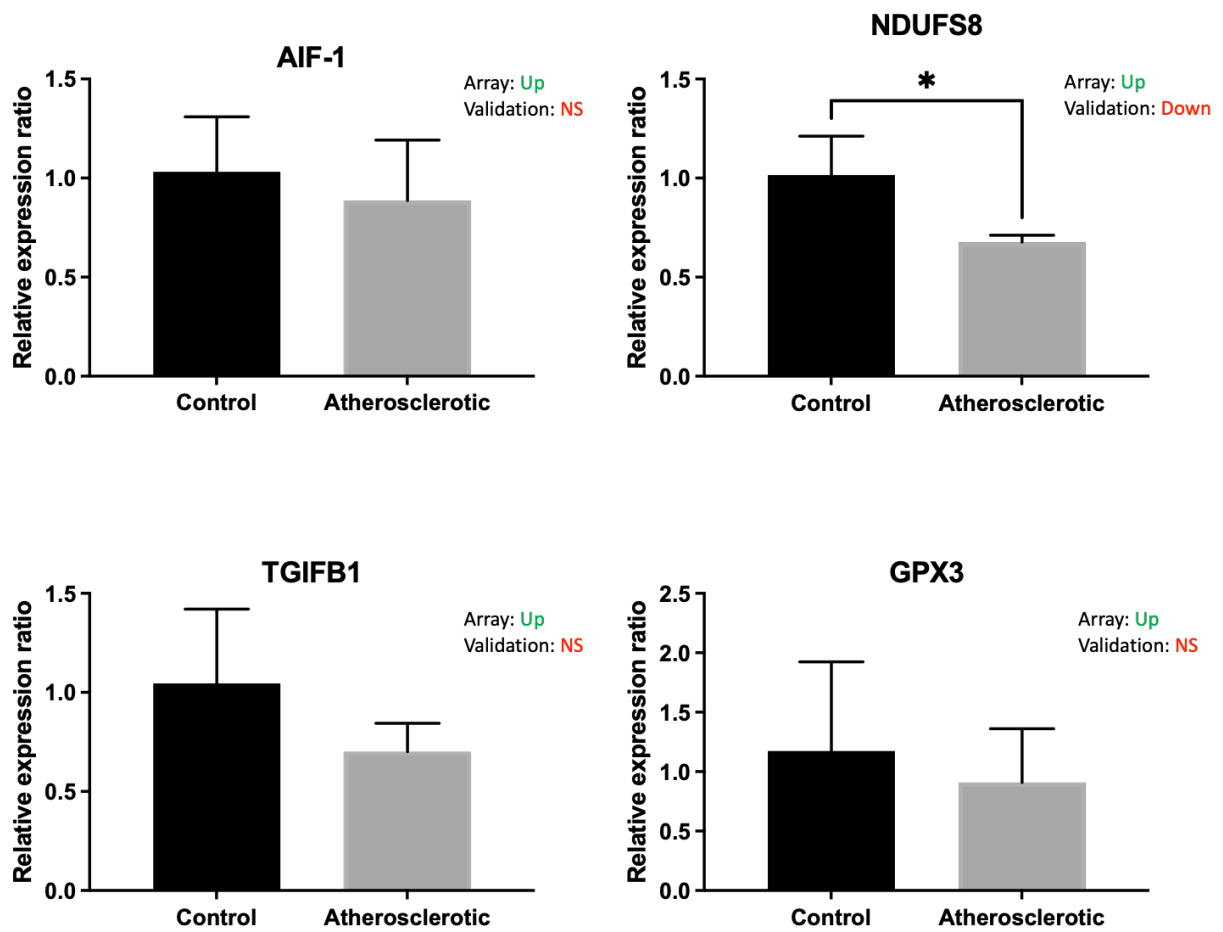


Figure 5.8 Validation of neuroinflammatory and oxidative phosphorylation up-regulated genes in the hippocampus by qRT-PCR.

The hippocampus of *ApoE*^{-/-} mice fed with a western diet (atherosclerotic) was examined after isolation with LCM. Changes in the mitochondrial Complex I genes *NDUFS8* were validated by qRT-PCR. (Mann-Whitney U test; data are means \pm SEM; n=3 in duplicate).

Table 5.15 Summary of pathways of pathogenic interest in the hippocampus of *ApoE^{-/-}* cohort 2 mice

Pathway	Pathway enrichment analysis	Change	P-value	FDR value
Oxidative phosphorylation	DAVID	UP-regulated	2.20E-05	0.0053
Metabolic pathways	DAVID	UP-regulated	8.40E-05	0.0099
Calcium signalling	DAVID	DOWN-regulated	2.80E-05	6.70E-04
Natural killer cell mediated cytotoxicity	DAVID	UP-regulated	3.4E-5	0.0660
Complex I biogenesis	IMPaLA	UP-regulated	2.09E-06	0.00979
Reduction of cytosolic Ca ⁺⁺ levels	IMPaLA	DOWN-regulated	7.94E-05	0.0136

Table 5.16 Candidate genes selected for qRT-PCR validation

Pathway	Gene	FC	P-value
Calcium cell signalling	<i>Atp2b2</i>	2.34	0.0116
cAMP	<i>Prkaca</i>	2.25	0.0057
	<i>Adcy8</i>	1.45	0.0157
Oxidative phosphorylation	<i>Gsto1</i>	-1.67	0.0051
	<i>Ndufs8</i>	-2.1	0.0078
Inflammation	<i>Tgfb1</i>	-1.57	0.0043
	<i>Aif1</i>	-1.89	0.0299

(Green: UP-REGULATED, Red: DOWN-REGULATED, FC: fold change).

Table 5.17 Housekeeping gene selection for qRT-PCR analysis

	Probeset ID	Mean signal intensity (n=12)	Signal intensity range
β -Actin	TC0600003135.mm.2	17.010559	16.75348 - 17.26856
GAPDH	TC0500003538.mm.2	17.792482	16.51532 - 18.30581

A similar signal intensity across both probe sets with lower range detected for GAPDH compared to β -Actin.

5.3.8 Summary of transcriptomic analysis of control and atherosclerotic

ApoE^{-/-} cohort 2 hippocampus

- High FDR values
- Different results in different software
- Calcium signalling is upregulated
- Metabolic pathways are downregulated
- Mitochondrial pathways are downregulated
- qRT-PCR did not validate the results from the transcriptomic analysis

5.4 Discussion

Microarray analysis identified changes in the transcriptome of *ApoE*^{-/-} cohort 2 atherosclerotic mice hippocampus compared to controls. In general, pathway analysis of microarray results indicated up-regulation of mitochondrion and complex I pathways in IMPaLA and DAVID. Only IMPaLA show downregulation of signalling pathways linked to Ca⁺ signalling, neuronal system and ion channel transport in atherosclerotic mice compared to controls. IMPaLA evaluated a larger number of pathway sources while DAVID analysis focused on KEGG pathways.

Inflammatory-related genes in atherosclerotic mice were upregulated compared to controls but FDR values were high, and technical validation of the candidate genes using qRT-PCR from these pathways not confirm the findings from the microarray analysis. This was the case for all the genes selected for validation, with qRT-PCR demonstrating up-regulation of oxidative phosphorylation in relation to mitochondria Complex I, while transcriptomic analysis showed down-regulation.

Even though the observed changes might vary on subsequent analysis the implications of dysregulation of oxidative phosphorylation, Ca⁺ transport and cAMP signalling pathways in atherosclerosis in the hippocampus was cautiously analysed. The microarray analysis was performed in cohort 2 *ApoE*^{-/-} mice which showed a different profile during cellular characterisation using immunohistochemistry. The change has been proposed to be due to an underlying infection in control mice masking the effects of atherosclerosis, and the functional annotation clustering indicated significant upregulation of T-cell mediated cytotoxicity potentially indicating inflammation in the hippocampus but other factors might potentially be driving the observed changes (Section 3.4.4). For this reason, the results should be replicated on a third *ApoE*^{-/-} mouse cohort followed by validation of gene expression changes.

5.4.1 Atherosclerotic *ApoE*^{-/-} mouse cohort 2 presented changes in metabolic, lipid and myelin related transcripts

Microarray data analysis identified dysregulation of 1450 transcripts in atherosclerotic mice hippocampus compared to controls, suggesting that systemic atherosclerosis elicited by a Western diet (high-fat diet) has an effect on gene expression in the hippocampus of *ApoE*^{-/-} mice. Prior to the pathway analysis, a detailed search for immune and inflammatory-related genes in the list of differentially expressed transcripts was conducted. The analyses aimed to determine the expression of the inflammatory-associated markers investigated in previous chapters: *Aif1* (IBA-1), *Gfap* (GFAP), *Icam1* (ICAM-1). Atherosclerotic-related genes were also investigated in these list including *Il1b* (IL-1B), *Ace* (ACE), *App* (APP) and *Lrp* (LRP) which have been also been shown to be related to vascular dysfunction and AD (Orsucci et al., 2013). The details of these transcripts revealed an up-regulation of inflammatory transcripts *Aif1*, *Trem2* (TREM2), *Tgfb1* (TGF-β1). This is consistent with the results observed in the characterisation and assessment of microglia expression in *ApoE*^{-/-} mice cohort 1 which expressed an increase % area of immunopositive IBA-1 microglia in all brain areas of atherosclerotic mice compared to controls. However, up-regulation of *Aif1* (IBA-1) was not validated and *ApoE*^{-/-} cohort 2 did not show increase immunoreactivity of IBA-1 in any of the investigated brain areas, which might indicate this gene was incorrectly identified as up-regulated by the microarray analysis. Further investigation on mRNA and protein levels needs to be investigated to identify if the changes are related to atherosclerosis or other variables.

The following genes were downregulated in the microarray analysis, but the lipid metabolism pathway was not identified as significantly different between controls and atherosclerotic mice. *Lrp8* (APOER2) and *Ldlr* (LDLR), APOE receptors that bind and

internalise APOE-containing lipoproteins, with ApoER2 only expressed in neurons while LDLR, LDLRP and VLDLPR expressed in neurons, astrocytes, microglia and pericytes (Adorni et al., 2019; Pocivavsek et al., 2009). In ordinary conditions, APOER2 prevents the accumulation of LDL-cholesterol, therefore its downregulation is consistent with atherosclerosis pathogenesis and indicating damage to this pathway which is consistent with previous evidence in atherosclerosis (Tuomisto et al., 2005). *Ldlrad3* and *Ldlrad4* encode the ligand-binding domain of LDLR therefore their downregulation could affect the binding of LDL to the receptor (Fan et al., 2001).

Furthermore, initial analysis also detected the upregulation of *Mog* (MOG: myelin oligodendrocyte glycoprotein) and *Mag* (MAG: myelin associated-glycoprotein), which are important in the myelination of nerves in the CNS and have been shown to be upregulated in mice fed with a high-fat diet. These changes had previously been observed in 8 week old C57BL/6 mice fed with a 60% (high) fat diet and it is proposed to be a consequence of a disruption in the synthesis and metabolism of fatty acids and lipids (Poitelon et al., 2020; Yoon et al., 2019). The current findings on *ApoE*^{-/-} mice are additionally validated by previous research showing that high-fat diet affects fatty acids (Butler et al., 2020).

Functional annotation analysis with bioinformatic tools, DAVID annotated oxidative phosphorylation and metabolic pathways were up-regulated and all down-regulated pathways failed to reach statistical significance after post-hoc analysis. On the other hand, IMPaLA showed up-regulation of Complex I biogenesis pathway only and down-regulated significant expression of Ca⁺² reduction of cytosolic levels, neuronal system, ion and voltage-gated Na channel and cAMP signalling pathway. DAVID functional annotation clustering analysis identified down-regulation of ion-channel activity, Ca⁺²

and Na transport pathways that were also noted in IMPaLA which is based on a greater number of databases (Reactome, Wikipathways and KEGG) than DAVID.

The results from the current research support previous literature that demonstrate transcriptomic changes in wild type mice brains elicited by a high-fat diet, but the changes in gene expression had not been investigated in *ApoE*^{-/-} mice, specifically in the hippocampus (Oppi et al., 2019). This data is preliminary as *ApoE*^{-/-} mouse cohort 2 was used for the microarray analysis and the characterisation studies did not show any significant changes using astrocytic, microglia and endothelial markers. The results differed from the *ApoE*^{-/-} mouse cohort 1 suggesting alteration of key cellular functions is possibly a result of metabolic changes exerted by atherosclerosis, but other factors could possibly be driving the observed changes. Further replication is necessary to obtain a better understanding of the observed transcriptomic alterations.

5.4.2 Differentially expressed genes associated with mitochondrial metabolic pathways

Functional annotation clustering analysis in DAVID suggested up-regulation of oxidative phosphorylation and mitochondrion pathways in the hippocampus of atherosclerotic mice compared to controls. IMPaLA showed significant up-regulation of mitochondrial Complex I biogenesis only. Closer evaluation of the data showed transcripts encoding for mitochondrial Complex I, Complex IV and complex V subunits were up-regulated and transcripts in Complex IV were down-regulated. To further investigate mitochondrial dysfunction in atherosclerotic mice hippocampus, the qRT-PCR validation focused on one element of Complex I activity (*Ndufs8*).

The mitochondrial electron transport chain (ETC) is composed of proton-pumping multi-subunit protein assemblies, known as complexes (I-IV), that are embedded in the

mitochondrial inner membrane, where electrons are used to create a proton gradient across the mitochondrial membrane (Guerrero-Castillo et al., 2017). Complex I (NADH:ubiquinone oxidoreductase) consist of 45 subunits, and it catalyses the first step of the mitochondrial ETC, its role is crucial in oxidative phosphorylation which is the process dedicated to the production of ATP from electrons collected from catabolic processes (glycolysis, fatty acid oxidation and the tricarboxylic acid cycle) (Guerrero-Castillo et al., 2017). The mRNA levels of Complex sub-units *Ndufa7*, *Ndufs8* (transfer of electrons to ubiquinone); *Ndufs6*, *Ndufv3* (NADH binding and oxidation); *Ndufa10*, *Ndufb5*, *Ndufb8*, (proton pumping) were significantly increased in atherosclerotic *ApoE*^{-/-} hippocampus compared to controls.

Complex I mutations and dysfunction is associated with increased ROS in different cell types, including neurones and astrocytes and has been linked to cognitive impairment and neurodegenerative disorders (Denver et al., 2019; Mor and Murphy, 2020). Research has focused on Complex I and oxidative stress as a decrease in mitochondrial activity in cells leads to the production of ROS and ROS-mediated damage. Mitochondrial hyperactivity related with increase in Complex I subunits has previously been described in mouse dopaminergic neuronal cultures and more recently, in a study on the CNS of *C.elegans*. The increased mitochondrial activity led to PD phenotypes and suggested to be an early event of neuropathologies that cause oxidative damage and ultimately functional mitochondrial loss (Mor and Murphy, 2020; Pacelli et al., 2015). Oxidative damage and mitochondrial dysfunction have been implicated in the pathogenesis of VD and AD and but the main question as to whether they are involved in the onset and progression of the pathology or are a consequence of the neurodegenerative process is still debated (Orsucci et al., 2013; Stahon et al., 2016).

In atherosclerotic mice hippocampus the qRT-PCR results contradicted these findings showing down-regulation of NDUFS8 in the hippocampus compared to controls, while the microarray data analysis presented up-regulation of mitochondrial Complex I. The results could suggest a decrease of Complex I activity in the CNS of mice with systemic atherosclerosis. Neurons rely on oxidative phosphorylation to generate energy and are also more sensitive to mitochondrial ROS formation than other cells, therefore mitochondrial dysfunction is thought to be directly involved in cell autonomous neuronal death (McAvoy and Kawamata, 2019). Complex I activity is reduced in astrocytes compared to neurons, which overall effect during physiological condition is a reduced respiration that increases ROS production (Lopez-Fabuel et al., 2016). The decrease of astrocytic ROS production leads to brain metabolism defects, neuronal damage and cognitive impairment in mice revealing the functional of Complex I in astrocytes (Vicente-Gutierrez et al., 2019). Changes in mitochondria metabolism during inflammation could also contribute to microglia activation. While impairment of mitochondrial fission reduces the production of pro-inflammatory factors, the inhibition of Complex I activity activates microglia (Park et al., 2013; Ye et al., 2016)

Mitochondrial dysfunction is associated with the development of metabolic alterations. Any disruption in energy metabolism, especially in neurons, can lead to increased energy demand that results in cellular stress. Mitochondria are vital for oxidative energy metabolism; therefore, mitochondrial dysfunction is a major contributor to metabolic stress. Increased production of ATP results in higher ROS production. Functional abnormalities in the mitochondria can cause oxidative stress (Su et al., 2010). This oxidative stress affects mitochondrial DNA and leads to an aberration in mitochondrial quality control and ETC enzymes, such as Complex I subunits, which results in metabolic deficiency. Along with morphological abnormalities in

mitochondria, increased calcium influx and overproduction of ROS may accelerate the formation of inner mitochondrial transition pore, which allows free movement of ions and small molecules leading to mitochondrial membrane depolarization and ATP depletion that triggers apoptosis (Muddapu et al., 2020; Pacelli et al., 2015) Systemic atherosclerosis potentially leads to metabolic alterations due to the large production of ROS and alterations in lipid metabolism, but this would have to be confirmed with further analysis.

5.4.3 Down-regulation of calcium transport and cAMP pathways

Analysis of the atherosclerotic against control microarray datasets using IMPaLA revealed the significant down-regulation of Ca^{2+} and Na^+ and other voltage-gated ion transport pathways. Further examination showed the majority of the genes associated with these pathways were Ca^{2+} channels and cAMP involved in diverse key functions, such as the maintenance of physiological homeostasis and cell proliferation. Disruption of these pathways could potentially be associated with lipid and metabolic changes exacerbated by the absence of *ApoE*^{-/-}, high fat diet or an unknown infection.

Several of the down-regulated genes identified in the current study are involved in extrusion of calcium from cells (PMCA, ATP2B2, ATP2A2, SERCA, NCX) but also excitatory Ca^{2+} influx through calcium voltage-gated calcium channels (VGCC). PMCA and SERCA maintain low cytoplasmic Ca^{2+} levels in resting cells while NCX is the major secondary regulator of Ca^{2+} but it generates a membrane potential, as it exchanges 3 Na^+ for one Ca^{2+} .

In healthy cells VGCC, and other channels, are necessary for Ca^{2+} to enter in to the cytosol. Ca^{2+} stored in the endoplasmic reticulum (ER) is released through ryanodine (**RyR**) and 1,4,5-triphosphate receptors (IP3R). IP3R activation is mediated by

inositol 1,4,5-trisphosphate (IP3), a second messenger activated through phospholipase C γ (*Plc γ*) and phospholipase C β (*Plc β*). Increase of Ca²⁺ cytosolic levels activates sarco/endoplasmic reticulum Ca²⁺-ATPase (*SERCA*) and transport Ca²⁺ ions back to the ER lumen (Glaser et al., 2019). *SERCA* also interacts with ER chaperone calnexin (*CNX*) at the mitochondrial matrix and aids to determine the content of Ca²⁺ in the ER and regulates the crosstalk between mitochondrial and ER Ca²⁺ (Lynes et al., 2013).

Calcium signalling is essential to maintain homeostasis in the CNS and plays a major role in regulating multiple cellular processes, including cellular excitability, ER stress, mitochondrial dysfunction, apoptosis, the release of neurotransmitters and signal transduction (Giacomello et al., 2013; Nakka et al., 2016). Abnormal influx, extrusion, buffering and sequestration of calcium results in calcium imbalance, which may initiate detrimental mechanism(s) that ultimately result in neuronal degeneration and cell death (Giacomello et al., 2013). As could be expected, disruption of Ca²⁺ homeostasis strongly correlates with ageing and neurodegenerative disorders including loss of WM integrity following an ischaemic stroke in aged mice (Baltan, 2009; Kuchibhotla et al., 2009; Lipskaia et al., 2014). Yoon et al. (2019) found impaired Ca²⁺ signalling in the cerebral cortex of mice fed with high-fat diet, and also presented downregulation of myelination-related genes, neurogenesis and synaptic signalling.

The role of Ca²⁺ in mitochondrial function is thought to be important as the mitochondrial matrix contains Ca²⁺-sensitive enzymes that lead to increase in mitochondrial calcium and increased ATP production when they are altered. The uptake of mitochondrial Ca²⁺ regulates the Ca²⁺ in the matrix and the activity of the Ca²⁺ sensitive mitochondrial dehydrogenases. The increase of metabolic demand leads to an increase in cytosolic and, subsequently, matrix Ca²⁺ which purpose is to

couple the increase in metabolic demand, increasing ATP production (Pinton et al., 2008).

The reduction in matrix Ca^{2+} is reported to decrease oxidative phosphorylation and ATP production and oxidation of NADPH resulting in reduced antioxidant capacity. The depletion of antioxidants alleviates ROS level above a certain threshold, which subsequently affects the mitochondrial morphology and leads to metabolic stress (Muddapu et al., 2020). The metabolic demand of neurons coupled with impaired glutamate transporter function due to metabolic stress could lead to excessive glutamate accumulation and activation of *N*-methyl-D-aspartate (NMDA, ***Grin2a***) glutamate receptor, allowing Ca^{2+} influx at an accelerated rate. Neurons and glial cells disrupting calcium homeostasis in the mitochondria and ER and producing excessive levels of ROS. The excess Ca^{2+} and metabolic stress leads to astrogliosis and microglia activation realising inflammatory cytokines. The increased inflammatory response could lead to excess ROS formation and further exacerbate the metabolic changes. In *ApoE*^{-/-} the down-regulation of calcium transporters could potentially be a compensatory mechanism to increase cytosolic Ca^{2+} levels which could also result in the down-regulation of NMDA receptors.

Ca^{2+} signalling pathways can directly or indirectly regulate adenylate cyclases (AC, ***Adcy8, Adcyap1r1***) and subsequently cyclic adenosine monophosphate (cAMP) and its effector protein kinase A (PKA, ***Prkaca***). In physiological conditions, cAMP plays a key role in maintaining BBB permeability through regulation and formation of tight junctions between endothelial cells of the brain microvasculature (Wolburg et al., 1994). It is also known that localized cAMP changes are sufficient at modifying the permeability of the endothelial barrier (Viña et al., 2021).

Depletion of oxygen and glucose such as during a cerebrovascular event causes delayed mitochondrial degradation in astrocyte end-feet leading to the intracellular calcium (Ca^{2+}) increases to a toxic concentration and glutamatergic activation and eventually neuronal excitotoxicity and death. This evidence confirms that astrocytes have an important role in neurovascular coupling. In mice, the *ApoE*^{-/-} model showed increase Ca^{2+} responses in endothelial cells before and during plaque formation in the aorta, and the changes were attributed to deterioration of the endothelium lining of the vessels in atherosclerosis (Prendergast et al., 2014). This could have potential consequences in tight junction proteins and the integrity of the BBB. The Ca^{2+} signalling changes occur in endothelial cells in the absence of an ischemic event, implying cellular changes associated with lipid degradation or metabolic dysfunction (Prendergast et al., 2014). BBB dysfunction leads to an increase in intracellular calcium which in turn impacts the modification of tight junctions and ICAM-1 can activate a Ca^{2+} signalling pathway that can lead to cytoskeleton changes in microvascular endothelial cells of the brain, causing BBB damage (Chen et al., 2016; Etienne-Manneville et al., 2000).

5.4.4 Increased immune response suggested by analysis of *ApoE*^{-/-} cohort 1

As demonstrated in Chapter 3 *ApoE*^{-/-} mice fed with a high-fat diet developed atherosclerosis and is associated with neuroinflammation without the presence of an ischemic event; the changes involve astrogliosis and endothelial cell activation in the WM and generalised microglial activation. Functional annotation grouping analysis (DAVID) of the atherosclerotic and controls datasets identified dysregulation of 6 genes associated with T-cell mediated cytotoxicity, more specifically MHC class-I (MHC-I).

Recent studies have shown that infection and injury in the CNS can induce the of MHC-I molecules (Lv et al., 2015). MHC-I molecules have been detected in the CNS of acute ischemic stroke mice, but as these mice do not present plaque rupture and vessel occlusion, the up-regulation of this pathway is possibly related to infection (Xia et al., 2017).

Initial investigation of the data revealed up-regulation of *Aif-1* gene in atherosclerotic *ApoE^{-/-}* mice hippocampus which encodes for the known microglia cell marker IBA-1. In relation with the histological findings of *ApoE^{-/-}* mice cohort 2, there was no significant changes in the immunoreactivity of IBA-1 of atherosclerotic mice compared to controls and qRT-PCR showed no significant changes. The dysregulation of a single gene can have large impact depending on their modification and location and elicit protein changes (Ozsolak and Milos, 2011). However, the correlation between mRNA and protein expression is not linear, postulating many challenges to genomic analyses. This discrepancy arises from various post-transcriptional and post-translational modifications, functional interactions of proteins, and gene regulation, which could function solely at the mRNA level, at the protein level, or at both levels (Zubay, 1995). The correlation between mRNA and protein species has been found to be poor and the linearity of the correlation differs in different gene groups: the linearity is poor in structural genes and genes functioning in protein synthesis. There is a better correlation, for example, in transcription factors (Tuomisto et al., 2005). It is for this reason that, microarray findings have to be confirmed with independent methods both at mRNA and at protein level.

The current model also presented a downregulation of *Trem2*, a microglial receptor-adaptor complex known to mediate several neuroinflammatory responses related to phagocytosis but also known to interact with APOE in microglia. APOE and other lipids

can activate TREM2 which in turn phosphorylates its DNAX-activation protein 12 (DAP12), leading to recruiting Syk kinase and activate downstream signalling molecules including phosphatidylinositol 3-kinase (PI3K), and phospholipase C (*Plcy*) amongst others. The activation of this signalling molecules leads to PIP2/3-mediated activation of AKT and mTOR complex 2 resulting in metabolic homeostasis and RAS/MEK/ERK activation leading to transcriptional regulation of pro-inflammatory molecules, and calcium modulation (Konishi and Kiyama, 2018). The APOE-TREM2 pathway regulates microglia metabolic homeostasis and suppresses TGF β 1 (*Tgfb1*) which tightly controls microglia homeostasis through similar pathways (Krasemann et al., 2017). The impairment of this pathway would delay clearance of myelin-derived lipids which has been previously shown to be regulated by TREM2 (Nugent et al., 2020). The up-regulation of TREM-2 might implicate a compensatory mechanism due to the lack of APOE in the *ApoE*^{-/-} mouse model and exacerbated by the increase of plasma cholesterol added by the high fat diet. TGF β 1 signalling is vital to prevent excessive microglia activation metabolic homeostasis the disruption of the APOE-TREM-2 pathway would lead to decrease of TGF β 1 suppression and microglial changes (Casserly and Topol, 2004). Validation using qRT-PCR did not find significant changes between atherosclerotic and control mice hippocampus.

There have been contradictory reports of the effects of TREM2 in neurodegeneration with *Trem2*^{-/-} mice showing decrease microglia motility and phagocytosis (Mazaheri et al., 2017; Schoch et al., 2021). On the other hand Ruganzu et al. (2021) demonstrated that overexpression of TREM2 inhibits the activation of JAK/SOCS pathway involved in IFN γ pathway activation and reduces synaptic and neuronal loss in AD mouse model. Furthermore, it elevates microglia M2 phenotype markers.

5.4.5 Limitations

The principal disadvantage of this part of the study is the use of the *ApoE*^{-/-} mice cohort 2 as it was the frozen tissue available for transcriptomic analysis. These animals showed a different histological characterization to *ApoE*^{-/-} cohort 1 mice therefore, the same transcriptomic analysis should be done in a third *ApoE*^{-/-} mouse cohort. Furthermore, the current analysis used n = 6 controls and n = 4 atherosclerotic mice, the relatively small sample size determines a larger inherent sampling error and effects are harder to detect in smaller samples. Increasing the sample size in a new cohort *ApoE*^{-/-} and including a set of C57BL/6 fed with high fat diet would boost the statistical power of the research and also provide further insight into the transcriptomic changes due to systemic atherosclerosis.

An advantage of microarray analysis is the possibility to perform time-scale analyses in cell cultures or in animal experiments, and with the aid of data clustering, it is possible to visualize gene expression patterns. However, microarrays are prone to various problems which include, but are not limited to, the interpretation of the results as there is a non-linearity of correlation between mRNA and protein expression and problems in reporting of the results. Furthermore, the transcriptomic changes identified in RNA extracted directly from mice CNS tissue are required to be related to human disease pathogenesis as the ultimate goal is to identify key therapeutic targets. The use of LCM for the microarray analysis allow to analyse transcriptomic changes on isolation with the possibility of analysing other neuroanatomically relevant areas from the same specimen. Future studies could consider dissecting the whole hippocampus for the initial assessment of the differences between the *ApoE*^{-/-} control and atherosclerotic mice transcriptome, because this protocol will yield a higher quantity and quality of RNA and provide an overview of the hippocampus.

A validation attempt of the microarray analysis results used the same mice and only employed qRT-PCR. The technical repeat did not replicate the results from the transcriptomic analysis. The results could be related to RNA quality as this could have been compromised by storage conditions; even though all samples were tested for RNA this factor could still influence gene expression and validation experiments. Later studies should focus on validating the genes expressing the highest fold change between the two mice diets. The microarray analysis using a fold change model can confidently select the genes that are differentially expressed as it reduces the possibility of genes being identified due to chance or natural variability.

Another limitation was the availability of tissue as, ideally, validation would have been performed in RNA samples obtained from multiple and different mouse cohorts. Alternatively NanoString analysis could have been used to validate the findings and investigate the expression of a larger number of genes. A significant advantage is the high sensitivity of this technology and accuracy of quantification of low quality and quantity mRNA within the sample, allowing the use of FFPE tissue. Furthermore, the automated process removes the need to amplify mRNA. Future studies should include immunohistochemistry functional validation to assess the expression and localisation of the proteins encoded by candidate genes identified in transcriptomic studies.

Another consideration is that tissue samples obtained from mice usually obtain a better quality of RNA which is reflected on higher RIN compared to human post-mortem tissue. This is due to the possibility of immediate tissue recovery after mice perfusion which is not possible with other types of samples. However, the functional data obtained in animal model studies should be interpreted with cautions as these models

do not recapitulate all aspects of the disease process. Future research should compare the results from the current study in post-mortem tissue to validate these findings.

5.4.6 Conclusion

The research in the current chapter aimed to determine whether systemic atherosclerosis damage promotes the activation of inflammatory mechanisms or alteration of related pathways in neurovascular cells in the hippocampus of *ApoE*^{-/-} mice from cohort 2. Overall, transcriptomic analysis of atherosclerotic *ApoE*^{-/-} mouse hippocampus using microarray, revealed up-regulation of mitochondrial, Complex I and T-cell mediated cytotoxicity pathways and down-regulation of Ca²⁺ signalling pathways; which could be potentially linked to systemic atherosclerosis. The current study supports previous research indicating the involvement of Ca²⁺ signalling impairment on the cerebral cortex of mice fed with a high fat diet and dysregulation of vascular risk factors associated with neurodegeneration and AD (Liang et al., 2008; Yoon et al., 2019). The implications and possible drivers were discussed, and there seem to be transcriptomic changes occurring in *ApoE*^{-/-} mice. However, these findings from the microarray analysis were inconclusive, requiring another set of data to more concretely determine the variations caused by atherosclerosis and high fat diet and its drivers.

Future research should investigate transcriptomic changes on a third cohort of *ApoE*^{-/-} mice and interrogate single-cell changes occurring in the WM region and cerebral cortex. Furthermore, research into transcriptomic changes of PCSK9 mice models and wild type mice fed with a high fat diet could allow to identify drivers of systemic atherosclerosis by comparing the *ApoE*^{-/-} knock out mouse model. The analysis could reveal differences between these models to identify the inflammatory changes driven

by the lack of APOE or high fat diet and potentially identify metabolic changes caused by systemic atherosclerosis. Also, the addition of different timepoints could reveal important changes that were missed by focussing on a single model and timepoint.

Chapter VI: GENERAL DISCUSSION

Systemic atherosclerosis is an inflammatory disease caused by elevated cholesterol and risk factors (aging, type 2 diabetes mellitus, arterial hypertension, insulin resistance) that cause damage to the endothelial cells of blood vessels. The accumulation of oxidised LDL cholesterol in atherosclerosis elicits an inflammatory response and forms atherosclerotic plaques.

The risk of atherosclerosis increases with age and is considered a risk factor for VD and AD. As a CVD, atherosclerosis is commonly associated with ischemic stroke, microinfarcts, WMH which predict cognitive impairment. To date, the majority of research has focused on the consequences of brain hypoperfusion and stroke in systemic atherosclerosis. Histological characterisation of atherosclerotic *ApoE*^{-/-} mice has demonstrated microglia and vascular inflammation in the basal ganglia driven by IL-1beta prior to an ischemic event (Denes et al., 2012). However, the inflammatory response in other brain cells and the mechanisms driving the observed changes are currently unknown. Therefore, the current project aimed to define the cellular and genetic changes that occur in the brains of two systemic atherosclerotic mouse models (*ApoE*^{-/-} and PCSK9 induced) in the absence of vascular occlusion. Through examination of IBA-1, GFAP and ICAM-1 immunostaining patterns associated with neuroinflammation to determine the immunoreactive profile indicated damage of the CNS potentially associated with NVU dysfunction. The findings presented in this thesis partially support the original hypothesis that systemic atherosclerosis leads to dysfunction of NVU, glial activation and contributes to neurodegeneration. The immunoreactive profile of atherosclerotic *ApoE*^{-/-} cohort 1 mice identified increase of astrocytic GFAP and endothelial cells ICAM-1 in the corpus callosum, as well as, IBA-1⁺ microglia in the hippocampus, corpus callosum and cerebral cortex. The glia and blood vessel profiles demonstrate a range of inflammation which may reflect a damage

to the BBB, dysfunction of the NVU, metabolic changes or a combination of all, suggesting that the variety of mechanisms affecting systemic atherosclerosis may be associated with inflammation in the CNS.

6.1 Histological characterisation of control and atherosclerotic mouse model

In support of the literature, the current study demonstrated that increased microglia immunoreactivity is a prominent feature of atherosclerotic mice. Furthermore, inflammation associated with astrogliosis and endothelial cell activation was also featured in the corpus callosum of atherosclerotic *ApoE*^{-/-} cohort 1 mice. Moreover, the presence of diffuse ICAM-1 immunoreactivity surrounding the blood vessels in the hippocampus may indicate BBB leakage. However, demyelination was not a feature of this model and other markers of microglia neuroinflammation, BBB damage or leakage were not successfully optimised. The transcriptomic analysis revealed upregulation of myelination associated genes *Mog* and *Mag* and associated with white matted changes but LFB staining showed no evidence of WM changes between controls and atherosclerotic mice. The LFB analysis was only performed on cohort 1 mice *ApoE*^{-/-} while microarray analysis was done in cohort 2 *ApoE*^{-/-} mice.

Interestingly, the *ApoE*^{-/-} cohort 2 mice presented a different pattern of staining compared to cohort 1, displaying a trend of increased immunoreactive profile for IBA-1 and ICAM-1. The different pattern of staining could be related to the presence of an immune reaction to an infection in control mice or changes in the mouse microbiome.

6.2 *Different atherosclerotic mice models display similar patterns of inflammation*

The current study investigated whether an atherosclerotic mouse model which is considered 'milder' would present a similar immunohistological profile on the NVU cells investigated in *ApoE*^{-/-} mice. Furthermore, APOE is known to have anti-inflammatory functions, including inhibition of the c-Jun N-terminal kinase cascade and removal of cellular debris. Therefore, the absence of APOE could exacerbate the inflammation observed in the current study. The PCSK9 induced mouse model was chosen as it does not alter the mouse genetic profile and APOE is functional. To the author's knowledge, there are no previous histological studies characterising the microglial, astrocytic and endothelial profiles associated with atherosclerosis due to Western diet feeding in this model. While the expression profile of GFAP, IBA-1 and ICAM-1 was similar between both models, none of the findings reached statistical significance.

6.3 *Transcriptomic profiling of ApoE*^{-/-} *mice identify dysregulation of calcium signalling.*

Gene expression profiling of atherosclerotic and control *Apoe*^{-/-} cohort 2 mice identified up-regulation of calcium signalling and down-regulation of oxidative phosphorylation in the mRNA level that were likely caused by high-fat diet feeding related to development of atherosclerotic plaques.

Calcium also has an essential role in the regulation of several physiological processes in the CNS including cell migration, BBB function, inflammation, and cellular communication. Multiple ATP-transporters including calcium ATPase channels and SERCA, which maintain Ca²⁺ concentrations in the cells, are also shown to be downregulated in atherosclerotic mice compared to controls. Astrocytes modulate the

activity of neighbouring cells such as neurons, microglia and oligodendrocytes through Ca^{2+} mediated intracellular communication mechanisms (Verderio and Matteoli, 2001). A reduction in Ca^{2+} signalling is often associated with loss of WM integrity indicating oligodendrocyte damage and axonal dysfunction, but these changes were not investigated in *ApoE*^{-/-} cohort 2 (Baltan, 2009). Fluctuating Ca^{2+} signalling also promotes microglia migration to sites of injury in the CNS, therefore decreased Ca^{2+} signalling is consistent with the reduced IBA-1 immunoreactive microglia observed in *ApoE*^{-/-} cohort 2.

Microarray analysis also revealed significant up-regulation of a limited number of genes involved in the immune response, but it could not be confirmed if these changes were due to systemic atherosclerosis or the potential presence of infection in these mice. These changes were not reflected in the pathway analysis which reveal high FDR values in most of the relevant pathways. It should also be acknowledged that validation using qRT-PCR did not corroborate the findings of the microarray analysis, showing a decrease of mitochondrial *Ndusf8* in *ApoE*^{-/-} cohort 2 controls, while microarray analysis indicated up-regulation. The hypothesis that mechanisms underlying the pathogenesis of systemic atherosclerosis lead to changes in the CNS in the absence of atherosclerotic plaque rupture and ischemic stroke could not be satisfactorily confirmed and another *ApoE*^{-/-} mouse cohort is necessary to convincingly determine the presence of transcriptomic changes in atherosclerotic mice.

6.4 Potential drivers of the observed changes

Metabolic syndrome is characterized by insulin resistance, diabetes mellitus, obesity, elevated blood pressure, and hyperglycaemia. It is a risk factor for development of human coronary artery disease and also dementia (Isomaa et al., 2001). A number of mouse models of metabolic syndrome exhibit accelerated

atherosclerotic plaque lesion formation (Kennedy et al., 2010). *ApoE*^{-/-} mice do not normally become obese, nor do they develop IR, even on a high-fat diet (Gao et al., 2007; Hofmann et al., 2008). However, under the proper dietary conditions they develop a glucose intolerance and elevated systemic inflammation associated with A β plasma concentrations. Kennedy et al., (2010) fed 8-week-old *ApoE*^{-/-} mice for 17 weeks (double the amount from the mice use in the current project) with a high-fat diet containing 10-60% kcal from fat and no added cholesterol 0.003%, compared to 0.15% by weight in Western diet. However most studies showing changes in the CNS associated with high-fat diet fed mice for a longer period of time (between 12-20 weeks) (Cavaliere et al., 2019; Kennedy et al., 2010; Kothari et al., 2017). Therefore, the changes observed in the current research could be an early indication of metabolic changes occurring, a neuroprotective response.

6.5 Future studies and limitations

The main limitation of this study is the lack of concordance of results between *ApoE*^{-/-} mouse cohorts. The transcriptomic changes observed in *ApoE*^{-/-} cohort 2 atherosclerotic mice are, potentially, masked by changes in control mice due to an external uncontrolled variant. Mouse studies have shown a direct role of the gut microbiome in weight gain and neuroinflammation; therefore, in future studies this would have to be closely monitored. Furthermore, a wider study is necessary to investigate if the genetic changes are related to a high fat or high sugar diet, as well as to atherosclerosis. Presumably the observed changes are related to an increase of lipoprotein deposition leading to metabolic changes and inflammation. However, a high sugar content such as the Western diet has been shown also elicit similar effects in

female wild type mice (Daly et al., 2020). Future studies should include male and female mice and compare the effect of a high-sugar, high-fat diet, and systemic atherosclerosis on the NVU. Such research should be continued by individual investigation of the transcriptomic profile of the different element of the NVU to precisely identify the mitochondrial dysfunction occurring in atherosclerotic mice.

The present study only used microarray analysis to identify changes in the ApoE^{-/-} cohort 2 mice transcriptome which proved advantageous as the data could be analysed outside the laboratory. Furthermore, microarray analysis protocols for hybridization and pipelines for data analysis are well-established. However, new technologies such as RNA-Seq could be used as this type of analysis could potentially provide information about more mouse gene transcripts as they are not reliant on previous sequence information. RNA-Seq provides further advantages such as identification of differentially expressed introns or paralogous genes (Martin et al., 2016). This new generation transcriptomic analysis could also be used to identify cell specific genes without the need to use LCM to isolate microglia, astrocytes or neurons from the tissue.

Mouse models of atherosclerosis have some limitations as atherosclerosis is an inflammatory disease but there are significant differences between mice and human immune systems (Tao and Reese, 2017). Due to their hyper-hygienic environments, mice bred on a laboratory are kept 'free' of specific pathogens, which are important for basal levels of activation and function of the immune system. For this reason, genetically modified mouse models had to be generated to study atherosclerosis. As with any other animal models the relevance of discoveries from such studies to humans have been questioned due to the differences between species, in the case of atherosclerosis mouse models the metabolism of lipids between species differs.

Furthermore, knockout experimental models might not represent the specific mutations, such as the ones associated with atherosclerosis (von Scheidt et al., 2017). Mutation specific models might not represent sporadic systemic atherosclerosis; therefore, future research should study both models and compare the transcriptomic and cellular changes. The next stage should use human post-mortem tissue from aged patients with and without systemic atherosclerosis to confirm the changes observed in mice.

6.6 Conclusion

Although the results from this thesis are not entirely conclusive, *ApoE*^{-/-} cohort 1 clearly revealed neuroinflammation in relation to systemic atherosclerosis presenting higher vulnerability in the WM. These changes appear to also be present in PCSK9 induced mice but the low number of mice likely affected the statistical power of this analysis and warrants further investigation. Evidently a clear alteration in *ApoE*^{-/-} results in glial inflammation, however this study was unable to determine the cause of such changes. It is extremely important to continue to validate these findings to determine the role of the NVU and metabolic changes in the neuroinflammation associated to systemic atherosclerosis, The dissimilar results obtained from *ApoE*^{-/-} cohort 2 demonstrates the importance of replication and its implications of reproducibility is an important aspect of science, now more than ever. The results from the transcriptomic analysis suggest a change in the normal function of the hippocampus between control and atherosclerotic mice but the driving factors eliciting this change in *ApoE*^{-/-} cohort 2 remains to be determined. No other study to date has successfully characterised microglia, astrocytes, and endothelial cells in the *ApoE*^{-/-} and PCSK9 induced mouse models of atherosclerosis. Future research should focus on determining the mechanisms responsible for driving neuroinflammation in systemic atherosclerosis and define if the observed changes are pro- or anti-inflammatory, as this could reveal potential therapeutic targets for vascular dementia.

My PhD project was affected by the COVID-19 pandemic as I was unable to finish a series of experiments. Before the COVID-19 pandemic there was a plan to analyse the cerebral cortex of cohort 2 mice using microarray and to raise another set of *ApoE*^{-/-} mice which would include a histological characterisation followed by a microarray study of the hippocampus, cerebral cortex and corpus callosum and potentially single cell

analysis. The qPCR validation of cohort 2 could have been repeated to successfully analyse the down-regulated genes.

There was also a plan to include behavioural analysis through use of the new object recognition equipment. Furthermore, a microglia morphology quantification was being coordinated with a colleague in the United States but contact was lost during lockdown and I was not able to finish the analysis without his cooperation.

References

- Abbott, N.J., Rönnebeck, L., and Hansson, E. (2006). Astrocyte–endothelial interactions at the blood–brain barrier. *Nat. Rev. Neurosci.* 7, 41–53.
- Abifadel, M., Varret, M., Rabès, J.-P., Allard, D., Ouguerram, K., Devillers, M., Cruaud, C., Benjannet, S., Wickham, L., Erlich, D., et al. (2003). Mutations in PCSK9 cause autosomal dominant hypercholesterolemia. *Nat. Genet.* 34, 154–156.
- Adorni, M.P., Ruscica, M., Ferri, N., Bernini, F., and Zimetti, F. (2019). Proprotein Convertase Subtilisin/Kexin Type 9, Brain Cholesterol Homeostasis and Potential Implication for Alzheimer’s Disease. *Front. Aging Neurosci.* 11.
- Aird, W.C. (2007). Phenotypic heterogeneity of the endothelium: I. Structure, function, and mechanisms. *Circ. Res.* 100, 158–173.
- Al-Mashhadi, S., Simpson, J.E., Heath, P.R., Dickman, M., Forster, G., Matthews, F.E., Brayne, C., Ince, P.G., Wharton, S.B., and Medical Research Council Cognitive Function and Ageing Study (2015). Oxidative Glial Cell Damage Associated with White Matter Lesions in the Aging Human Brain. *Brain Pathol.* 25, 565–574.
- Andriezen, W.L. (1893). The neuroglia elements in the human brain. *Br. Med. J.* 2, 227–230.
- Apaijai, N., Moisescu, D.M., Palee, S., McSweeney, C.M., Saiyasit, N., Maneechote, C., Boonnag, C., Chattipakorn, N., and Chattipakorn, S.C. (2019). Pretreatment With PCSK9 Inhibitor Protects the Brain Against Cardiac Ischemia/Reperfusion Injury Through a Reduction of Neuronal Inflammation and Amyloid Beta Aggregation. *J. Am. Heart Assoc.* 8.
- Argaw, A.T., Asp, L., Zhang, J., Navrazhina, K., Pham, T., Mariani, J.N., Mahase, S., Dutta, D.J., Seto, J., Kramer, E.G., et al. (2012). Astrocyte-derived VEGF-A drives blood-brain barrier disruption in CNS inflammatory disease. *J. Clin. Invest.* 122, 2454–

2468.

Arimura, K., Ago, T., Kamouchi, M., Nakamura, K., Ishitsuka, K., Kuroda, J., Sugimori, H., Ooboshi, H., Sasaki, T., and Kitazono, T. (2012). PDGF Receptor α Signaling in Pericytes Following Ischemic Brain Injury. *Curr. Neurovasc. Res.* 9, 1–9.

Armulik, A., Genové, G., and Betsholtz, C. (2011). Pericytes: developmental, physiological, and pathological perspectives, problems, and promises. *Dev. Cell* 21, 193–215.

Arvanitakis, Z., Capuano, A.W., Leurgans, S.E., Buchman, A.S., Bennett, D.A., and Schneider, J.A. (2017). The Relationship of Cerebral Vessel Pathology to Brain Microinfarcts. *Brain Pathol.* 27, 77–85.

Baker, D. (1998). Natural Pathogens of Laboratory Mice, Rats, and Rabbits and Their Effects on Research. *Clin. Microbiol. Rev.* 11, 231–266.

Baker, M. (2016). 1,500 scientists lift the lid on reproducibility | Nature. *Nature* 533, 454–454.

Baltan, S. (2009). Ischemic injury to white matter: An age-dependent process. *Neuroscientist* 15, 126–133.

Barlow, G.M., Yu, A., and Mathur, R. (2015). Role of the Gut Microbiome in Obesity and Diabetes Mellitus. *Nutr. Clin. Pract.* 30, 787–797.

Barua, S., Kim, J.Y., Yenari, M.A., and Lee, J.E. (2019). The role of NOX inhibitors in neurodegenerative diseases. *IBRO Reports* 7, 59.

Bell, R.D., Winkler, E.A., Sagare, A.P., Singh, I., LaRue, B., Deane, R., and Zlokovic, B. V (2010). Pericytes Control Key Neurovascular Functions and Neuronal Phenotype in the Adult Brain and during Brain Aging. *Neuron* 68, 409–427.

Bell, R.D., Winkler, E.A., Singh, I., Sagare, A.P., Deane, R., Wu, Z., Holtzman, D.M., Betsholtz, C., Armulik, A., Sallstrom, J., et al. (2012). Apolipoprotein e controls

cerebrovascular integrity via cyclophilin A. *Nature* 485, 512–516.

Björkhem, I., Meaney, S., and Fogelman, A.M. (2004). Brain Cholesterol: Long Secret Life behind a Barrier. *Arterioscler. Thromb. Vasc. Biol.* 24, 806–815.

Bjørklund, M.M., Hollensen, A.K., Hagensen, M.K., Dagnæs-Hansen, F., Christoffersen, C., Mikkelsen, J.G., and Bentzon, J.F. (2014). Induction of atherosclerosis in mice and hamsters without germline genetic engineering. *Circ. Res.* 114, 1684–1689.

Boche, D., Perry, V.H., and Nicoll, J.A.R. (2013). Review: Activation patterns of microglia and their identification in the human brain. *Neuropathol. Appl. Neurobiol.* 39, 3–18.

Böttcher, C., Schlickeiser, S., Sneebauer, M.A.M., Kunkel, D., Knop, A., Paza, E., Fidzinski, P., Kraus, L., Snijders, G.J.L., Kahn, R.S., et al. (2019). Human microglia regional heterogeneity and phenotypes determined by multiplexed single-cell mass cytometry. *Nat. Neurosci.* 22, 78–90.

Bras, J., Guerreiro, R., Darwent, L., Parkkinen, L., Ansorge, O., Escott-Price, V., Hernandez, D.G., Nalls, M.A., Clark, L.N., Honig, L.S., et al. (2014). Genetic analysis implicates APOE, SNCA and suggests lysosomal dysfunction in the etiology of dementia with Lewy bodies. *Hum. Mol. Genet.* 23, 6139–6146.

Brendel, A.B., Greulich, R.S., Niederman, F., and Trang, S. (2020). Towards a Greater Diversity of Replication Studies. *AISS Trans. Replication Res.* 6, 20.

Brown, A.M., and Ransom, B.R. (2015). Astrocyte glycogen as an emergency fuel under conditions of glucose deprivation or intense neural activity. *Metab. Brain Dis.* 30, 233–239.

Bushong, E.A., Martone, M.E., Jones, Y.Z., and Ellisman, M.H. (2002). Protoplasmic astrocytes in CA1 stratum radiatum occupy separate anatomical domains. *J. Neurosci.*

22, 183–192.

Butler, M.J., Perrini, A.A., and Eckel, L.A. (2020). Estradiol treatment attenuates high fat diet-induced microgliosis in ovariectomized rats. *Horm. Behav.* 120, 104675.

Canuel, M., Sun, X., Asselin, M.C., Paramithiotis, E., Prat, A., and Seidah, N.G. (2013). Proprotein Convertase Subtilisin/Kexin Type 9 (PCSK9) Can Mediate Degradation of the Low Density Lipoprotein Receptor-Related Protein 1 (LRP-1). *PLoS One* 8, e64145.

Caplan, L.R. (2015). Lacunar Infarction and Small Vessel Disease: Pathology and Pathophysiology. *J. Stroke* 17, 2.

Carrano, A., Hoozemans, J.J.M., Vies, S.M. van der, Horssen, J. van, Vries, H.E. de, and Rozemuller, A.J.M. (2012). Neuroinflammation and Blood-Brain Barrier Changes in Capillary Amyloid Angiopathy. *Neurodegener. Dis.* 10, 329–331.

Casserly, I., and Topol, E.J. (2004). Convergence of atherosclerosis and Alzheimer's disease: inflammation, cholesterol, and misfolded proteins. *Lancet* 363, 1139–1146.

Castro Dias, M., Odriozola Quesada, A., Soldati, S., Bösch, F., Gruber, I., Hildbrand, T., Sönmez, D., Khire, T., Witz, G., McGrath, J.L., et al. (2021). Brain endothelial tricellular junctions as novel sites for T cell diapedesis across the blood-brain barrier. *J. Cell Sci.* 134.

Cavaglia, M., Dombrowski, S.M., Drazba, J., Vasanji, A., Bokesch, P.M., and Janigro, D. (2001). Regional variation in brain capillary density and vascular response to ischemia. *Brain Res.* 910, 81–93.

Cavaliere, G., Trinchese, G., Penna, E., Cimmino, F., Pirozzi, C., Lama, A., Annunziata, C., Catapano, A., Mattace Raso, G., Meli, R., et al. (2019). High-Fat Diet Induces Neuroinflammation and Mitochondrial Impairment in Mice Cerebral Cortex and Synaptic Fraction. *Front. Cell. Neurosci.* 13.

Chavakis, T., Bierhaus, A., and Nawroth, P.P. (2004). RAGE (receptor for advanced glycation end products): a central player in the inflammatory response. *Microbes Infect.* 6, 1219–1225.

Chen, A., Akinyemi, R.O., Hase, Y., Firbank, M.J., Ndung'u, M.N., Foster, V., Craggs, L.J.L., Washida, K., Okamoto, Y., Thomas, A.J., et al. (2016). Frontal white matter hyperintensities, clasmotodendrosis and gliovascular abnormalities in ageing and post-stroke dementia. *Brain* 139, 242–258.

Chen, W.-H., Jin, W., Lyu, P.-Y., Liu, Y., Li, R., Hu, M., and Xiao, X.-J. (2017). Carotid Atherosclerosis and Cognitive Impairment in Nonstroke Patients. *Chin. Med. J. (Engl.)* 130, 2375–2379.

Cheng, T., Petraglia, A.L., Li, Z., Thiyagarajan, M., Zhong, Z., Wu, Z., Liu, D., Maggirwar, S.B., Deane, R., Fernández, J.A., et al. (2006). Activated protein C inhibits tissue plasminogen activator–induced brain hemorrhage. *Nat. Med.* 12, 1278–1285.

Civeira, F., Pocoví, M., Alegría, E., Alonso, R., Carmena, R., Casanovas, J.A., Defesche, J.C., Jensen, H.K., Hopkins, P.N., Illingworth, D.R., et al. (2004). Guidelines for the diagnosis and management of heterozygous familial hypercholesterolemia. *Atherosclerosis* 173, 55–68.

Clarke, L.E., Liddelow, S.A., Chakraborty, C., Münch, A.E., Heiman, M., and Barres, B.A. (2018). Normal aging induces A1-like astrocyte reactivity. *115*, 1896–1905.

Coltman, R., Spain, A., Tsenkina, Y., Fowler, J.H., Smith, J., Scullion, G., Allerhand, M., Scott, F., Kalaria, R.N., Ihara, M., et al. (2011). Selective white matter pathology induces a specific impairment in spatial working memory. *Neurobiol. Aging* 32, 2324.e7-2324.e12.

Colton, C.A., and Wilcock, D.M. (2010). Assessing Activation States in Microglia. *CNS Neurol. Disord. - Drug Targets* 9, 174–191.

Courtoy, P.J., and Boyles, J. (1983). Fibronectin in the microvasculature: localization in the pericyte-endothelial interstitium. *J. Ultrastruct. Res.* 83, 258–273.

Crabbe, J.C., Wahlsten, D., and Dudek, B.C. (1999). Genetics of Mouse Behavior: Interactions with Laboratory Environment. *Science* (80-.). 284, 1670–1672.

Crowe, E.P., Tuzer, F., Gregory, B.D., Donahue, G., Gosai, S.J., Cohen, J., Leung, Y.Y., Yetkin, E., Nativio, R., Wang, L.-S., et al. (2016). Changes in the Transcriptome of Human Astrocytes Accompanying Oxidative Stress-Induced Senescence. *Front. Aging Neurosci.* 8, 208.

Csiszar, A., Ungvari, Z., Koller, A., Edwards, J.G., and Kaley, G. (2004). Proinflammatory phenotype of coronary arteries promotes endothelial apoptosis in aging. *Physiol. Genomics* 17, 21–30.

Cunningham, C., Wilcockson, D.C., Campion, S., Lunnon, K., and Perry, V.H. (2005). Central and Systemic Endotoxin Challenges Exacerbate the Local Inflammatory Response and Increase Neuronal Death during Chronic Neurodegeneration. *J. Neurosci.* 25, 9275–9284.

Daly, C.M., Saxena, J., Singh, J., Bullard, M.R., Bondy, E.O., Saxena, A., Buffalino, R.E., Melville, M.F., Freeman, L.R., CM, D., et al. (2020). Sex differences in response to a high fat, high sucrose diet in both the gut microbiome and hypothalamic astrocytes and microglia. 1–15.

Daneman, R. (2012). The blood-brain barrier in health and disease. *Ann. Neurol.* 72, 648–672.

Daneman, R., and Prat, A. (2015). The blood-brain barrier. *Cold Spring Harb. Perspect. Biol.* 7, a020412.

Daya, S., and Berns, K.I. (2008). Gene therapy using adeno-associated virus vectors. *Clin. Microbiol. Rev.* 21, 583–593.

Denes, A., Drake, C., Stordy, J., Chamberlain, J., McColl, B.W., Gram, H., Crossman, D., Francis, S., Allan, S.M., and Rothwell, N.J. (2012). Interleukin-1 Mediates Neuroinflammatory Changes Associated With Diet-Induced Atherosclerosis. *J. Am. Heart Assoc.* 1, e002006–e002006.

Denver, P., D’Adamo, H., Hu, S., Zuo, X., Zhu, C., Okuma, C., Kim, P., Castro, D., Jones, M.R., Leal, C., et al. (2019). A Novel Model of Mixed Vascular Dementia Incorporating Hypertension in a Rat Model of Alzheimer’s Disease. *Front. Physiol.* 0, 1269.

Deramecourt, V., Slade, J.Y., Oakley, A.E., Perry, R.H., Ince, P.G., Maurage, C.-A., and Kalaria, R.N. (2012). Staging and natural history of cerebrovascular pathology in dementia. *Neurology* 78, 1043–1050.

Devine, L., Lightman, S.L., and Greenwood, J. (1996). Role of LFA-1, ICAM-1, VLA-4 and VCAM-1 in lymphocyte migration across retinal pigment epithelial monolayers in vitro. *Immunology* 88, 456–462.

Ding, R., Hase, Y., Ameen-Ali, K., and Ndung’u, M. (2020). Loss of capillary pericytes and the blood–brain barrier in white matter in poststroke and vascular dementias and Alzheimer’s disease. *Brain Pathol.* 1–15.

Dolan, H., Crain, B., Troncoso, J., Resnick, S.M., Zonderman, A.B., and O’Brien, R.J. (2010). Atherosclerosis, dementia, and alzheimer’s disease in the BLSA cohort. *Ann. Neurol.* 68, n/a-n/a.

Drake, C., Boutin, H., Jones, M.S., Denes, A., McColl, B.W., Selvarajah, J.R., Hulme, S., Georgiou, R.F., Hinz, R., Gerhard, A., et al. (2011). Brain inflammation is induced by co-morbidities and risk factors for stroke. *Brain. Behav. Immun.* 25, 1113–1122.

Duncombe, J., Lennen, R.J., Jansen, M.A., Marshall, I., Wardlaw, J.M., and Horsburgh, K. (2017). Ageing causes prominent neurovascular dysfunction associated

with loss of astrocytic contacts and gliosis. *Neuropathol. Appl. Neurobiol.* *43*, 477–491.

Duong, M.T., Nasrallah, I.M., Wolk, D.A., Chang, C.C.Y., and Chang, T.-Y. (2021). Cholesterol, Atherosclerosis, and APOE in Vascular Contributions to Cognitive Impairment and Dementia (VCID): Potential Mechanisms and Therapy. *Front. Aging Neurosci.* *0*, 142.

Engelhardt, B., Vestweber, D., Hallmann, R., and Schulz, M. (1997). E- and P-selectin are not involved in the recruitment of inflammatory cells across the blood-brain barrier in experimental autoimmune encephalomyelitis. *Blood* *90*, 4459–4472.

Erdo, F., Denes, L., and De Lange, E. (2017). Age-associated physiological and pathological changes at the blood–brain barrier: A review. *J. Cereb. Blood Flow Metab.* *37*, 4–24.

Etienne-Manneville, S., Manneville, J.-B., Adamson, P., Wilbourn, B., Greenwood, J., and Couraud, P.-O. (2000). ICAM-1-Coupled Cytoskeletal Rearrangements and Transendothelial Lymphocyte Migration Involve Intracellular Calcium Signaling in Brain Endothelial Cell Lines. *J. Immunol.* *165*, 3375–3383.

Fadul, M.M., Heath, P.R., Cooper-Knock, J., Kurz, J.M., Al-Azzawi, H.A., Ali, Z., Smith, T., Matthews, F.E., Brayne, C., Wharton, S.B., et al. (2020). Transcriptomic analysis of age-associated periventricular lesions reveals dysregulation of the immune response. *Int. J. Mol. Sci.* *21*, 1–21.

Falk, E., Nakano, M., Bentzon, J.F., Finn, A. V., and Virmani, R. (2013). Update on acute coronary syndromes: the pathologists' view. *Eur. Heart J.* *34*, 719–728.

Fan, Q.-W., Iosbe, I., Asou, H., Yanagisawa, K., and Michikawa, M. (2001). EXPRESSION AND REGULATION OF APOLIPOPROTEIN E RECEPTORS CELLS OF THE CENTRAL NERVOUS SYSTEM IN CULTURE: A REVIEW IN THE. *J. Amer. Aging Assoc* *24*, 1–10.

Fan, Y., Yang, X., Tao, Y., Lan, L., Zheng, L., and Sun, J. (2015). Tight junction disruption of blood–brain barrier in white matter lesions in chronic hypertensive rats. *Neuroreport* 26, 1039–1043.

Fernández-Arjona, M. del M., Grondona, J.M., Granados-Durán, P., Fernández-Llebrez, P., and López-Ávalos, M.D. (2017). Microglia Morphological Categorization in a Rat Model of Neuroinflammation by Hierarchical Cluster and Principal Components Analysis. *Front. Cell. Neurosci.* 11, 235.

Van Der Flier, W.M., Skoog, I., Schneider, J.A., Pantoni, L., Mok, V., Chen, C.L.H., and Scheltens, P. (2018). Vascular cognitive impairment. *Nat. Rev. Dis. Prim.* 4, 1–16.

Fontainhas, A.M., Wang, M., Liang, K.J., Chen, S., Mettu, P., Damani, M., Fariss, R.N., Li, W., and Wong, W.T. (2011). Microglial Morphology and Dynamic Behavior Is Regulated by Ionotropic Glutamatergic and GABAergic Neurotransmission. *PLoS One* 6, e15973.

Francesca, A., De Simone, R., Penna, G., and Adorini, L. (2000). Functional maturation of adult mouse resting microglia into an APC is promoted by granulocyte-macrophage colony-stimulating factor and interaction with Th1Cells. *J. Immunol.* 164, 1705–1712.

Frías-Anaya, E., Gromnicova, R., Kraev, I., Rogachevsky, V., Male, D.K., Crea, F., Hawkes, C.A., and Romero, I.A. (2021). Age-related ultrastructural neurovascular changes in the female mouse cortex and hippocampus. *Neurobiol. Aging.*

Furnkranz, A., Schober, A., Bochkov, V.N., Bashtrykov, P., Kronke, G., Kadl, A., Binder, B.R., Weber, C., and Leitinger, N. (2005). Oxidized phospholipids trigger atherogenic inflammation in murine arteries. *Arterioscler. Thromb. Vasc. Biol.* 25, 633–638.

Gargiulo, S., Gramanzini, M., and Mancini, M. (2016). Molecular Imaging of Vulnerable

Atherosclerotic Plaques in Animal Models. *Int. J. Mol. Sci.* 17, 1511.

Garwood, C.J., Ratcliffe, L.E., Simpson, J.E., Heath, P.R., Ince, P.G., and Wharton, S.B. (2017). Review: Astrocytes in Alzheimer's disease and other age-associated dementias: a supporting player with a central role. *Neuropathol. Appl. Neurobiol.* 43, 281–298.

Gehrmann, J., and Kreutzberg, G.W. (1991). Characterisation of two new monoclonal antibodies directed against rat microglia. *J. Comp. Neurol.* 313, 409–430.

Geranmayeh, M.H., Rahbarghazi, R., and Farhoudi, M. (2019). Targeting pericytes for neurovascular regeneration. *Cell Commun. Signal.* 17, 1–13.

Gerhardt, H., Wolburg, H., and Redies, C. (2000). N-cadherin mediates pericytic-endothelial interaction during brain angiogenesis in the chicken. *Dev. Dyn.* 218, 472–479.

Giacomello, M., De Mario, A., Scarlatti, C., Primerano, S., and Carafoli, E. (2013). Plasma membrane calcium ATPases and related disorders. *Int. J. Biochem. Cell Biol.* 45, 753–762.

Giugliano, R.P., Mach, F., Zavitz, K., Kurtz, C., Im, K., Kanevsky, E., Schneider, J., Wang, H., Keech, A., Pedersen, T.R., et al. (2017). Cognitive Function in a Randomized Trial of Evolocumab. [Http://Dx.Doi.Org/10.1056/NEJMoa1701131](http://Dx.Doi.Org/10.1056/NEJMoa1701131) 377, 633–643.

Glaser, T., Arnaud Sampaio, V.F., Lameu, C., and Ulrich, H. (2019). Calcium signalling: A common target in neurological disorders and neurogenesis. *Semin. Cell Dev. Biol.* 95, 25–33.

Gold, G., Giannakopoulos, P., Herrmann, F.R., Bouras, C., and Kövari, E. (2007). Identification of Alzheimer and vascular lesion thresholds for mixed dementia. *Brain* 130, 2830–2836.

Gomes-Leal, W. (2019). Why microglia kill neurons after neural disorders? the friendly fire hypothesis. *Neural Regen. Res.* 14, 1499–1502.

Goodall, E.F., Wang, C., Simpson, J.E., Baker, D.J., Drew, D.R., Heath, P.R., Saffrey, M.J., Romero, I.A., and Wharton, S.B. (2018). Age-associated changes in the blood-brain barrier: comparative studies in human and mouse. *Neuropathol. Appl. Neurobiol.* 44, 328–340.

Gordon, G.R.J., Howarth, C., and MacVicar, B.A. (2011). Bidirectional control of arteriole diameter by astrocytes. *Exp. Physiol.* 96, 393–399.

Grainger, D.J., Reckless, J., and McKilligin, E. (2004). Apolipoprotein E Modulates Clearance of Apoptotic Bodies In Vitro and In Vivo, Resulting in a Systemic Proinflammatory State in Apolipoprotein E-Deficient Mice. *J. Immunol.* 173, 6366–6375.

Greenwood, J., Heasman, S.J., Alvarez, J.I., Prat, A., Lyck, R., and Engelhardt, B. (2011). Review: Leucocyte-endothelial cell crosstalk at the blood-brain barrier: A prerequisite for successful immune cell entry to the brain. *Neuropathol. Appl. Neurobiol.* 37, 24–39.

Grinberg, L.T., and Heinsen, H. (2010). Toward a pathological definition of vascular dementia. *J. Neurol. Sci.* 299, 136–138.

Grinberg, L.T., and Thal, D.R. (2010). Vascular pathology in the aged human brain. *Acta Neuropathol.* 119, 277–290.

Guerrero-Castillo, S., Baertling, F., Kownatzki, D., Wessels, H.J., Arnold, S., Brandt, U., and Nijtmans, L. (2017). The Assembly Pathway of Mitochondrial Respiratory Chain Complex I. *Cell Metab.* 25, 128–139.

Gwon, S.-Y., Lee, H.M., Rhee, K.-J., and Sung, H.J. (2019). Microarray and proteome array in an atherosclerosis mouse model for identification of biomarkers in whole blood.

Int. J. Med. Sci. 16, 882.

Habas, K., and Shang, L. (2018). Alterations in intercellular adhesion molecule 1 (ICAM-1) and vascular cell adhesion molecule 1 (VCAM-1) in human endothelial cells. *Tissue Cell* 54, 139–143.

Hafezi-Moghadam, A., Thomas, K.L., and Wagner, D.D. (2007). ApoE deficiency leads to a progressive age-dependent blood-brain barrier leakage. *Am. J. Physiol. - Cell Physiol.* 292.

Hakim, A.M. (2019). Small Vessel Disease. *Front. Neurol.* 0, 1020.

Hall, C.N., Reynell, C., Gesslein, B., Hamilton, N.B., Mishra, A., Sutherland, B.A., O'Farrell, F.M., Buchan, A.M., Lauritzen, M., and Attwell, D. (2014). Capillary pericytes regulate cerebral blood flow in health and disease. *Nature* 508, 55–60.

Halliday, M.R., Rege, S. V, Ma, Q., Zhao, Z., Miller, C.A., Winkler, E.A., and Zlokovic, B. V (2016). Accelerated pericyte degeneration and blood–brain barrier breakdown in apolipoprotein E4 carriers with Alzheimer's disease. *J. Cereb. Blood Flow Metab.* 36, 216–227.

Han, H., Wang, Y.H., Qu, G.J., Sun, T.T., Li, F.Q., Jiang, W., and Luo, S.S. (2013). Differentiated miRNA expression and validation of signaling pathways in apoE gene knockout mice by cross-verification microarray platform. *Exp. Mol. Med.* 45, e13–e13.

Hansson, G.K., and Hermansson, A. (2011). The immune system in atherosclerosis. *Nat. Immunol.* 12, 204–212.

Hase, Y., Craggs, L., Hase, M., Stevenson, W., Slade, J., Lopez, D., Mehta, R., Chen, A., Liang, D., Oakley, A., et al. (2017). Effects of environmental enrichment on white matter glial responses in a mouse model of chronic cerebral hypoperfusion. *14*, 1–14.

Hayek, T., Oiknine, J., Brook, J.G., and Aviram, M. (1994). Increased Plasma and Lipoprotein Lipid Peroxidation in apo E-Deficient Mice. *Biochem. Biophys. Res.*

Commun. 201, 1567–1574.

Haynes, S.E., Hollopeter, G., Yang, G., Kurpius, D., Dailey, M.E., Gan, W.-B., and Julius, D. (2006). The P2Y₁₂ receptor regulates microglial activation by extracellular nucleotides. *Nat. Neurosci.* 2006 912 9, 1512–1519.

Hendrickx, D.A.E., van Eden, C.G., Schuurman, K.G., Hamann, J., and Huitinga, I. (2017). Staining of HLA-DR, Iba1 and CD68 in human microglia reveals partially overlapping expression depending on cellular morphology and pathology. *J. Neuroimmunol.* 309, 12–22.

Henkel, J.S., Beers, D.R., Wen, S., Bowser, R., and Appel, S.H. (2009). DECREASED mRNA EXPRESSION OF TIGHT JUNCTION PROTEINS IN LUMBAR SPINAL CORDS OF PATIENTS WITH ALS. *Neurology* 72, 1614–1616.

Hui, D.Y., and Basford, J.E. (2005). Distinct signaling mechanisms for apoE inhibition of cell migration and proliferation. *Neurobiol. Aging* 26, 317–323.

Iadecola, C. (2010). The overlap between neurodegenerative and vascular factors in the pathogenesis of dementia. *Acta Neuropathol.* 120, 287–296.

Ikram, M.A., Bersano, A., Manso-Calderón, R., Jia, J.-P., Schmidt, H., Middleton, L., Nacmias, B., Siddiqi, S., and Adams, H.H.H. (2017). Genetics of vascular dementia – review from the ICVD working group. *BMC Med.* 2017 151 15, 1–7.

Imamura, K., Hishikawa, N., Sawada, M., Nagatsu, T., Yoshida, M., and Hashizume, Y. (2003). Distribution of major histocompatibility complex class II-positive microglia and cytokine profile of Parkinson's disease brains. *Acta Neuropathol.* 106, 518–526.

Ito, D., Imai, Y., Ohsawa, K., Nakajima, K., Fukuuchi, Y., and Kohsaka, S. (1998). Microglia-specific localisation of a novel calcium binding protein, Iba1. *Mol. Brain Res.* 57, 1–9.

Jawien, J. (2012). The role of an experimental model of atherosclerosis: apoE-

knockout mice in developing new drugs against atherogenesis. *Curr. Pharm. Biotechnol.* *13*, 2435–2439.

Jeong, H.-K., Ji, K., Min, K., and Joe, E.-H. (2013). Brain inflammation and microglia: facts and misconceptions. *Exp. Neurobiol.* *22*, 59–67.

Jurga, A.M., Paleczna, M., and Kuter, K.Z. (2020). Overview of General and Discriminating Markers of Differential Microglia Phenotypes. *Front. Cell. Neurosci.* *14*.

Kalaria, R.N. (2016). Neuropathological diagnosis of vascular cognitive impairment and vascular dementia with implications for Alzheimer's disease. *Acta Neuropathol.* *131*, 659–685.

Kearney, M. (2019). The Long Term Plan is a game changer. NHS.

Kennedy, A.J., Ellacott, K.L.J., King, V.L., and Hasty, A.H. (2010). Mouse models of the metabolic syndrome. *DMM Dis. Model. Mech.* *3*, 156–166.

Keren-Shaul, H., Spinrad, A., Weiner, A., Matcovitch-Natan, O., Dvir-Szternfeld, R., Ulland, T.K., David, E., Baruch, K., Lara-Astaiso, D., Toth, B., et al. (2017). A Unique Microglia Type Associated with Restricting Development of Alzheimer's Disease. *Cell* *169*, 1276-1290.e17.

Kim, S.W., Roh, J., and Park, C.S. (2016). Immunohistochemistry for pathologists: Protocols, pitfalls, and tips. *J. Pathol. Transl. Med.* *50*, 411–418.

Kitagawa, K., Matsumoto, M., Sasaki, T., Hashimoto, H., Kuwabara, K., Ohtsuki, T., and Hori, M. (2002). Involvement of ICAM-1 in the progression of atherosclerosis in APOE-knockout mice. *Atherosclerosis* *160*, 305–310.

Konishi, H., and Kiyama, H. (2018). Microglial TREM2/DAP12 signaling: A double-edged sword in neural diseases. *Front. Cell. Neurosci.* *12*.

von Kortzfleisch, V.T., Karp, N.A., Palme, R., Kaiser, S., Sachser, N., and Richter, S.H. (2020). Improving reproducibility in animal research by splitting the study population

into several 'mini-experiments.' *Sci. Reports* 2020 101 10, 1–16.

Kothari, V., Luo, Y., Tornabene, T., O'Neill, A.M., Greene, M.W., Geetha, T., and Babu, J.R. (2017). High fat diet induces brain insulin resistance and cognitive impairment in mice. *Biochim. Biophys. Acta - Mol. Basis Dis.* 1863, 499–508.

Koudinov, A.R., and Koudinova, N. V. (2005). Cholesterol homeostasis failure as a unifying cause of synaptic degeneration. *J. Neurol. Sci.* 229–230, 233–240.

Krasemann, S., Madore, C., Cialic, R., Baufeld, C., Calcagno, N., El Fatimy, R., Beckers, L., O'Loughlin, E., Xu, Y., Fanek, Z., et al. (2017). The TREM2-APOE Pathway Drives the Transcriptional Phenotype of Dysfunctional Microglia in Neurodegenerative Diseases. *Immunity* 47, 566-581.e9.

Kuchibhotla, K. V, Lattarulo, C.R., Hyman, B.T., and Bacskai, B.J. (2009). Synchronous hyperactivity and intercellular calcium waves in astrocytes in Alzheimer mice. *Science* 323, 1211–1215.

Kumar, S., Kang, D.W., Rezvan, A., and Jo, H. (2017). Accelerated atherosclerosis development in C57Bl6 mice by overexpressing AAV-mediated PCSK9 and partial carotid ligation. *Lab. Investig.* 97, 935–945.

Lagace, T.A. (2014). PCSK9 and LDLR degradation: Regulatory mechanisms in circulation and in cells. *Curr. Opin. Lipidol.* 25, 387–393.

Lawson, L.J., Perry, V.H., Dri, P., and Gordon, S. (1990). Heterogeneity in the distribution and morphology of microglia in the normal adult mouse brain. *Neuroscience* 39, 151–170.

Lee, S.-H. (2020). *Cerebral Small Vessel Disease*. (Springer, Singapore), pp. 61–79.

Lee, S.J., and Benveniste, E.N. (1999). Adhesion molecule expression and regulation on cells of the central nervous system. *J. Neuroimmunol.* 98, 77–88.

Lee, Y.W., Eum, S.Y., Chen, K.C., Hennig, B., and Toborek, M. (2004). *Gene*

expression profile in interleukin-4-stimulated human vascular endothelial cells. *Mol. Med.* 10, 19–27.

De Leeuw, F.E., De Kleine, M., Frijns, C.J.M., Fijnheer, R., Van Gijn, J., and Kappelle, L.J. (2002). Endothelial cell activation is associated with cerebral white matter lesions in patients with cerebrovascular disease. In *Annals of the New York Academy of Sciences*, (Ann N Y Acad Sci), pp. 306–314.

Leijenaar, J.F., van Maurik, I.S., Kuijer, J.P.A., van der Flier, W.M., Scheltens, P., Barkhof, F., and Prins, N.D. (2017). Lower cerebral blood flow in subjects with Alzheimer's dementia, mild cognitive impairment, and subjective cognitive decline using two-dimensional phase-contrast magnetic resonance imaging. *Alzheimer's Dement. Diagnosis, Assess. Dis. Monit.* 9, 76–83.

Li, F., Xu, D., Hou, K., Gou, X., and Li, Y. (2020). The role of P2Y12 receptor inhibition in ischemic stroke on microglia, platelets and vascular smooth muscle cells. *J. Thromb. Thrombolysis* 50, 874–885.

Li, Q., Yang, Y., Reis, C., Tao, T., Li, W., Li, X., and Zhang, J.H. (2018). Cerebral Small Vessel Disease. *Cell Transplant.* 27, 1711.

Liang, W.S., Reiman, E.M., Valla, J., Dunckley, T., Beach, T.G., Grover, A., Niedzielko, T.L., Schneider, L.E., Mastroeni, D., Caselli, R., et al. (2008). Alzheimer's disease is associated with reduced expression of energy metabolism genes in posterior cingulate neurons. *Proc. Natl. Acad. Sci.* 105, 4441–4446.

Libby, P. (2008). The molecular mechanisms of the thrombotic complications of atherosclerosis. *J. Intern. Med.* 263, 517–527.

Libby, P. (2021). Inflammation in Atherosclerosis-No Longer a Theory. *Clin. Chem.* 67, 131–142.

Liddel, S.A., and Barres, B.A. (2017). Review Reactive Astrocytes: Production,

Function, and Therapeutic Potential. *Immunity* 46, 957–967.

Liddel, S.A., Guttenplan, K.A., Clarke, L.E., Bennett, F.C., Bohlen, C.J., Schirmer, L., Bennett, M.L., Münch, A.E., Chung, W.-S., Peterson, T.C., et al. (2017). Neurotoxic reactive astrocytes are induced by activated microglia. *Nat.* 2017 5417638 541, 481–487.

Lipskaia, L., Keuylian, Z., Blirando, K., Mougnot, N., Jacquet, A., Rouxel, C., Sghairi, H., Elaib, Z., Blaise, R., Adnot, S., et al. (2014). Expression of sarco (endo) plasmic reticulum calcium ATPase (SERCA) system in normal mouse cardiovascular tissues, heart failure and atherosclerosis. *Biochim. Biophys. Acta - Mol. Cell Res.* 1843, 2705–2718.

Liu, C., Zou, L., Tang, X., Zhu, W., Zhang, G., Qin, Y., and Zhu, W. (2019). Changes of White Matter Integrity and Structural Network Connectivity in Nondemented Cerebral Small-Vessel Disease.

Liu, L.R., Liu, J.C., Bao, J.S., Bai, Q.Q., and Wang, G.Q. (2020). Interaction of Microglia and Astrocytes in the Neurovascular Unit. *Front. Immunol.* 11, 1024.

London, E., Nesterova, M., and Stratakis, C.A. (2017). Acute vs chronic exposure to high fat diet leads to distinct regulation of PKA. *J. Mol. Endocrinol.* 59, 1–12.

Lopez-Fabuel, I., Douce, J. Le, Logan, A., James, A.M., Bonvento, G., Murphy, M.P., Almeida, A., and Bolaños, J.P. (2016). Complex I assembly into supercomplexes determines differential mitochondrial ROS production in neurons and astrocytes. *Proc. Natl. Acad. Sci.* 113, 13063–13068.

Löscher, W., and Potschka, H. (2005). Blood-brain barrier active efflux transporters: ATP-binding cassette gene family. *NeuroRx* 2, 86–98.

Lou, N., Takano, T., Pei, Y., Xavier, A.L., Goldman, S.A., and Nedergaard, M. (2016). Purinergic receptor P2RY12-dependent microglial closure of the injured blood–brain

barrier. *Proc. Natl. Acad. Sci.* 113, 1074–1079.

Luissint, A.-C., Artus, C., Glacial, F., Ganeshamoorthy, K., and Couraud, P.-O. (2012). Tight junctions at the blood brain barrier: physiological architecture and disease-associated dysregulation. *Fluids Barriers CNS* 9, 23.

Lusis, A.J. (2000). Atherosclerosis. *Nature* 407, 233–241.

Lv, D., Shen, Y., Peng, Y., Liu, J., Miao, F., and Zhang, J. (2015). Neuronal MHC class I expression is regulated by activity driven calcium signaling. *PLoS One* 10.

Lynes, E.M., Raturi, A., Shenkman, M., Sandoval, C.O., Yap, M.C., Wu, J., Janowicz, A., Myhill, N., Benson, M.D., Campbell, R.E., et al. (2013). Palmitoylation is the switch that assigns calnexin to quality control or ER Ca²⁺ signaling. *J. Cell Sci.* 126, 3893–3903.

Mahley, R.W. (2016). Central nervous system lipoproteins: ApoE and regulation of cholesterol metabolism. *Arterioscler. Thromb. Vasc. Biol.* 36, 1305–1315.

Manso-Calderón, R. (2019). Genetics in vascular dementia. *Future Neurol.* 14.

Marschallinger, J., Iram, T., Zardeneta, M., Lee, S.E., Lehallier, B., Haney, M.S., Pluvinage, J. V., Mathur, V., Hahn, O., Morgens, D.W., et al. (2020). Lipid-droplet-accumulating microglia represent a dysfunctional and proinflammatory state in the aging brain. *Nat. Neurosci.* 2020 232 23, 194–208.

Martin, S.A.M., Dehler, C.E., and Król, E. (2016). Transcriptomic responses in the fish intestine. *Dev. Comp. Immunol.* 64, 103–117.

Martins, I.J., Hone, E., Foster, J.K., Sünram-Lea, S.I., Gnjec, A., Fuller, S.J., Nolan, D., Gandy, S.E., and Martins, R.N. (2006). Apolipoprotein E, cholesterol metabolism, diabetes, and the convergence of risk factors for Alzheimer's disease and cardiovascular disease. *Mol. Psychiatry* 2006 118 11, 721–736.

Matejuk, A., and Ransohoff, R.M. (2020). Crosstalk Between Astrocytes and Microglia:

An Overview. *Front. Immunol.* *0*, 1416.

Matias, I., Morgado, J., and Gomes, F.C.A. (2019). Astrocyte Heterogeneity: Impact to Brain Aging and Disease. *Front. Aging Neurosci.* *0*, 59.

Matsumoto, L., Suzuki, K., Mizuno, Y., Ohike, Y., Ozeki, A., Ono, S., Takanashi, M., Sawaki, D., Suzuki, T., Yamazaki, T., et al. (2018). Association of subclinical carotid atherosclerosis with immediate memory and other cognitive functions. *Geriatr. Gerontol. Int.* *18*, 65–71.

Maxwell, K.N., and Breslow, J.L. (2004). Adenoviral-mediated expression of Pcsk9 in mice results in a low-density lipoprotein receptor knockout phenotype. *Proc. Natl. Acad. Sci. U. S. A.* *101*, 7100–7105.

Mazaheri, F., Snaidero, N., Kleinberger, G., Madore, C., Daria, A., Werner, G., Krasemann, S., Capell, A., Trümbach, D., Wurst, W., et al. (2017). TREM 2 deficiency impairs chemotaxis and microglial responses to neuronal injury. *EMBO Rep.* *18*, 1186–1198.

McAvoy, K., and Kawamata, H. (2019). Glial mitochondrial function and dysfunction in health and neurodegeneration. *Mol. Cell. Neurosci.* *101*, 103417.

Meagher, L., Mahiouz, D., Sugars, K., Burrows, N., Norris, P., Yarwood, H., Becker-Andre, M., and Haskard, D.O. (1994). Measurement of mRNA for E-selectin, VCAM-1 and ICAM-1 by reverse transcription and the polymerase chain reaction. *J. Immunol. Methods* *175*, 237–246.

Miller, S.J. (2018). Astrocyte heterogeneity in the adult central nervous system. *Front. Cell. Neurosci.* *12*, 15.

Mino, T., Saito, H., Takeuchi, J., Ito, K., Takeda, A., Ataka, S., Shiomi, S., Wada, Y., Watanabe, Y., and Itoh, Y. (2017). Cerebral blood flow abnormality in clinically diagnosed Alzheimer's disease patients with or without amyloid β accumulation on

positron emission tomography. *Neurol. Clin. Neurosci.* 5, 55–59.

Mittelbronn, M., Dietz, K., Schluesener, H.J., and Meyermann, R. (2001). Local distribution of microglia in the normal adult human central nervous system differs by up to one order of magnitude. *Acta Neuropathol.* 2000 1013 101, 249–255.

De Montgolfier, O., Pinçon, A., Pouliot, P., Gillis, M.A., Bishop, J., Sled, J.G., Villeneuve, L., Ferland, G., Lévy, B.I., Lesage, F., et al. (2019). High Systolic Blood Pressure Induces Cerebral Microvascular Endothelial Dysfunction, Neurovascular Unit Damage, and Cognitive Decline in Mice. *Hypertension* 73, 217–228.

Moore, K.J., and Tabas, I. (2011a). Macrophages in the Pathogenesis of Atherosclerosis. *Cell* 145, 341–355.

Moore, K.J., and Tabas, I. (2011b). Macrophages in the Pathogenesis of Atherosclerosis. *Cell* 145, 341–355.

Mor, D.E., and Murphy, C.T. (2020). Mitochondrial hyperactivity as a potential therapeutic target in Parkinson's disease. *Transl. Med. Aging* 4, 117.

Moroni, F., Ammirati, E., Rocca, M.A., Filippi, M., Magnoni, M., and Camici, P.G. (2018). Cardiovascular disease and brain health: Focus on white matter hyperintensities. *IJC Hear. Vasc.* 19, 63–69.

Muddapu, V.R., Dharshini, S.A.P., Chakravarthy, V.S., and Gromiha, M.M. (2020). Neurodegenerative Diseases – Is Metabolic Deficiency the Root Cause? *Front. Neurosci.* 14, 213.

Nakka, V.P., Prakash-babu, P., and Vemuganti, R. (2016). Crosstalk Between Endoplasmic Reticulum Stress, Oxidative Stress, and Autophagy: Potential Therapeutic Targets for Acute CNS Injuries. *Mol. Neurobiol.* 53, 532–544.

Nimmerjahn, A., Kirchhoff, F., and Helmchen, F. (2005). Resting microglial cells are highly dynamic surveillants of brain parenchyma in vivo. *Science* 308, 1314–1318.

Niu, J., Tsai, H.-H., Hoi, K.K., Huang, N., Yu, G., Kim, K., Baranzini, S.E., Xiao, L., Chan, J.R., and Fancy, S.P.J. (2019). Aberrant oligodendroglial–vascular interactions disrupt the blood–brain barrier, triggering CNS inflammation. *Nat. Neurosci.* 2019 225 22, 709–718.

Nugent, A.A., Lin, K., Lengerich, B. van, Lianoglou, S., Przybyla, L., Davis, S.S., Llapashtica, C., Wang, J., Kim, D.J., Xia, D., et al. (2020). TREM2 Regulates Microglial Cholesterol Metabolism upon Chronic Phagocytic Challenge. *Neuron* 105, 837-854.e9.

de Oliveira, J., Engel, D.F., de Paula, G.C., dos Santos, D.B., Lopes, J.B., Farina, M., Moreira, E.L.G., and de Bem, A.F. (2020). High Cholesterol Diet Exacerbates Blood-Brain Barrier Disruption in LDLr^{-/-} Mice: Impact on Cognitive Function. *J. Alzheimer's Dis.* 78, 97–115.

Oppi, S., Lüscher, T.F., and Stein, S. (2019). Mouse Models for Atherosclerosis Research—Which Is My Line? *Front. Cardiovasc. Med.* 6, 46.

Orsucci, D., Mancuso, M., Caldarazzo Ienco, E., Simoncini, C., Siciliano, G., and Bonuccelli, U. (2013). Vascular Factors and Mitochondrial Dysfunction: a Central Role in the Pathogenesis of Alzheimer's Disease. *Curr. Neurovasc. Res.* 10, 76–80.

Ozsolak, F., and Milos, P.M. (2011). RNA sequencing: Advances, challenges and opportunities. *Nat. Rev. Genet.* 12, 87–98.

Pacelli, C., Giguère, N., Bourque, M.-J.J., Lévesque, M., Slack, R.S.S., and Trudeau, L.-É.É. (2015). Elevated Mitochondrial Bioenergetics and Axonal Arborization Size Are Key Contributors to the Vulnerability of Dopamine Neurons. *Curr. Biol.* 25, 2349–2360.

Pantoni, L. (2010). Cerebral small vessel disease: from pathogenesis and clinical characteristics to therapeutic challenges. *Lancet Neurol.* 9, 689–701.

Park, J., Choi, H., Min, J.-S., Park, S.-J., Kim, J.-H., Park, H.-J., Kim, B., Chae, J.-I., Yim, M., and Lee, D.-S. (2013). Mitochondrial dynamics modulate the expression of

pro-inflammatory mediators in microglial cells. *J. Neurochem.* 127, 221–232.

Pekny, M., and Hol, E.M. (2015). Glial fibrillary acidic protein (GFAP) and the astrocyte intermediate filament system in diseases of the central nervous system. *Curr. Opin. Cell Biol.* 32, 121–130.

Pekny, M., and Nilsson, M. (2005). Astrocyte activation and reactive gliosis. *Glia* 50, 427–434.

Pendse, A.A., Arbones-Mainar, J.M., Johnson, L.A., Altenburg, M.K., and Maeda, N. (2009). Apolipoprotein E knock-out and knock-in mice: atherosclerosis, metabolic syndrome, and beyond. *J. Lipid Res.* 50, S178.

Peppiatt, C.M., Howarth, C., Mobbs, P., and Attwell, D. (2006). Bidirectional control of CNS capillary diameter by pericytes. *Nature* 443, 700–704.

Perez-Nievas, B.G., and Serrano-Pozo, A. (2018). Deciphering the astrocyte reaction in Alzheimer's disease. *Front. Aging Neurosci.* 10, 114.

Pinton, P., Giorgi, C., Siviero, R., Zecchini, E., and Rizzuto, R. (2008). Calcium and apoptosis: ER-mitochondria Ca²⁺ transfer in the control of apoptosis. *Oncogene* 27, 6407–6418.

Plump, A.S., Smith, J.D., Hayek, T., Aalto-Setälä, K., Walsh, A., Verstuyft, J.G., Rubin, E.M., and Breslow, J.L. (1992). Severe hypercholesterolemia and atherosclerosis in apolipoprotein E-deficient mice created by homologous recombination in ES cells. *Cell* 71, 343–353.

Pocivavsek, A., Burns, M.P., and Rebeck, G.W. (2009). Low Density Lipoprotein Receptors Regulate Microglial Inflammation Through C-Jun N-Terminal Kinase. *Glia* 57, 444.

Poirier, S., Mayer, G., Benjannet, S., Bergeron, E., Marcinkiewicz, J., Nassoury, N., Mayer, H., Nimpf, J., Prat, A., and Seidah, N.G. (2008). The proprotein convertase

PCSK9 induces the degradation of low density lipoprotein receptor (LDLR) and its closest family members VLDLR and ApoER2. *J. Biol. Chem.* 283, 2363–2372.

Poitelon, Y., Kopec, A.M., and Belin, S. (2020). Myelin Fat Facts: An Overview of Lipids and Fatty Acid Metabolism. *Cells* 9.

Poschl, E., Schlötzer-Schrehardt, U., Brachvogel, B., Saito, K., Ninomiya, Y., and Mayer, U. (2004). Collagen IV is essential for basement membrane stability but dispensable for initiation of its assembly during early development. *Development* 131, 1619–1628.

Prendergast, C., Quayle, J., Burdyga, T., and Wray, S. (2014). Atherosclerosis differentially affects calcium signaling in endothelial cells from aortic arch and thoracic aorta in Apolipoprotein E knockout mice. *Physiol. Rep.* 2.

Price, B.R., Norris, C.M., Sompol, P., and Wilcock, D.M. (2018). An emerging role of astrocytes in vascular contributions to cognitive impairment and dementia. *J. Neurochem.* 144, 644–650.

Reed, B., Villeneuve, S., Mack, W., DeCarli, C., Chui, H., and Jagust, W. (2014). Associations between serum cholesterol levels and cerebral amyloidosis. *JAMA Neurol.* 71, 195–200.

Revesz, T., Holton, J.L., Lashley, T., Plant, G., Frangione, B., Rostagno, A., and Ghiso, J. (2009). Genetics and molecular pathogenesis of sporadic and hereditary cerebral amyloid angiopathies. *Acta Neuropathol.* 2009 1181 118, 115–130.

Riddell, D.R., Zhou, H., Atchison, K., Warwick, H.K., Atkinson, P.J., Jefferson, J., Xu, L., Aschmies, S., Kirksey, Y., Hu, Y., et al. (2008). Impact of Apolipoprotein E (ApoE) polymorphism on brain ApoE levels. *J. Neurosci.* 28, 11445–11453.

Rio-Hortega, P. (1919). El " Tercer elemento de los centros nerviosos" I-IV. *Boletín La Soc. Española Biol.* 8, 67–166.

Rosenberg, G.A. (2009). Matrix metalloproteinases and their multiple roles in neurodegenerative diseases. *Lancet Neurol.* 8, 205–216.

Rosenegger, D.G., Tran, C.H.T., Wamsteeker Cusulin, J.I., and Gordon, G.R. (2015). Tonic local brain blood flow control by astrocytes independent of phasic neurovascular coupling. *J. Neurosci.* 35, 13463–13474.

Rousselet, E., Marcinkiewicz, J., Kriz, J., Zhou, A., Hatten, M.E., Prat, A., and Seidah, N.G. (2011). PCSK9 reduces the protein levels of the LDL receptor in mouse brain during development and after ischemic stroke [S]. *J. Lipid Res.* 52, 1383–1391.

Ruganzu, J.B., Zheng, Q., Wu, X., He, Y., Peng, X., Jin, H., Zhou, J., Ma, R., Ji, S., Ma, Y., et al. (2021). TREM2 overexpression rescues cognitive deficits in APP/PS1 transgenic mice by reducing neuroinflammation via the JAK/STAT/SOCS signaling pathway. *Exp. Neurol.* 336, 113506.

Sagare, A.P., Bell, R.D., Zhao, Z., Ma, Q., Winkler, E.A., Ramanathan, A., and Zlokovic, B. V. (2013). Pericyte loss influences Alzheimer-like neurodegeneration in mice. *Nat. Commun.* 4, 2932.

Saji, N., Toba, K., and Sakurai, T. (2016). Cerebral Small Vessel Disease and Arterial Stiffness: Tsunami Effect in the Brain? *Pulse* 3, 182–189.

Sarkar, S., and Biswas, S.C. (2021). Astrocyte subtype-specific approach to Alzheimer's disease treatment. *Neurochem. Int.* 145, 104956.

Sasaki, Y., Ohsawa, K., Kanazawa, H., Kohsaka, S., and Imai, Y. (2001). Iba1 is an actin-cross-linking protein in macrophages/microglia. *Biochem. Biophys. Res. Commun.* 286, 292–297.

Schoch, K.M., Ezerskiy, L.A., Morhaus, M.M., Bannon, R.N., Sauerbeck, A.D., Shabsovich, M., Jafar-nejad, P., Rigo, F., and Miller, T.M. (2021). Acute Trem2 reduction triggers increased microglial phagocytosis, slowing amyloid deposition in

mice. *Proc. Natl. Acad. Sci.* *118*, 2100356118.

Schreyer, S.A., Wilson, D.L., and Leboeuf, R.C. (1998). C57BL/6 mice fed high fat diets as models for diabetes-accelerated atherosclerosis. *Atherosclerosis* *136*, 17–24.

Seidah, N.G., Benjannet, S., Wickham, L., Marcinkiewicz, J., Jasmin, S.B., Stifani, S., Basak, A., Prat, A., and Chrétien, M. (2003). The secretory proprotein convertase neural apoptosis-regulated convertase 1 (NARC-1): Liver regeneration and neuronal differentiation. *Proc. Natl. Acad. Sci.* *100*, 928–933.

Shabir, O., Pendry, B., Lee, L., Eyre, B., Sharp, P., Rebollar, M.A., Howarth, C., Heath, P.R., Wharton, S.B., Francis, S.E., et al. (2020a). Assessment of neurovascular coupling & cortical spreading depression in mixed models of atherosclerosis & Alzheimer's disease. *BioRxiv* 2020.08.13.249987.

Shabir, O., Sharp, P., Rebollar, M.A., Boorman, L., Howarth, C., Wharton, S.B., Francis, S.E., and Berwick, J. (2020b). Enhanced Cerebral Blood Volume under Normobaric Hyperoxia in the J20-hAPP Mouse Model of Alzheimer's Disease. *Sci. Rep.* *10*.

Shapiro, M.D., and Fazio, S. (2017). PCSK9 and Atherosclerosis - Lipids and Beyond. *J. Atheroscler. Thromb.* *24*, 462.

Silberberg, D.H., Manning, M.C., and Schreiber, A.D. (1984). Tissue culture demyelination by normal human serum. *Ann. Neurol.* *15*, 575–580.

Silvestrini, M., Viticchi, G., Falsetti, L., Balucani, C., Vernieri, F., Cerqua, R., Luzzi, S., Bartolini, M., and Provinciali, L. (2011). The role of carotid atherosclerosis in Alzheimer's disease progression. *J. Alzheimers. Dis.* *25*, 719–726.

Simpson, J.E., Wharton, S.B., Cooper, J., Gelsthorpe, C., Baxter, L., Forster, G., Shaw, P.J., Savva, G., Matthews, F.E., Brayne, C., et al. (2010). Alterations of the blood–brain barrier in cerebral white matter lesions in the ageing brain. *Neurosci. Lett.*

486, 246–251.

Sluiter, T.J., van Buul, J.D., Huveneers, S., Quax, P.H.A., and de Vries, M.R. (2021). Endothelial Barrier Function and Leukocyte Transmigration in Atherosclerosis. *Biomedicines* 9, 328.

Sofroniew, M. V (2014). Astrogliosis. *Cold Spring Harb. Perspect. Biol.* 7, a020420.

Sousa, C., Golebiewska, A., Poovathingal, S.K., Kaoma, T., Pires-Afonso, Y., Martina, S., Coowar, D., Azuaje, F., Skupin, A., Balling, R., et al. (2018). Single-cell transcriptomics reveals distinct inflammation-induced microglia signatures. *EMBO Rep.* 19, e46171.

Stahon, K.E., Bastian, C., Griffith, S., Kidd, G.J., Brunet, S., and Baltan, S. (2016). Age-Related Changes in Axonal and Mitochondrial Ultrastructure and Function in White Matter. *J. Neurosci.* 36, 9990–10001.

Steyers, C.M., and Miller, F.J. (2014). Endothelial Dysfunction in Chronic Inflammatory Diseases. *Int. J. Mol. Sci.* 2014, Vol. 15, Pages 11324-11349 15, 11324–11349.

Stranahan, A.M., and Mattson, M.P. (2010). Selective vulnerability of neurons in layer II of the entorhinal cortex during aging and Alzheimer's disease. *Neural Plast.* 2010.

Streit, W.J., and Kreutzberg, G.W. (1988). Response of endogenous glial cells to motor neuron degeneration induced by toxic ricin. *J. Comp. Neurol.* 268, 248–263.

Su, B., Wang, X., Zheng, L., Perry, G., Smith, M.A., and Zhu, X. (2010). Abnormal mitochondrial dynamics and neurodegenerative diseases. *Biochim. Biophys. Acta - Mol. Basis Dis.* 1802, 135–142.

Tabas, I., García-Cardena, G., and Owens, G.K. (2015). Recent insights into the cellular biology of atherosclerosis. *J. Cell Biol.* 209, 13–22.

Tachibana, M., Mohri, I., Hirata, I., Kuwada, A., Kimura-Ohba, S., Kagitani-Shimono, K., Fushimi, H., Inoue, T., Shiomi, M., Kakuta, Y., et al. (2019). Clasmatodendrosis is

associated with dendritic spines and does not represent autophagic astrocyte death in influenza-associated encephalopathy. *Brain Dev.* 41, 85–95.

Takahashi, K., Mizuarai, S., Araki, H., Mashiko, S., Ishihara, A., Kanatani, A., Itadani, H., and Kotani, H. (2003). Adiposity Elevates Plasma MCP-1 Levels Leading to the Increased CD11b-positive Monocytes in Mice. *J. Biol. Chem.* 278, 46654–46660.

Tsuang, D., Leverenz, J.B., Lopez, O.L., Hamilton, R.L., Bennett, D.A., Schneider, J.A., Buchman, A.S., Larson, E.B., Crane, P.K., Kaye, J.A., et al. (2013). APOE ϵ 4 increases risk for dementia in pure synucleinopathies. *JAMA Neurol.* 70, 223–228.

Tuomisto, T.T., Binder, B.R., and Ylä-Herttuala, S. (2005). Genetics, genomics and proteomics in atherosclerosis research. *Ann. Med.* 37, 323–332.

Valdearcos, M., Robblee, M.M., Benjamin, D.I., Nomura, D.K., Xu, A.W., and Koliwad, S.K. (2014). Microglia Dictate the Impact of Saturated Fat Consumption on Hypothalamic Inflammation and Neuronal Function. *Cell Rep.* 9, 2124–2138.

Verderio, C., and Matteoli, M. (2001). ATP Mediates Calcium Signaling Between Astrocytes and Microglial Cells: Modulation by IFN- γ . *J. Immunol.* 166, 6383–6391.

Verheijen, J., and Sleegers, K. (2018). Understanding Alzheimer Disease at the Interface between Genetics and Transcriptomics. *Trends Genet.* 34, 434–447.

Vicente-Gutierrez, C., Bonora, N., Bobo-Jimenez, V., Jimenez-Blasco, D., Lopez-Fabuel, I., Fernandez, E., Josephine, C., Bonvento, G., Enriquez, J.A., Almeida, A., et al. (2019). Astrocytic mitochondrial ROS modulate brain metabolism and mouse behaviour. *Nat. Metab.* 2019 12 1, 201–211.

Viña, D., Seoane, N., Vasquez, E.C., and Campos-Toimil, M. (2021). cAMP Compartmentalization in Cerebrovascular Endothelial Cells: New Therapeutic Opportunities in Alzheimer's Disease. *Cells* 10, 1951.

Vinuesa, A., Bentivegna, M., Calfa, G., Filipello, F., Pomilio, C., Bonaventura, M.M.,

- Lux-Lantos, V., Matzkin, M.E., Gregosa, A., Presa, J., et al. (2019). Early Exposure to a High-Fat Diet Impacts on Hippocampal Plasticity: Implication of Microglia-Derived Exosome-like Extracellular Vesicles. *Mol. Neurobiol.* 56, 5075–5094.
- VIRMANI, R., BURKE, A.P., KOLODZIE, F.D., and FARB, A. (2002). Vulnerable Plaque: The Pathology of Unstable Coronary Lesions. *J. Interv. Cardiol.* 15, 439–446.
- Voelkl, B., Altman, N.S., Forsman, A., Forstmeier, W., Gurevitch, J., Jaric, I., Karp, N.A., Kas, M.J., Schielzeth, H., Van de Castele, T., et al. (2020). Reproducibility of animal research in light of biological variation. *Nat. Rev. Neurosci.* 2020 217 21, 384–393.
- Waller, R., Baxter, L., Fillingham, D.J., Coelho, S., Pozo, J.M., Mozumder, M., Frangi, A.F., Ince, P.G., Simpson, J.E., and Highley, J.R. (2019). Iba-1-/CD68+ microglia are a prominent feature of age-associated deep subcortical white matter lesions. *PLoS One* 14, e0210888.
- Wang, D.D., and Bordey, A. (2008). The astrocyte odyssey. *Prog. Neurobiol.* 86, 342–367.
- Wang, X., Feuerstein, G.Z., Gu, J.-L., Lysko, P.G., and Yue, T.-L. (1995). Interleukin-1 β induces expression of adhesion molecules in human vascular smooth muscle cells and enhances adhesion of leukocytes to smooth muscle cells. *Atherosclerosis* 115, 89–98.
- Wharton, S.B., Simpson, J.E., Brayne, C., and Ince, P.G. (2015). Age-Associated White Matter Lesions: The MRC Cognitive Function and Ageing Study. *Brain Pathol.* 25, 35–43.
- WHO (2020). World Health Organization. The top 10 causes of death. (World Health Organization).
- Williams, K.J., and Tabas, I. (1995). The response-to-retention hypothesis of early

atherogenesis. *Arterioscler. Thromb. Vasc. Biol.* 15, 551–561.

Winkler, E.A., Sagare, A.P., and Zlokovic, B. V. (2014). The Pericyte: A Forgotten Cell Type with Important Implications for Alzheimer's Disease? *Brain Pathol.* 24, 371–386.

Wolburg, H., Neuhaus, J., Kniesel, U., Krauss, B., Schmid, E.M., Ocalan, M., Farrell, C., and Risau, W. (1994). Modulation of tight junction structure in blood-brain barrier endothelial cells. Effects of tissue culture, second messengers and cocultured astrocytes. *J. Cell Sci.* 107, 1347–1357.

Wolf, D., and Ley, K. (2019). Immunity and Inflammation in Atherosclerosis. *Circ. Res.* 124, 315–327.

Xia, J., Zhang, Y., Zhao, H., Wang, J., Gao, X., Chen, J., Fu, B., Shen, Y., Miao, F., Zhang, J., et al. (2017). Non-invasive monitoring of CNS MHC-I molecules in ischemic stroke mice. *Theranostics* 7, 2837–2848.

Yang, C., Hawkins, K.E., Doré, S., and Candelario-Jalil, E. (2019). Neuroinflammatory mechanisms of blood-brain barrier damage in ischemic stroke. <https://doi.org/10.1152/Ajpcell.00136.2018> 316, C135–C153.

Ye, J., Jiang, Z., Chen, X., Liu, M., Li, J., and Liu, N. (2016). Electron transport chain inhibitors induce microglia activation through enhancing mitochondrial reactive oxygen species production. *Exp. Cell Res.* 340, 315–326.

Yoon, G., Cho, K.A., Song, J., and Kim, Y.-K. (2019). Transcriptomic Analysis of High Fat Diet Fed Mouse Brain Cortex. *Front. Genet.* 0, 83.

Yue, W., Wang, A., Liang, H., Hu, F., Zhang, Y., Deng, M., Li, T., Hu, X., Ye, Z., Shen, Y., et al. (2016). Association between Carotid Intima-Media Thickness and Cognitive Impairment in a Chinese Stroke Population: A Cross-sectional Study. *Sci. Rep.* 6, 19556.

Zhou, T., Huang, Z., Sun, X., Zhu, X., Zhou, L., Li, M., Cheng, B., Liu, X., and He, C.

(2017). Microglia Polarization with M1/M2 Phenotype Changes in rd1 Mouse Model of Retinal Degeneration. *Front. Neuroanat.* 11, 77.

Ziebell, J.M., Taylor, S.E., Cao, T., Harrison, J.L., and Lifshitz, J. (2012). Rod microglia: Elongation, alignment, and coupling to form trains across the somatosensory cortex after experimental diffuse brain injury. *J. Neuroinflammation* 9, 1–11.

Zimetti, F., Caffarra, P., Ronda, N., Favari, E., Adorni, M.P., Zanotti, I., Bernini, F., Barocco, F., Spallazzi, M., Galimberti, D., et al. (2017). Increased PCSK9 Cerebrospinal Fluid Concentrations in Alzheimer's Disease. *J. Alzheimer's Dis.* 55, 315–320.

Zimmer, H., Riese, S., and Régnier-Vigouroux, A. (2003). Functional characterization of mannose receptor expressed by immunocompetent mouse microglia. *Glia* 42, 89–100.

Zlokovic, B. V. (2011). Neurovascular pathways to neurodegeneration in Alzheimer's disease and other disorders. *Nat. Rev. Neurosci.* 12, 723–738.

Zlokovic, B. V (2008). The blood-brain barrier in health and chronic neurodegenerative disorders. *Neuron* 57, 178–201.

Zrzavy, T., Machado-Santos, J., Christine, S., Baumgartner, C., Weiner, H.L., Butovsky, O., and Lassmann, H. (2018). Dominant role of microglial and macrophage innate immune responses in human ischemic infarcts. *Brain Pathol.* 28, 791–805.

Zubay, G.L.; P.W.W.; V.D.E. (1995). *Principles of biochemistry.*

Appendices

Appendix I: Mouse cohorts information

Case number	Mouse type	Diet	Cohort	Born	Diet change	Dissection date	Weight
183886	ApoE	Western Diet	1	03/17	05/17	08/17	Not measured
183882	ApoE	Western Diet	1				
183883	ApoE	Western Diet	1				
183887	ApoE	Western Diet	1				
183884	ApoE	Western Diet	1				
183881	ApoE	Western Diet	1				
183880	ApoE	Western Diet	1				
192050	ApoE	Normal Diet	1	03/11/17	no change	23/03/18	Not measured
192051	ApoE	Normal Diet	1				
192052	ApoE	Normal Diet	1				
192053	ApoE	Normal Diet	1				

192054	ApoE	Normal Diet	1				
192055	ApoE	Normal Diet	1				
192056	ApoE	Normal Diet	1				
231520	ApoE	Western Diet	2	28/12/18	25/02/19	20/05/19	32.1
231521	ApoE	Western Diet	2				32.4
231522	ApoE	Western Diet	2				32.7
231523	ApoE	Western Diet	2				31.4
231524	ApoE	Western Diet	2				33.5
231525	ApoE	Western Diet	2				29.7
230519	ApoE	Normal Diet	2	11/12/18	no change	29/04/19	31.3
230520	ApoE	Normal Diet	2				30.94
230521	ApoE	Normal Diet	2				31.53
231527	ApoE	Normal Diet	2	27/12/18		16/05/19	28.6
231528	ApoE	Normal Diet	2				32.2

231529	ApoE	Normal Diet	2				29.5
188686	Pcsk9	Western Diet	1	04/18	06/18	11/09/18	not measured
191575	Pcsk9	Western Diet	1				
191587	Pcsk9	Western Diet	1				
191570	Pcsk9	Western Diet	1				
194548	Pcsk9	Western Diet	1				
235197	Pcsk9	Normal Diet	1	15/1/19	no change	20/05/19	33.2
235196	Pcsk9	Normal Diet	1		no change		32.5
235195	Pcsk9	Normal Diet	1		no change		29.5

Appendix II: Laboratory Solutions

All products were purchased from Sigma-Aldrich (Poole, Dorset, UK) unless otherwise stated.

Histology solutions

Luxol Fast Blue (LFB)

1.0 g of Luxol fast blue MBS (Gurr, Poole, England) was mixed with 100 ml of methanol and 5ml of 100% acetic acid.

Cresyl Fast Violet (CFV)

0.5% Cresyl fast violet (TSC Biosciences, Buckingham, United Kingdom) dissolved in distilled water and 0.25% acetic acid.

Tris-buffered saline (TBS)

TBS solution (pH 7.6) contained 50mM Tris and 150mM sodium chloride (NaCl) dissolved in distilled water.

Peroxide blocking solution (3%)

1% (v/v) Hydrogen peroxide (H₂O₂) was diluted in methanol.

Heat Induced Antigen Retrieval

Tri-sodium citrate (TSC)

3.0g of Na₃C₆H₅O₇ (Fisher chemicals, Loughborough, UK) were dissolved in 1 L of distilled water making up a 10mM concentration. The pH was adjusted to 6.5 by adding hydrochloric acid (HCl) or to pH 8 with sodium hydroxide (NaOH).

Ethylenediaminetetraacetic acid (EDTA)

0.3g of EDTA (Fisher Chemicals) was diluted in 1L of distilled water and adjusted to pH8 using sodium hydroxide (NaOH).

Pressure cooker buffers

Menapath Access Revelation a pH 6 antigen retrieval solution from Menarini Diagnostics (Wokingham, United Kingdom) and Access Super RTU pH9 antigen retrieval solution from Menarini Diagnostics

Immunohistochemistry

All immunohistochemistry was performed using an appropriate Vectastain Elite ABC kit to detect goat IgG, rabbit IgG, rat IgG or mouse IgG (Vector Laboratories, Peterborough, United Kingdom).

Blocking solution

1.5% (v/v) normal goat/rabbit/horse blocking serum, diluted in TBS.

Primary antibodies

All antibody dilutions were made with the appropriate blocking solution, i.e. 1.5% species specific normal serum.

Secondary antibodies

0.5% (v/v) secondary biotinylated anti-rabbit IgG / anti-goat IgG / anti-mouse IgG antibody, was diluted in TBS.

Avidin-biotinylated complex with horse radish peroxidase (ABC-HRP)

1.0% (v/v) of reagent A and 1.0% (v/v) of reagent B diluted with 10 mL of TBS.

3,3'-diaminobenzidine (DAB)

The 3,3'-diaminobenzidine (DAB) kit from Vector Laboratories was made by adding 100 µL of buffer, 100 µL of hydrogen and 200 µL of DAB diluted into 5 mL of distilled water.

Polymerase Chain Reaction (PCR)

Forward and Reverse β -actin (ACTB) primers

Primers were optimised by and borrowed from Dr. Mead's laboratory. They were purchased from Sigma-Aldrich (Poole, Dorset, UK) to amplify across exons 3 and 4. The forward primer consisted of 20 base pair (bp) (TGCTGGAAGGTGGACAGTGAGG), as did the reverse primer (CATTGCTGACAGGATGCAGAAGG), and produced a 150 bp product.

Tris-Acetate-EDTA (TAE) buffer

This consisted of 40 mM tris base, 40 mM glacial acetic acid, and 1 mM ethylenediaminetetraacetic acid (EDTA) (pH 8.0).

Agarose gel

3% (w/v) agarose and 0.002% (v/v) ethidium bromide (Thermo Fisher Scientific, Waltham, MA, USA) in TAE buffer.

Molecular weight markers

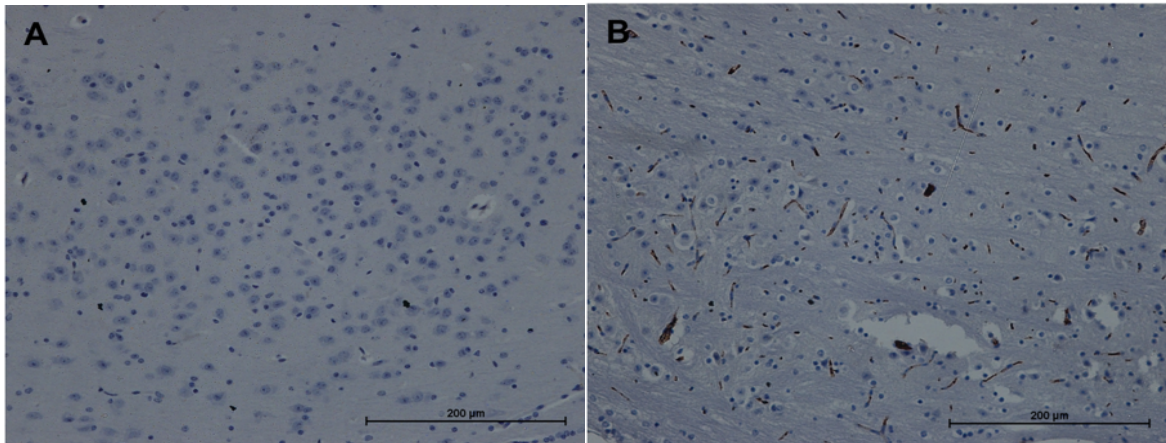
Hyperladder IV (Bioline, UK) was used to determine the size of the nucleic acids and consists of 12 DNA fragments ranging from 500 bp to 25 bp.

Quantitative Polymerase Chain Reaction (qPCR)

Appendix III: Antibody optimisation

Microglia

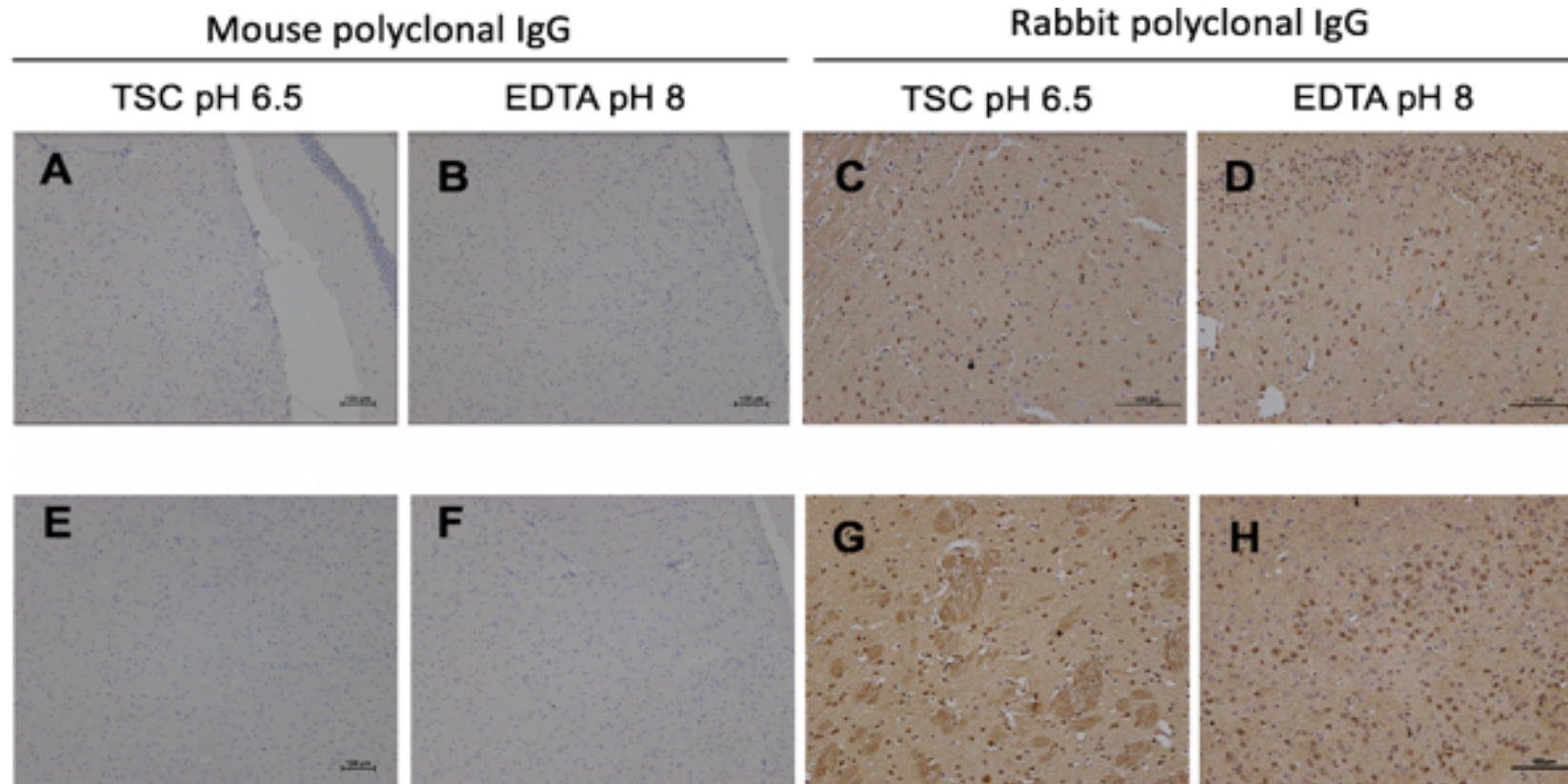
Major histocompatibility complex II



Representative images of f MHC-II optimisation 1:10 in the pressure cooker and microwave.

MHC-II antibody (mouse polyclonal IgG, Dako) an proinflammatory marker. Concentrations of 1:50, 1:25, 1:10 using the microwave and the pressure cooker with pH6 and pH8 reagents for antigen retrieval method were tried. All incubation periods were 1 hour at RT. All conditions showed non-specific immunoreactivity towards blood vessels with no staining of microglia cell bodies or their dendrites. Scale bar represents 200 μm

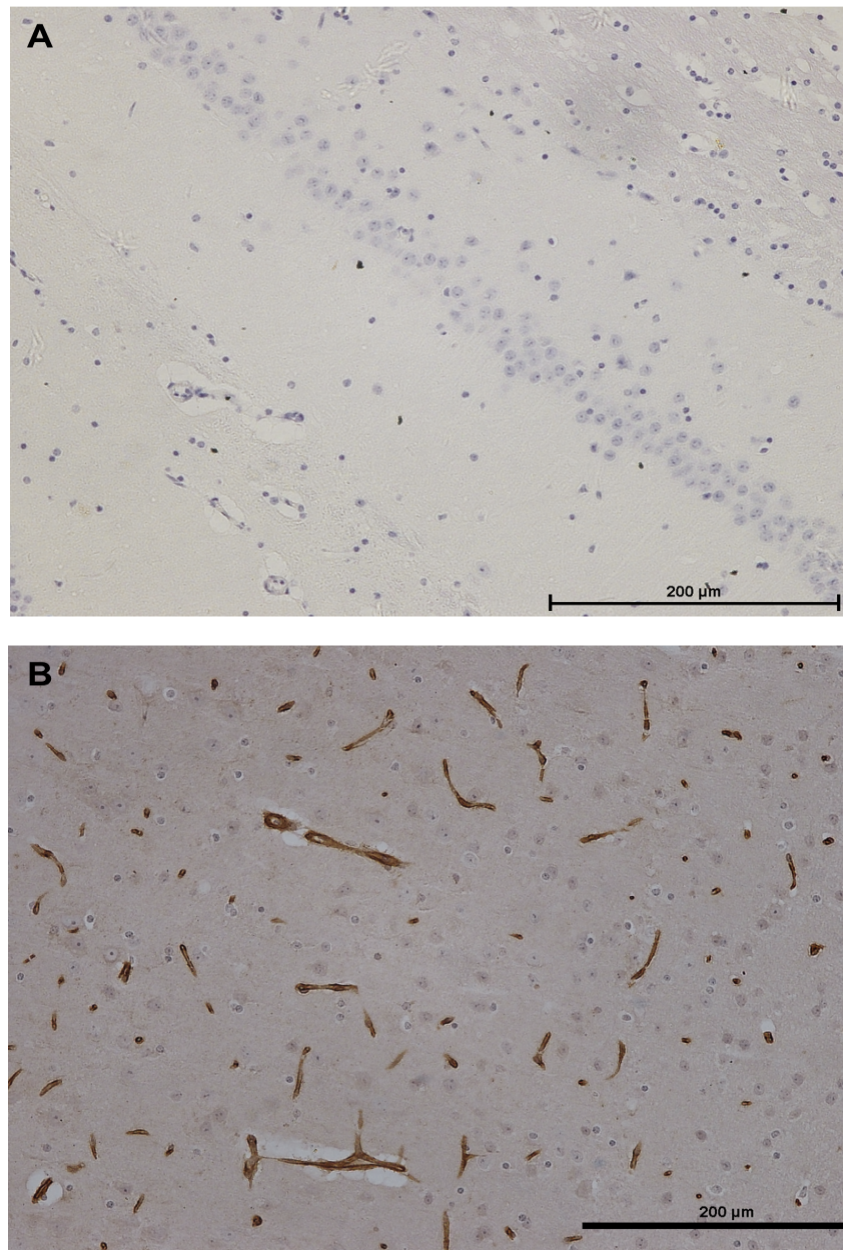
Aquaporin 4



Representative images of AQ4 optimisation using different antibodies, antigen retrieval methods and concentrations.

A - D represent 1:200 dilution. E - H represent 1:100 dilution. 1:50 dilution (not shown) all with 1 hour primary antibody incubation at RT. Anti-AQ4 mouse polyclonal IgG (AbCam) antibody showed no immunoreactivity while Anti-AQ4 rabbit polyclonal IgG (Thermo Fisher) show a high level of background staining and non-specific staining of neuronal nuclei and cytoplasm. As AQ4 is present on astrocytic end-feet it was expected to show immunolabelling of astrocytic processes with intense immunoreactivity around the blood vessels but there was no specific staining using these antibodies. Scale bar represents 100 μm

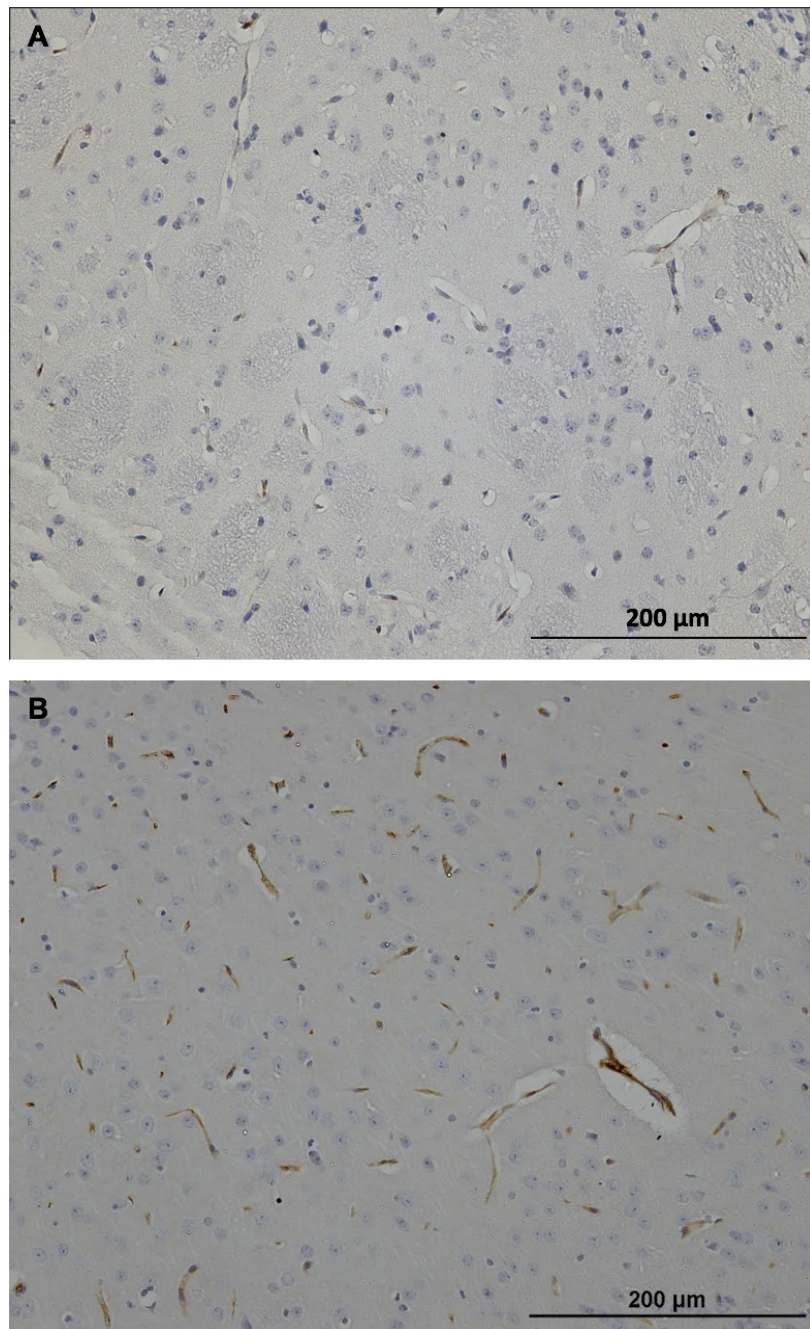
Collagen IV



Representative image of blood vessels immunolabeling using Col-IV in the hippocampus

Negative control showing no Col-IV staining (A). Col-IV⁺ vessels on the thalamus (B) at a 1:250 concentration and 1 hr primary antibody incubation at RT. All heat induced antigen retrieval methods were tried at three different concentrations (1:1000, 1:500, 1:250). No specific immunopositive staining was observed in either the no primary antibody or isotype negative control, Col-IV immunolabelled the basement membrane resulting on a thick and dense morphology surrounding blood vessels. However there was background staining. Scale bar represents 200 μm

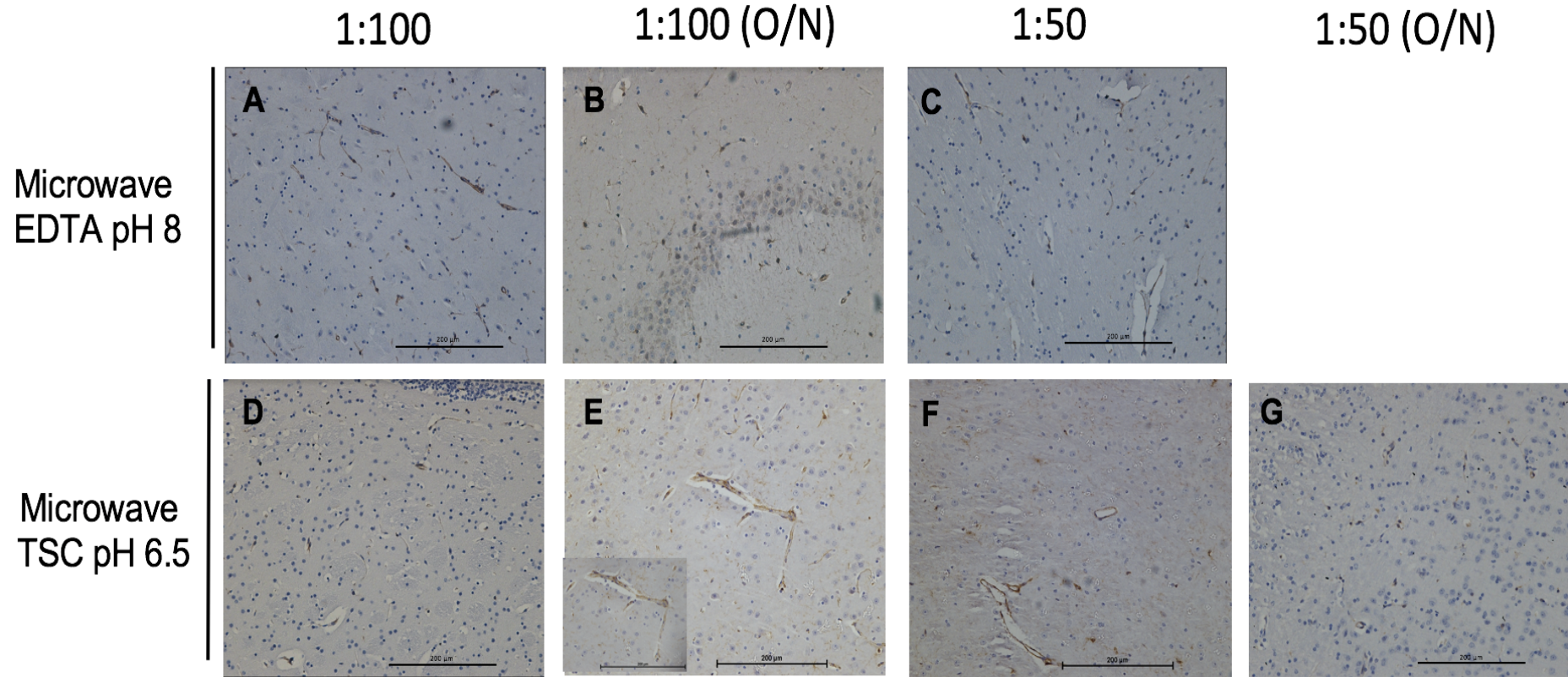
CD31



Representative image of CD31 optimisation as an endothelial cell marker.

Negative isotype control showed some low intensity specific immunopositive staining CD31 staining (A). Anti-CD31 antibody (mouse monoclonal IgG, DAKO) showed immunoreactive staining on endothelial cells delineating blood vessels (B) using the microwave with TSC (pH 6.5) at 1:500 concentration and 1 hr RT incubation period. The staining observed resulted on very faint labelling of different size vessels but the nuclei of the endothelial cells can be seen. Scale bar represents 200 µm

PDGFR- β



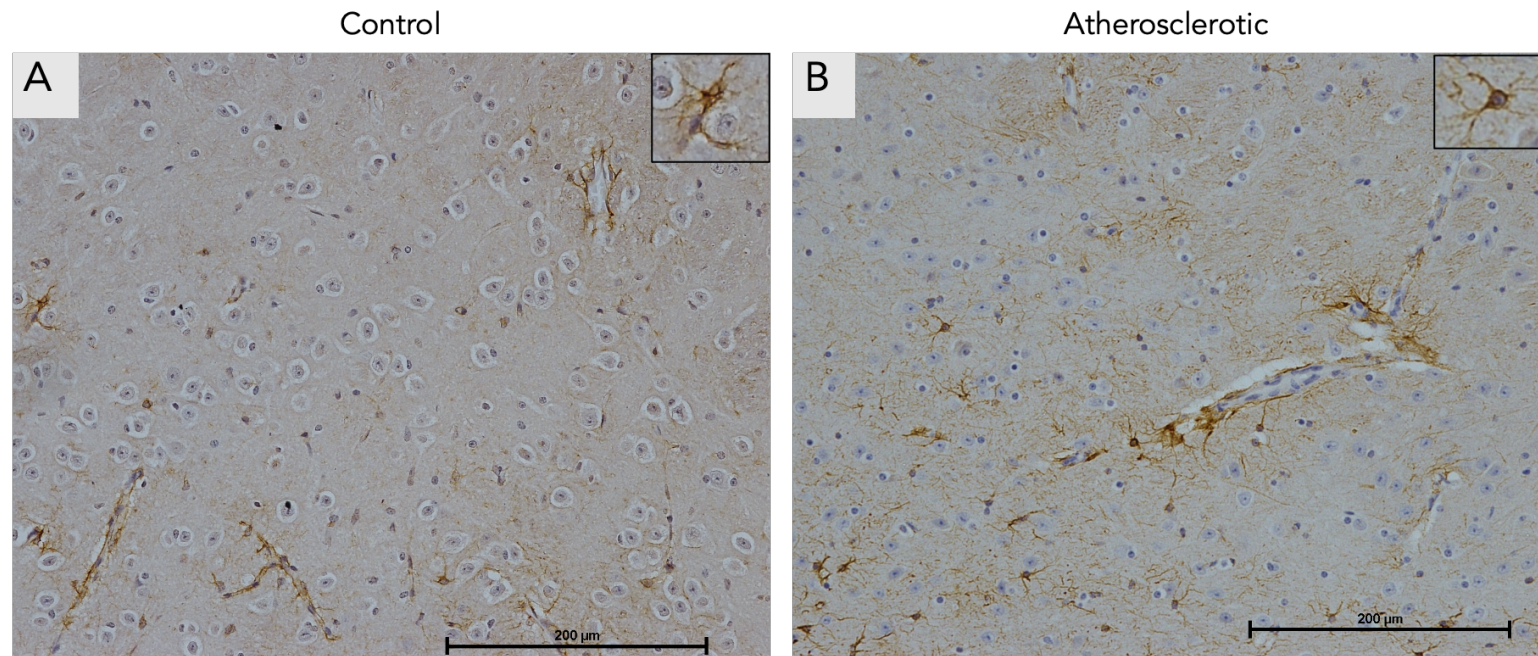
PDGF-R β immunopositive stained pericytes on mouse tissue.

PDGF-R β ⁺ pericytes can be observed surrounding the blood vessels (E). Different antigen retrieval methods led to staining of the tissue such as TSC pH 8 on the microwave at a 1:50 concentration (A). However, the most effective protocol for the PDGF-R β antibody was the microwave with TSC pH6.5 at a 1:100 concentration with an overnight incubation period (E). Scale bar represents 200 μ .

Appendix IV: Characterisation of the thalamus and striatum of *ApoE*^{-/-} cohort 1 mice

Glial fibrillary acidic protein

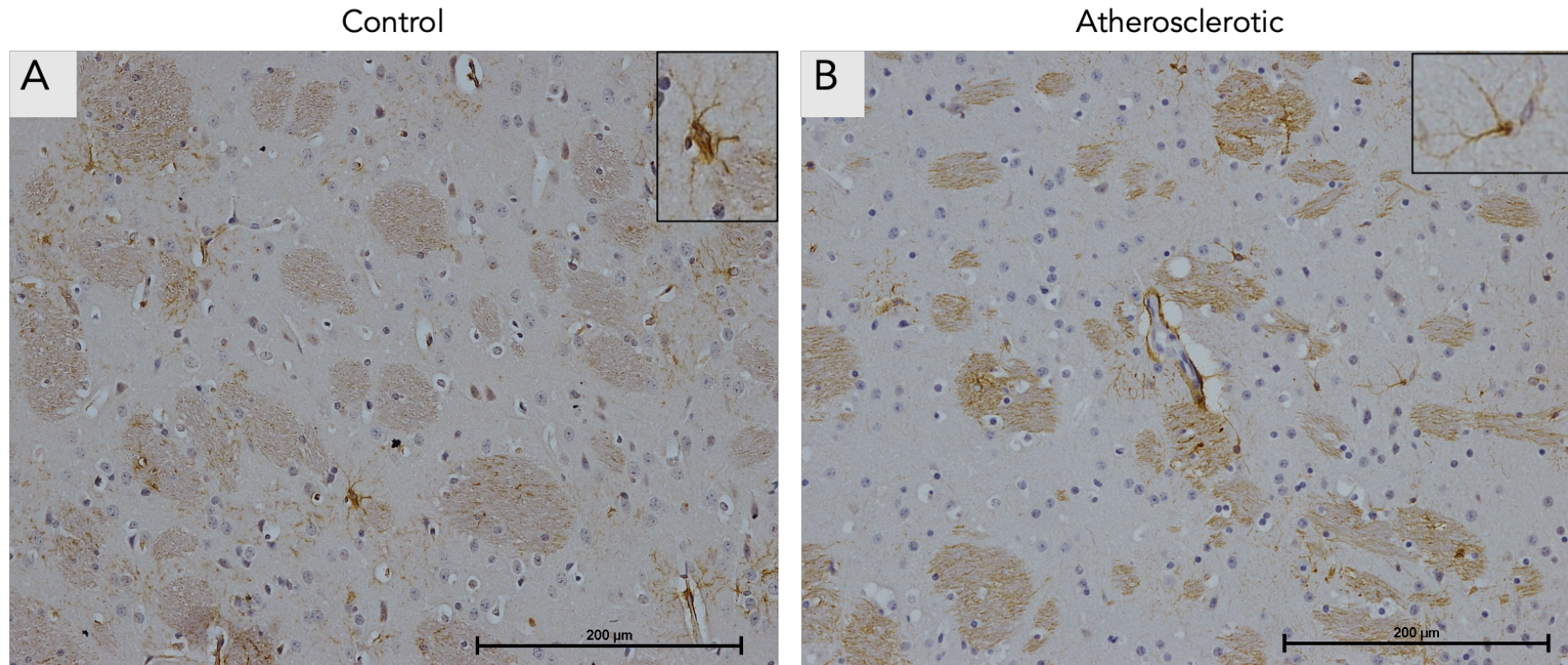
Thalamus



Thalamus of *apoE*^{-/-} from cohort 1 with GFAP⁺ astrocytes

GFAP immunolabelled the astrocyte cell body and fine branching processes resembling the typical stellate astrocyte profile in the thalamus with a uniform, but, sparse distribution. Control mice showed fewer processes compared to atherosclerotic mice. However, the astrocytic end-feet surrounding the vessels are more noticeable in controls than in atherosclerotic mice. Scale bar 200 µm.

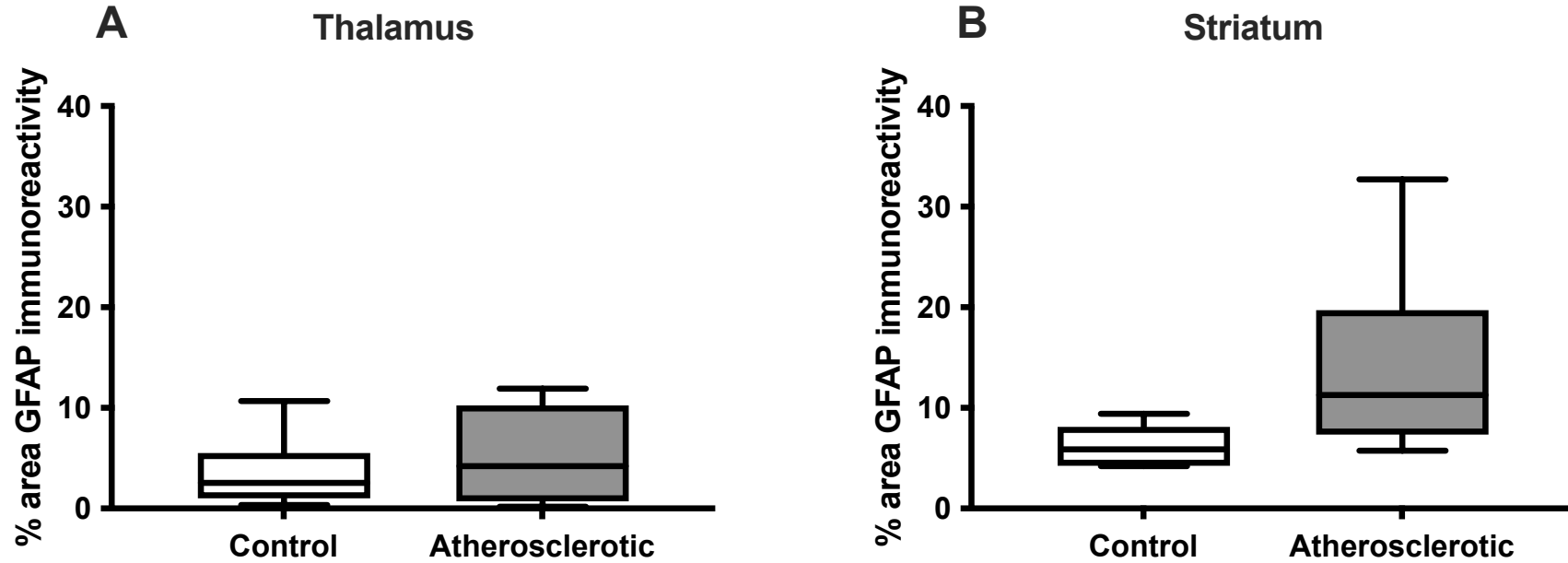
Striatum



The striatum of apoE^{-/-} from cohort 1 with GFAP⁺ astrocytes

Control diet in the right-hand side and atherosclerotic on the left-hand side. Control mice showed a low number of sparse GFAP⁺ astrocytic cell bodies with a low number of short processes being noticeable, also, patches of fine astrocytic processes can be appreciated. These are striatopallidal fibres, also known as pencil fibres of the striatum. Scale bar 200 µm.

GFAP statistical analysis of the Thalamus and Striatum



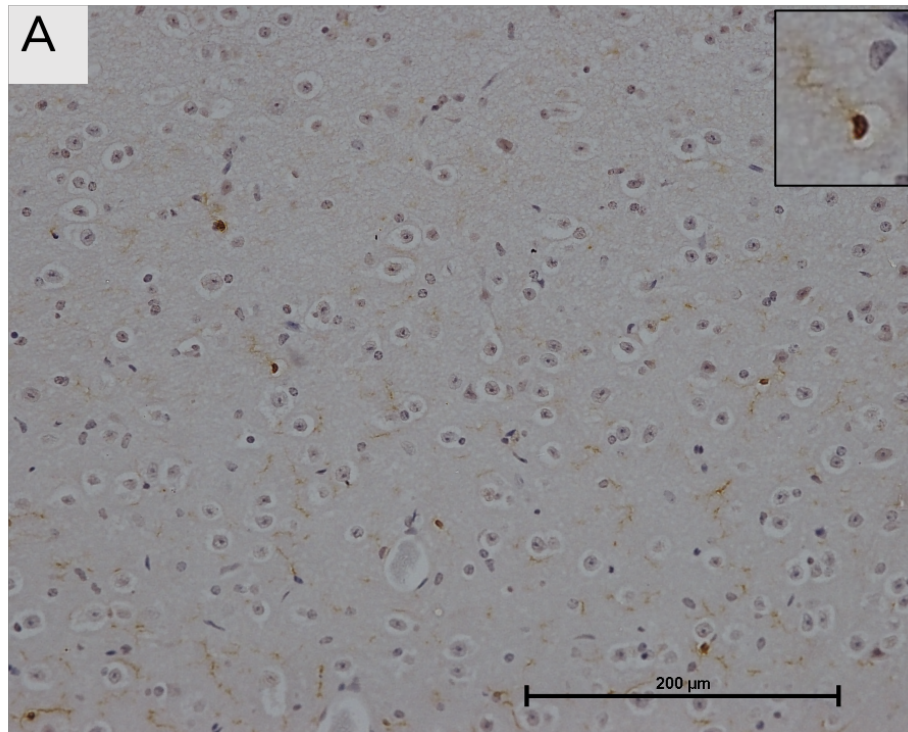
No difference between control and atherosclerotic mice from the cohort 1 in the thalamus or striatum of

The thalamus of control mice was lower than atherosclerotic mice following a similar trend as the other brain areas. The immunoreactivity of astrocytes in atherosclerotic mice was higher to control mice however this did not pass Bonferroni correction.

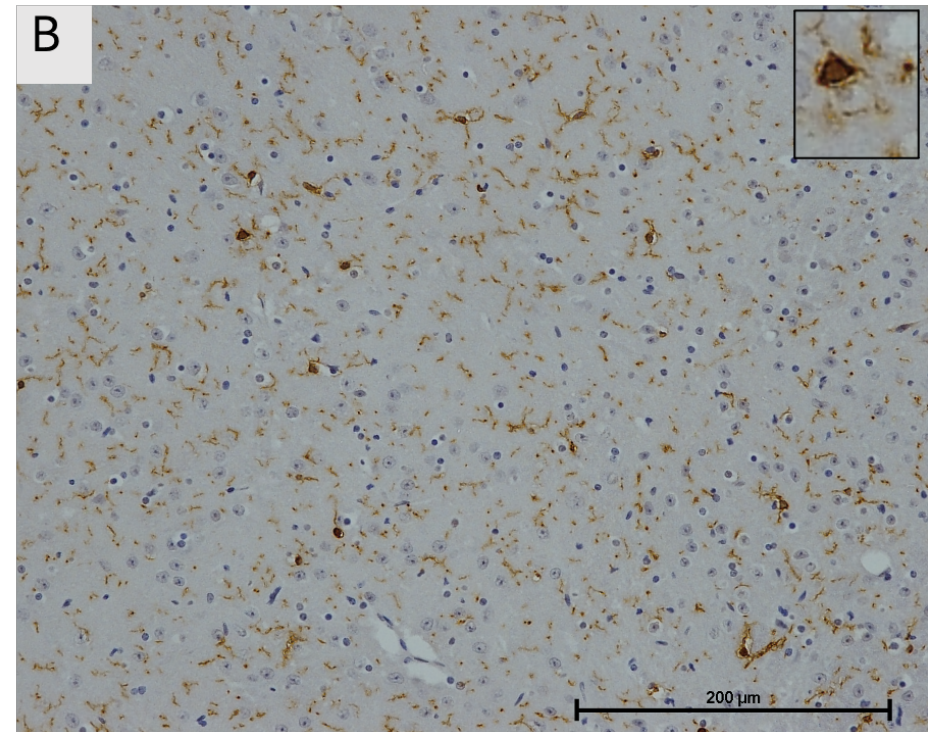
IBA-1

Thalamus

Control



Atherosclerotic

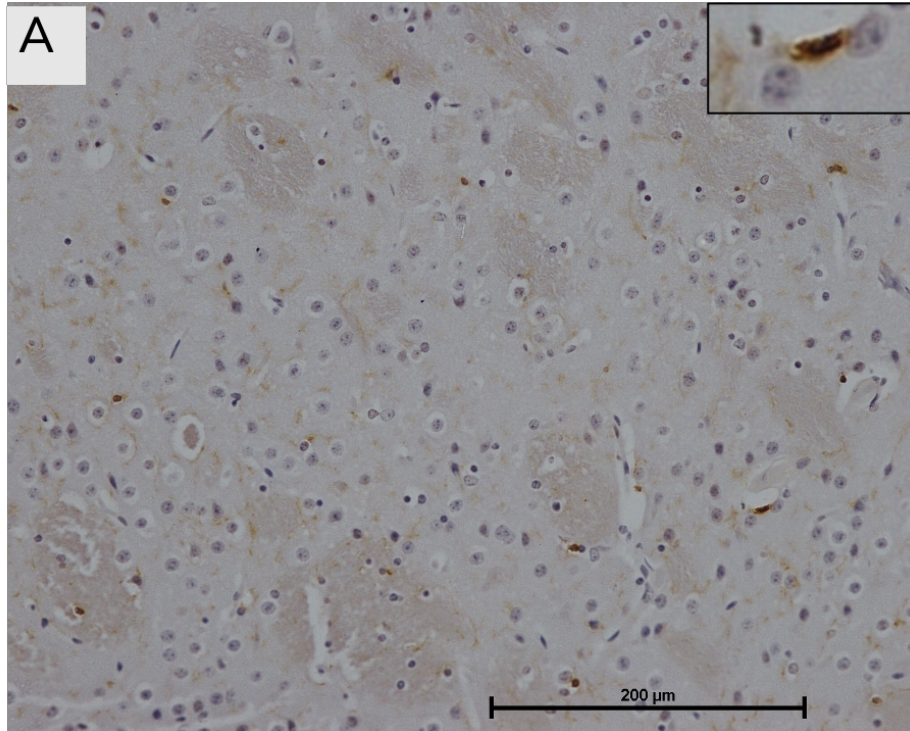


Representation of IBA-1 microglia in the thalamus of *ApoE*^{-/-}

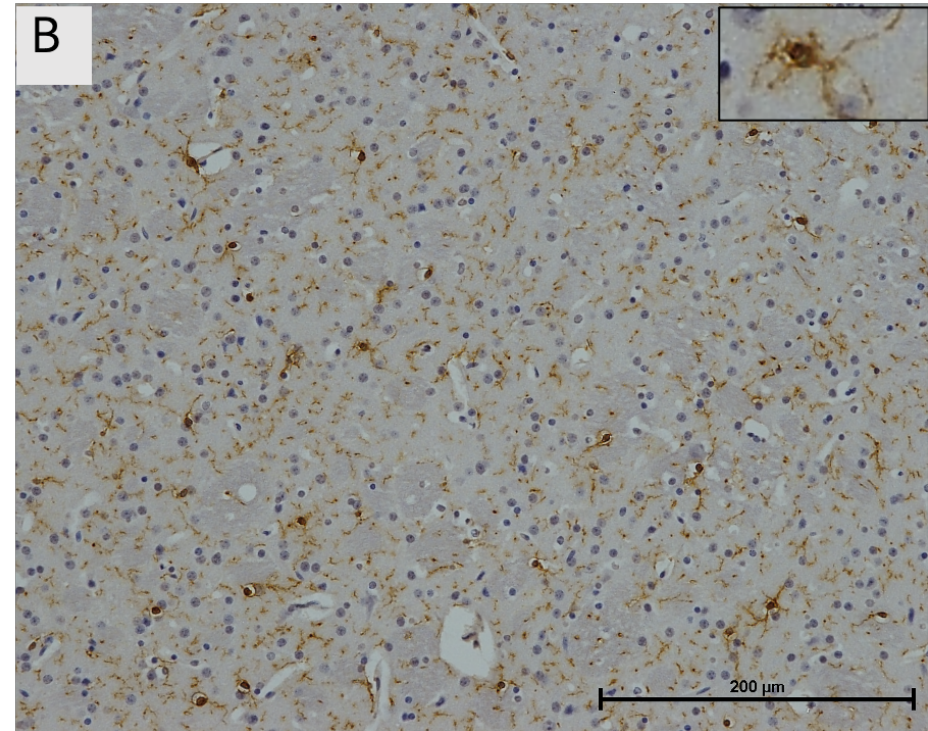
Control mice (A) showed a low number of sparse IBA-1 microglia with few visible cell bodies and short processes. Atherosclerotic (B) showed more intense staining on cell bodies and processes and a discontinued morphology of the processes. Scale bar 200 μm.

Striatum

Control



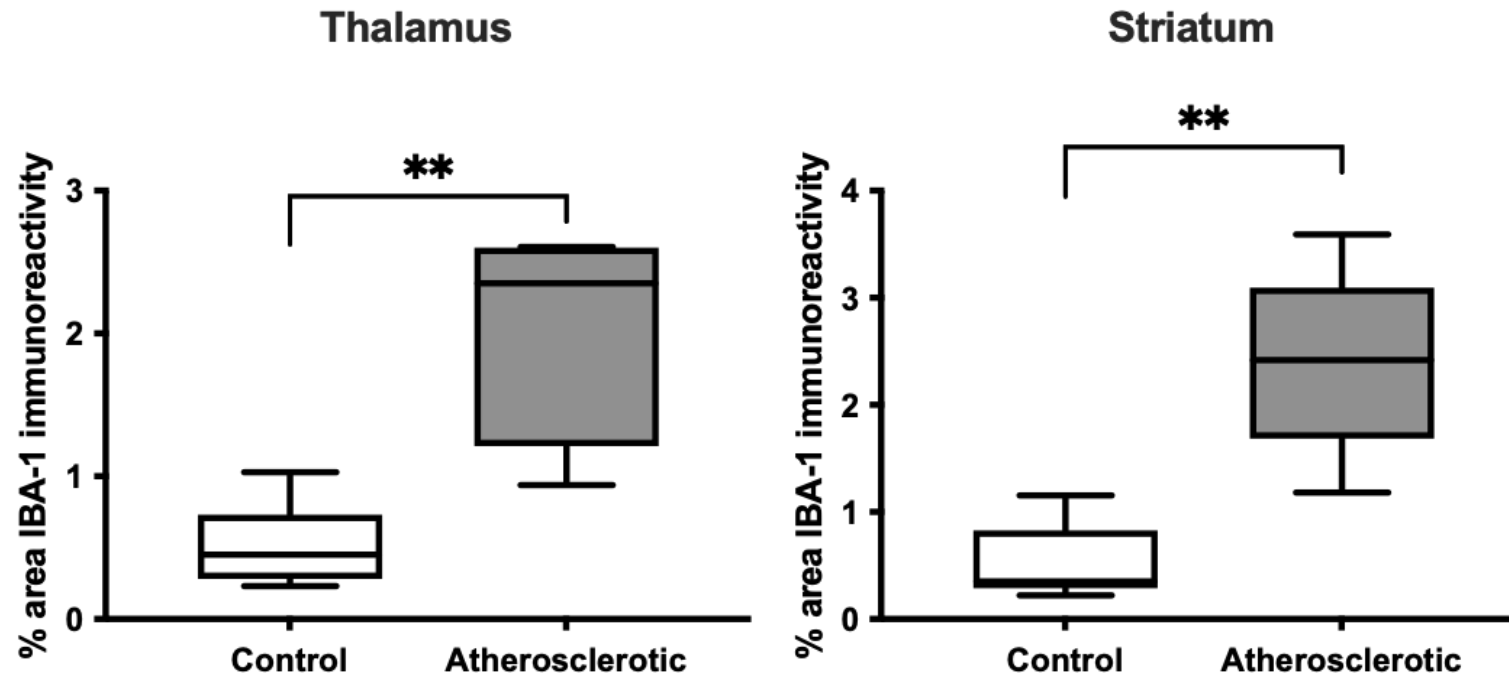
Atherosclerotic



Representation of IBA-1 microglia in the striatum of *ApoE*^{-/-}

Control mice (A) showed a low number of sparse IBA-1 microglia with few visible cell bodies and short processes. Atherosclerotic (B) showed more intense staining on cell bodies and processes and a discontinued morphology of the processes. Scale bar 200 μm.

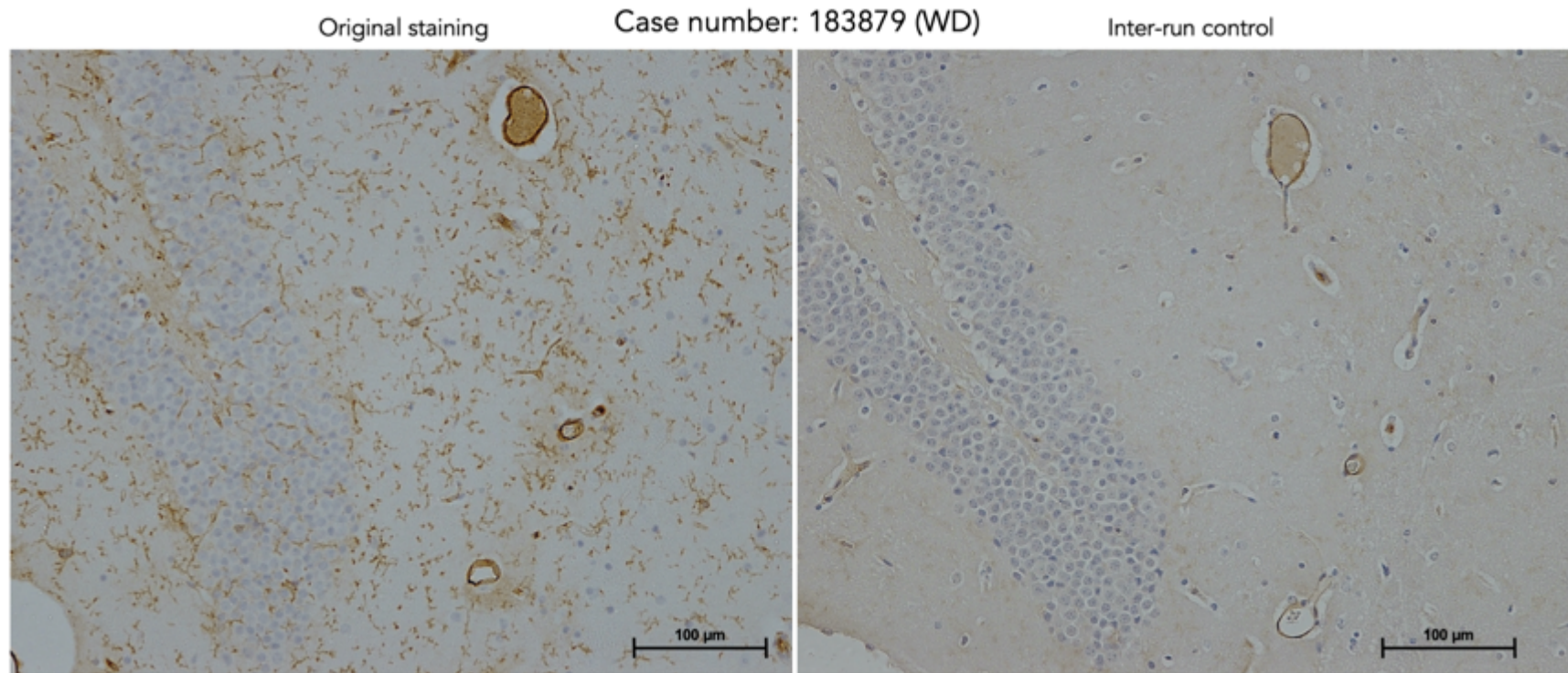
IBA-1 statistical analysis of the Thalamus and Striatum



Significant increase of microglia IBA-1 % area of immunoreactivity in the thalamus and striatum of *ApoE*^{-/-} cohort 1 atherosclerotic mice compared to controls

The thalamus and striatum of *ApoE*^{-/-} atherosclerotic mice was higher than control mice.

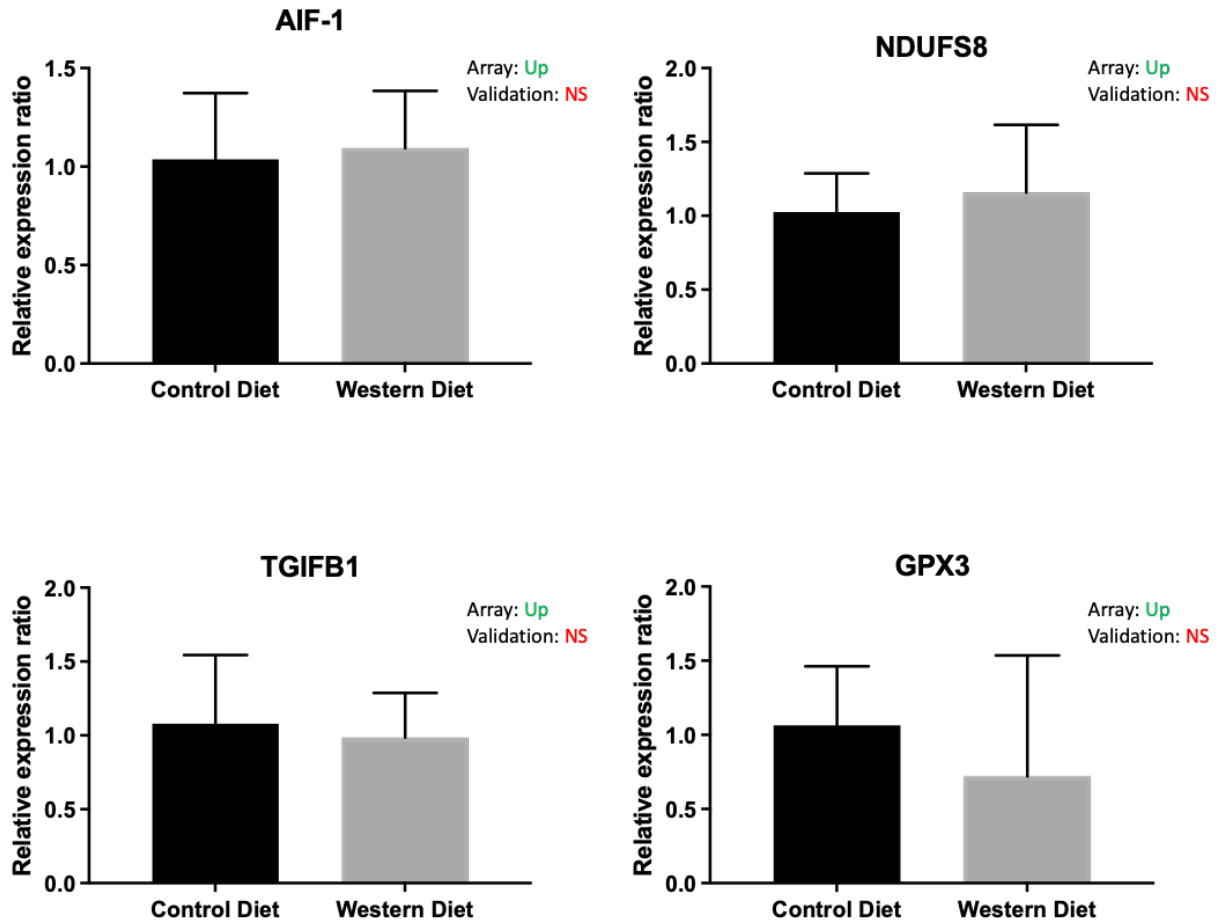
ICAM-1 immunoreactivity



Original staining case comparison of ICAM-1 staining

The same case (183879) was stained on two separate occasions to identify a similar level of IBA-1 immunoreactivity. The original staining (A) at the time where all cases from cohort 1 were stained. The same case (183879) stained at the time cohort 2 was stained (B). The images show a different pattern of staining, with the second staining showing a weak ICAM-1 immunoreactivity with a low number of endothelial cells in blood vessels showing some staining, and no ICAM⁺ microglia. Scale bar represents 100 µm.

Appendix VI: qRT-PCR of the cerebral cortex of *ApoE*^{-/-} cohort 2 mice



Investigation of neuroinflammatory and oxidative phosphorylation up-regulated genes in the cerebral cortex by qRT-PCR.

The cerebral cortex of *ApoE*^{-/-} mice fed with a western diet (atherosclerotic) was examined after isolation with LCM. Changes in the mitochondrial Complex I genes *NDUFS8* were validated by qRT-PCR. (Mann-Whitney U test; data are means ± SEM; n=3 in duplicate).

Appendix VI: List of differentially expressed transcripts in the hippocampus of control and atherosclerotic ApoE^{-/-} mouse cohort 2